Experimental and Numerical Study of Micro-Fluidic Oscillators for Flow Separation Control

Shiqi Wang

To cite this version:

Shiqi Wang. Experimental and Numerical Study of Micro-Fluidic Oscillators for Flow Separation Control. Fluid mechanics [physics.class-ph]. INSA de Toulouse, 2017. English. NNT : 2017ISAT0017 . tel-01710768

HAL Id: tel-01710768

https://theses.hal.science/tel-01710768

Submitted on 16 Feb 2018

HAL is a multi-disciplinary open access archive for the deposit and dissemination of scientific research documents, whether they are published or not. The documents may come from teaching and research institutions in France or abroad, or from public or private research centers.

L'archive ouverte pluridisciplinaire **HAL**, est destinée au dépôt et à la diffusion de documents scientifiques de niveau recherche, publiés ou non, émanant des établissements d'enseignement et de recherche français ou étrangers, des laboratoires publics ou privés.

THÈSE

En vue de l'obtention du

DOCTORAT DE L'UNIVERSITÉ DE TOULOUSE

Délivré par:
Institut National des Sciences Appliquées de Toulouse (INSA de Toulouse)
Discipline ou spécialité:
Dynamiques des fluides

Présentée et soutenue par
WANG Shiqi

Le **1 Septembre 2017**

Titre de la thèse:
Experimental and Numerical Study of Micro-Fluidic Oscillators for Flow Separation Control

---

JURY:
Laurent KEIRSBULCK, Professeur. Université de Valencienne. Rapporteur
Sedat TARDU, Maître de Conférences. Institut Polytechnique de Grenoble. Rapporteur
Irina GRAUR MARTIN, Professeur. Université d'Aix-Marseille. Examinatrice
Emmanuel GUILMINEAU, Chargé de Recherche. Ecole Centrale de Nantes. Examinateur
Nicolas MAZELLIER, Maître de Conférences. Université d'Orléans. Examinateur
Stéphane COLIN, Professeur. INSA de Toulouse. Examinateur.
Lucien BALDAS, Maître de Conférences. INSA de Toulouse. Directeur de Thèse
Azeddine KOURTA, Professeur. Université d'Orléans. Directeur de Thèse

---

Ecole doctorale :
Aéronautique, Astronautique (AA)
Unité de recherche :
Institut Clément Ader (ICA, CNRS UMR 5312)
Directeur(s) de Thèse :
(Directeur) Lucien BALDAS, Maître de conférences, INSA de Toulouse
(Directeur) Azeddine KOURTA, Professeur, Université d'Orléans

Acknowledgement

The present research work has been carried out in Institut Clément Ader (ICA) of Institut National des Sciences Appliquées de Toulouse (INSA-Toulouse) with the collaboration of PRISME Laboratory of Orléans University during years 2013-2017 in the framework of GdR contrôle des décollements.

Foremost, I would like to express my sincere gratitude to my supervisors, Dr. Lucien Baldas and Prof. Azeddine Kourta who had proposed this project and offered me this precious chance persuing a degree abroad. Moreover, without their continuous interest, support and guidance during this study, I can't accomplish it so smoothly.

Next, I would like to express my sincere thanks to Prof. Stéphane Colin and Dr. Nicolas Mazellier, who had contributed a lot of works, shared many helpful discussions and meaningful ideas during this study.

Also, I would like to thank Dr. Stéphane Orieux, Mr. Nicolas Laurien and Mr. Stéphane Loyer for their kindly help in preparing and doing the experimental tests during this study.

I am also most grateful to the reviewers of my thesis, Prof. Laurent Keirsbulck and Dr. Sedat Tardu, and other members in my defense committee, Prof. Irina Graur Martin and Dr. Emmanuel Guilmineau for their valuable feedbacks.

It is pleasure to thank my colleagues and also my friends in my team, Jie Chen, Hacene, Ernane, Yanfeng, Macros, Christine, Pascale, Ahmad, Varun, Guillermo, Daniel, Dominique, etc. for their valuable help and support both in my work and life. Many thanks also to the friends I have met in the lab and life, to name Tao Li, Jian Fu, Yiwei, Xiaohu, C. Chen, Donghai, Lunde, R. Xue, etc. who had made my life in Toulouse so colorful.

I appreciate a lot the scholarship offered by China Scholarship Council (CSC).

I owe special thanks to my wife, Nan Zhao, for supporting me during the hardships of such a long journey, for being patience and, for believing in me.

And last, but not least, I thank my parents, An'yu Wang and Qiuxiang Bai, and my sister, Xiaoxing Wang, who continuously encouraged me over the past years to go and find my way, even when it took me so far away from home. I feel very indebted to my family for their continuous encouragement and support to my study in abroad.

Abstract

Fluidic oscillators which can generate periodic excitations are very promising for active flow control applications, due to their reliability and robustness, as their internal flow oscillation is totally self-induced and self-sustained. The main objective of this work is to identify the underlying mechanisms controlling the dynamics of this kind of fluidic oscillator and to propose guiding lines for the design of oscillators. Experimental analysis of several oscillator prototypes and associated numerical simulations have permitted to explain that the jet switching in this kind of oscillator is controlled by pressure gradients in two critical parts of the device. From these analyses, a simple function has been proposed to estimate the oscillation frequency. Two synchronization methods, allowing the control of the phase lag between the actuators, have been proposed and validated experimentally and by numerical simulations. An array of micro-fluidic oscillators has then been designed and tested on a ramp separated flow, showing much higher efficiency compared to other kind of fluidic actuators tested on similar wall flows in previous studies.

KEY WORDS :

Fluidic Oscillator, Coanda effect, Active flow control, Ramp flow, PIV, OpenFoam, Hot-wire anemometry

Résumé

Les oscillateurs fluidiques qui peuvent générer des excitations périodiques sont des actionneurs très prometteurs pour des applications de contrôle actif des écoulements. Les oscillations sont en effet complètement auto-induites et produites en l'absence de parties mobiles ce qui rend ces actionneurs très intéressants en termes de fiabilité et de robustesse. Ce travail de thèse avait pour objectif principal d'identifier les mécanismes physiques qui contrôlent la dynamique de fonctionnement de ce type d'oscillateurs fluidiques et de proposer des lignes directrices pour la conception d'oscillateurs dont les performances soient adaptées aux applications de contrôle d'écoulements envisagées. L'analyse expérimentale de plusieurs prototypes couplée à des simulations numériques a permis de mettre en évidence que le mécanisme de basculement du jet dans ce type d'oscillateurs est contrôlé par les gradients de pression existants au niveau de deux parties critiques de ces actionneurs. A partir de cette analyse, une relation simple a été établie permettant d'estimer la fréquence des oscillations. Deux méthodes de synchronisation, permettant le contrôle du déphasage entre les actionneurs, ont été proposées et validées expérimentalement ainsi qu'à l'aide de simulations numériques. Une matrice de micro-oscillateurs fluidiques a été conçue, fabriquée et finalement intégrée sur une rampe installée en soufflerie. L'analyse expérimentale de son efficacité pour le contrôle de l'écoulement séparé a mis en évidence un gain important par rapport aux résultats obtenus lors de travaux précédents sur des écoulements de paroi similaires à l'aide d'autres types d'actionneurs fluidiques.

MOTS CLES:

Oscillateur fluidique, Effet Coanda, Contrôle actif d'écoulement, PIV, Ecoulement sur une rampe, OpenFoam, Anémométrie Fil Chaud

Résumé long en français

Au cours des dernières décennies, de nombreux travaux ont concerné l'étude des actionneurs pour le contrôle actif d'écoulement, avec différents objectifs tels que la réduction de la traînée sur les corps non profilés [1], l'augmentation de la portance des surfaces portantes [2,3] ou encore l'amélioration du mélange dans les chambres de combustion [4,5], etc. De nombreux travaux de recherche (par ex. Greenblatt and Wygnansky [6]) ont montré que, comparativement aux méthodes de contrôle passives traditionnelles ou aux méthodes d'aspiration ou de soufflage continu, le contrôle actif d'écoulement basé sur des excitations fluidiques périodiques est beaucoup plus efficace, avec un gain de deux ordres de grandeur en termes de quantité de mouvement ajoutée. Ces perturbations périodiques peuvent être fournies par différents types d'actionneurs tels que les actionneurs ZNMF (Zero Net Mass Flow), les actionneurs plasma et les MEMS (Micro-Electro-Mechanical-Systems)[7]. Parmi eux, les oscillateurs fluidiques peuvent émettre des jets oscillants dans une grande plage de fréquence et de vitesse de fonctionnement lorsqu'ils sont alimentés en fluide sous pression, sans nécessiter de partie mobile car leurs oscillations sont totalement auto induites et auto-entretenues et ne dépendent que de la dynamique interne de l'écoulement, ce qui constitue un excellent avantage en termes de fiabilité et de robustesse [8-10].

Le comportement d'un oscillateur fluidique à double boucle de rétroaction produisant deux jets pulsés est tout à fait différent de celui d'autres types d'oscillateurs basés sur l'effet Coanda, comme l'oscillateur fluidique sonique [37] ou l'oscillateur fluidique à jet balayant [43] et ne peut pas être clairement expliqué par les théories existantes. Ce travail de thèse s'est ainsi focalisé sur la clarification des mécanismes sous-jacents qui contrôlent la dynamique de ce type d'oscillateur fluidique dans le but de proposer des outils d'aide à la conception d'oscillateurs offrant les performances (fréquence et vitesse du jet pulsé) attendues pour les applications de contrôle auxquelles ils sont destinés. A partir de cette analyse, une matrice d'oscillateurs a aussi été développée et testée pour contrôler un écoulement séparé sur une rampe.

Après une brève introduction sur les différentes stratégies de contrôle des écoulements et sur les actionneurs fluidiques typiques, l'étude bibliographique a porté sur les différents types d'oscillateurs fluidiques, soulignant l'intérêt d'utiliser des oscillateurs fluidiques à double boucle de rétroaction générant deux jets pulsés pour les applications de contrôle d'écoulements et mettant en évidence le manque de connaissances sur les mécanismes physiques régissant leur comportement. Le cœur de ce travail de thèse a ensuite été présenté en quatre parties principales, concernant respectivement l'analyse expérimentale des performances de 4 prototypes d'oscillateurs, la simulation numérique des écoulements instationnaires dans ces oscillateurs pour identifier les principaux mécanismes physiques contrôlant leur dynamique de fonctionnement, le développement de procédés de synchronisation d'un ensemble d'oscillateurs et l'application de ce réseau d'actionneurs fluidiques à la commande de l'écoulement séparé sur une rampe.

Quatre nouveaux prototypes d'oscillateurs ont été conçus et caractérisés expérimentalement à la fois par anémométrie fil chaud et à l'aide de capteurs de pression à large bande passante. Ces mesures ont confirmé que la vitesse moyenne des jets pulsés générés est contrôlée par l'aire de la section du col de la buse d'alimentation et la pression totale d'entrée. Cependant, l'amplitude de la vitesse de sortie et son évolution avec le temps peuvent également être affectées par la section du col de la buse ainsi que par d'autres facteurs géométriques internes tels que la symétrie interne du dispositif. En outre, la longueur et le diamètre de la boucle de rétroaction jouent un rôle important sur les performances de l'oscillateur, en particulier sa réponse en fréquence. Une relation, déduite des mesures expérimentales, a été proposée pour estimer la fréquence d'oscillation en fonction de la longueur de ces boucles de rétroaction.

Les modèles numériques développés sous OpenFOAM ont permis une estimation assez précise de la fréquence de fonctionnement. Une analyse détaillée des résultats des simulations a montré que, dans ce type d'oscillateur fluidique, la déviation du jet principal est provoquée non seulement par la différence de pression entre les ports de contrôle de l'oscillateur, mais aussi par la différence de pression entre ses branches. Dans les configurations étudiées, la valeur seuil de la différence de pression entre les ports de contrôle permettant de provoquer par elle-même la déviation du jet est beaucoup plus élevée que la différence de pression nécessaire entre les branches. Cependant, lors de la combinaison de ces deux effets, le basculement du jet devient beaucoup plus facile.

On a montré que le mécanisme de commutation était lié à la propagation aller-retour des ondes de pression dans les branches de l'oscillateur et ses boucles de rétroaction: juste après la commutation du jet, une onde de compression à haute pression se propage dans la branche dans laquelle le jet est attaché et dans la boucle de rétroaction correspondante tandis qu'une onde de détente basse pression se propage dans l'autre branche et l'autre boucle de retour. Lorsque ces ondes arrivent au niveau des ports de contrôle, elles se réfléchissent et le jet est déstabilisé par l'inversion de la différence de pression à sa base. La commutation se produit lorsque les ondes de pression réfléchies ont atteint la base des branches provoquant l'inversion de la différence de pression entre les branches. Les ondes de pression se propageant approximativement à la vitesse du son C_o, la période d'oscillation T peut être liée à la longueur de boucle de retour L_f par la relation nouvellement proposée $T = 4L_f / C_o$, ce qui confirme la relation empirique déduite des résultats expérimentaux. Une relation plus précise a également été proposée pour calculer la fréquence d'oscillation, en tenant compte de la vitesse de l'écoulement dans les branches et les boucles de rétroaction de l'oscillateur. Ces simulations numériques ont également permis d'expliquer la non-dépendance de la fréquence d'oscillation à la pression d'alimentation.

Deux nouvelles méthodes, basées sur des interconnexions entre les boucles de rétroaction, ont été proposées pour synchroniser deux oscillateurs similaires. Ces deux méthodes ont été validées expérimentalement et numériquement. La première conduit à une fréquence proche de celle des oscillateurs fonctionnant séparément et les jets pulsés générés par ces deux dispositifs sont quasiment en opposition de phase. La deuxième méthode conduit à une fréquence beaucoup plus faible et une différence de phase entre les actionneurs proche d'un quart de période. Les simulations numériques ont également permis d'expliquer le comportement dynamique des oscillateurs synchronisés et de prouver la faisabilité de la synchronisation d'un réseau de 4 oscillateurs fluidiques en utilisant la première méthode d'interconnexion.

Dans la dernière partie de ce travail, 12 oscillateurs fluidiques identiques ont été intégrés dans une rampe pour tester leur capacité à contrôler la séparation de l'écoulement. La synchronisation de ce réseau d'oscillateurs fluidiques en utilisant la première méthode d'interconnexion a été validée expérimentalement. Les champs d'écoulement moyen et fluctuant sur la rampe, avec et sans action de ce réseau d'oscillateurs fluidiques, ont été acquis par PIV dans une soufflerie. Les résultats obtenus montrent que ce réseau d'oscillateurs fluidiques est très prometteur, compte tenu du faible coefficient de quantité de mouvement $C\mu$ nécessaire pour éliminer totalement la séparation, comparativement aux valeurs optimales trouvées dans la littérature. L'analyse du champ moyen turbulent a montré que les mécanismes de contrôle sous-jacents étaient liés à une augmentation de la turbulence dans la région de la rampe due aux jets pulsés générés par les oscillateurs, conduisant à une augmentation nette par rapport au cas sans actionnement, de la force transférée de l'écoulement principal vers la couche de cisaillement.

Contents

Nomenclature

Roman Symbols

A_o	outlet slot area (m^2)
A_t	throat section area (m^2)
c	wave propagation velocity ($\mathrm{m\ s}^{-1}$)
c_a	bulk propagation velocity ($\mathrm{m\ s}^{-1}$)
C	average pressure wave propagation velocity inside the oscillator ($\mathrm{m\ s}^{-1}$)
C_{CFL}	cell courant number
C_d	drag coefficient
C_l	lift coefficient
C_o	speed of sound in ambient environment ($\mathrm{m\ s}^{-1}$)
C_μ	injection momentum coefficient
D	diameter of feedback tube (m)
D'	width of feedback channel (m)
F^+	non-dimensional oscillation frequency
f	oscillation frequency (Hz)
f_m	measured oscillation frequency (Hz)
$f_\mathrm{s\text{-}s}$	oscillation frequency simulated from scanned geometry (Hz)
$f_\mathrm{s\text{-}d}$	oscillation frequency simulated from designed geometry (Hz)
H	depth of a fluidic oscillator (m)
h	ramp step height (m)
K	constant for air ($\mathrm{m\ s}^{-1}\ \mathrm{K}^{-0.5}$)
l	length or distance (m)
L	characteristic length (m)
Lr	recirculation region length (m)
L_t	length of feedback loop connection tube (m)
L_f	feedback loop length (m)
m	mass flux (kg)
$\dot{m}$	mass flow rate (kg/s)
m_b	blowing mass flow rate (kg/s)
Ma	Mach number

P	pressure (Pa)
P_{cr}	critical pressure (Pa)
P_{atm}	atmosphere pressure (Pa)
P_{i}	inlet total pressure (Pa)
ΔP	pressure difference (Pa)
$\mathbf{P}$	production of turbulent kinetic energy (m^2 s^{-3})
R	aerodynamic force on an airfoil (N)
R_d	drag force on an airfoil (N)
R_l	lift force on an airfoil (N)
R_g	specific gas constant (J kg^{-1} K^{-1})
Re	Reynolds number
S	surface area of an airfoil (m^2)
Sr	Strouhal number
Sr_{m}	modified Strouhal number
t	time (s)
t_d	deflection time (s)
Δt	basic time unit (s)
T	oscillation period (s)
T_a	temperature (K)
T_{atm}	atmosphere temperature (K)
$T_i{}^*$	inlet total temperature (K)
ΔT	time difference or time duration (s)
u	local fluid velocity (m s^{-1})
u'	fluctuation of velocity in *x* direction (m s^{-1})
U	velocity (m s^{-1})
U_∞	free stream velocity (m s^{-1})
U_b	blowing jet velocity (m s^{-1})
$U_b^{\max}$	maximum velocity of unsteady blowing jet (m s^{-1})
U_b^{rms}	root mean square value of the velocity of unsteady blowing jet (m s^{-1})
U_x	velocity in x direction (m s^{-1})
U_y	velocity in y direction (m s^{-1})
U_a	area-averaged velocity (m s^{-1})

v'	fluctuation component of velocity in y direction (m s^{-1})
V_R	velocity ratio
w	throat section width of a fluidic oscillator (m)
Y^+	dimensionless wall distance

Greek Symbols

τ_t	transmission time (s)
τ_s	switching time (s)
ξ	empirical constant
γ	heat capacity ratio
λ	dimensionless velocity coefficient
δ	boundary layer thickness (m)
μ	dynamic viscosity (kg m^{-1} s^{-1})
ν	kinematic viscosity (m^2 s^{-1})
η	incidence angle of an airfoil (^{o})
ω	span width of a controlled flow (m)
ρ	density (kg m^{-3})
χ	expansion rate of shear layer thickness
ψ	force loss or force gain approximation (m s^{-2})
Φ	gradient of stagnation pressure in streamwise direction (Pa m^{-1})

Abbreviations

AFC	Active Flow Control
BC	Boundary Condition
CFL	Courant-Friedrichs-Lewy
FBL	Feedback Loop Length
HPCW	High Pressure Compression Wave
LPEW	Low Pressure Expansion Wave
MEMS	Micro-Electro-Mechanical-Systems
PIV	Particle Image Velocimetry
RMS	Root Mean Square
RANS	Reynolds-averaged Navier–Stokes
TKE	Turbulent Kinetic Energy
ZNMF	Zero Net Mass Flow

Introduction

The study of actuators for active flow control has been in rapid expansion in the last several decades, pursuing different goals such as reducing drag on bluff bodies[1], increasing lift of airfoils[2, 3] or enhancing mixing in combustion chambers[4, 5], etc. Compared to traditional passive control methods or steady blowing methods, the active flow control based on periodic fluidic excitations is much more efficient, with a gain of two orders of magnitude in terms of added momentum, as demonstrated by numerous researches (e.g., Greenblatt and Wygnanski [6]). These periodic fluidic disturbances can be provided by various kinds of actuators such as ZNMF (Zero Net Mass Flow) actuators, plasma actuators and MEMS (Micro-Electro-Mechanical-Systems)[7]. Among them, fluidic oscillators can emit oscillating jets in a large operating frequency and velocity range when supplied with a pressurized fluid without requiring any moving part, since their oscillations are totally self-induced and self-sustained and only depend on the internal flow dynamics, which is a great advantage in terms of reliability and robustness[8-10].

Compared to the other kinds of oscillators based on the Coanda effect, like the sonic fluidic oscillator or sweeping jet fluidic oscillator, the behavior of a pulsing jet relaxation fluidic oscillator is quite different and cannot be clearly explained by the existing theories. The present thesis is thus focusing on making clear the underlying mechanisms controlling the dynamics of this kind of fluidic oscillator with the objective to propose guiding lines for the design of oscillators providing the performances (pulsed jet frequency and velocity) requested by flow control applications. It is also intended, from this analysis, to develop and test oscillator prototypes to control a ramp separated flow.

In the first chapter, a general description of the boundary layer separation phenomenon is given and various separation control methods are introduced. A detailed review about all kinds of fluidic oscillators, including their classifications, their operating dynamic, etc. is also presented. The typical separation control applications on ramp or hump flows are also briefly reviewed with a focus on the optimal configurations identified.

In the second chapter, four oscillator prototypes are designed and experimentally characterized. The outlet velocity temporal evolution patterns are presented. The influence of the feedback loop length and diameter on the oscillation frequency is examined.

Numerical modeling of the oscillators based on an open source code is presented in the third chapter. The optimal numerical schemes are identified after a sensitivity study and validated by comparison with experimental data.

A detailed numerical study of the internal flow patterns of a fluidic oscillator is then conducted in chapter four. The influence of the inlet pressure on the fluidic oscillator's performances is also analyzed.

Since the fluidic oscillator's performances are very sensitive to internal and external parameters, some methods have to be developed to force an "in phase" running of a series of oscillators, which is very important for analyzing their control efficiency. Chapter five is thus fully devoted to introduce two synchronization methods that have been both experimentally and numerically validated and analyzed in detail.

An array of miniaturized fluidic oscillators, synchronized by one of the proposed methods, is then tested in a wind tunnel to control a separated flow on a ramp. The experimental characterization of the ramp flow without and with control is performed for various operating conditions thanks to hot wire and PIV measurements and the efficiency of the oscillator array is analyzed and presented in chapter six.

Finally, the main conclusions and the major perspectives of this work are summarized in chapter seven.

Chapter 1. Background of the Study and Literature Review

1.1 Phenomenon of boundary layer separation

Let's consider a flat plate in a fluid, e.g., air, flow with a relative "free stream" velocity U_∞: due to the viscosity of the fluid, there will be a velocity profile from 0 on the plate wall to a maximum U_∞ in the free stream. This profile builds up gradually from the point called the leading edge where the fluid starts to flow past the surface. This region next to the plate surface where the velocity profile in the flow is influenced by the shear stress at the wall is called “the boundary layer”. The thickness δ of this boundary layer is defined as the distance from the wall to the point where the velocity is 99% of the “free stream” velocity.

The value of δ will increase with the distance from the leading edge up to a maximum in the fully developed flow as shown in Figure 1-1 for a flat plate. Simultaneously the drag force on the plate due to the shear stress at the surface increases from zero at the beginning of the plate to a constant maximum value in the fully developed flow region.

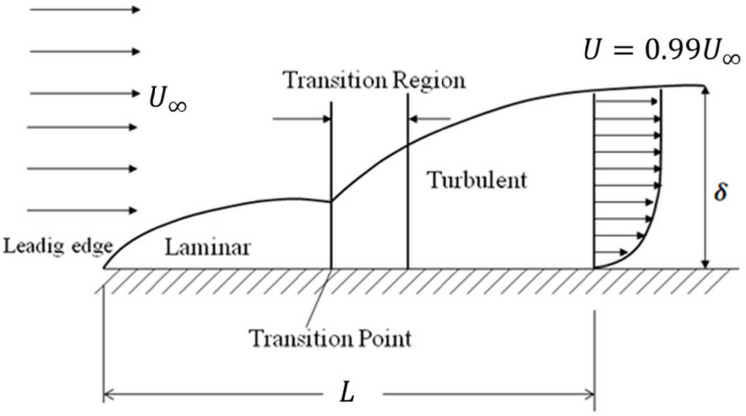

Figure 1-1. Boundary layer on a flat plate

Depending on the Reynolds number defined by Eq.(1-1), this boundary layer can be laminar, transitional or turbulent.

$$Re = \frac{\rho L U_\infty}{\mu} \tag{1-1}$$

where ρ is the density of fluid, L is a characteristic length, U_∞ is the free stream velocity, μ is the dynamic viscosity of the fluid. For a flat plate, L is the distance from the leading edge.

The thickness of the boundary layer will become thinner if the pressure decreases in the direction of flow when the fluid accelerates, thus maintaining the fluid close to the wall, as in the case of a convergent flow. Nevertheless, the situation will be totally different if the pressure increases along the flow direction. The velocity of the fluid within the boundary layer will quickly decrease and reverse in direction when the fluid momentum is too low to overcome the adverse pressure gradient. The boundary layer will be lifted away from the surface if this velocity reversal occurs as shown in Figure 1-2. .

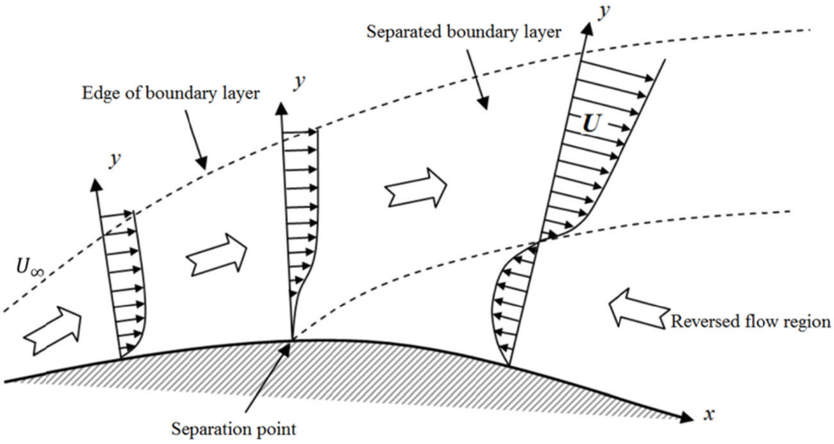

Figure 1-2. Separation of a boundary layer[11]

This phenomenon called boundary layer separation, can lead to serious accidents in some industrial applications, especially the wing stall of a plane. Considering an airfoil section which is located in a flow with a free stream velocity U_∞, as shown in the schematic Figure 1-3, the aerodynamic force R it bears has two components: a drag force R_d in the main flow direction and a lift force R_l in the perpendicular direction. The aerodynamic lift force results from a pressure force on the intrados (or the lower wall of the airfoil) and a suction force on the extrados. This lift force increases with the flow velocity.

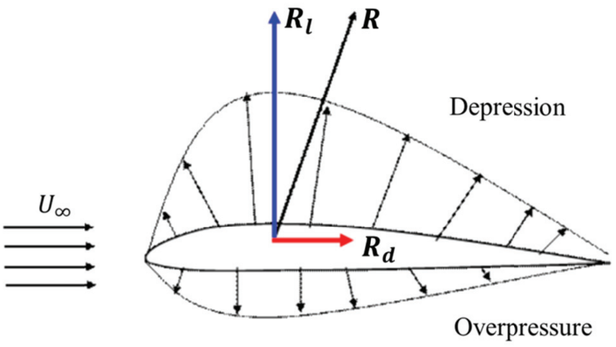

Figure 1-3. Aerodynamic forces on an airfoil section[12]

Two coefficients can be defined associated to the lift and the drag forces:

A lift coefficient (C_l):

$$C_l = \frac{R_l}{\frac{1}{2}\rho S U_\infty^2} \tag{1-2}$$

A drag coefficient (C_d):

$$C_d = \frac{R_d}{\frac{1}{2}\rho S U_\infty^2} \tag{1-3}$$

where S is the upper or lower side surface area of airfoil. The value of the lift and drag coefficients are linked to the incidence angle η of the airfoil relative to the flow. The typical evolution of C_l and C_d with η is shown in Figure 1-4. As it can be easily observed, with the augmentation of η, the lift increases significantly. This property is exploitable in the landing phase when the plane needs a sufficient lift at a low velocity. However, a large augmentation of η may trigger a sudden fall of the lift value due to the boundary layer separation on the extrados. This boundary layer separation produces indeed a recirculation bubble on the extrados in which the velocity is much lower and thus the pressure is much higher than in the main flow. The presence of this high pressure zone leads both to a decrease of the lift and to an increase of the drag. This sudden fall of the lift value is named “stall” which is of course very dangerous for the plane and should be totally avoided.

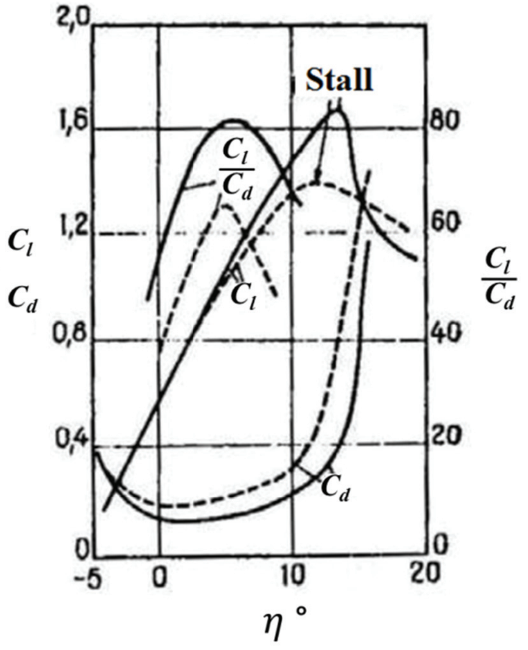

Figure 1-4. Variation of C_l and C_d in function of η in case of a plane airfoil.[13] ——— $Re = 6.5\times10^5$, -------$Re = 3.1\times10^4$

1.2 Separation control methods

In aerodynamics, flow separation can often result in increased drag, particularly pressure drag which is caused by the pressure difference between front and rear surfaces of the object as it travels through the fluid. For this reason, much effort and research has gone into the design of aerodynamic and hydrodynamic surfaces which delay the flow separation. Researchers have proposed many solutions to achieve this goal. In general, these solutions lie in two categories: passive and active flow control strategies.

Passive flow control techniques

Passive control techniques are the most conventional and simplest ways to reduce the aerodynamic drag, which are based on the modification of the shape of the wall. However, this simplicity is also the main drawback of such devices which are often irrelevant when the flow configuration changes [14]. The most representative applications of passive control may be the vortex generators and the wing fences employed on airfoils as illustrated in Figure 1-5.

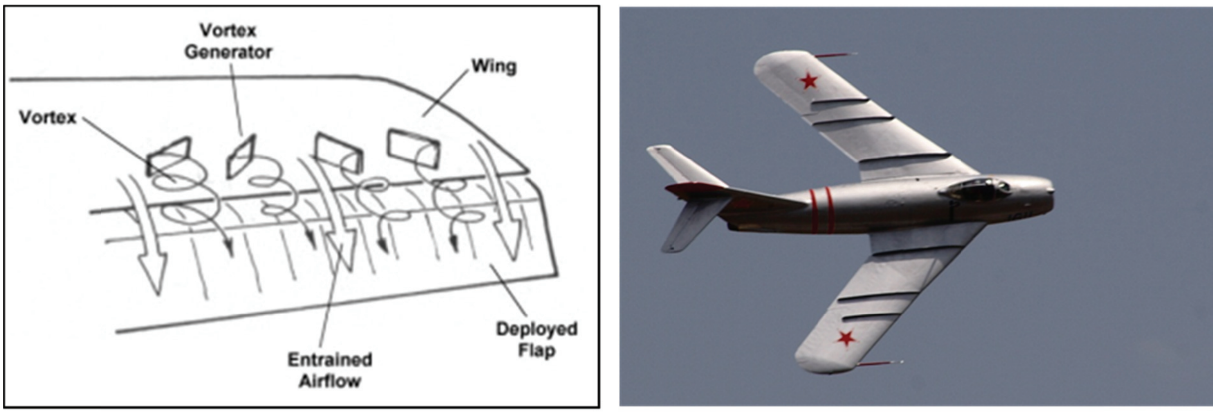

(a) (b)

Figure 1-5. a) sketch of a working vortex generator;[15] b) wing fences on the airfoil of Mig-17

Vortex generators are widely employed on airplanes and can be considered as wings, at reduced scale, perpendicular to the main wing. As it can be seen in Figure 1-5a, the vortex generators are mounted with an angle of attack relative to the airflow in order to generate a series of vortices along the surface of the wing. As the created streamwise vortices develop downstream of the wing and induce momentum transfer between the free-stream and the near wall region, the boundary layer separation and the aerodynamic stalling can be delayed and the effectiveness of wings and control surfaces can thus be largely improved. The application of vortex generators on a modified Ahmed body has also been exploited by Aider et al.[16] and it has been demonstrated that this kind of control method can lead to a significant drag reduction for low aspect ratio 3D bluff-bodies, like road vehicles.

Wing fences, also called boundary layer fences, are fixed aerodynamic devices attached to the aircraft wings. They are often used to obstruct span-wise airflow along the wing and prevent the entire wing from stalling at once. They are often seen on swept-wing aircrafts as shown in Figure 1-5b.

Active flow control techniques

On the contrary, active control methods permit to modify the boundary layer in relation with the flow configuration and need energy supply. Thus, these methods necessarily require actuators to interact with the flow. Many different types of actuators, such as thermal actuators, electromagnetic actuators, pneumatic actuators, synthetic jets, oscillators, etc.[17, 18], have been developed for active flow control applications. A detailed summary and comparison of various actuators have been proposed by Cattafesta et al. [7] as shown in Table 1-1.

These actuators can be classified into three main categories: fluidic actuators, moving surface actuators and plasma actuators. In each category, some sub-categories can also be found. Among those, the fluidic oscillators are drawing more and more attention because they can operate in a large operating frequency and velocity range when supplied with a pressurized fluid, without requiring any moving part. Their oscillations are totally self-induced and self-sustained and only depend on the internal flow dynamics, which is a great advantage in terms of reliability and robustness.

Table 1-1. Summary of common unsteady flow control actuators proposed by Cattafesta et al. [7]

Type	**Subtype**	**Advantages**	**Disadvantages**
Fluidic			
	ZNMF	Requires no external fluid source	Peak velocities typically limited to low to moderate subsonic speeds
		Amenable to various types of drivers and sizes	Resonant devices
		Suitable for feedback control	
	Unsteady valves	Capable of high velocities with either fast time response or high bandwidth but generally not both	May not be amenable to feedback control
			Requires an external flow source
	Oscillators	Capable of producing large disturbances	Standard versions not suitable for feedback control
		Amenable to a range of sizes and hence frequencies	Requires an external flow source
		Potential extensions possible to enable independent control of frequency and velocity	
	Combustion	Capable of producing large perturbations in high-speed flows	Currently limited to relatively low frequencies (a few hundred hertz)
			Requires combustion

Moving surface			
	Piezoelectric flaps	Simple design amenable to different frequency ranges of interest	Has constant product of max deflection and bandwidth
		Can produce spanwise or streamwise vorticity	Susceptible to fluid loading
		Suitable for feedback control	Resonant devices
	Active dimples	Potentially suitable for feedback control of turbulent wall-bounded flows	Further development needed to achieve required size and frequency response
Plasma			
	SDBD	Easily installed on models	Limited velocity output
		Low mass	Requires high voltage (kV)
		Fast time response	
		No moving parts	
	Sparkjet	All solid-state device capable of producing large perturbations in high-speed flows	Potential issues associated with EMI, acoustic level, and high temperature

Abbreviations: EMI, electromagnetic interference; SDBD, single dielectric barrier discharge; ZNMF, zero-net mass flux

1.3 Introduction to fluidic oscillators

Fluidic oscillators were originally developed in the 1960s as amplifiers for fluidic logic applications, as detailed in the works of Morris[19], Foster[20] and Kirshner[21]. The comprehensive introduction and overview of the fluidic amplifier technology can be found in the book of Kirshner[22] and NASA report[23, 24].

Fluidic oscillators have also been widely used as flowmeter devices since their operating frequency can be directly related to the flow rate in some operation conditions[25-28]. During the last decade however, the interest for fluidic oscillators has been renewed, notably due to the possible application of this kind of actuator for flow control. Fluidic oscillators are very attractive within the aerodynamic community for flow control purpose for the reason that they are able to produce unsteady blowing within a wide range of operating frequency and without moving parts, which reduces reliability and lifetime issues and facilitates their implementation in harsh environments such as high temperature. An overview of the works recently conducted on fluidic oscillators for flow control applications can be found in the review papers of Gregory and Tomac[29], and Raghu[30].

According to Gregory and Tomac[29], these devices can be classified into two main categories related to different underlying operating mechanics: Wall-attachment fluidic oscillators and jet-interaction fluidic oscillators. However, in his review paper[30], Raghu Surya separates the oscillators into "pulsing jet fluidic oscillators" and "sweeping jet fluidic oscillators" depending on the properties of the generated jets.

Wall-attachment fluidic oscillators

The working principle of these devices is based on the bi-stable attachment of a jet to adjacent walls due to the Coanda effect. They can thus also be called Coanda fluidic oscillators. As shown in Figure 1-6, there are two typical types of wall-attachment fluidic oscillators according to the form of the feedback control loops and thus the source of disturbance provoking the oscillation.

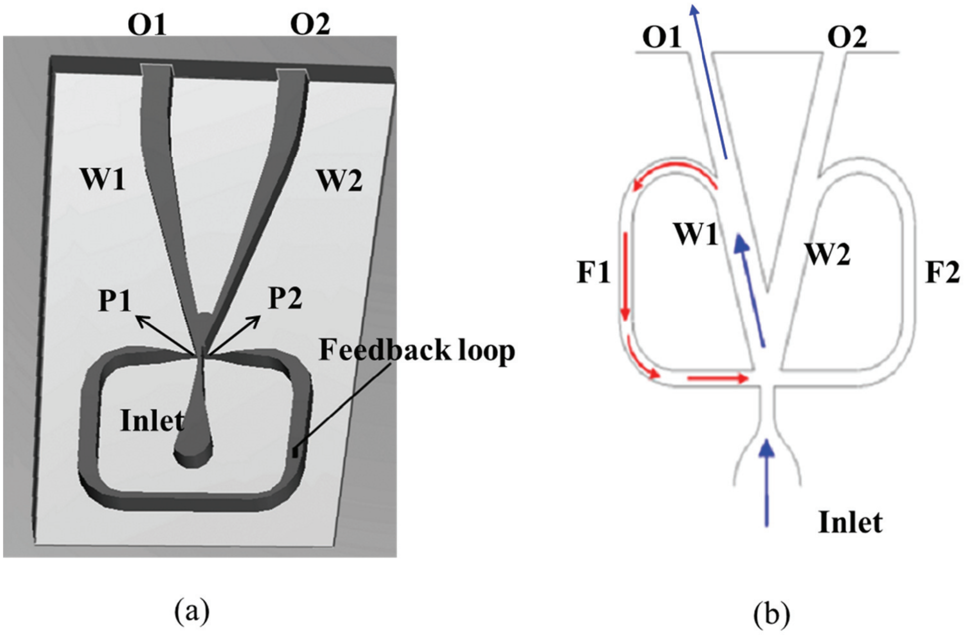

Figure 1-6. Illustration of the basic configurations of wall-attachment fluidic oscillators: (a) sonic oscillator [31]and (b) relaxation oscillator[8]. The primary flow direction is from bottom to top in both cases

Sonic oscillators operate typically by the propagation of compression and expansion waves at sonic speed through the feedback loop that connects the two control ports P1 and P2 (Figure 1-6a). When the power jet attaches to the right wall W2, entrainment of the jet decreases the local pressure at the right control port P2 due to the limited volume available for entrainment. This reduction in pressure produces an expansion wave that propagates through the feedback loop. Simultaneously, as soon as the jet attaches the right wall W2, the pressure at the left outlet O1 (ambient) acts on the left control port P1. This sudden increase in pressure produces a compression wave in the feedback loop, starting from the left control port P1. When the disturbances propagate through the loop and reach the opposite side control ports, the jet switches between attachment walls. Thus, the interconnected control ports set up a self-sustained oscillation of the power jet between the two attachment walls.

Relaxation oscillators, also named “negative fluidic oscillators” in the original patent of Warren[32], have two feedback loops, F1 and F2 (cf. Figure 1-6b). It is also composed of two outlets O1 and O2. The main jet issuing from the inlet nozzle attaches to one of the two walls W1 or W2. The attachment either to wall W1 or to wall W2 depends on the initial conditions or is the result of specific actions on the jet. If there was no feedback loop and if the outlet sections were large, the attachment to wall W1 or wall W2 would be stable and the flow would exit through the corresponding outlet, O1 or O2, respectively. With feedback loops, when the jet is attached to wall W1, part of the flow fills in the feedback loop F1 and a pressure increase in the left side of the device is observed, due to the hydraulic restriction at outlet O1. This pressure increase forces the jet to switch toward the right side. Following the jet switching, the same phenomenon develops in the right side of the oscillator and results in a self-sustained oscillating behavior, with a pulsed flow alternatively exiting outlets O1 and O2.[29, 33]

These two wall-attachment oscillators can also be called pulsing jet oscillators since the jet is ejected from the two outlets alternatively, resulting a temporally unsteady pulsing jet at each outlet.

Jet-interaction fluidic oscillators

Even without attachment walls nor feedback loops, there are in these devices internal feedback paths that drive the instability. The basic principle is the unsteady interaction of jets within a cavity that lead to an unsteady external jet. The temporal development of flow jets inside a typical jet-interaction fluidic oscillator is shown in Figure 1-7.[34] In this fluidic oscillator, there are two inlets but only one outlet. With constant inlet flow in both inlets, after complex interactions inside the cavity, the resulting outlet jet is unsteady and its direction varies within an range with a certain frequency. This kind of generated jet is called sweeping jet since it oscillates spatially.

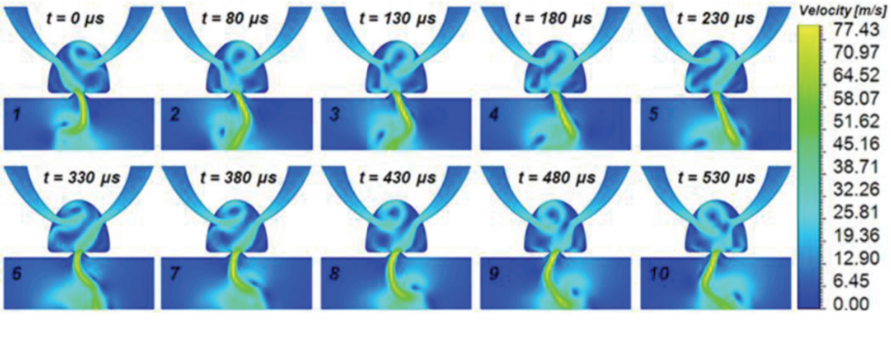

Figure 1-7. Two-dimensional CFD results of a jet-interaction fluidic oscillator internal and external flows[34]

Sweeping jet Coanda fluidic oscillators

Figure 1-8a presents the conceptual geometry of a typical sweeping jet Coanda oscillator, and its inner flow pattern. The generated jet with water is visualized in Figure 1-8b and its sweeping pattern is similar to that of the jet-interaction fluidic oscillator (cf. Figure 1-7).

However, its oscillation is provoked by the self-induced switching motion of the internal jet which is initiated by the back flow through the feedback channels due to the Coanda effect.

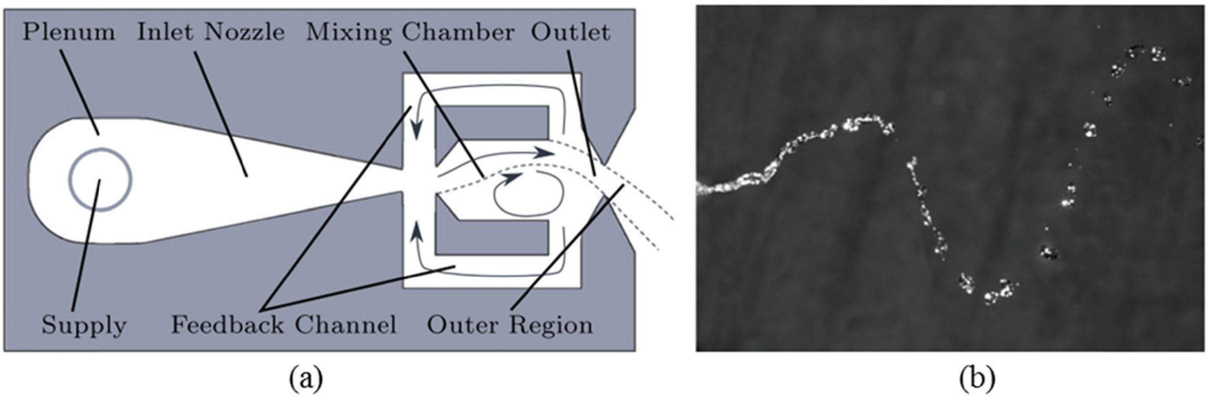

Figure 1-8. a) sketch of the geometry of a sweeping jet Coanda fluidic oscillator and its internal flow pattern; b) its sweeping pattern visualized with water[35]

Other kind of oscillators

In their review on fluidic oscillators, Campagnuolo and Henry [33] also introduced some other kinds of fluidic oscillators like wedgetone oscillators, ringtone oscillators and vortex oscillators.

However, among all kinds of fluidic osicllators described above, the wall-attached fluidic oscillators based on the Coanda effect seems the more promising ones for the simplicity to control the oscillation frequency.

1.4 Coanda oscillators: the state of art

Coanda effect is a basic fluidic principle, named after Henri Marie Coanda (1885-1972) who was a Romanian aeronautical engineer and inventor. One of his major contributions to fluid technology is his discovery in the 1930s of the “Coanda Effect” which explains why, when a free jet emerges from a nozzle or orifice, it will tend to be attracted to a nearby curved surface. This phenomenon is illustrated in Figure 1-9.

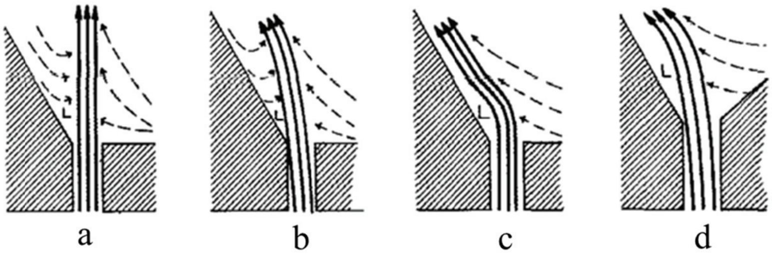

Figure 1-9. Coanda effect [36]

a) A free jet (solid lines) passes through a narrow pass opening into a large chamber where it entrains fluid molecules (dashed lines) from both sides.

b) In the chamber, less air is available for entrainment on the left side of the jet than on the right side because of the angle of the nearby surface. Thus a partial vacuum or low pressure area forms at the left of the jet and tends to attract the jet towards the angled surface

c) As long as the supply of molecules on the other side remains constant the low pressure area continues to attract the jet and forces it to flow closely to the angled surface until additional molecules can be introduced into the low pressure area.

d) The effect only works when the curvature or angle is not too sharp. If both sides of the nozzle are angled the low pressure area tends to form on the side with smallest angle. [36]

1.4.1 Sonic fluidic oscillator

The sonic fluidic oscillator was firstly patented by Warren[37], but it was made famous by the study of Spyropoulos[38]. After the studies of Tippetts et al. [25], Viets[39], Hayashi et al.[40] and Raman et al. [41], it has been illustrated that there exists a critical value of *Re* under which no fluctuation would occur. The feedback loop length, diameter, operating medium and the size of control ports all play important roles in determining the oscillation frequency. The longer the feedback loop length is, the lower the frequency is because of the longer wave propagation time along the tube. Moreover, the smaller the diameter is, the lower the frequency is because of the higher fluidic resistance. It has been found that there exists a pressure difference threshold between the control ports to deflect the jet, and only above this threshold value can the jet deflection happen. [42]

Tesař et al.[31] studied a sonic fluidic oscillator which can generate hybrid-synthetic jet with suction effect, as shown in Figure 1-10. The authors argued that the oscillator operates in two regimes: one is the constant Strouhal number regime at low inlet *Re* conditions and the other one is the constant propagation velocity regime at high inlet *Re* conditions.

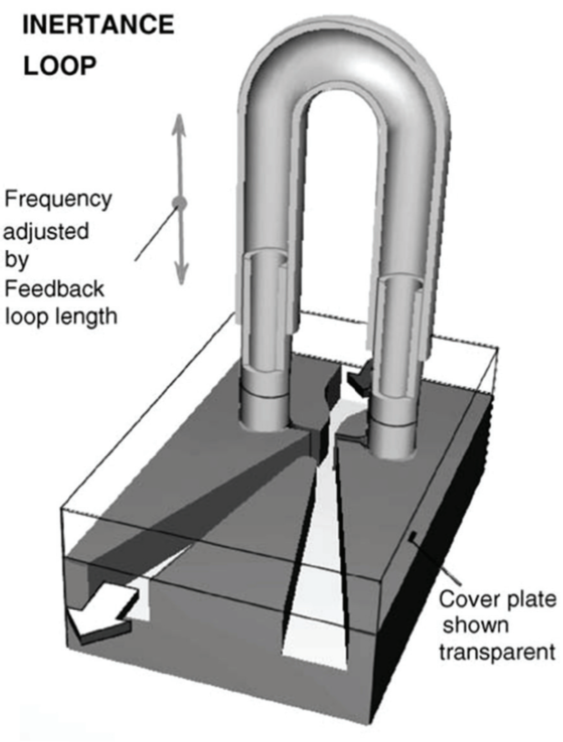

Figure 1-10. A sonic fluidic oscillator based on a bi-stable diverter valve developed by Tesař V. et al. [31]

In order to clarify and find an invariant of the investigated phenomenon, the bulk propagation velocity in the feedback loop c_a was initially defined by:

$$c_a = \frac{2L_t}{T} = 2fL_t \tag{1-4}$$

where L_t is the length of connection tube, T is the oscillation period, and f is the oscillation frequency. Then, a modified Strouhal number Sr_m was introduced by multiplying the relative length L_t / w by the Strouhal number Sr based on the oscillation frequency, the velocity u of the main jet in the inlet throat section and the width w of this throat section.

$$Sr = \frac{fw}{u} \tag{1-5}$$

$$Sr_m = 2 \cdot Sr \cdot L_t / w = 2fL_t / u \tag{1-6}$$

The Sr_m dependence on Re is shown in Figure 1-11. It is apparent that the non-dependence of Strouhal number to Reynolds number usually admitted[25] only holds at very low Re, and that there is a distinctly different regime at the high Re range of investigation. When Re is low, approximately $Re < 3500$, which may be interpreted as the laminar regime of the jet issuing from the supply nozzle, Sr_m is apparently independent of Re : this is the so-called constant Strouhal number regime.

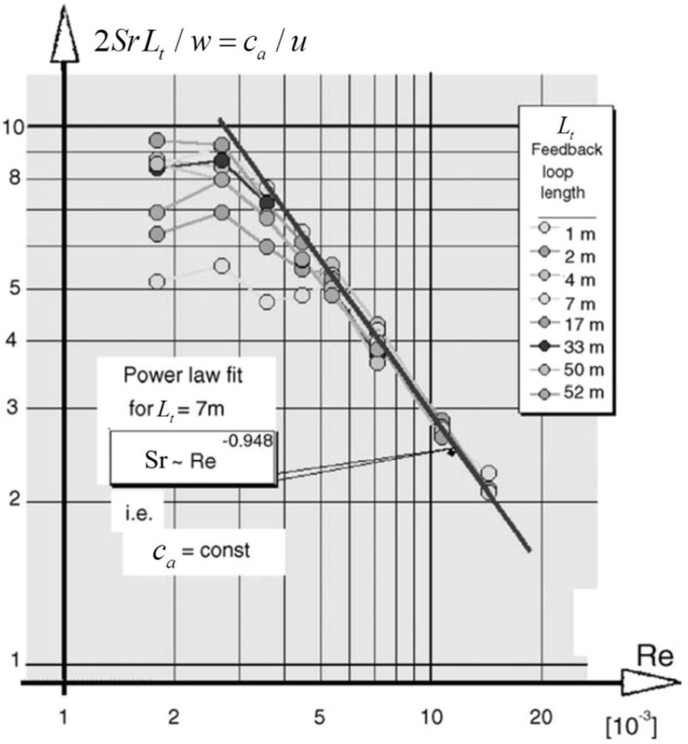

Figure 1-11. Modified Strouhal number Sr_m as a function of Reynolds number Re[31]

c_a is also plotted as a function of inlet nozzle Reynolds number as shown in Figure 1-12. Two variation regimes can also be found in this figure: in the first regime, the propagation velocity increases linearly with inlet *Re*; in the second regime, the velocity stays constant which is called the constant propagation velocity regime. This is in accordance with the observations by Spyropoulos[38] and Hayashi[40] that when the inlet pressure (or inlet flowrate) is low, the frequency increases with the inlet pressure, while the frequency keeps constant once the inlet pressure is higher than a critical value.

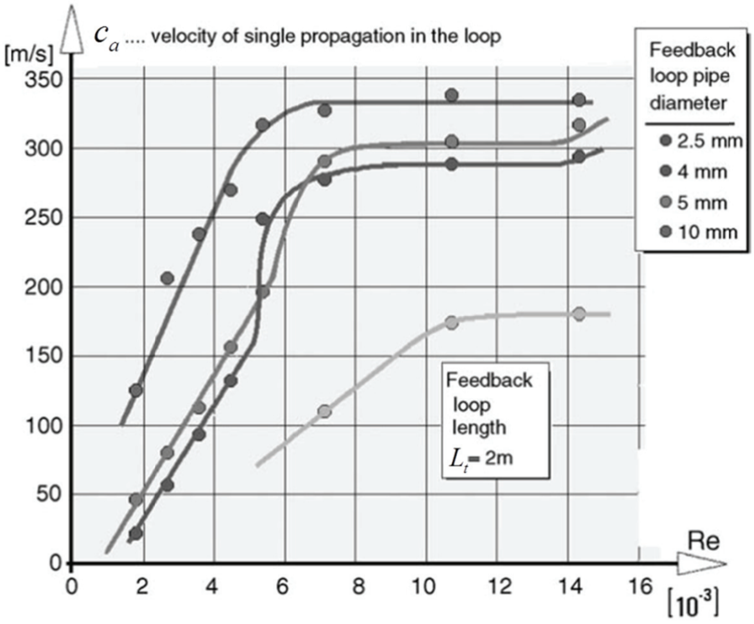

Figure 1-12. Propagation velocity development as a function of inlet *Re*, for different feedback tube diameters[31]

1.4.2 Sweeping jet Coanda fluidic oscillator

The sweeping jet Coanda fluidic oscillator, as shown in Figure 1-8, has been widely studied in recent years for active flow control applications, though it was initially patented by Stouffer[43] as an ‘oscillating spray device’. It was firstly used to suppress the cavity resonance[44], and then applied to the airfoil to delay the flow separation and improve the performance of airfoil and flap.[45-48] Recently, it has been applied on the vertical tail of a Boeing 757 plane in a real flight test.[49] It was also tested to reduce the drag on a rectangular bluff body [35, 50, 51]. It’s efficiency has been demonstrated both experimentally[10] and numerically[52] [53], both in the incompressible regime[54-56] and compressible regime with maximum outlet Mach number of 1[57]. Two frequencies were found by Gosen et al[57] in the spectra of the oscillation signals as shown in Figure 1-13. The main frequency was of the order of 500 Hz, related to the volumetric growth of the recirculation bubble required to provoke the jet switching and to the flow rate injected by the feedback channel in this recirculation bubble. The second frequency also called resonance frequency, was of the order of 3000 Hz and linked to the pressure wave propagation in the feedback channel. This bi-frequency phenomenon linked to the co-existence of a capacitive and a propagative effect, was also found in the study of a monostable fluidic oscillator by Khelfaoui et al.[58].

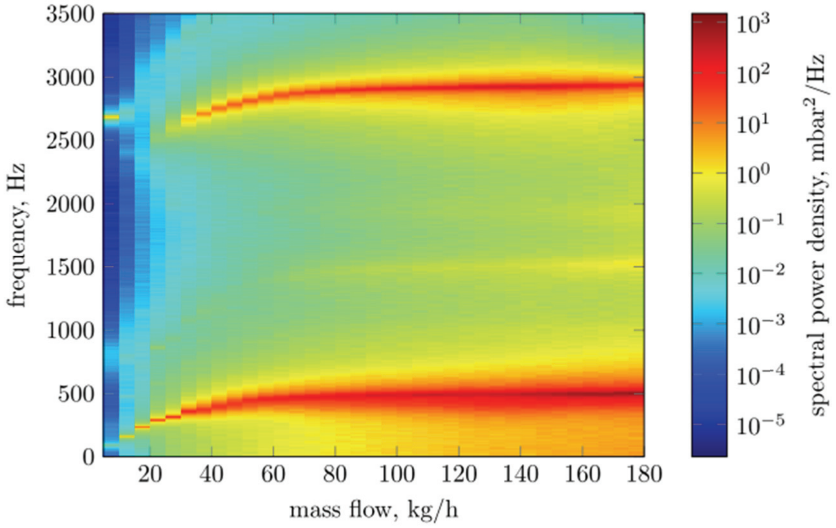

Figure 1-13. Frequency spectra of differential signal between symmetrically paired pressure taps for investigated supply rates[57]

The oscillator's main frequency is plotted versus the supply flowrate and the Mach number in the outlet nozzle as shown in Figure 1-14. It can be clearly observed that the main frequency is only independent of the supply rate within a limited range when the inlet flow rate or pressure is higher. The frequency increases with the inlet pressure almost linearly in low inlet flow rate conditions. This kind of frequency variation pattern is very similar to that of sonic fluidic oscillators (cf. Figure 1-12).

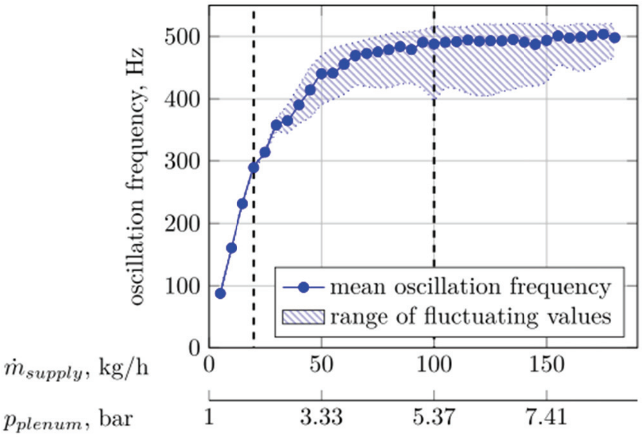

Figure 1-14. Oscillation frequency as a function of the supply rate [57]

1.4.3 Pulsing jet relaxation fluidic oscillator

The basic geometry of a typical pulsing jet relaxation fluidic oscillator is shown in Figure 1-6b and it was firstly patented by Warren[32] as a "negative feedback oscillator". It was declared that its oscillation performance is a function of the pressure of the fluid power source, the area of the attached-wall region, the distance from the power nozzle to the splitter, the type of fluid employed, etc. But no specific function was proposed.

In the work of Simoes et al. [59], as shown in Figure 1-15, the microfluidic oscillators include a Supply input (S), an interaction region, two Outputs (O), and two Feedback Arms (FA) (or loops). The authors proposed an equation to predict the oscillation frequency, in case of gases as working material:

$$f = \frac{1}{2\left(\tau_t + \tau_s\right)} = 1/2\left(\frac{L_f}{c} + \frac{\xi l}{u}\right) \tag{1-7}$$

where τ_t is the transmission time of the pressure wave through the feedback loop, τ_s is the switching time that depends on the jet velocity, L_f is the Feedback Loop Length (FBL), c is the speed of wave propagation (if the duct is not small, the speed of wave propagation tends to the speed of sound), u is the velocity of main jet, l is the nozzle-to-splitter distance and ξ is an empirical constant which has a value between one and two.

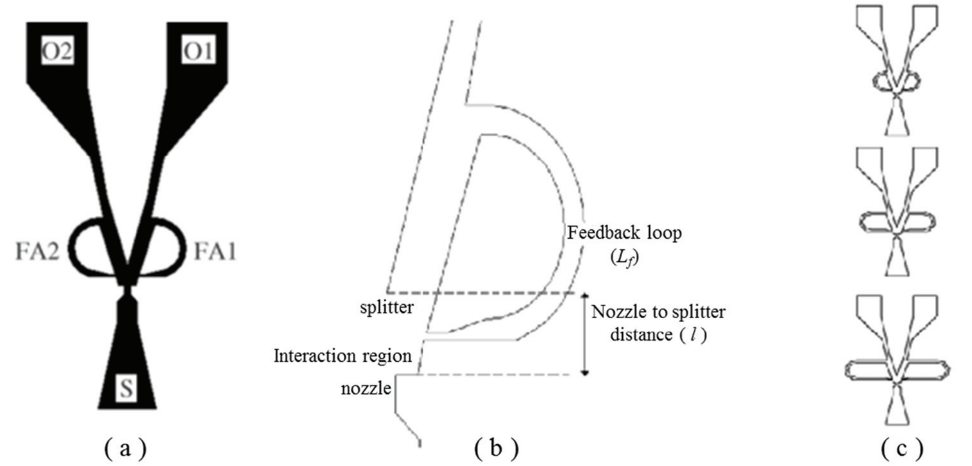

Figure 1-15. Geometrical characteristics of Simoes' device: a) main parts of the device, b) detail of the interaction region, and c) configurations with feedback arms of different lengths[59]

Experiments were carried out to test their behaviors, especially their oscillation frequency by hot wire anemometers, and with different gases (nitrogen, argon and carbon dioxide) as working material. Figure 1-16 shows the experimental evolution of the oscillation frequency as a function of the gas mass flow rate, with the length of the feedback arm as a parameter. As the oscillation frequency increases with the volumetric flow rate in incompressible and moderately compressible conditions (e.g., supply flow less than 200 sccm), these devices can be used as flowmeters. When the inlet flow continues increasing, the frequency becomes relatively stagnant, which is similar to the response pattern of sonic fluidic oscillators (cf. Figure 1-12) or sweeping jet Coanda fluidic oscillators (cf. Figure 1-14).

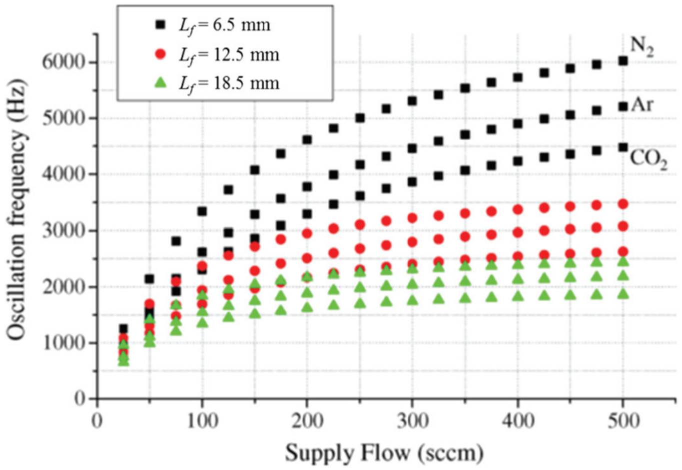

Figure 1-16. Oscillation frequency as a function of FBL L_f[59]

Cerretelli et al.[8] studied a similar fluidic oscillator whose schematic is shown in Figure 1-17. This pulsing jet relaxation fluidic oscillator has been successfully tested in various applications, like the flow control in a hump diffuser [60, 61], the separation control on wind turbine blades[62] and airfoil [63].

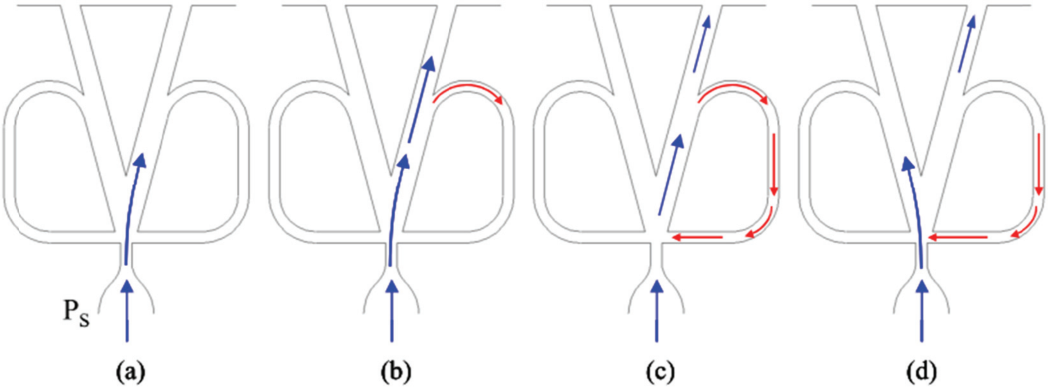

Figure 1-17. Pulsing jet relaxation fluidic oscillator: switching mechanism. P_s indicates the supply total pressure[8]

According to the authors, the operation of this kind of oscillator can be analyzed in two parts: one is the switching of the bi-stable amplifier, and the other is the response of the feedback network. Two oscillators were designed and named Oscillator A and Oscillator B, whose key geometrical parameters are summarized in Table 1-2. They have the same nozzle width, same nozzle depth and same exit channel width, but very different feedback loop capacitor volumes. Oscillator A has a capacitor volume which is 20 times larger than that of oscillator B.

Table 1-2. Features of the fluidic oscillators in Cerretelli's study [8]

	Oscillator A	Oscillator B
Nozzle width	0.050 in.	0.050 in.
Nozzle depth	0.120 in.	0.120 in.
Exit channel width	0.055 in.	0.055 in.
Capacitor volume	0.320 in^3	0.016 in^3

The measured frequency responses to the inlet pressure and the sample jet velocity signals of both oscillator A and B are shown in Figure 1-18. It can be observed that the maximum jet velocity for both oscillators can reach about 200 m/s. However, oscillator B is almost pressure-controlled as its frequency varies with the inlet pressure which is similar to those described above (cf. Figure 1-14, Figure 1-16), while oscillator A is almost pressure-insensitive and operates at a constant frequency in the same inlet pressure range. These different frequency responses have not yet been clearly explained.

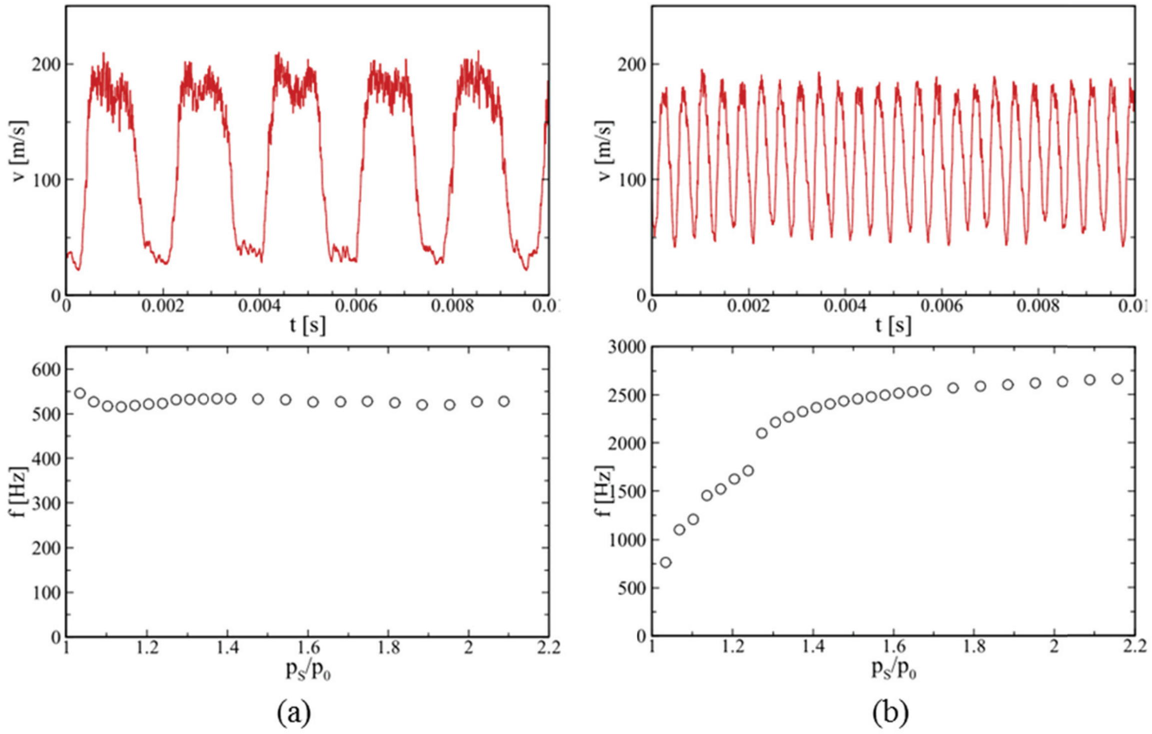

Figure 1-18. Frequency response to inlet pressure and sampled velocity signal by hot wire measurement, a) oscillator A, b) oscillator B [8]

In the experimental study of Tesař and Peszynski on this kind of oscillator[64], the frequency response is plotted as a function of the inlet mass flow rate(cf. Figure 1-19). In this case, the frequency increases proportionally to the inlet mas flow rate, which is completely different to what was observed by Simoes et al[59] (cf. Figure 1-16) and by Cerretelli et al[8] (cf. Figure 1-18). No reasonable physical explanation has been proposed yet to explain the strong differences in behaviors observed between the various oscillators described above.

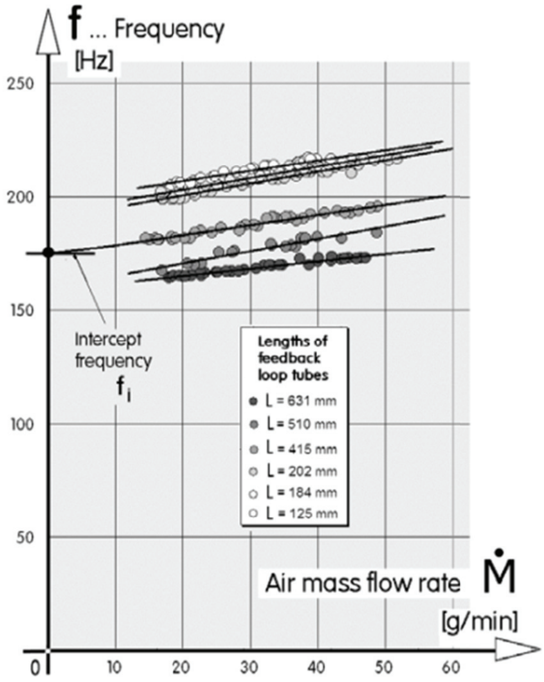

Figure 1-19. Measured oscillation frequency as a function of the inlet flow rate, with different FBLs [64]

1.4.4 Other kinds of Coanda oscillator

Khelfaoui et al.[58] studied the mechanism of the jet switching in a mono-stable fluidic oscillator both numerically and experimentally. The schematic of the studied device is shown in Figure 1-20.

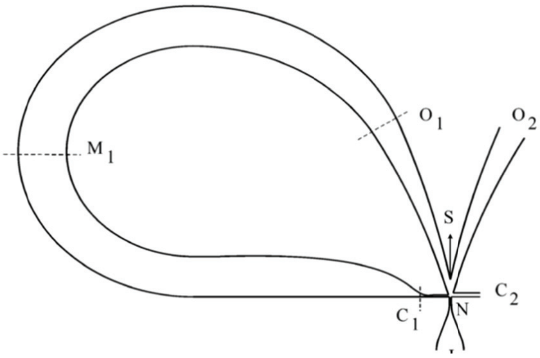

Figure 1-20. Sketch of a mono-stable fluidic oscillator based on an amplifier [58]

This kind of oscillator has only one feedback loop. One of the interests of this design is to allow the suction of a secondary fluid by the control port C_2 for micro-mixing applications. The authors experimentally and numerically studied three different configurations in order to explain its behavior. They pointed out the relationships between key parameters such as supply pressure, oscillation frequency, threshold pressure levels and geometrical parameters and examined the oscillation modes in detail.

Two oscillation modes were found, similar to the findings of Gosen et al[57]. It was thus demonstrated that the main oscillation is controlled by a capacitive effect, in relation with the volume connected to the closed branch while the secondary oscillation, superimposed to the main one, is driven by a propagative effect, in relation with the propagation of pressure waves in the feedback loop.

Tesař et al[65] proposed more recently a new concept of fluidic oscillator, as illustrated in Figure 1-21. The main feature of this new design is the absence of feedback loop channels compared to the above mentioned oscillators. Its jet switching is controlled by the compression and expansion waves in the resonance channels. As shown in Figure 1-21, the resonance channel which is connected to the control terminal X_1 is closed, and the other channel X_2 is open into atmosphere. The jet oscillation is caused by weak shock waves generated by the sudden change in pressure, traveling forth and back through the resonance channel. Its switching frequency is mainly determined by the length *L* of the resonance channel and independent of the mass flowrate passing through the oscillator. However, it is difficult to keep an array of this kind oscillator synchronized since it is difficult to make any link between two oscillators without modifying the resonance channel working dynamics.

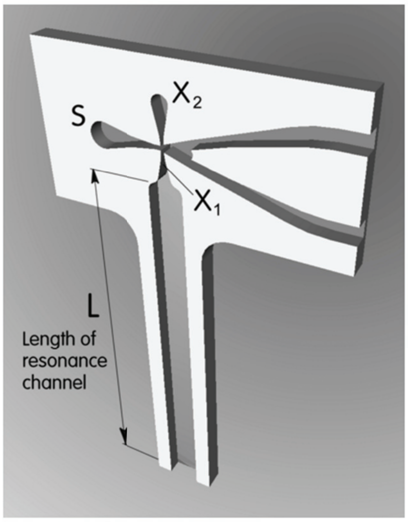

Figure 1-21. New idea of fluidic oscillator proposed by Tesař et al.[65]

1.5 Efficient separation control by periodic jets

It has been demonstrated by numerous researches [6, 66-68] that active flow control based on periodic fluidic excitations is much more efficient, with a gain of as high as two orders of magnitude in terms of added momentum coefficient compared to control based on steady blowing. For the purpose to evaluate and compare the efficiency of an injection jet on the separation control, two dimensionless numbers, the injection momentum coefficient C_μ and the velocity ratio V_R, are defined.

For steady blowing,

$$C_\mu = \frac{m_b U_b}{\frac{1}{2}\rho U_\infty^2 L\omega} \tag{1-8}$$

$$V_R = \frac{U_b}{U_\infty} \tag{1-9}$$

where ω is the span width of the controlled flow, m_b is the blowing mass flow rate, U_b is the blowing velocity, and L is the flow characteristic length. For unsteady injection, the mean values of momentum added are used to calculate C_μ, while the maximum blowing velocity $U_b^{\max}$ is used to calculate V_R :

$$C_\mu = \frac{\overline{m_b U_b}}{\frac{1}{2}\rho U_\infty^2 L\omega} \tag{1-10}$$

$$V_R = \frac{U_b^{\max}}{U_\infty} \tag{1-11}$$

In most of the previous works, L is the distance between the injection location and the diffuser trailing edge [69] or the reattachment point[70-72], but it may also be defined as the ramp heights[73, 74]. In the present work, L will be defined as the length between the ramp slant edge and the separation point.

In the unsteady injection case, a dimensionless injection frequency F^+ is also defined:

$$F^+ = fL / U_\infty \tag{1-12}$$

where f is the oscillation frequency, U_∞ is the free stream velocity.

Since the fluidic oscillators developed in this thesis aims to be applied to the flow separation control on a ramp, the key parameters of some representative works on ramp or hump flows are listed in Table 1-3. Large discrepancies can be observed between the optimal values of some of these parameters, especially C_μ, found by the different groups, which can be explained by the differences in the studied configurations(e.g., geometry of the ramp or the hump, position and orientation of the controlling jets, etc.). However, the optimal values found for the velocity ratio V_R are between 2 and 3 for all the studies and the optimal F^+ is about 1 in a majority of cases. It was also found in the study of Seifert et al [70], that the superposition of weak suction on the periodic excitation enhances the control efficiency.

Table 1-3. Key parameters of representative studies on separation control of ramp or hump flow

authors	**flow type**	**actuation method**	**U_∞ m/s**	**C_μ**	**V_R range**	**F^+ range**	**Optimal C_μ**	**Optimal V_R**	**Optimal F^+**
Cerretelli et al.[61]	Hump diffuser	Discrete steady blowing	2.16	0 - 6%	(0,7.7)	--	4%	2	--
Cerretelli et al.[69]	Hump diffuser	Fluidic oscillator	25.9	0 - 6%	8	0.6 - 5	5%	--	0.7
Vikas et al.[75]	Straford ramp	Discrete steady blowing	40 - 60	--	(8,10)	--	--	--	--
Seifert et al.[70]	Wall-Mounted Hump	Slot steady blowing	85	--	--	--	2%	2	--
		Slot steady suction		0-4%	--	--	0.8%	1.26	--
		Oscillatory excitation		--	--	0.4-2.0	--	--	1.6
Greenblatt [71, 72]	Wall-Mounted Hump	Slot steady suction	34	0.24%	0.814	--	--	--	--
		Slot zero mass flux Oscillatory excitation	13.6 – 40.8	0.01%-3%	0.65 - 2	0.45-1.94	--	>1	1.05-1.35
Zhang et al[73]	Two-Dimensional Ramp	Discrete synthetic jets	6.5	--	0.63 - 1.57	0.8 -2.4	--	--	--
Kourta et al[76, 77]	Two-Dimensional Ramp	Discrete pulsed jets	20	0.165%	3	0.795 & 1.98	--	--	--
Joseph et al.[74]	Two-Dimensional Ramp	Discrete pulsed jets	20 - 40	0.08% - 1.9%	2-6	0.1 - 4	1.9%	--	2.7

1.6 Conclusions

The study of actuators for active flow control has been in broad expansion in the last decades, with different goals such as reducing drag on bluff bodies, increasing lift on airfoils or enhancing mixing in combustion chambers. Compared to traditional passive control methods or steady blowing methods, the active flow control based on periodic fluidic excitations is much more efficient. Various kinds of actuators which can provide periodic fluidic disturbances have been summarized. Among them, fluidic oscillators can emit oscillating jets when supplied with a pressurized fluid without requiring any moving part. Their oscillations are indeed totally self-induced and self-sustained and only depend on the internal flow dynamics, which shows a great advantage in terms of reliability and robustness.

Various kinds of fluidic oscillators have been reviewed and three sub-categories of Coanda fluidic oscillator have been highlighted: including the sonic fluidic oscillator, the sweeping jet Coanda fluidic oscillator and the pulsing jet relaxation fluidic oscillator.

For both of sonic fluidic oscillators and sweeping jet oscillators, with fixed geometry and operating medium, the frequency increases with the inlet flow rate at low *Re* conditions. This increases the complexity in determining the factors optimizing the flow control efficiency since the frequency is correlated to the injection momentum which is proportional to the inlet mass flowrate. However, in a pulsing jet relaxation fluidic oscillator, it is possible to have a quasi-constant frequency response, independent of the inlet pressure or flowrate while keeping all the advantages of other kinds of fluidic oscillators, such as a high velocity and frequency range, the facility to control the oscillation frequency, the possibility to synchronize an array of more than two oscillators, etc.

It has been demonstrated that the jet switching in a sonic fluidic oscillator is controlled by the wave propagation along the feedback loop, and it that operates in two regimes: the constant Strouhal number regime at low inlet *Re* conditions and the constant propagation velocity regime at high inlet *Re* conditions. The jet switching process inside a sweeping jet Coanda fluidic oscillator is rather controlled by the growing of the recirculation bubble in the mixing chamber which is fueled by the feedback channel flow. However, the pulsing jet relaxation fluidic oscillator operates differently compared to the two other kinds of fluidic oscillator. Despite the tentatives made by several researchers to identify the physical mechanisms governing the dynamic behaviors of these devices, no clear consensus has been found yet in the literature.

The main objective of the present work will thus be to study in detail the working dynamics of a pulsing jet relaxation fluidic oscillator in order to propose guiding rules for its design and its application to active flow control.

Chapter 2. Design and Experimental Characterization of Fluidic Oscillator Prototypes

A first oscillator prototype designed during the work of W. Ghozlani [12], has been tested in the framework of two experimental campaigns. However, these measurements have evidenced important assembly difficulties leading to leakages and possible modifications of the device's internal dimensions, making it very difficult to analyze the behavior of this oscillator in relation with the geometrical and operation parameters. In addition, numerical models built on the CFD software ANSYS/FLUENT have shown an important sensibility to critical settings such as the transient discretization scheme and the time step, not allowing their exploitation for an in-depth analysis of the actuator's behavior. This part of our work is detailed in Annex 1.

As a consequence, four new oscillator prototypes have been developed, solving the identified assembly problems, in order to get more accurate experimental data which could help in identifying and understanding the relation between the actuator's performances and the geometrical parameters as well as operating conditions.

These four actuators have the same designed central part in order to better compare their performances. However, two of them have a fully 2D shape (i.e., large ratio of depth to transversal dimensions), including the feedback loops, in order to facilitate the validation of the 2D numerical models presented in chapter 3, while the two other ones have changeable feedback loops permitting the analysis of the influence of the length and volume of the feedback tubes on the oscillator's performances.

2.1 Design of new prototypes

The first and second prototypes have feedback loops of rectangular sections with the same depth (10 mm) as for the central part, ensuring a two-dimensional behavior of the flow in the whole device. The feedback loops of these two prototypes have the same volume but different widths (1.26 mm and 3.2 mm) and lengths. These two devices are named Osc.1 and Osc.2 respectively and their detailed sketches and dimensions are shown separately in Figure 2-1 and Figure 2-2. The feedback loop length of Osc.1 (from section A1 to section P1) is L_f = 391 mm, while that of Osc.2 is L_f = 163 mm. The third and fourth prototypes, named Osc.3 and

Osc.4, have the same geometry, as shown in Figure 2-3. Their feedback loops are changeable by linking connectors α and β in each side by plastic tubes of different internal diameters and lengths. The objective are here firstly to test the influence of the geometrical uncertainties linked to the manufacturing and assembling processes on the oscillator's performances and secondly to test methods allowing the synchronization of several similar actuators.

In the sketches of Figure 2-1 and Figure 2-2, in order to facilitate the analysis of the oscillator's internal flow patterns in the following chapters, six representative sections, noted A, B, C, D, E, P, have been selected; they represent the branch inlet, the branch center, the loop inlet, the loop center, the loop outlet and the control port, respectively, with 1 representing the oscillator's left side and 2 representing its right side.

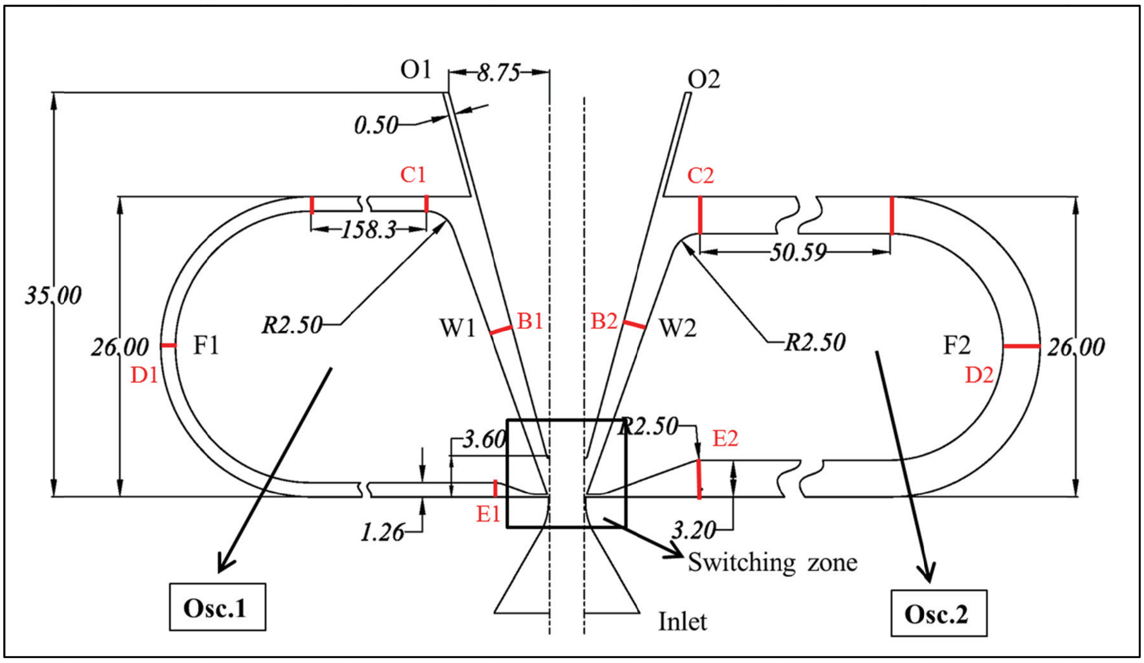

Figure 2-1. Sketches and designed dimensions of Osc.1 (left side) and Osc.2(right side), (in mm)

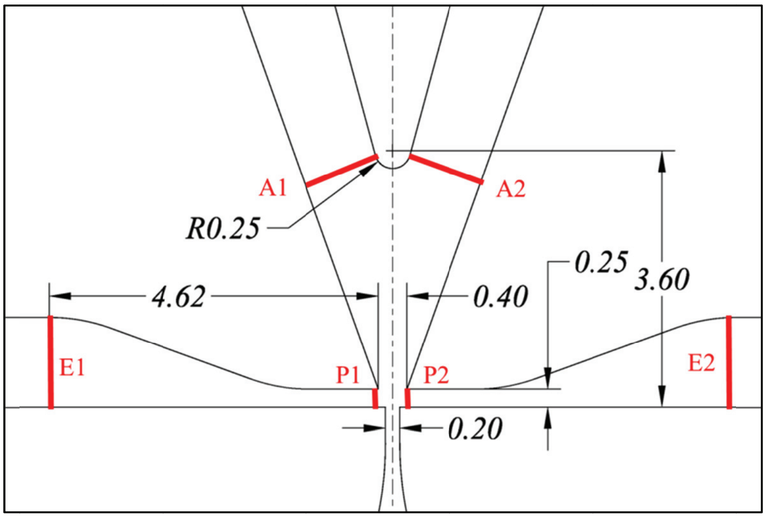

Figure 2-2. Detailed dimensions of the switching zone of the designed oscillator prototypes, (in mm)

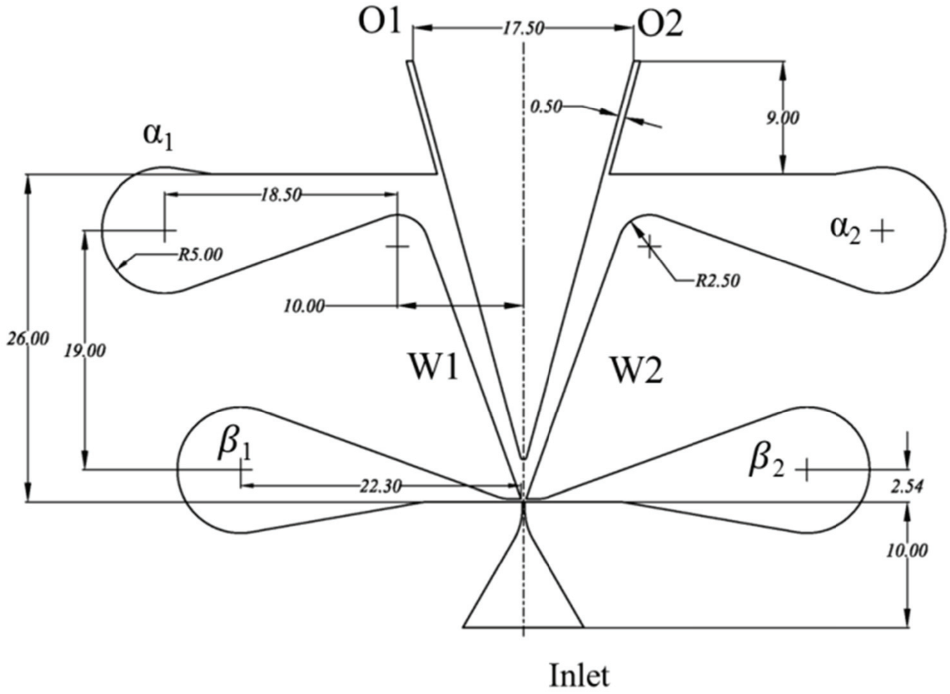

Figure 2-3. Sketch and overall dimensions of Osc.3 and Osc.4, (in mm)

Due to the complex geometry of the prototypes, especially the high aspect ratio and small width of the throat section, it is very difficult to realize the design by direct milling. Instead, the oscillators are composed of several aluminum sub-pieces assembled between three plates also made in aluminum (cf. Figure 2-4). Osc.2, for example, is shown in Figure 2-4: it consists of an inlet plate and a main body which includes a base plate, a cover plate and an air channel layer. The inlet plate is attached to the main body by fastening it to the base and cover plate with screws. Between the inlet plate and main body, there is a gasket to avoid leakage. (cf. Figure

2-4b), as well as between the cover/base plate and air channel layer (cf. Figure 2-4c). The air channel is formed by five separated pieces (cf. Figure 2-4a), and their relative positions are fixed by locating pins. Each piece has at least two locating pins. At last, the main body is assembled by fastening screws.

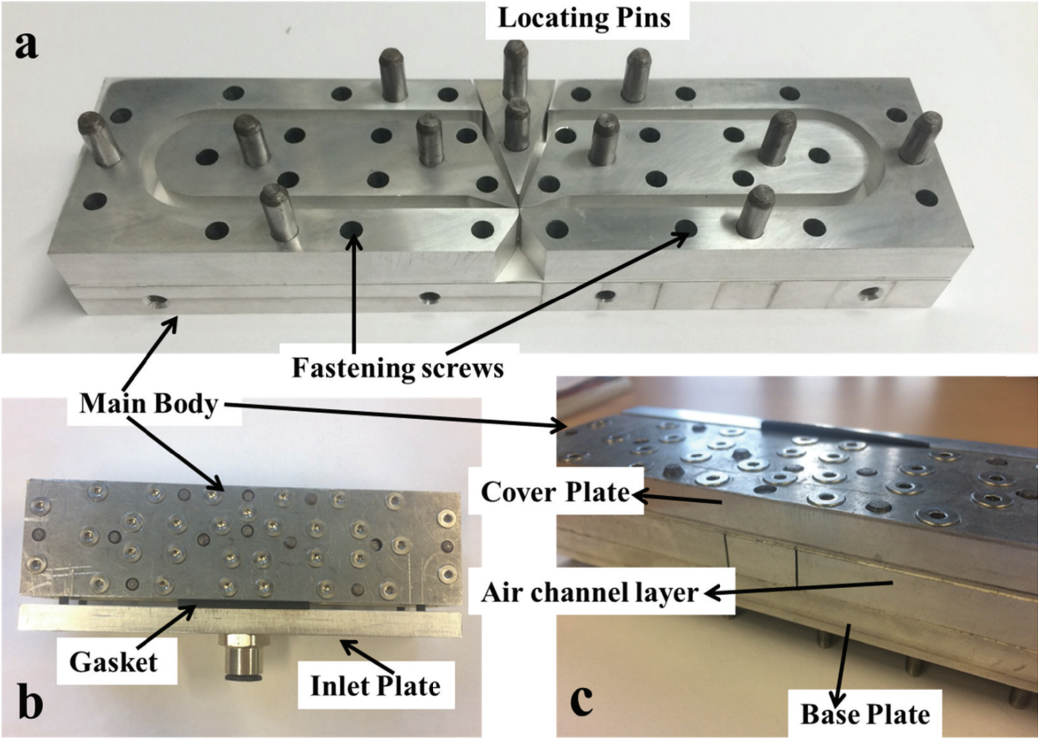

Figure 2-4. Photos of assembled Osc.2

2.2 Hot wire characterization of Osc.1 and Osc.2

In order to get more information about the performance of a typical fluidic oscillator and to better validate the numerical models, hot wire anemometry is used to measure the frequency response and the outlet velocity evolution pattern of Osc.1 and Osc.2.

2.2.1 Description of the test bench

The calibrated velocity range of the hot wire (TSI 1210-T1.5, single cylindrical sensor, wire diameter 3.8 μm, wire length 1.27 mm) is 0 to 140 m/s. Two separate coordinate systems are established in both outlets as shown in Figure 2-5. The origin of each coordinate system is defined as the outlet slot edge which is in the same side as the outlet flow direction, e.g., the left slot edge for the left outlet.

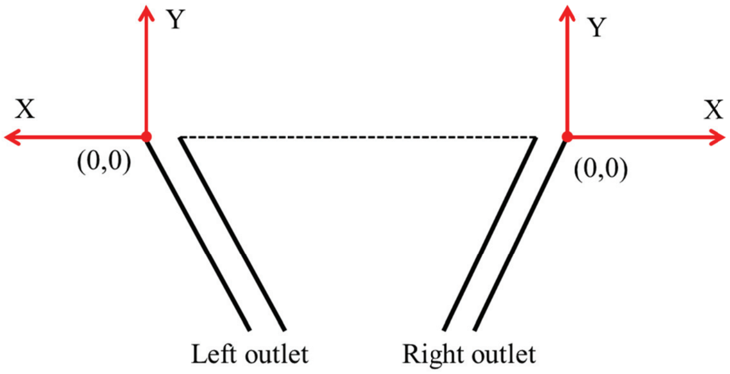

Figure 2-5. Definition of coordinate systems

The frequency and temporal velocity evolution pattern are measured at the point (-0.25, 0) (in mm) for inlet absolute pressures in the range from 0.1 MPa to 0.3 MPa. The acquisition frequency is 25 kHz and the sampling duration is 10 s. A picture of the test bench is shown in Figure 2-6. A micrometric in-line positioning stage is used to set the Y coordinate with an accuracy of 0.01 mm, while a positioning table associated to a distance-monitor allows to set the X coordinate with a precision of 0.001 mm. The micro camera serves to monitor the position of the hot-wire and find the zero coordinate with a high accuracy.

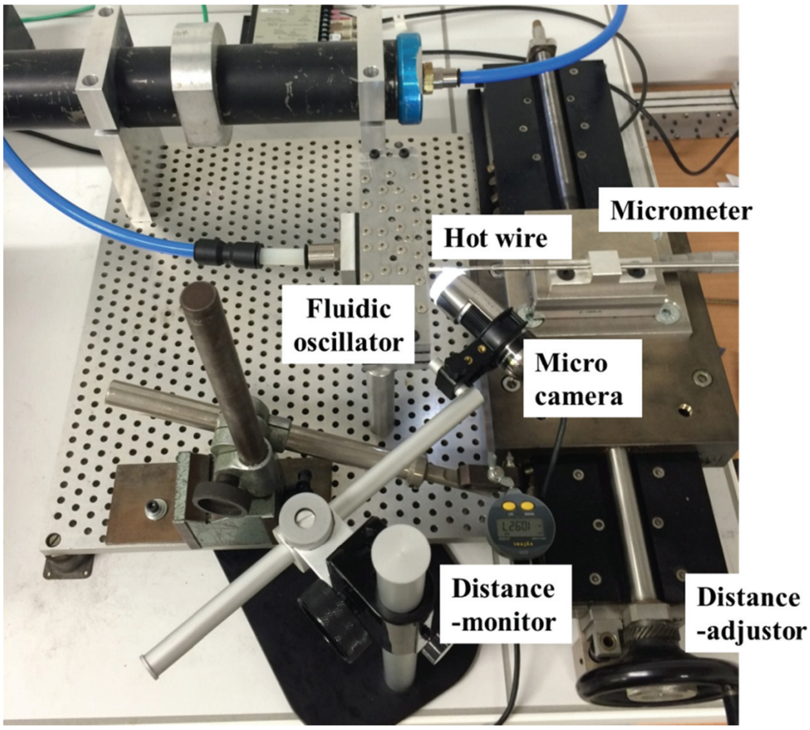

Figure 2-6. Test bench for hot-wire measurements

2.2.2 Frequency response

The measured frequency of Osc.1 and Osc.2 for inlet pressures ranging from 0.1 to 0.3 MPa is shown in Figure 2-7. It can be easily observed that these two devices have totally different frequency responses even though their central parts have the same dimensions in design and their feedback loops have the same volume. This result implies that in this bi-stable pulsed-jet oscillator design, the volume of the feedback loops is not the key parameter controlling of the oscillation frequency unlike what was demonstrated by Kelfhaoui et al.[58] for a mono-stable oscillator.

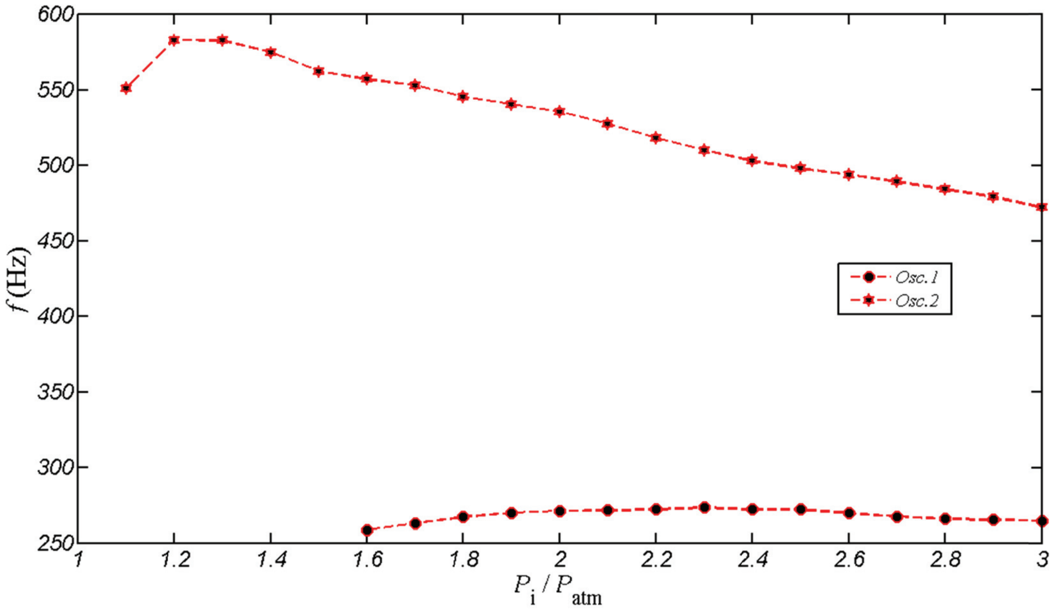

Figure 2-7. Frequency response of Osc.1 (L_f= 391 mm) and Osc.2 (L_f= 163 mm) measured by hot wire

In addition, oscillations are more difficult to induce for Osc.1 which only begins to oscillate when the inlet pressure is higher than 0.16 MPa while in case of Osc.2, the threshold value is 0.11 MPa. The simplicity and robustness to initiate the oscillation are very important for the application of the fluidic oscillator to separation control. The difficulty of Osc.1 to initiate its oscillation could be due to the small feedback loop width. A more detailed analysis, in particular using numerical simulation to have access to the internal flow pattern, is however needed to confirm this assumption.

However, it should be noted that the frequency decrease observed for Osc.2 when the inlet pressure increases has never been identified in literature.

2.2.3 Sample velocity signals of Osc.1

The velocity signals of Osc.1 in the center of both outlets (-0.25, 0) when P_i = 0.2 MPa are shown in Figure 2-8. The single hot wire used in these experiments gives only access to the magnitude of the velocity but not its direction. Thus the smaller peak of the signal corresponds to a suction flow at the considered outlet, which could improve the control efficiency of the actuator as already shown by Seifert and Pack [70]. ΔT_1 is the duration when the jet suction in, while ΔT_2 is the duration when the jet blowing out.

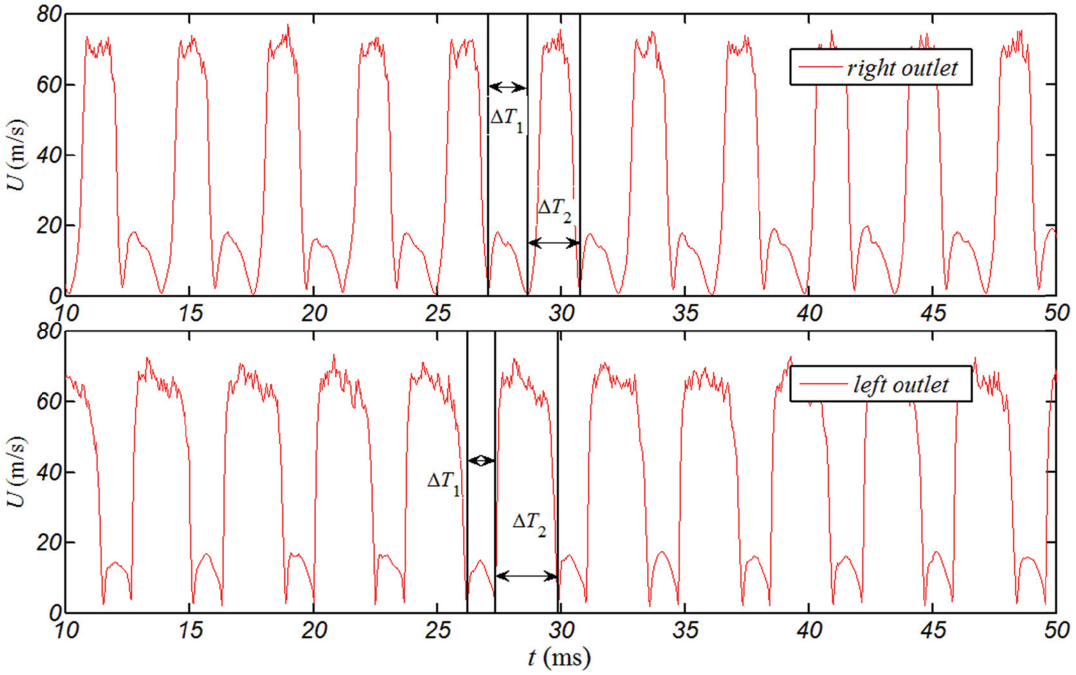

Figure 2-8. Velocity evolution with time in the center of both outlets of Osc.1, $P_i = 0.20$ MPa

From the sample signals, the mass flux on each outlet during one period can be calculated and the inlet total mass flow rate can also be obtained by multiplying the sum of the mass fluxes on each outlet on one period by the oscillation frequency.

By assuming that both the outlet velocity and air density in each outlet slot are uniform, and that all the outlet areas are the same as the designed one, the mass flux m in a time interval ΔT can be calculated by

$$m=\int_{\Delta T} dm=\int_{\Delta T}\rho A_o U_b dt=\rho A_o\int_{\Delta T}U_b dt=\rho A_o\sum_{\Delta T}(U_b dt) \qquad (2\text{-}1)$$

where ρ is the air density at atmospheric conditions, A_o is the area of outlet slot in design, U_b is the instantaneous velocity measured by hot wire, dt is the data acquisition time interval. Thus, the inlet mass flow rate can be calculated by

$$\dot{m}=f\bullet(-m_1+m_2-m_3+m_4) \qquad (2\text{-}2)$$

where m_1 is the left outlet suction mass flux during ΔT_1, m_2 is the left outlet ejection mass flux during ΔT_2, m_3 is the right outlet suction mass flux during ΔT_1, m_4 is the left outlet ejection mass flux during ΔT_2 in one period, and f is the oscillation frequency. In the end, the inlet mass flow rate is calculated to be $\dot{m}=0.2167\rho A_o f=3.404\times10^{-4}kg/s$.

As the inlet total pressure is equal to 0.2 MPa (i.e., higher than the critical pressure of about 0.18 MPa needed to reach sonic conditions in a simply convergent nozzle, cf. Figure A1-2, Annex 1), it can be assumed that the flow velocity is sonic at the throat. Assuming in addition that the velocity is uniform in this cross section, the throat width w can be calculated by from the sonic mass flow rate relation:

$$w = A_t / H = \frac{\dot{m}\sqrt{T_{\mathrm{i}}^{*}}}{KP_{\mathrm{i}}H} = 0.073 \;\; mm \tag{2-3}$$

where A_t is the throat area, H is the depth, T_{i}^{*} is the inlet total temperature, K is a constant which is 0.0404 (m s^{-1} $\mathrm{k}^{-0.5}$) for air, P_{i} is the inlet total pressure. The throat width calculated from the inlet mass flow rate is only about 0.073 mm which is much smaller than the designed 0.2 mm value.

The maximum velocities at both outlets are similar and of the order of 70 m/s. However, the main ejection time ΔT_2 is much longer at the left outlet than that at the right one which implies that the internal geometry is not totally symmetrical.

2.2.4 Sample velocity signals of Osc.2

The velocity signals of Osc.2 in the center of both outlets (-0.25, 0) when P_{i} = 0.2 MPa are shown in Figure 2-9. The average velocity at the left outlet is about 80 m/s with an amplitude of 80 m/s, while at the right outlet, the average velocity is about 115 m/s and the amplitude is about 30 m/s which is much smaller. In both of the outlets, no suction flow has been found.

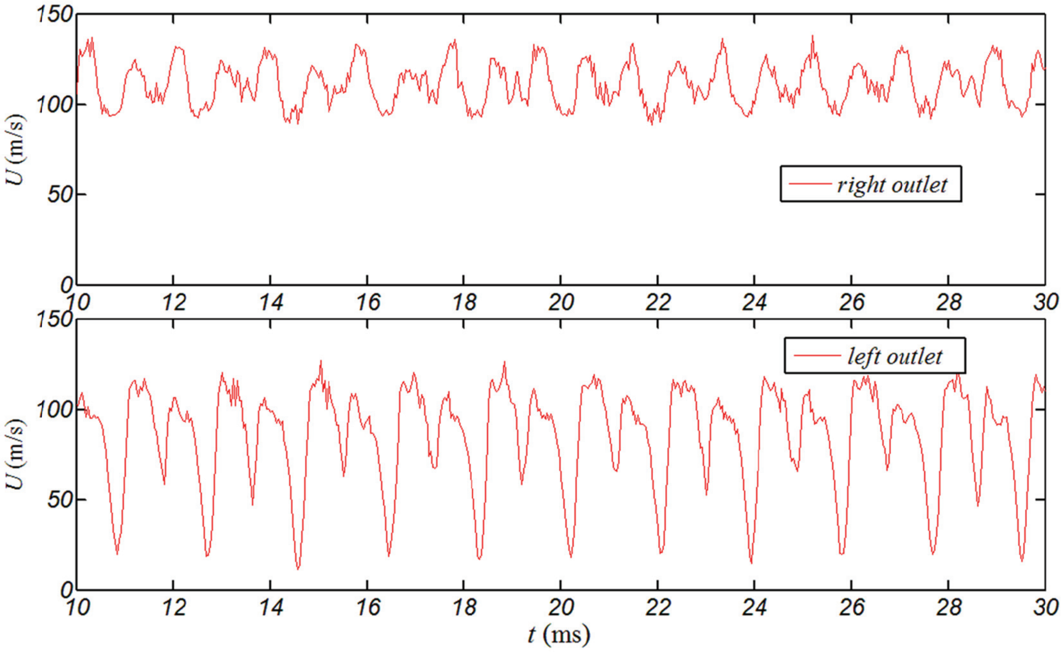

Figure 2-9. Sample velocity evolution pattern in the center of both outlets of Osc.2, P_{i} = 0.20 MPa

With the same method used in the case of Osc.1, the total mass flowrate in the Osc.2 is calculated to be $\dot{m} = 0.37235\rho A_o f = 11.56\times10^{-4} kg/s$. And the real area of the throat section can be also roughly estimated by the equation (2-3): w = 0.246 mm. Again, the calculated throat width has 25% deviation to the designed 0.2 mm width. These large deviations of the throat dimension for both Osc.1 and Osc.2 have been verified by the X-ray tomography technology described in chapter 3.

In addition to the designed difference of the feedback loops' width and length, these big deviations in real throat width may also contribute to the large difference observed between Osc.1 and Osc.2 of the jet velocity evolution with time.

2.2.5 Sensitivity of the internal geometry

As described above, the real critical dimensions, like the throat section area, are very different to the designed ones due to assemblage uncertainties. In order to verify the sensitivity of the performances to the internal geometry, the oscillators have been disassembled and re-assembled. Then their frequency responses were measured by a pressure transducer (Endevco high sensitivity piezoresistive pressure transducer, model 8506-2, whose pressure range is 0-2 psi, and resonance frequency is 45 kHz) in a large inlet pressure range from 0.1 MPa to 0.7 MPa. The test bench is the same as that shown in Figure 2-6, but in a simplified version: the hot wire is replaced by the pressure transducer, as shown in Figure 2-10, no camera is needed since the distance to the outlet has no effect on the measured frequency.

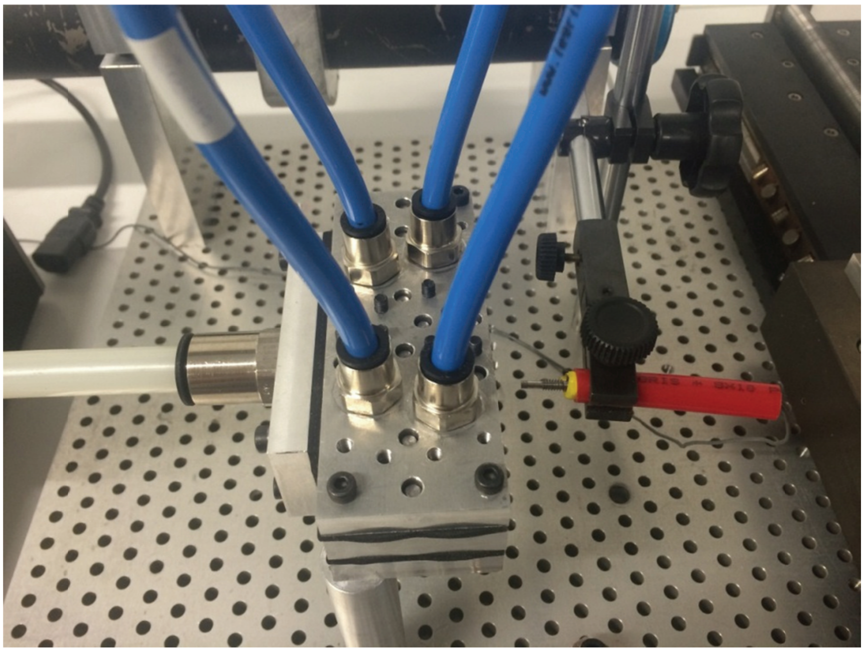

Figure 2-10. Position of the pressure transducer relative to the tested oscillator

The results are shown in Figure 2-11. For both Osc.1 and Osc.2, the frequency response profiles are very similar to those shown in Figure 2-7. As P_i is larger than 0.3 MPa, the frequency of Osc.2 stops decreasing and keeps almost constant.

Compared to the values presented in Figure 2-7 where Osc.1 frequency keeps constant at 265 Hz and Osc.2's frequency declines from 580 Hz to 470 Hz as the inlet pressure increases from 0.12 to 0.3 MPa, a 20% frequency decrease for Osc.1 and a 10% frequency decrease for Osc.2 have been observed. These frequency deviations imply that the oscillator's performance is very sensitive to its internal geometry, and that the internal geometry, especially the critical dimensions like the throat section, are very sensitive to the assemblage and installation method.

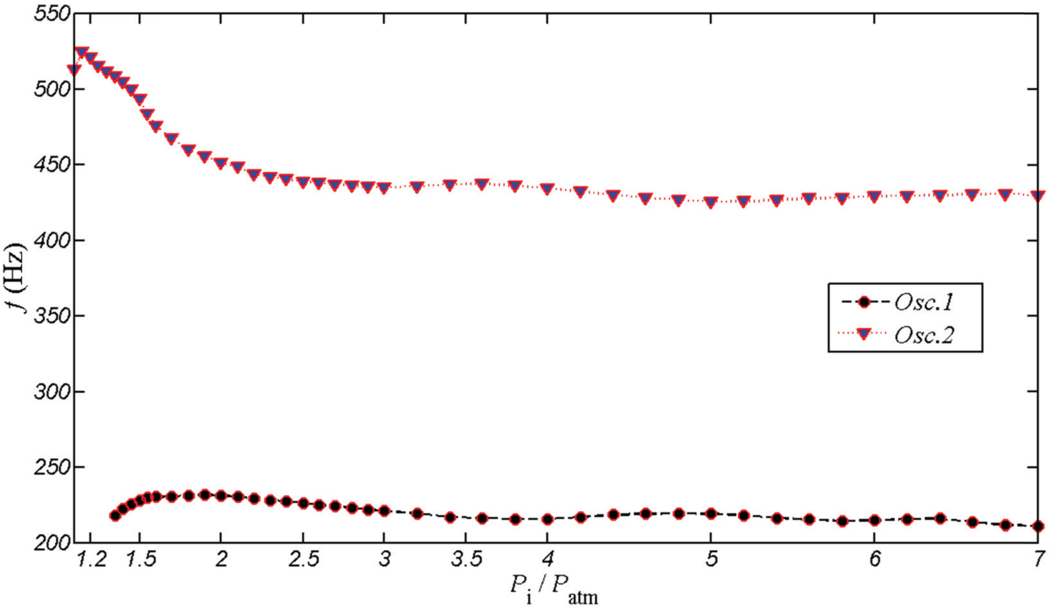

Figure 2-11. Frequency responses of Osc.1 and Osc.2 as a function of P_i/P_{atm}, after re-assembling process

2.2.6 Remarks and comments

1, the oscillator's performances, either frequency or temporal evolution of velocity, are very sensitive to its internal geometry

2, the throat width plays a key role not only on the average outlet velocity value due to mass conservation, but also on the temporal evolution of velocity. With a larger throat width, a higher average outlet velocity can be expected, however, no suction flow appears and the amplitude of the velocity variations is much smaller.

3, the outlet velocity evolution pattern may be controlled by modifying the internal geometry in order to obtain the outlet velocity evolution pattern needed.

2.3 Frequency characterization of Osc.3

The objective of these tests was to identify the relation between the oscillation frequency and the FBL. A pressure sensor has thus been preferred to a hot wire for robustness reasons. The test bench is similar to that described in section 2.2.5. The inlet total pressure range is from 0.1 MPa to 0.7 MPa and the data acquisition frequency is 25 kHz while the acquisition duration is 10 s. Since Osc.3 and Osc.4 have identical internal geometry, only the frequency response of Osc.3 is measured in this part of the work. The comparison between their performances will be presented in chapter 5 preliminarily to the synchronization test.

2.3.1 Influence of FBL on the oscillation frequency

The frequency responses for Osc.3 with 4mm diameter feedback loops of different lengths are shown in Figure 2-12 for P_i ranging from 0.1 to 0.3 MPa. Whatever the feedback loop characteristics, the measured frequencies when $P_\mathrm{i} \geq 0.3$ MPa are almost constant, and thus not presented in the figure. For comparison, the frequency response of Osc.1, whose feedback loop section area is the same as that of a 4mm diameter tube, is also presented. In each case, the oscillation frequency starts to increase with the inlet pressure, but reaches a constant and maximum value for inlet pressures higher than a critical value of about 0.17 MPa for both devices and whatever the FBL. The frequency response profiles are similar to the cases of both sonic fluidic oscillators(cf. Figure 1-12) and sweeping Coanda fluidic oscillators(cf. Figure 1-14).

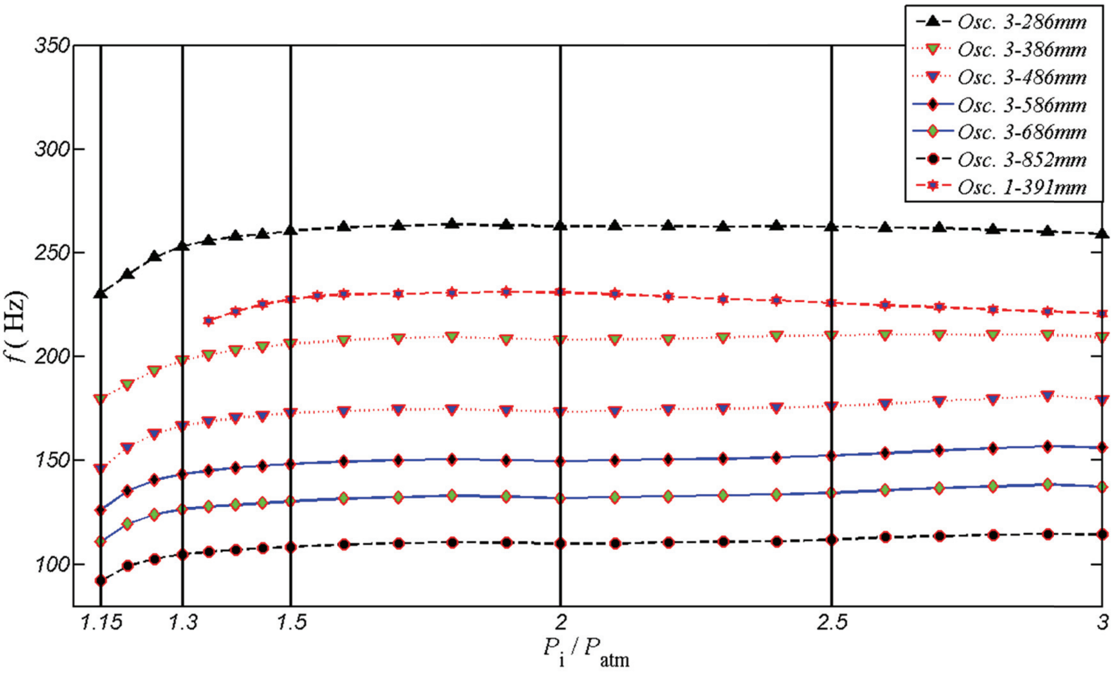

Figure 2-12. Frequency response versus inlet pressure for Osc.1 and for Osc.3 with various FBL.

A first analysis of the frequency response of the oscillator, as shown in Figure 2-12, suggests that when the sonic regime is reached at the nozzle, i.e., when the inlet pressure P_i is higher than 0.17 MPa, the frequency f can be approximated by the equation

$$f \approx C_o / \left(4L_f\right) \tag{2-4}$$

where C_o is the sound velocity at ambient conditions (≈340 m/s) and L_f is the FBL from section A to section P (cf. Figure 2-1 and Figure 2-2), including the connecting tube length and the internal channel length (86 mm). In Table 1, the measured frequencies, for a supply pressure of 0.2 MPa, are compared to the frequencies calculated according to Eq.(2-4). Deviations between calculated and experimental values of the frequency are always smaller than 15%.

Table 2-1. Comparison between the measured and estimated frequencies at $P_\mathrm{i} = 0.2$ MPa

	L_f (mm)	$C_o/(4\,L_f)$ (Hz)	f (Hz)	deviation
Osc.3	286	297	263	13%
Osc.3	386	220	208	5.8%
Osc.3	486	175	174	0.6%
Osc.3	586	145	150	-3.3%
Osc.3	686	124	132	-6.1%
Osc.3	852	100	110	-9.1%

With the purpose to further explore the relationship between the frequency response and the FBL, the oscillation period is drawn in Figure 2-13 as a function of the FBL for five values of the inlet pressure (0.115, 0.13, 0.15, 0.2 and 0.25 MPa as indicated by the vertical black lines in Figure 2-12). A linear fitting of these curves is performed and the regression equations are presented in Figure 2-13, in which T is the oscillation period.

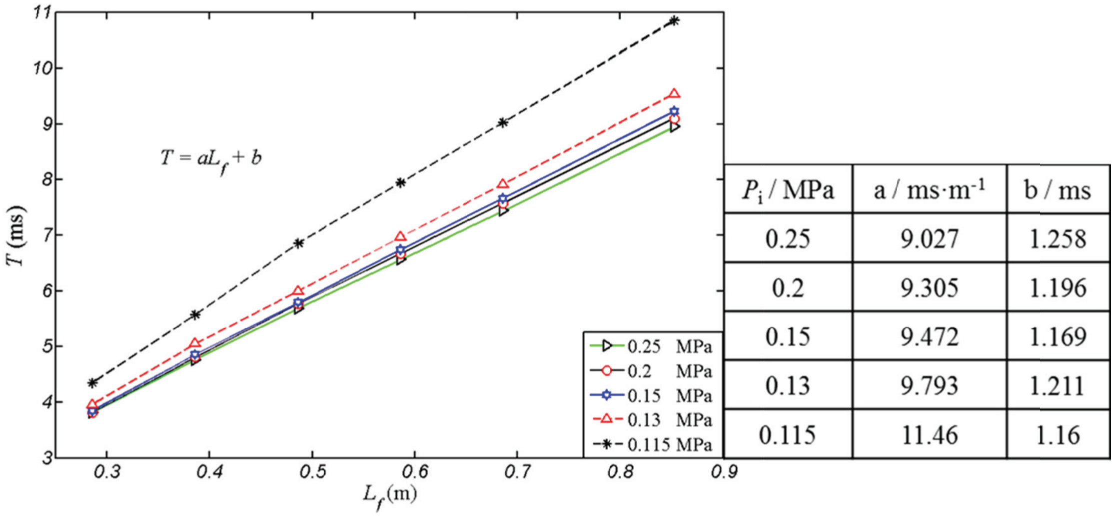

P_i / MPa	a / ms·m^{-1}	b / ms
0.25	9.027	1.258
0.2	9.305	1.196
0.15	9.472	1.169
0.13	9.793	1.211
0.115	11.46	1.16

Figure 2-13. Oscillation period as a function of the FBL of Osc.3. A linear fitting $T = a\,L_f + b$ is proposed.

In each case, the oscillation period has an almost perfect linear relationship with the FBL. However, as the inlet pressure increases, the slope of the regression line decreases. Compared to the estimated function which has been proposed:

$$T = \frac{1}{f} = \frac{4}{C_o} L_f \tag{2-5}$$

with $4/C_o = 11.7\times10$ s m^{-1}, the slope coefficient experimentally obtained has a close value (11.46×10 s m^{-1}) only for the lowest tested P_i (0.115 MPa). However, Eq. (2-5) can be modified in a similar way than in the paper of Simoes et al.[59] (cf. Eq.(1-7)), by introducing a constant switching time:

$$T = \frac{1}{f} = \frac{4}{C} L_f + 2\tau_s = \frac{4}{C_o + \overline{u}} L_f + 2\tau_s \tag{2-6}$$

where C is the average propagation velocity of the pressure wave inside the oscillator which can be estimated as the sum of the sound velocity C_o and the average velocity $\overline{u}$ of the fluid, while τ_s is the jet switching duration. With this modified expression of T, the variation of the slope coefficients for different inlet pressures can be relatively well explained: as the inlet pressure increases, the air flow velocity in the air channels also increases while the sound velocity remains the same, thus the slope coefficient decreases. However, according to Simoes et al.[59], the jet switching time τ_s can be estimated to be of the order of 0.02 ms which is much smaller than the implied value obtained from the linear fitting which is around 0.6 ms (τ_s = b/2). Thus, the validity of the assumptions made to obtain Eq.(2-6) is still unclear, in particular concerning the role played by the pressure waves in the switching mechanism. In order to better understand the physical phenomena controlling the dynamics of the oscillator's internal unsteady flow, numerical simulations have been implemented and are presented in the following chapter.

2.3.2 First observations of the influence of feedback loops diameter/width

The frequency responses for various feedback tubes diameters have also been tested. Four diameters were chosen which are 5.5 mm, 4.0 mm, 2.7 mm and 2.0 mm. Their relative variation trend is the same whatever the FBL is. Thus, only the results for a FBL L_f=586mm are shown in Figure 2-14 for illustration.

Two main behaviors can be observed. Firstly, the relation between the feedback loop diameter and the frequency evolves with the inlet pressure. For relatively small supply pressure, the oscillation frequency is higher for larger diameters. On the contrary, for inlet pressures higher than 0.5 MPa, the larger the diameter the lower the oscillation frequency is.

In addition, the oscillations are more easy to activate when the diameter of the feedback loops is larger. It can be observed indeed that the device starts to oscillate for smaller inlet pressures when the feedback tube diameter is larger (e.g., $P_i \geq 0.115$ MPa for 4 mm tubes and $P_i \geq 0.17$ MPa for 2 mm diameter tubes).

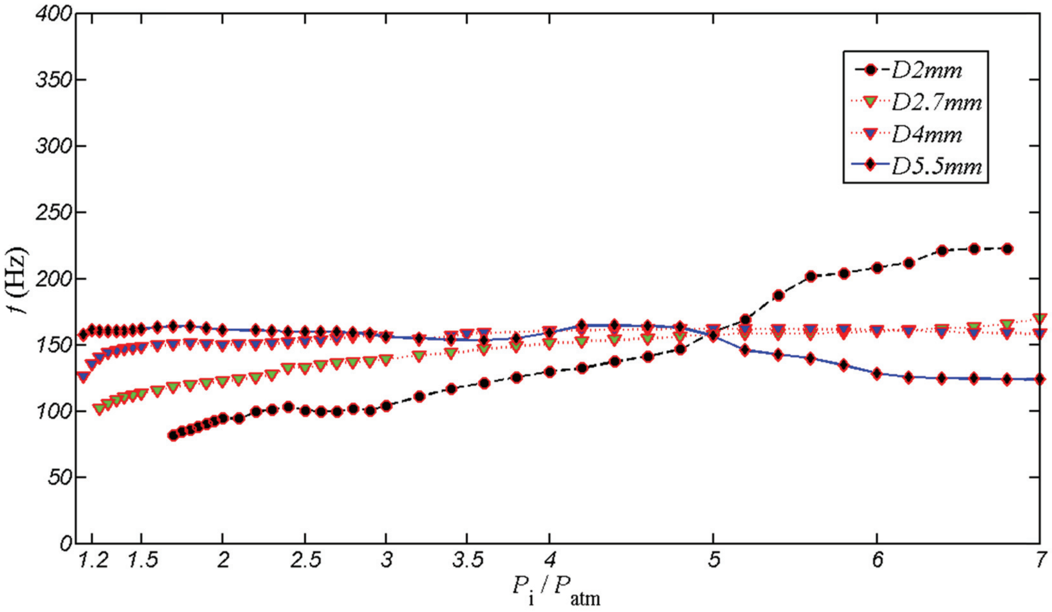

Figure 2-14. Oscillation frequency as a function of the inlet total pressure for various feedback loop diameters but same FBL L_f = 586 mm

All the above observations imply that in addition to the FBL, the feedback loop diameter also plays an important role on the oscillator's performance. In addition, it seems that a large feedback loop diameter could lead to the non-dependence of the oscillation frequency to the inlet pressure, which could be a great advantage for flow control application. However, the underlying mechanisms of the observed behaviors still need more exploration.

2.4 Conclusions

According to the experimental studies described in this chapter, it can be concluded that the outlet average velocity is controlled by the oscillator's throat section and inlet pressure. However, the outlet velocity amplitude and temporal evolution profile can be affected also by the throat section and/or other internal geometrical factors. With a small throat width (Osc.1), a suction flow phenomenon has been observed and the velocity amplitude is about 2 times the average velocity value. The ejected flow is similar to a typical pulsed jet in which the maximum velocity keeps nearly constant during the ejection phase. With a larger throat width (Osc.2) however, the velocity amplitude is of the same order as the average velocity value, and no suction appears.

Both the feedback loop length and diameter play important roles on the oscillator's performances, in particular its frequency response. An equation, deducted from the acquired experimental data, has been proposed to estimate the oscillation frequency as a function of the feedback loops length. However, the validity of the assumptions made to obtain this equation is still unclear, in particular concerning the role played by the pressure waves in the switching mechanism. In addition, further investigations should be conducted to better understand the influence of the feedback loops diameter on the oscillation frequency and on the minimal supply pressure needed to initiate the oscillating mechanism. In order to better understand the physical phenomena controlling the dynamics of the oscillator's internal unsteady flow, and due to the very small dimensions of the studied devices making it very difficult to visualize internal flows or to get local velocity or pressure data, numerical simulations have thus been implemented and are presented in the following chapters.

Chapter 3. Numerical Tools and Validation

In order to complete the experimental analysis of the oscillators' behavior and thus to better understand the physical phenomena controlling the dynamics of their internal unsteady flow, numerical models of these actuators have been developed and tested. Due to the tiny dimensions of the studied devices, the very short time scales of the involved unsteady flows, as well as their transonic characteristics, it was indeed very difficult to get local experimental data, such as velocity or pressure.

As detailed in Annex 1, first numerical models built on the CFD software ANSYS/FLUENT have shown an important sensibility to critical settings such as the transient discretization scheme and the time step, not allowing their exploitation for the detailed analysis of the oscillator's behavior. New numerical simulations have then been performed on the open source CFD package OpenFOAM because of its free license, high parallel capacity efficiency and flexibility. This chapter, after a brief presentation of this CFD code, will thus be focused on the description of the developed numerical models and their validation thanks to comparisons with the experimental measurements previously performed.

3.1 Introduction to OpenFOAM

OpenFOAM (Open source Field Operation And Manipulation) is a free, open source software for computational fluid dynamics (CFD), based on the Finite Volume Method, written in C++, fully objective-oriented, developed primarily by CFD Direct, on behalf of the OpenFOAM Foundation. The code has been used to solve problems in CFD, electromagnetics, solid mechanics and even finances. OpenFOAM can serve both the engineering use because of various integrated solvers and free license, and academic research because of its flexibility to be modified and expanded [78].

To run a simulation, OpenFOAM should be installed in a LINUX environment, and a *main* folder is needed, containing three sub-folders:

Folder *0* or *time directories*, which contains the boundary conditions and initial fields to begin the simulation.

Folder *constant*, which contains the mesh folder and the files for fluid and turbulence properties.

Folder *system*, which contains the solver specifications, numerical discretization schemes and calculation control parameters.

A schematic illustration of the organization of folders is shown in Figure 3-1, which is a general and summarized example. The *time directories* folder is rather a set of folders that contains saved results for the user's specified time steps than a single folder.

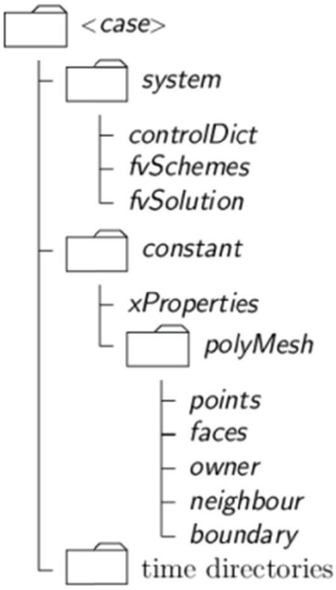

Figure 3-1. Sketch of the organization of an OpenFOAM case folder[79]

The OpenFOAM version used in this thesis is the 2.3.0 which was released on 17, February 2014.

Since the oscillator's internal flow is sonic in the throat, supersonic just beyond the throat and subsonic in the other parts for most of the operating cases, the sonicFoam solver is chosen in this study. The governing equations are compressible Navier-Stokes equations in their conservative form, including the continuity equation or mass conservation equation, the momentum conservation equation and the energy conservation equation with the following approximations and hypothesis:

○ continuum hypothesis;

○ compressible gas fluid flow;

○ non-reactive mono-species gases;

○ non-hypersonic flows (Ma < 6 for air);

○ low temperature differences to neglect radiation;

○ thermodynamic equilibrium so that the perfect gas equation can be used;

○ Newtonian fluid with the dynamic viscosity varying only with temperature;

○ Froude number large enough to neglect gravity effects.

For more detailed information about both usage and underlying theory, it is possible to refer to the official guide of OpenFOAM and general fluid dynamics textbooks [79] [80] [81] [82].

3.2 Numerical settings

The solver chosen here is sonicFoam which is integrated in OpenFOAM as a transient solver for transonic/supersonic flow of a compressible gas.

Given the complexity of the internal geometry and the turbulent flow, a series of numerical sensitivity studies have been carried out to find out the optimal numerical settings considering both accuracy and cost. This study is detailed in Annex 2.

Discretization schemes

Table 3-1 summarizes the discretization schemes adopted after the sensibility study.

Table 3-1. Adopted discretization schemes

	Scheme	***Precision***
ddt	backward	2nd order
gradSchemes	Gauss linear	2nd order
LaplacianSchemes	Gauss linear corrected 0.5	Blend of 1st and 2nd order
divSchemes	Gauss linearUpwind grad( )	2nd order

Boundary conditions

Similarly, Table 3-2 summarizes the type of boundary conditions used for each equation.

Table 3-2. Boundary conditions used in the simulations for each equation

equation	***inlet***	***wall***	***outlet***
p	totalPressure	zeroGradient	fixedValue
U	pressureInletVelocity	fixedValue	zeroGradient
T	inletOutlet	zeroGradient	inletOutlet
k	turbulentIntensity-KineticEnergyInlet intensity 0.05;	kqRWallFunction	zeroGradient
epsilon	turbulentMixingLength-DissipationRateInlet mixingLength 0.0005;	epsilonWallFunction	zeroGradient
omega	turbulentMixingLength-FrequencyInlet mixingLength 0.0005;	omegaWallFunction	zeroGradient

Turbulence model and other related schemes

Considering the calculation precision and efficiency, the realizable k-epsilon turbulent model, with moderate mesh density (average $Y^+ \approx 10$, cf. Figure A2-2, Annex 2) and normal wall function have been found to be the best choice for the following work. The optimized time step is 5×10^{-9} s, leading to a maximum courant number smaller than 0.3.

3.3 Validation of the numerical models

3.3.1 Measurement of the oscillators' internal geometry by X-ray tomography

As highlighted in section 2.2.3 and 2.2.4, the internal dimensions of the prototypes may undergo large modifications during the assembling process. X-ray tomography has thus been implemented to measure the real internal dimensions after assemblage. This micro-tomography system - Easytom 130, has a 3D resolution of 254 μm (normal case) to 5 μm (maximum zoomed case) per pixel, which permits to measure the inside channel dimensions without disassembling the oscillator.

The global view and zoomed view of the throat part of Osc.1 are shown in Figure 3-2. The throat width is measured to be about 0.10 mm which is much smaller than the designed one (0.2 mm)but very close to the width calculated from the outlet velocity measured by hot-wire (0.073 mm, cf. section 2.2.3). From Figure 3-2b, it can be also observed that the throat position is deviated from the designed symmetrical center line, and obviously prone to the left side branch. This observation explains why the jet ejected in left outlet slot last much longer than that in the right outlet slot as shown in Figure 2-8.

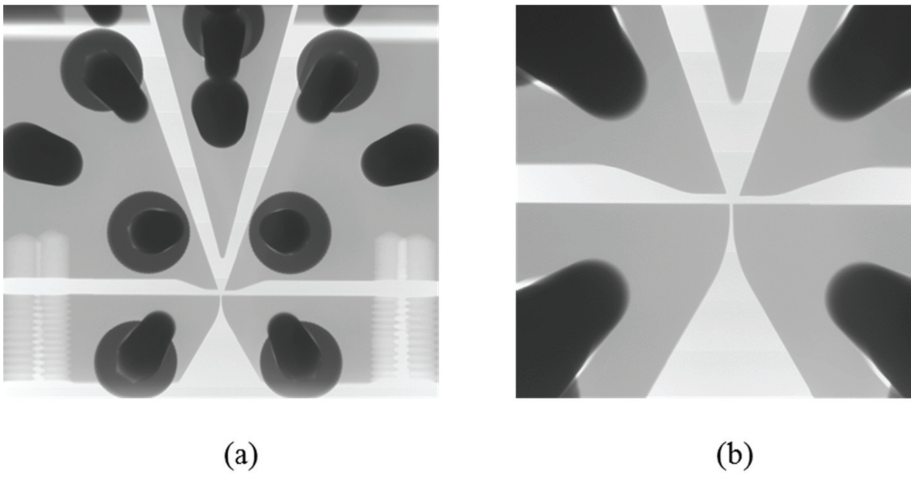
(a) (b)

Figure 3-2. X-ray visualization of internal channels of Osc.1. a) global view of the central part, b) zoomed view of the switching zone

Figure 3-3 shows the global view and zoomed view of the throat part of Osc.2. The throat width is measured to be about 0.28 mm which is also very close to the width calculated in section 2.2.4 from the outlet velocity measured by hot-wire (0.246 mm).

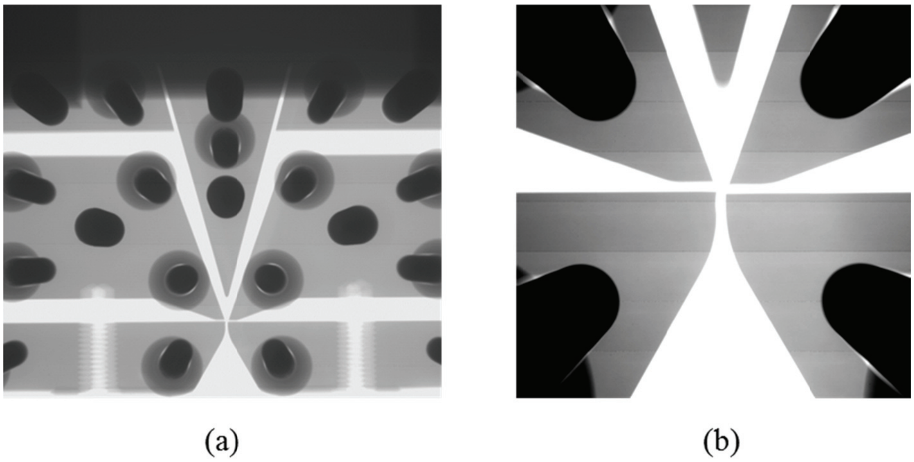

Figure 3-3. X-ray visualization of internal channels of Osc.2. a) global view of the central part, b) zoomed view of the switching zone

When the key dimensions of the internal geometry are measured from the X-ray photos, some problems must however be taken into account. Firstly, except in the central part of the image, the lens distortion is significant and does not permit to get accurate dimensions. In addition, when the oscillator is mounted and fixed on the test bench, the internal dimensions may also be affected by the stress due to the fastening process.

With the same numerical settings presented in section 3.2, flow simulations in both designed geometry and scanned geometry are carried out. The predicted results are compared to the measured ones in order to validate the chosen numerical settings.

3.3.2 Frequency prediction capability

Table 3-3 presents a comparison between the frequency deduced from numerical simulations on the scanned geometry $f_{\text{s-s}}$, the frequency obtained numerically on the designed geometry $f_{\text{s-d}}$ and the measured value f_{m} , for an inlet total pressure of 0.25MPa. The maximum deviation between the simulated and measured frequencies is about 5% which means that the chosen numerical tools and settings are very suitable to predict the oscillators' frequency and that the numerical models may be suitable for analyzing the oscillation dynamics.

Table 3-3. Comparison of predicted and measured frequency, P_{i}=0.25 MPa

	f_{m}/ (Hz)	$f_{\text{s-s}}$ / (Hz)	deviation	$f_{\text{s-d}}$ / (Hz)	deviation
Osc.1	272	286	+5.15%	275	-1.09%
Osc.2	497	485	-2.41%	506	+1.81%

3.3.3 Velocity prediction capability

For an inlet pressure of 0.2 MPa, the evolution with time of the outlet velocity magnitude in the center of both left and right outlet slots for Osc.1 and Osc.2, obtained from the numerical simulations on the scanned internal geometry, are presented in Figure 3-4 and Figure 3-5 respectively, and are compared to those obtained from hot wire measurements.

The simulated maximum velocity for Osc.1(cf. Figure 3-4) is about 110 m/s, which is much higher than the measured 70 m/s. The simulated maximum suction velocity is about 25 m/s which is also a little higher than the measured 20 m/s. This deviation of about 57% on maximum velocities could be partially explained by the possible errors made on the throat width due to the measurement problems described in section 3.3.1. Assuming a uniform velocity on the outlet section, it is indeed possible to calculate the ejected flowrate on a period from the velocity temporal evolution curve and thus to deduce a throat width of 0.073 mm, which is 27% smaller than the value used in the simulation.

In both measured and simulated results, the suction velocity can be obviously observed and the suction duration in one period in the left outlet slot is shorter than that in the right because of the asymmetry observed in the throat region. In addition, the simulated velocity evolution profile doesn’t present a plateau as in the experimental case (cf. Figure 3-4b), showing that in the simulations, the jet switching process is long compared to the oscillation period.

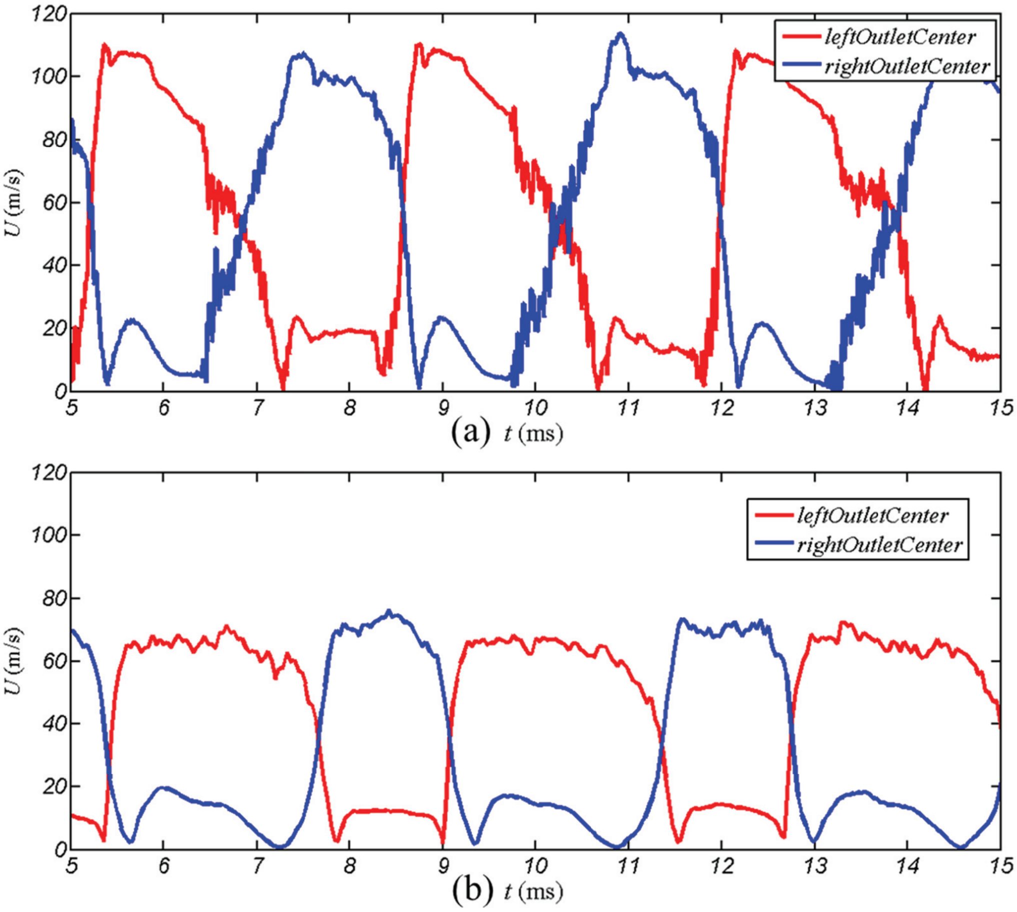

Figure 3-4. Velocity magnitude evolution with time in the center of Osc.1's both left and right outlet slots, P_i=0.2 MPa; a) results from simulation, b) results from hot wire measurements

For Osc.2, the higher velocity value in the right outlet slot than that in the left one, due to the internal geometry asymmetry and observed experimentally in Figure 3-5b, is well reproduced in the simulation(cf. Figure 3-5a). However, the simulated velocity amplitude is much larger than the measured one, though the average velocity obtained in numerical simulations is just a little lower than the experimental one.

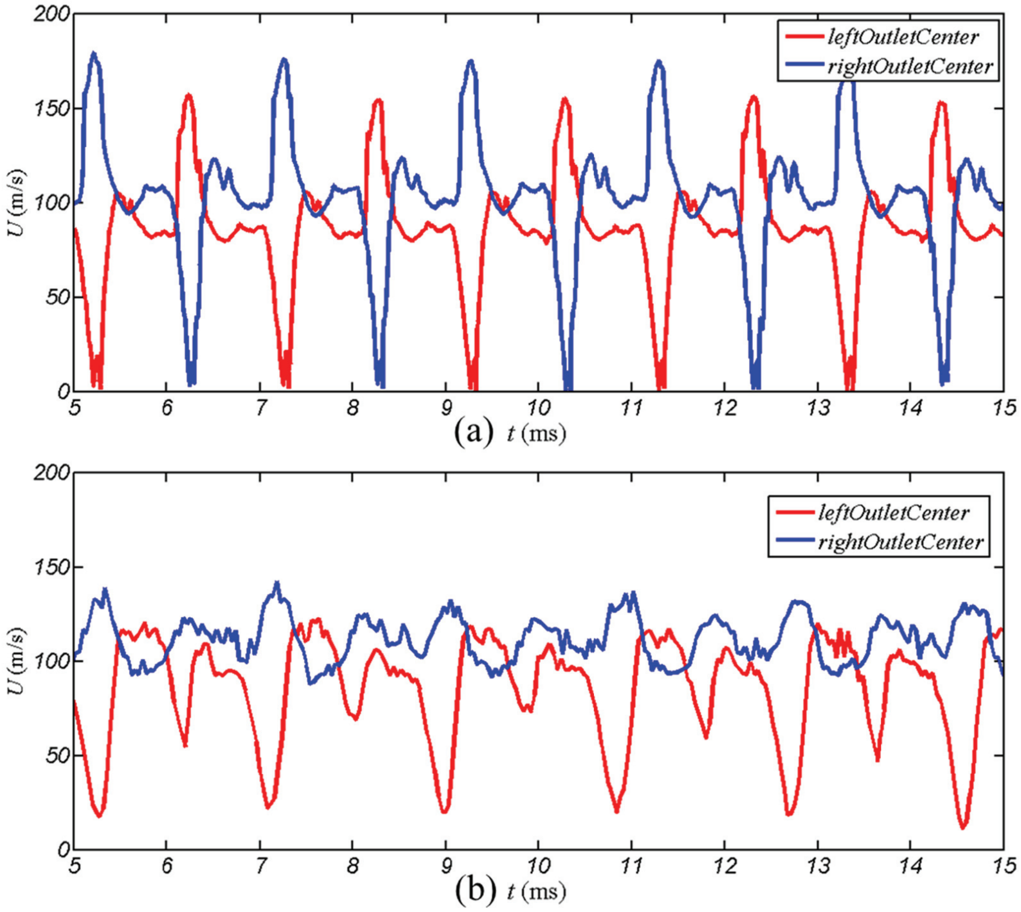

Figure 3-5. Velocity magnitude evolution with time in the center of Osc.2's both left and right outlet slots, P_i=0.2 MPa, a) results from simulation, b) results from hot wire measurements

3.4 Conclusions

Taking both the calculation precision and efficiency into account, the optimal choices of numerical settings for the present case are realizable k-epsilon turbulent model, moderate mesh density, normal wall function, time step of 5×10^{-9}s corresponding to a maximum courant number of 0.35 and second order discretization schemes for both spatial and temporal terms.

These settings offer a quite precise estimation of the operating frequency, but have a limited capability for predicting the outlet velocity evolution pattern. This is maybe due to the fact that the outlet velocity is much more sensitive to the internal geometry deviations. Despite these limitations, the developed numerical models are able to provide important data for a qualitative analysis of the internal unsteady flow, which could be exploited to better understand the physical mechanisms involved in the oscillating process.

Chapter 4. Numerical Analysis of Oscillation Dynamics

As it has been described in section 2.1, in the sketches of Figure 2-1 and Figure 2-2, in order to facilitate the analysis of the oscillator's behavior, e.g., pressure propagation, velocity evolution, etc., six representative sections, noted (A, B, C, D, E, P), have been selected; they represent the branch inlet, the branch center, the loop inlet, the loop center, the loop outlet and the control port, respectively, with 1 representing the oscillator's left side while 2 representing the right side. These sections have been reminded on windows I and II of Figure 4-2a.

As it has been discussed in section 3.4, the numerical simulations are able to provide important data for a qualitative analysis of the internal unsteady flow, and help understanding the underlying oscillation mechanics. Thus, a simulation on the designed geometry of Osc.1 has been carried out. In order to reach a regular periodic behavior, more than 20 periods are simulated. A sample signal of the area-average pressure in the left loop center section D1, corresponding to the last four periods of the simulation, is shown in Figure 4-1. The simulated oscillation period is 4.3 ms, which corresponds to an oscillation frequency of 231 Hz, close to the experimental frequency of 226 Hz (cf. Figure 2-11) obtained for the same operating conditions, i.e., at $P_i = 0.25$ MPa.

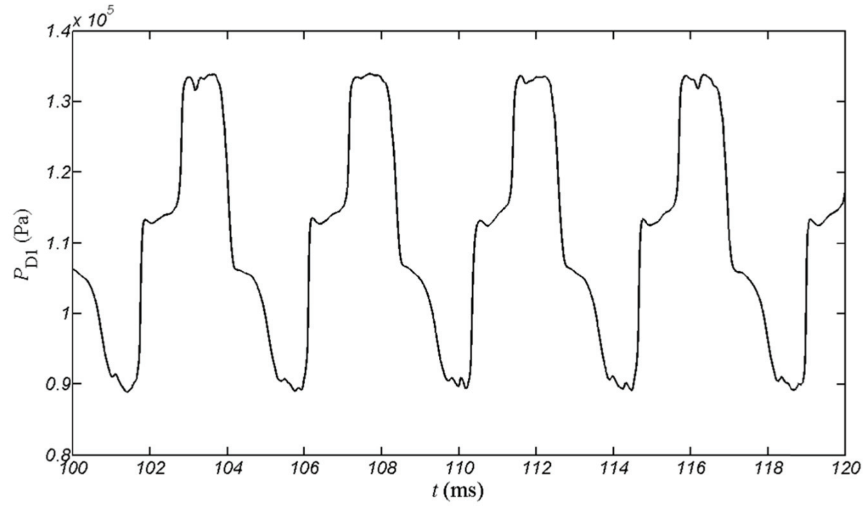

Figure 4-1. Area-averaged pressure in the left loop center section of Osc.1 versus time; $P_i = 0.25$ MPa

4.1 Identification of the key factors controlling the oscillations

4.1.1 Qualitative analysis of the switching process inside the oscillator

The switching process can be examined by comparing at the same time the pressure and velocity magnitude contours, as shown in Figure 4-2, Figure 4-3 and Figure 4-4. It can be clearly observed that the jet oscillation is mainly caused by the pressure wave propagation in the two feedback loops alternatively. In each of the following figures, the top left (window I) is a global view of the pressure contours and the top right (window Ⅱ) is a zoom of the pressure contours in the interaction zone. The down windows of these figures are their counterparts for the velocity magnitude contours (down left window Ⅲ and down right window Ⅳ). In the global views, a large part of the feedback loop in each side is not represented but symbolized by a blank space in the loop in order to save space. Six important times during the oscillation period *T*, which is equal to 4.3 ms in these simulations, have been chosen to highlight the dynamics of the jet switching process:

***t* = 0:** at this time, the main jet is just starting to switch from the right branch to the left branch as it can be observed on the velocity contours in window Ⅳ in Figure 4-2a. The main part of the flowrate is still leaving the oscillator through the right outlet, although the main jet has already been deviated in the left branch. The pressure in the right feedback loop is approximately 4×10^4 Pa higher than that in the left loop, especially between the control ports. This pressure difference between the control ports at the base of the jet is particularly important.

***t* = 0.03 *T*:** the switching time duration is quite short compared to the whole period *T*, as discussed in section 2.3.1. Just 0.03 *T* after its initial deflection, the main jet has totally attached to the left branch as shown in window Ⅳ in Figure 4-2b. In addition, as the main jet switches toward the left side, a high pressure wave propagates in the left side simultaneously to fill in the left feedback loop. Meanwhile, in the right side, air is evacuated from the right loop through the right branch. At this time, since the pressure at the right control port P2 is significantly higher than at the left one P1, the main jet is perfectly attached to the left branch.

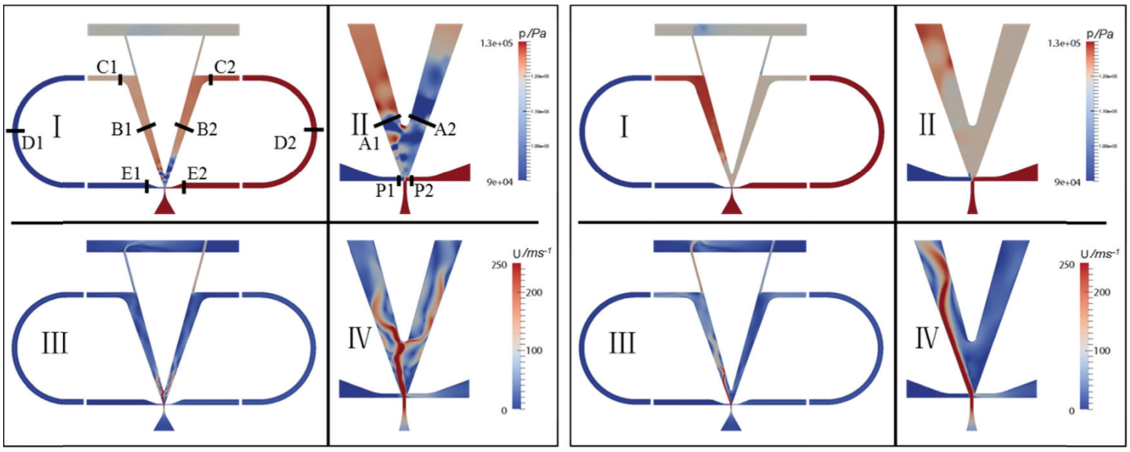

a) t* = 0** ***b) t* = 0.03 *T

Figure 4-2. Contours of static pressure (upper windows) and velocity magnitude (down windows) in a global view (left windows) and zoomed view (right windows) a) at $t = 0$; b) at $t = 0.03\ T$

***t* = 0.225*T*:** as the high pressure compression wave (HPCW) reaches the left control port P1, the low pressure expansion wave (LPEW) is still propagating in the right feedback loop. However, the pressure difference between the two control ports decreases, leading to a destabilization of the jet at its base as shown by the velocity contours in window Ⅳ in Figure 4-3a.

***t* = 0.258*T*:** once the HPCW and LPEW have reached the control ports, they reflect and propagate in the reverse directions. As a consequence, the pressure difference between the two control ports decreases rapidly and even reverse as illustrated by the pressure contours in windows Ⅰ and Ⅱ in Figure 4-3b. Under these pressure conditions, the jet detachment from the left wall becomes more obvious. However, even the jet becomes clearly unstable (window Ⅳ in Figure 4-3b), the main part of the fluid still flows out through the left branch and outlet.

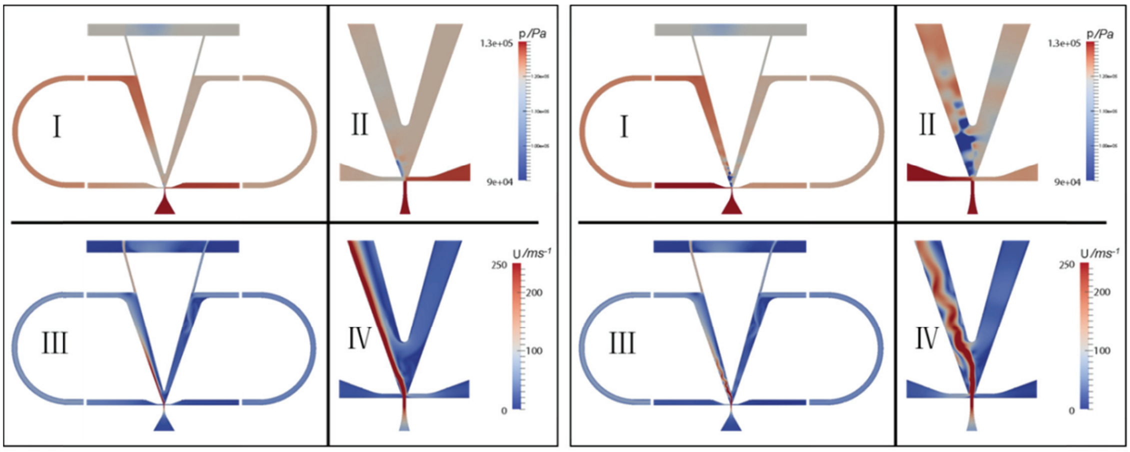

a) t* = 0.225 *T ***b) t* = 0.258 *T***

Figure 4-3. Contours of static pressure (upper windows) and velocity magnitude (down windows) in a global view (left windows) and zoomed view (right windows) a) at $t = 0.225T$; b) at $t = 0.258\ T$

***t* = 0.49 *T*:** due to the reflected propagation of HPCW and LPEW in the left and right loops and branches respectively, the pressure differences between left and right branches and between left and right control ports reach their maximum values (windows Ⅰ and Ⅱ in Figure 4-4a). These pressure conditions cause a strong bending of the jet which is about to switch to the right branch of the oscillator, as shown by the velocity contours in window Ⅳ in Figure 4-4a. A small part of the jet already flows through the right branch.

***t* = 0.5 *T*:** the jet switches rapidly from the left side to the right side as shown in window Ⅳ in Figure 4-4b. Then, another half period of the oscillation begins. The pressure and velocity fields are symmetrical to the ones presented in Figure 4-2a.

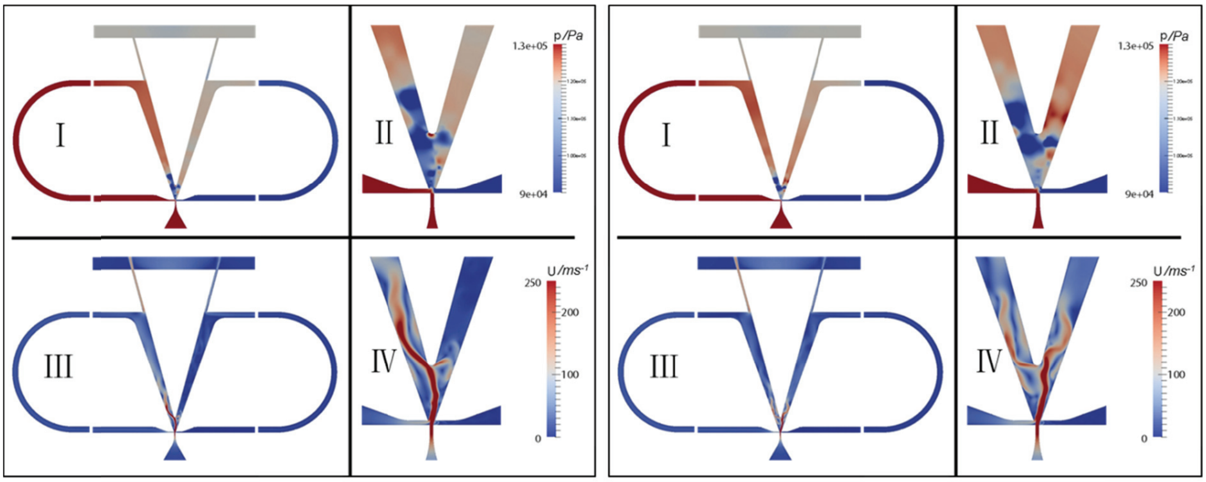

a) t* = 0.49 *T ***b) t* = 0.5 *T***

Figure 4-4. Contours of static pressure (upper windows) and velocity magnitude (down windows) in a global view (left windows) and zoomed view (right windows) a) $t = 0.49\ T$; b) $t = 0.5\ T$

From the above analysis of various snapshots of the pressure and velocity contours, we can conclude that the jet switching is mainly caused by the propagation of pressure waves inside the oscillator's feedback loops and branches. It seems that the pressure difference between the control ports at the jet base is not sufficient to cause the jet switching, which only occurs when, in addition, the pressure difference between the two branches reaches its maximal value, due to the reflected propagation of the pressure waves in the feedback loops. This back and forth propagation of the pressure waves during half a period may partially explain the coefficient 4 in Eq. (2-5) used to estimate the oscillation period, contrary to the coefficient 2 in the relation proposed by Simoes et al.[59].

4.1.2 Detailed study of the oscillation process inside the device

In order to confirm the assumptions made above about the physical mechanisms governing the oscillation dynamics, the evolution of the pressure and velocity magnitude with time in the six sections in each side of the oscillator as defined in Figure 2-1 and Figure 2-2, have been tracked and compared. The distances between these sections are l_{AB}=11.75 mm; l_{BC}=13.7 mm; l_{CD}=177.7 mm; l_{DE}=183.6 mm; l_{EP}=4.6 mm, respectively. The evolution of same parameters with time in the counterpart sections of right side of the device have also been tracked.

Figure 4-5 and Figure 4-7 respectively show the evolution with time over one period of the area-averaged static pressure and velocity in sections B1, C1, D1 and E1 (cf. Figure 2-1, Figure 2-2). Pressure and velocity evolutions in the two other sections (branch inlet A and control port P) on both sides are compared in Figure 4-6 and Figure 4-8, respectively.

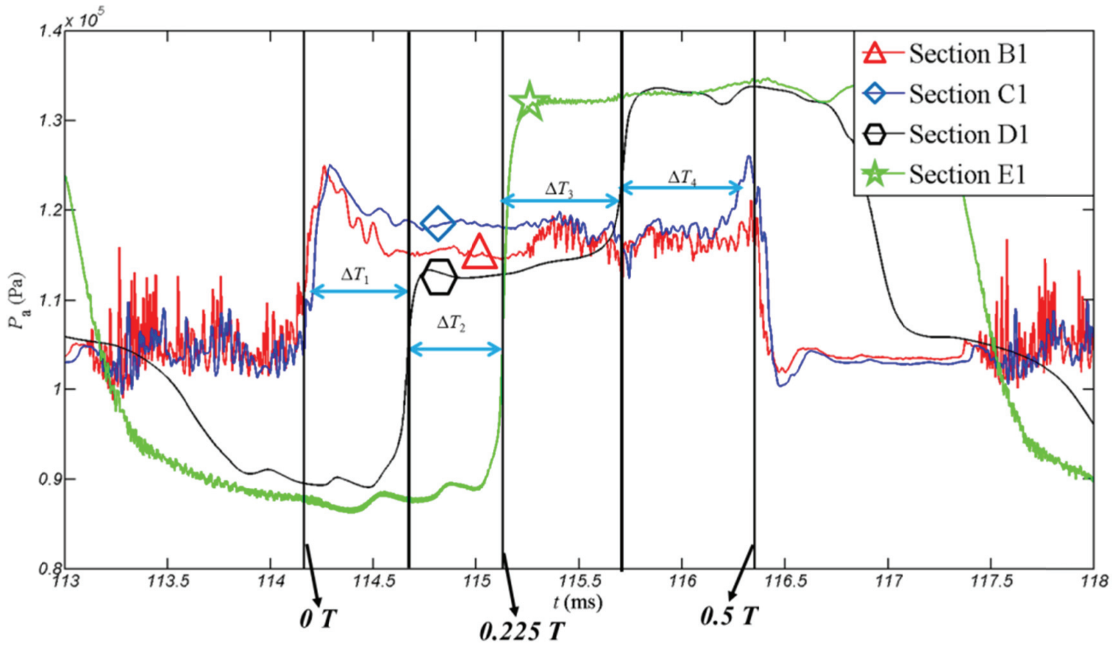

Figure 4-5. Evolution of the area-averaged pressure with time in sections B1, C1, D1 and E1

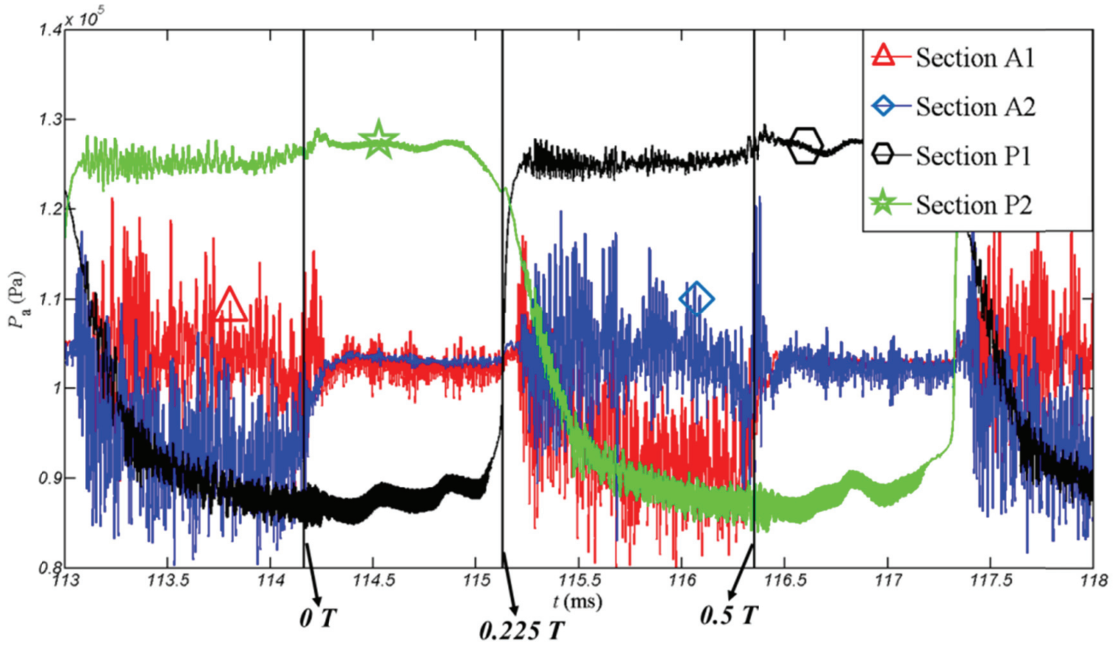

Figure 4-6. Evolution of the area-averaged pressure with time in sections A1, A2, P1 and P2

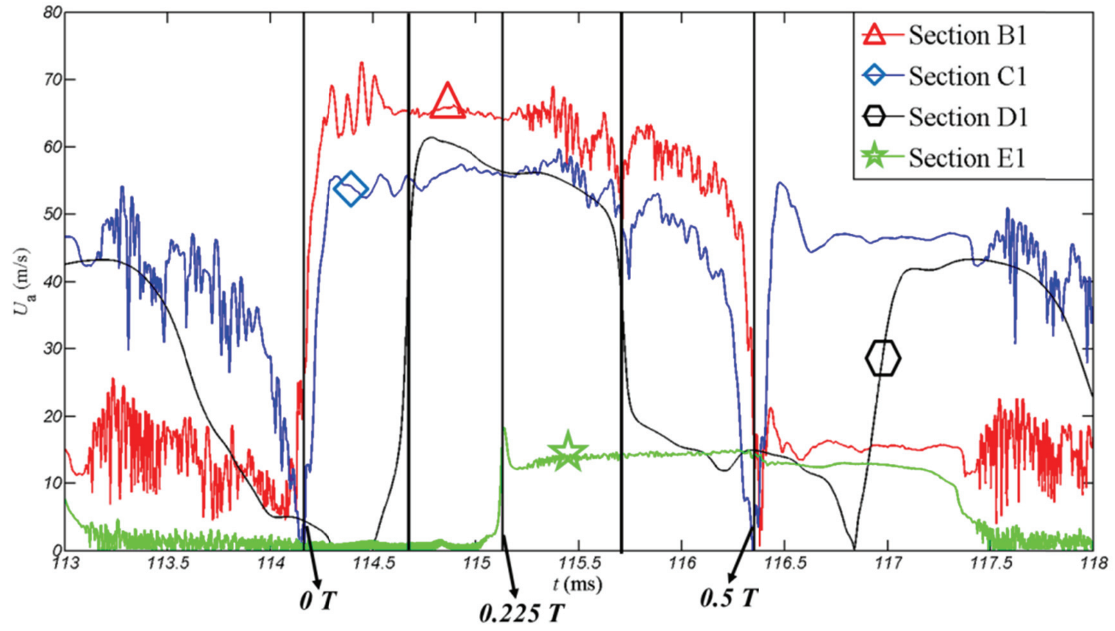

Figure 4-7. Evolution of the area-averaged velocity with time in sections B1, C1, D1 and E1

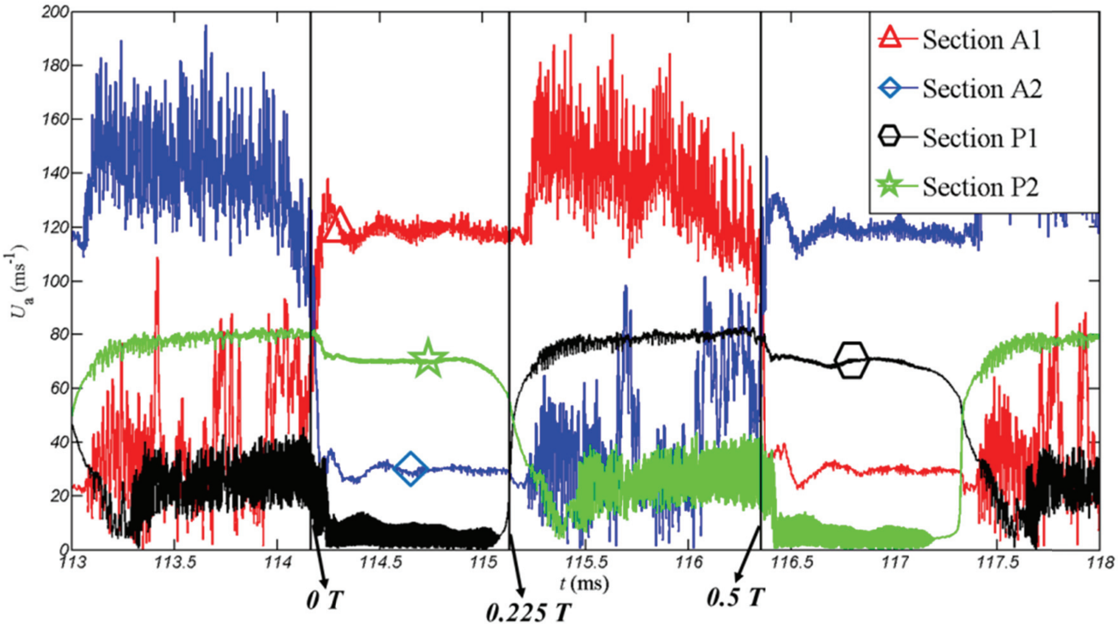

Figure 4-8. Evolution of the area-averaged velocity with time in sections A1, A2, P1 and P2.

In Figure 4-8, it can be observed that at the simulated time 114.2 ms, which corresponds to the starting point of the oscillation period defined in the previous section ($t = 0$), the velocity magnitude in section A2 (right branch inlet) begins to decrease dramatically from 120 m/s to 30 m/s, while the velocity magnitude in section A1 (left branch inlet) begins to increase significantly from 60 m/s to 120 m/s, which means that the main jet is switching from the right side branch to the left side around this time. As the jet switches from the right branch to the left one, the pressure in each section of the left side increases consequently, following the pressure wave propagation in the left branch and feedback loop. In Figure 4-5, it can be clearly seen that the wave propagates from section C1 (left loop inlet) to section D1 (left loop center) during a time interval $\Delta T_1 = 0.452$ ms with a velocity $U_1 = l_{CD}/\Delta T_1 = 393$ ms^{-1} and leads to a pressure augmentation of 20 kPa in both sections with a delay ΔT_1 between them. In the same way, a delay $\Delta T_2 = 0.474$ ms is needed for the pressure wave to reach section E1 (left loop outlet) with similar velocity $U_2 = l_{DE}/\Delta T_2 = 387$ ms^{-1} and pressure increase. The pressure propagation velocity in the loop during this period is approximately equal to the sum of the sound velocity (~ 340 m/s) and the local fluid velocity (~ 55 m/s as shown in Figure 4-7) since the pressure wave propagation has the same direction as the flow.

Just before the jet switching from right to left ($t = 0$), the pressure differences between both branch inlets (section A1, A2) and both control ports (section P1, P2) reach their maximum values, i.e., 10 and 40 kPa respectively (Figure 4-6). After switching, the pressure stays nearly constant at sections A1, A2, P1, P2 until the pressure waves reach section P1 and P2 leading to a sudden inversion of the pressure difference between both sides of the jet base. Even if this pressure difference is not sufficient to provoke the jet switching in the other direction, it induces a destabilization of the jet which is clearly evidenced by the strong chaotic temporal variations of the velocity (cf. Figure 4-8) and of the pressure (cf. Figure 4-6) at the branch inlets. The velocity increase in the left branch observed just after $t = 0.225T$ (cf. Figure 4-8) is due to the flow coming from the left control port and entrained by the main jet.

The velocity of the order of 30 m/s observed in Figure 4-8 at section A2 (blue diamond line between 0 T and 0.225 T) when the jet is attached to the left wall is due to the strong suction effect of the jet, the velocity in the right branch being directed towards the nozzle. During the same time interval, the velocity at section P1 is only of the order of 5 m/s (black hexagon between 0 T and 0.225 T) which indicates that the flow is blocked by the main jet attached to the left wall, while the velocity of the order of 70 m/s at section P2 (green star line between 0 T and 0.225 T) is due to the rapid emptying of the right feedback loop helped by the suction effect of the main jet.

The reflection of the pressure wave once it reaches the control port is shown in Figure 4-5 by the additional pressure jump occurring, between $t = 0.225T$ and $t = 0.5T$, in each section of the feedback loop with a time lag depending on the wave propagation velocity. The total propagation time after reflection along the feedback loop: $\Delta T = \Delta T_3 + \Delta T_4 = 1.14$ ms, implies a propagating velocity: $U_3 = l_{\mathrm{CE}}/\Delta T = (l_{\mathrm{CD}} + l_{\mathrm{DE}})/\Delta T = 317\ \mathrm{ms}^{-1}$,which is approximately equal to the difference between the sound velocity and the local fluid velocity (15 m/s) which is opposite to the wave propagation direction. At the end of this half period, when the pressure wave reaches section B1 leading to a sudden pressure increase in this section (cf. Figure 4-5, $t = 0.5$ T), the main jet is finally pushed toward the other side of the device and the second half period begins.

According to the above analysis, the jet oscillation frequency has a direct relationship with the forth and back propagation of the pressure wave in the branch and the feedback loop, from section A to section P.

The oscillation period can thus be estimated by the following function:

$$T = \frac{1}{f} = 2(\tau_t + \tau_s) = 2\left(\frac{1}{C_o + u_1} L_f + \frac{1}{C_o - u_2} L_f + \tau_s\right) \tag{4-1}$$

where L_f is the FBL, C_o is the sound velocity, u_1 is the local fluid velocity in front of the wave in the first quarter of the period while u_2 is the local fluid velocity in front of the reflected wave in the second quarter of the period, and τ_s is the switching time of the order of $0.01T$ which can be ignored and is in accordance with the estimation of Simoes et al.[59]. The error generated by modifying the terms $C_o + u_1$ and $C_o - u_2$ in Eq.(4-1) to the term $C_o + \overline{u}$ in Eq.(2-6) is accumulated to the intercept term b, resulting in a much larger value, which explains the large deviation between the empirical τ_s got from the data fitting (cf. Eq.(2-6) and Figure 2-13) and that from the estimation in literature.

In general, u_1 and u_2 are small compared to the sound velocity, especially when the supply pressure of the oscillator is low. If u_1 and u_2 are assumed negligible compared to C_o, in addition to the fact that τ_s can be ignored, Eq.(4-1) becomes

$$T = \frac{1}{f} = 2\tau_t = \frac{4L_f}{C_o} \tag{4-2}$$

which is exactly the same as the empirical formula Eq.(2-5) obtained from measured results.

4.2 Numerical study of the effects of two pressure differences

The results obtained above indicate that the jet switching is not only controlled by the pressure difference at the base of the jet, but also by the pressure difference in the two branches. In order to validate this assumption, three series of simplified simulations were carried out. A simplified geometry which represents the central part of a typical oscillator has been chosen, as shown in Figure 4-9. This simplified oscillator has the same dimensions as the above simulated oscillator but without feedback loops. Pressures at both branch outlets (sections G1 and G2) and both loop outlets (sections E1 and E2) can be set independently. In this way, the effect of the pressure difference between the two sides of the jet base and the effect of the pressure difference between the two branches can be tested separately or in combination.

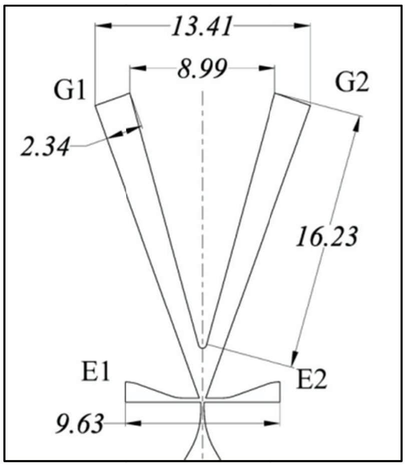

Figure 4-9. Simplified geometry which represents the central part of a typical oscillator

In the first step of this numerical analysis, the inlet total pressure is set to 0.25 MPa, and a static pressure of 0.1 MPa is imposed in sections Gl, G2, El and E2. Figure 4-10 (case 0) shows the velocity contours obtained for this basis case, indicating that the jet is attached to the right branch, despite the small recirculation zone visible between the jet and the wall.

4.2.1 Isolated effect of the pressure difference between the control ports

In the second step, starting from the configuration obtained in case 0, inlet pressure and outlet pressures are not changed while the pressure at section E1, P_{E1}, is reduced to 0.09 MPa which is the smallest pressure observed in this section in the preceding numerical simulations (cf. Figure 4-5). In the same way, the pressure at section E2, P_{E2}, is gradually increased from 0.1 to 0.2 MPa. A total of 5 simulations, denoted as cases 1-1, 1-2, 1-3, 1-4 and 1-5, are carried out, corresponding to P_{E2} of 0.125, 0.15, 0.16, 0.18 and 0.2 MPa, respectively.

The obtained velocity fields after a duration of 1 ms are presented in Figure 4-10. As the pressure at the right side is increased gradually, the jet gets more and more bended with even an attachment of the jet base to the left wall. Nevertheless, the jet always flows out through the right outlet, whatever the pressure difference at the control ports, proving that, for an inlet pressure of 0.25 MPa, the oscillations would not occur if the pressures in the two branches were kept at their initial level.

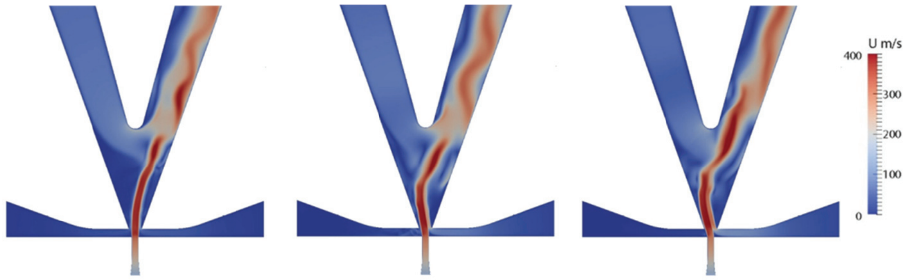

Case 0: $P_{E1}=P_{E2}=0.1$ MPa Case 1-1: $P_{E2}=0.125$ MPa Case 1-2: $P_{E2}=0.15$ MPa

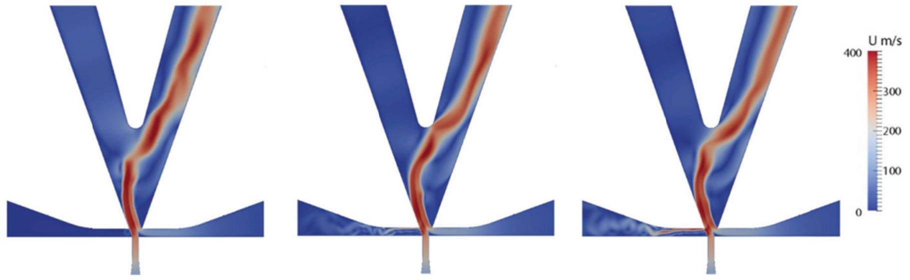

Case 1-4: $P_{E2}=0.16$ MPa Case 1-4: $P_{E2}=0.18$ MPa Case 1-5: $P_{E2}=0.2$ MPa

Figure 4-10. Velocity contours in the simplified oscillator model for different values of the pressure P_{E2} at the right control port. $P_i = 0.25$ MPa, $P_{G2} = P_{G1} = 0.1$ MPa, $P_{E1} = 0.1$ MPa (case 0) or 0.09 MPa for all other cases.

4.2.2 Isolated effect of the pressure difference between the two branches

In the third step, also starting from the simulation results of case 0, the inlet total pressure of 0.25 MPa is unchanged, P_{G1}, P_{E1} and P_{E2} are kept at 0.1 MPa while P_{G2} is gradually increased from 0.1 to 0.2 MPa in order to generate a pressure gradient between the two branches. A total of 8 values of P_{G2} have been tested: 0.11, 0.12, 0.125, 0.135, 0.145, 0.16, 0.18 and 0.2 MPa.

The obtained results are presented in Table 4-1. For low pressures (0.11 or 0.12 MPa) in the section G2, the jet does not switch to the opposite branch within the simulation time which was higher than half a period of the complete oscillation ($T/2 = 2.15$ ms; cf. section 4.1). Higher pressure differences between the branches lead to the jet deflection but with a dynamics strongly dependent on the pressure difference. The deflection time decreases when the pressure difference increases, to reach a minimal value of $0.01T$ for pressure differences between section G1 and G2 higher or equal to 0.18 MPa. The deflection time t_d is defined as the time needed for the jet totally entering the left branch from the beginning of the simulation.

Table 4-1. Time needed for jet switching as a function of the pressure difference between the two branch outlets

	P_{E1} (MPa)	P_{E2} (MPa)	P_{G1} (MPa)	P_{G2} (MPa)	t_d (ms)	t_d / T
Case 2-1	0.1	0.1	0.1	0.11	--	--
Case 2-2	0.1	0.1	0.1	0.12	--	--
Case 2-3	0.1	0.1	0.1	0.125	0.78	0.18 T
Case 2-4	0.1	0.1	0.1	0.135	0.58	0.13 T
Case 2-5	0.1	0.1	0.1	0.145	0.22	0.05 T
Case 2-6	0.1	0.1	0.1	0.16	0.22	0.05 T
Case 2-7	0.1	0.1	0.1	0.18	0.06	0.01 T
Case 2-8	0.1	0.1	0.1	0.2	0.06	0.01 T

4.2.3 Combined effects of both pressure differences

In this series of simulations, the combined effects of the two pressure differences are explored. Firstly, the pressures in the two control ports and the left outlet are fixed, and only the pressure in the right outlet is modified leading to an increasing value of $\Delta P_{G2\text{-}G1}$ and a fixed value of $\Delta P_{E2\text{-}E1} = 0.035$ MPa. Then, the pressure difference between the two outlets $\Delta P_{G2\text{-}G1}$ is kept constant as 0.01 MPa while the pressure difference between the control ports $\Delta P_{E2\text{-}E1}$ is gradually increased.

4.2.3.1 Increasing $\Delta P_{G2\text{-}G1}$ with fixed $\Delta P_{E2\text{-}E1}$

The right outlet pressure is modified gradually from 0.1 to 0.14 MPa. The inlet total pressure is still 0.25 MPa, the pressures at sections E1 and E2 are fixed to 0.09 and 0.125 MPa, respectively, while the left outlet pressure is 0.1 MPa as in the first series of simulations. The simulation result of case 1-1 is used as an initial condition for all tested configurations in this series of simulations. The time needed to complete the switching process in each case is presented in Table 4-2.

As observed in Figure 4-10 (case 1-1), an isolated $\Delta P_{E2\text{-}E1}$ = 0.035 MPa is not sufficient to provoke the jet switching. However, if in addition a pressure difference $\Delta P_{G2\text{-}G1}$ exists between the two branches, the jet switches to the other branch in a very short time, even when this difference is as low as 0.01 MPa (Case 3-1), which cannot trigger the switching process by itself as shown by case 2-1. When the right outlet pressure increases, the time needed to complete the switching decreases quickly to reach a minimum value for pressure differences between the branches higher than 0.14 MPa.

Table 4-2. Time needed to complete the switching process with increasing $\Delta P_{G2\text{-}G1}$ and fixed $\Delta P_{E2\text{-}E1}$

	P_{E1} (MPa)	P_{E2} (MPa)	P_{G1} (MPa)	P_{G2} (MPa)	t_d (ms)	t_d / T
Case 3-1	0.09	0.125	0.1	0.11	0.53	0.12 T
Case 3-2	0.09	0.125	0.1	0.12	0.16	0.04 T
Case 3-3	0.09	0.125	0.1	0.13	0.13	0.03 T
Case 3-4	0.09	0.125	0.1	0.14	0.10	0.02 T

4.2.3.2 Increasing $\Delta P_{E2\text{-}E1}$ with fixed $\Delta P_{G2\text{-}G1}$

The pressure in right control port P_{E2} is increased from 0.1 to 0.125 MPa, while the pressure in left control port P_{E1} is kept constant as 0.09 MPa. The inlet total pressure is still 0.25 MPa and the pressures at sections G1 and G2 are fixed to 0.1 and 0.11 MPa, respectively. The simulation result of case 2-1 is used as an initial condition for all tested configurations in this series of simulations. The time needed to complete the switching process in each case is presented in Table 4-3.

As presented in case 2-1, the jet switching cannot be provoked just by a pressure difference of 0.01 MPa between sections G1 and G2. Nevertheless, if in addition a pressure difference

$\Delta P_{\mathrm{E2\text{-}E1}}$ exists between the two control ports, even when this difference is as low as 0.035MPa which cannot trigger the switching process by itself as shown by case 1-1, the behavior of the jet is totally changed: it switches to the other branch in a very short time, except in the case where there is only a pressure difference of 0.01 MPa between the two control ports (case 4-1). The time needed to complete the switching decreases as the $\Delta P_{\mathrm{E2\text{-}E1}}$ value increases.

Compared to case 3-1, case 4-3 needs shorter time to complete the switching process, even though the same value of $\Delta P_{\mathrm{E2\text{-}E1}}$ and $\Delta P_{\mathrm{G2\text{-}G1}}$ are applied in both cases. In case 3-1, $\Delta P_{\mathrm{G2\text{-}G1}}$ is applied on the final configuration of Case1-1 for which $\Delta P_{\mathrm{E2\text{-}E1}}$ has played a role for a duration of $T/2$; on the contrary, in case 4-3, $\Delta P_{\mathrm{E2\text{-}E1}}$ is applied on the final configuration of case 2-1 for which $\Delta P_{\mathrm{G2\text{-}G1}}$ has played a role for a comparable duration. This implies that the switching process is also sensitive to the sequential order in which the pressure differences are applied between the two branches and between the two control ports.

Table 4-3. Time needed to complete the switching process with increasing $\Delta P_{\mathrm{E2\text{-}E1}}$ and fixed $\Delta P_{\mathrm{G2\text{-}G1}}$

	P_{E1} (MPa)	P_{E2} (MPa)	P_{G1} (MPa)	P_{G2} (MPa)	t_d (ms)	t_d / T
Case 4-1	0.09	0.1	0.1	0.11	> 3 ms	
Case 4-2	0.09	0.11	0.1	0.11	0.45 ms	0.105 T
Case 4-3	0.09	0.125	0.1	0.11	0.35 ms	0.081 T

All preceding simulation results thus confirm the hypothesis that the oscillation dynamics is not only controlled by the pressure difference between the two control ports $\Delta P_{\mathrm{P2\text{-}P1}}$, but also by the pressure difference between the two branches $\Delta P_{\mathrm{A2\text{-}A1}}$ or $\Delta P_{\mathrm{B2\text{-}B1}}$.

4.3 Numerical study of the influence of inlet pressure on the oscillation dynamics

4.3.1 First analysis on a simplified geometry

With the same simplified geometry as in section 4.2, the isolated effect of the inlet pressure on the oscillator dynamics has been studied. The two pressure differences (between the branches and between the control ports) are applied separately with a fixed value. The pressure difference between the branches $\Delta P_{\mathrm{G2\text{-}G1}}$ is set to 20 kPa, with $P_{\mathrm{G1}} = 0.1$ MPa, while $P_{\mathrm{G2}} = 0.12$ MPa. The pressure difference between the control ports $\Delta P_{\mathrm{E2\text{-}E1}}$ is set to 35 kPa, with $P_{\mathrm{E1}} = 0.09$ MPa, while $P_{\mathrm{E1}} = 0.125$ MPa. The initial status is obtained after a simulation duration of 5 ms with uniform boundary conditions $P_{\mathrm{G1}} = P_{\mathrm{G2}} = P_{\mathrm{E1}} = P_{\mathrm{E2}} = 0.1$ MPa in each case in order to get a fully converged initial flow field. The time needed to complete the switching process from the initial status in each case is shown in Table 4-4. The time averaged velocity U_t and Mach number Ma_t at the middle point of the throat section are also shown.

The velocity of the nozzle jet and the Mach number logically increase with the inlet pressure. Values of the Mach number higher than 1 at the throat can be explained by the fact that the sonic line shape is very complex due to the jet bending downstream from the nozzle exit. As the flow has more inertia with higher velocity, it becomes more difficult to be deflected to the other side. When a pressure difference $\Delta P_{\mathrm{G2\text{-}G1}}$ = 20 kPa is applied between the branches, no switching is indeed observed within the 3 ms simulation duration if the inlet pressure is higher than 0.2 MPa, while the switching time decreases to 0.2 ms when the inlet pressure is decreased from 0.2 MPa to 0.13 MPa. When the pressure difference is applied between the control port ($\Delta P_{\mathrm{E2\text{-}E1}}$ = 35 kPa), a similar behavior can be observed.

Table 4-4. Time needed to complete the switching process for various values of supply pressure P_{i}, and various values of $\Delta P_{\mathrm{E2\text{-}E1}}$ and $\Delta P_{\mathrm{G2\text{-}G1}}$

	P_{i} / MPa	U_t (m/s)	Ma_t	$\Delta P_{\mathrm{E2\text{-}E1}}$=35 kPa P_{G1}=P_{G2}=0.1 MPa	$\Delta P_{\mathrm{G2\text{-}G1}}$=20 kPa P_{E1}=P_{E2}=0.1 MPa
Case 5-1	0.30	342.5	1.1	> 3 ms	> 3 ms
Case 5-2	0.25	334.5	1.068	> 3ms	> 3 ms
Case 5-3	0.20	312	0.98	0.6 ms	> 3 ms
Case 5-5	0.15	250	0.763	0.52 ms	0.3 ms
Case 5-6	0.13	205	0.613	0.05 ms	0.2 ms

4.3.2 Detailed numerical analysis of the inlet pressure effects

Numerical simulations performed on the designed geometry of Osc.2(cf. the right part of Figure 2-1), for inlet pressure ranging from 0.11 MPa to 0.30 MPa show that the oscillation frequency is nearly constant at about 510 Hz. To explain this result, the pressure differences between the two sides of the oscillator in sections A (branch inlets), B (branch centers) and P (control ports) are analyzed for different values of inlet pressure.

In the case of 0.25 MPa inlet pressure, the variations of area-averaged velocity in y direction U_{y} in sections A1 and A2, as well as the above mentioned pressure differences are shown in Figure 4-11.

As it has been discussed at the end of section 4.1.2, the oscillation period can be roughly predicted by a simple function Eq.(4-2).

$$T = \frac{4L_f}{C_o} \tag{4-2}$$

Under this assumption and for analysis the relation between the oscillation dynamics and the FBL, the period of a working oscillator can be divided into four basic time units which are equal to:

$$\Delta t = L_f \,/\, C_o \tag{4-3}$$

At time t_0 which can be viewed as the beginning of a period, the main jet is switching from the left side to the right side since the area-average velocity U_y in section A1 is decreasing while that in section A2 is increasing dramatically. Just before this time, the value of $\Delta P_{\text{A1-A2}}$ becomes positive and reaches its highest value. Immediately after time t_0, both the values of $\Delta P_{\text{A1-A2}}$ and $\Delta P_{\text{B1-B2}}$ drop down severely because of the sudden switch of the main jet. As this jet has been switched and attached to the right side branch, the values of $\Delta P_{\text{A1-A2}}$ and $\Delta P_{\text{B1-B2}}$ becomes positive and steady again, since the flow velocity in the right branch becomes much higher than that of left branch.

At time t_1, i.e., one basic time unit Δt after t_0, as the high pressure compression wave (HPCW) arrives in section P2 and the low pressure expansion wave (LPEW) arrives in section P1 almost simultaneously, the pressure difference $\Delta P_{\text{P1-P2}}$ evolves suddenly from its highest positive value to a negative value inducing a destabilization of the main jet which explains the chaotic fluctuations observed on the area-averaged velocity U_y in sections A1 and A2, and on the pressure difference $\Delta P_{\text{A1-A2}}$. The HPCW and LPEW are then reflected back and continue propagating along the feedback loops. When they arrive in sections B2 and B1, respectively, the value of $\Delta P_{\text{B1-B2}}$ decreases quickly. Then the waves reach sections A2 and A1 leading to a similar decrease of $\Delta P_{\text{A1-A2}}$ and provoke the main jet switching from the right side to the left side at time t_2 which is just the half point of a period. Then, the other half period takes place similarly until time t_3.

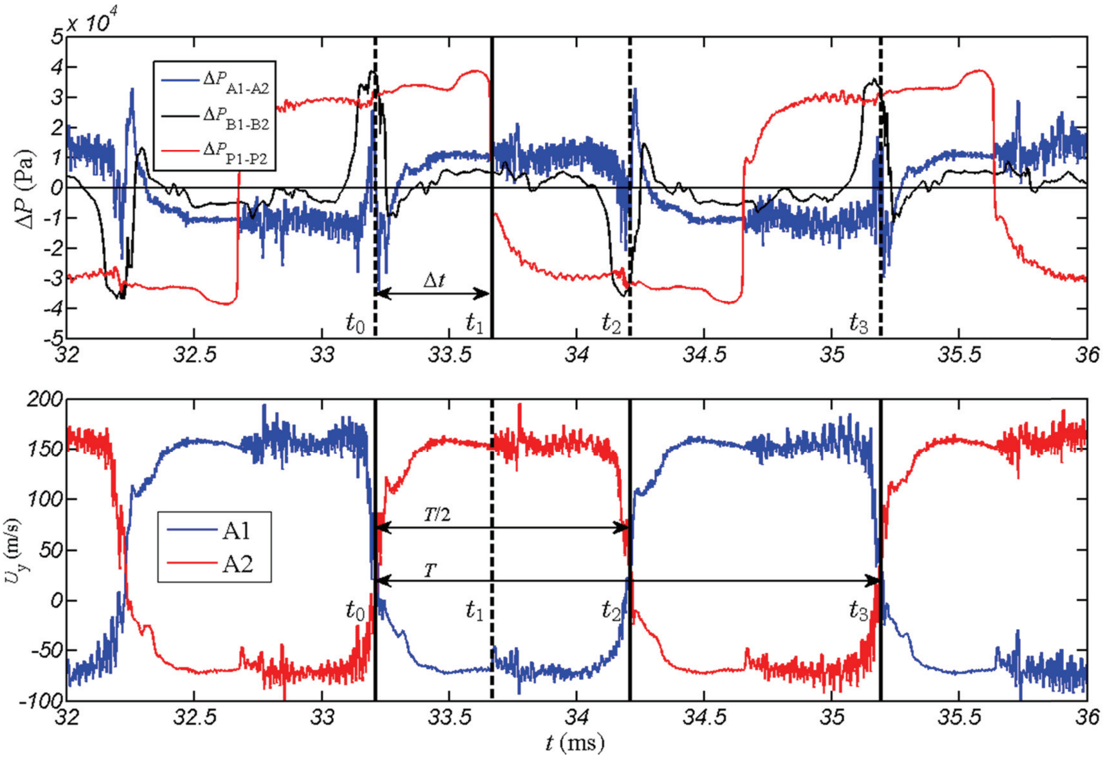

Figure 4-11. Area-average velocity U_y in sections A, and pressure differences between the two sides of the oscillator in sections A, B, P; P_i=0.25 MPa

The jet switching process can thus be linked to the evolution of the pressure difference between the two branches, which can be represented by $\Delta P_{B1\text{-}B2}$ and the evolution of the pressure difference between the control ports $\Delta P_{P1\text{-}P2}$.

From t_0 to t_1, i.e., the first quarter period, the pressures both in the left branch and left control port are higher than those in the right side, ($\Delta P_{P1\text{-}P2}$ ~ 35 kPa and $\Delta P_{B1\text{-}B2}$ ~ 5kPa). The main jet is perfectly attached to the right branch.

From t_1 to t_2, i.e., the second quarter period, the pressure in the left branch is still higher than that in the right branch ($\Delta P_{B1\text{-}B2}$ ~ 5kPa), while the pressure in the left control port becomes lower than that in the right control port ($\Delta P_{P1\text{-}P2}$ ~ -30 kPa). The main jet becomes unstable, but is still ejected through the right outlet.

Once the pressure in the right branch becomes also much lower than that in the left branch ($\Delta P_{B1\text{-}B2}$ ~ -35 kPa) at time t_2, the main jet switches suddenly from the right side to left one. A similar process then occurs during the second half period from t_2 to t_3.

The maximum value of $\Delta P_{P1\text{-}P2}$ which is reached just before t_1 (the end of the first quarter period), and the maximum $\Delta P_{B1\text{-}B2}$ value which is reached just before t_0 (the beginning or the ending of a period), are of the same order, i.e., 35 kPa for an inlet pressure of 0.25 MPa.

The maximum values of $\Delta P_{P1\text{-}P2}$ and $\Delta P_{B1\text{-}B2}$ are plotted in Figure 4-12 as function of the inlet pressure, in the range 0.11 MPa to 0.3 MPa. Both of these maximal pressure differences increase approximately linearly with the inlet pressure and their values stay close to each other. In addition, their evolutions with time are similar whatever the inlet pressure which leads to an almost constant frequency response. This can be explained by the fact that with higher inlet pressure, the mass flowrate and momentum of the main jet become higher. As a consequence, higher pressure differences between the control ports and between the branches are needed to provoke the jet switching.

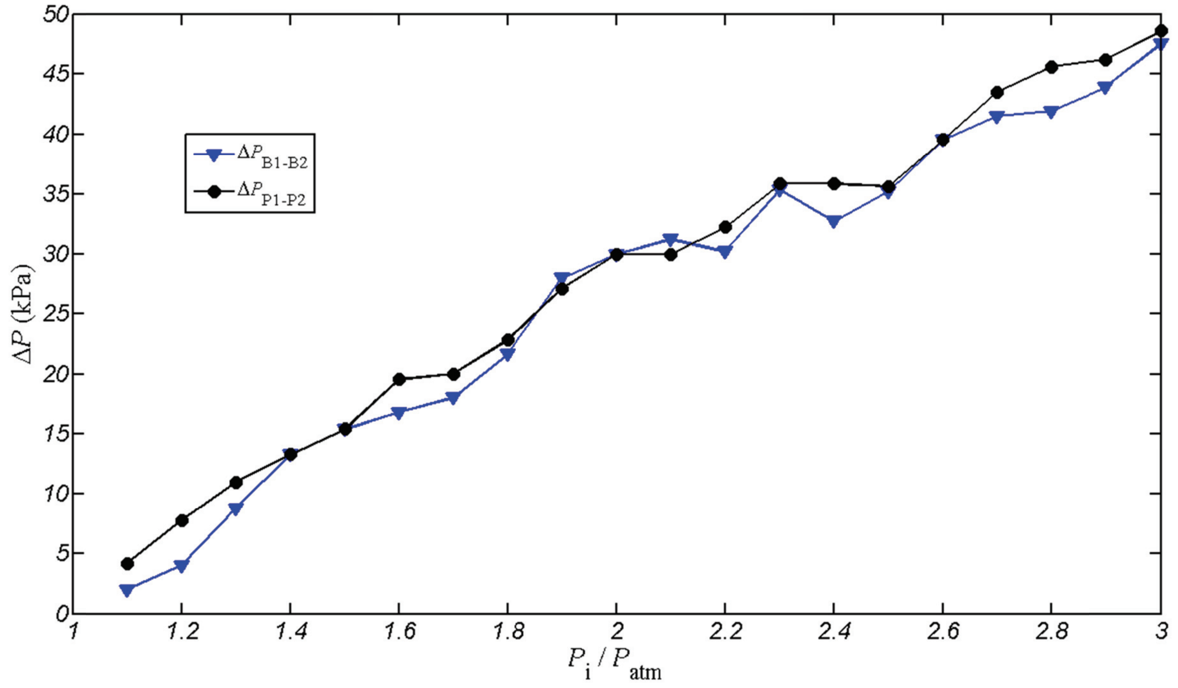

Figure 4-12. Maximal $\Delta P_{P1\text{-}P2}$ and maximal $\Delta P_{B1\text{-}B2}$ as functions of the inlet total pressure, for the designed geometry of Osc.2

4.4 Conclusions

It has been clarified that in a bi-stable pulsing jet relaxation fluidic oscillator, the main jet deflection is provoked not only by the pressure difference between the control ports $\Delta P_{P1\text{-}P2}$ like in the case of a sonic fluidic oscillator, but also by the pressure difference between the branches $\Delta P_{B1\text{-}B2}$. In general, the threshold value of $\Delta P_{P1\text{-}P2}$ needed to provoke by itself the jet deflection is much higher than that of $\Delta P_{B1\text{-}B2}$. However, when these effects are combined, the jet deflection happens for much lower values of these pressure difference. It has also been demonstrated that these pressure differences were due to the back and forth propagation of a high pressure compression wave and a low pressure expansion wave in the two branches and feedback loops, which leads to a new function to estimate the oscillation period

$$T = \frac{1}{f} = 2\tau_t = \frac{4L_f}{C_o} \tag{4-2}$$

in which a coefficient of 4 appears, contrary to the coefficient 2 in the relation proposed by Simoes et al.[59]. This new function deduced from numerical analysis, has also been obtained from the experimental results presented in section 2.3.1 (cf. Eq.(2-4) and Eq.(2-5)).

is exactly the same as the empirical formula Eq.(2-5) obtained from measured results.

Finally, we have shown that the maximal pressure differences between the branches and between control ports increase approximately linearly with the inlet pressure, and that the evolution of these pressure difference with time were similar whatever the inlet pressure, which leads to an almost constant frequency response. On the other hand, when the inlet pressure increases, the mass flowrate and momentum of the main jet become larger and, as a consequence, higher pressure differences between the control ports and between the branches are needed to provoke the jet switching. The balance between these two effects explains the non-dependence of the oscillation frequency to the supply pressure.

Chapter 5. Synchronization Study of Fluidic Oscillators

In order to use fluidic oscillators for controlling a separated flow, for instance on a ramp, an array of these fluidic actuators will be needed. However, even if all the devices have the same designed dimensions there exists minor differences because of the machining and assemblage dispersions, which lead to discrepancies on the working frequency and the time evolution profile of the jet velocity. In addition, it would be interesting to control the phase difference between the pulsed jets generated in the array in order to test the efficiency of various configurations (random phase lag, no phase lag, fixed phase lag,..). Therefore, efforts must be done to find some ways to synchronize similar but non-identical fluidic oscillators.

In the patents of Ciro et al.[83] and Koklu[84], methods to synchronize an array of both pulsed jets and sweeping jets wall-attached fluidic oscillators have been proposed using the concept of shared feedback accumulator which is complex to be controlled or to be modified. In this study, new and simpler methods to synchronize a fluidic oscillators array are proposed and studied both experimentally and numerically in order to clearly identify the underlying mechanisms governing the dynamics of synchronized oscillators.

5.1 Synchronization of two oscillators

First experimental tests have been performed on two oscillators, which is the simplest configuration. Different inter-connection patterns have been proposed and tested for validation.

5.1.1 Inter-connection patterns for the synchronization of two oscillators

The objective of this work was to verify if the synchronization of two oscillators was possible, simply thanks to inter-connections between their connectors, or, in other words, by sharing their feedback loops. The two oscillators are Osc.3 and Osc.5 which are identical in design as described in section 2.1 (cf. Figure 2-3).

Four inter-connection patterns have been proposed and are presented in Figure 5-1. In all these configurations, the lengths and diameters of the connecting tubes are the same.

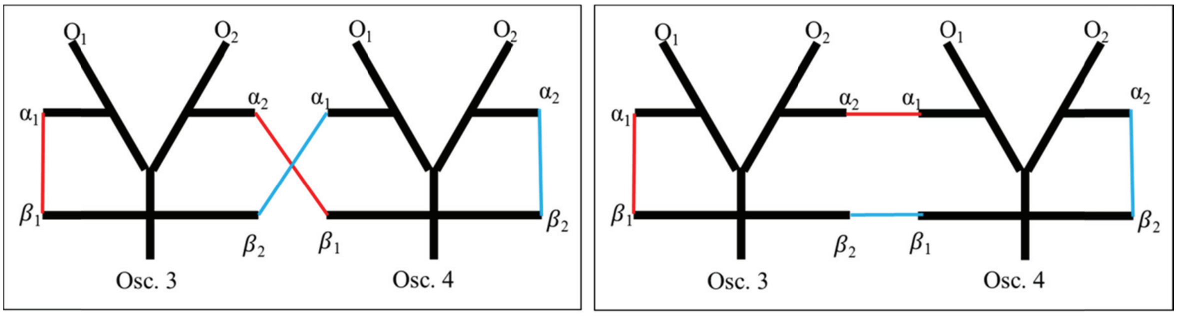

a) Method 1

b) Method 2

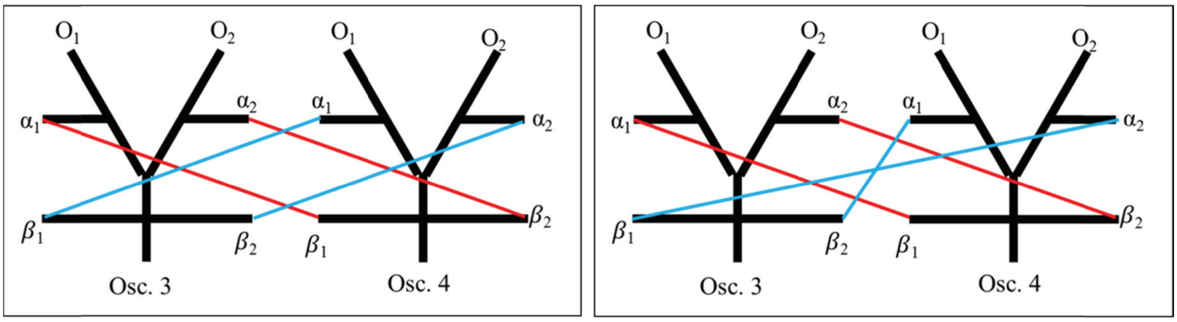

c) Method 3

d) Method 4

Figure 5-1. Inter-connection patterns proposed for the synchronization of two oscillators

5.1.2 Description of the test bench

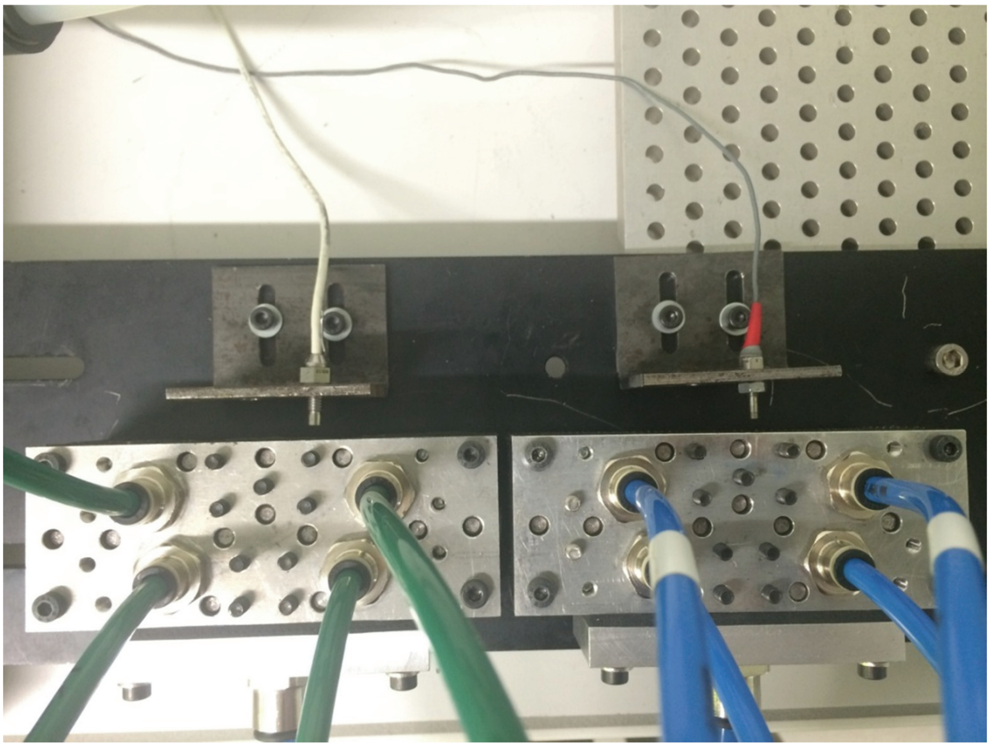

Figure 5-2. Test bench for the validation of the synchronization methods

The experimental test bench used for the validation of the synchronization methods presented above is shown in Figure 5-2. Two pressure sensors (Endevco 8510B-2 in the left sidewith 0-2 psig pressure range and 70 kHz resonance frequency; Endevco 8506-2 in the right side with 0-2 psig pressure range and 45 kHz resonance frequency) are placed in front of the right outlets of the two oscillators which are supplied at the same pressure. The tubes used to synchronize these oscillators have a length of 500 mm and a diameter of 4 mm. The acquisition frequency is 25 kHz for both pressure transducers.

5.1.3 Test results

Firstly, the frequency responses of each oscillator working separately have been measured for inlet pressures ranging from 0.12 MPa to 0.27 MPa and are presented in Figure 5-3. Limited but non negligible deviations can be clearly observed between the frequency responses of the two devices. These differences, between 2% and 8 %, are probably due to machining and assemblage dispersions as evoked at the beginning of this chapter.

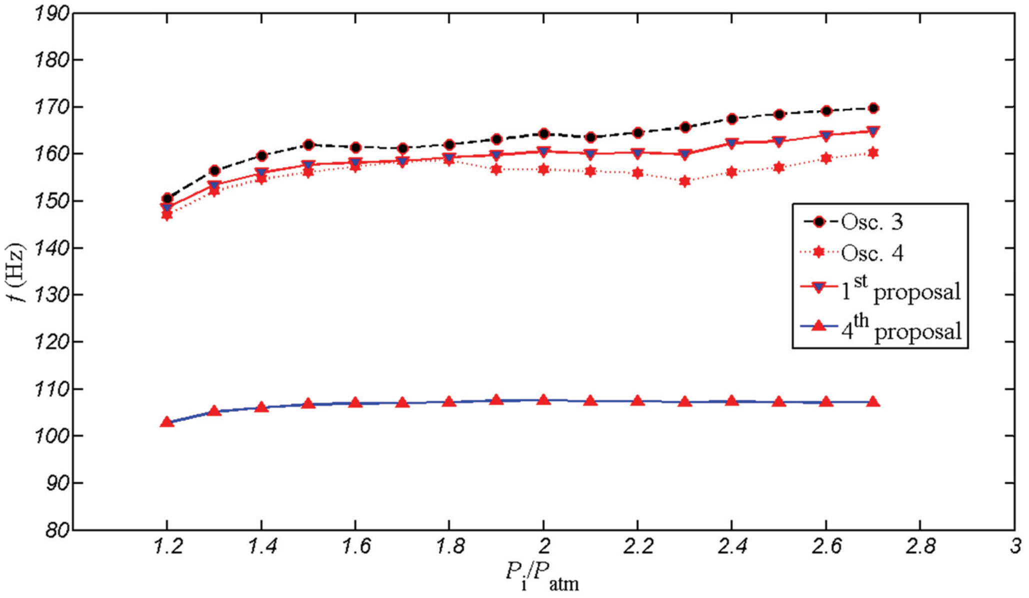

Figure 5-3. Separated frequency response of Osc.3 and Osc.4 and synchronized frequency

Tests have been then conducted, connecting the oscillators according the four patterns presented in Figure 5-1.

No oscillations have been observed with the synchronization methods 2 and 3. However, positive results have been obtained with the 1^{st} and 4^{th} inter-connection methods described above. These results are also presented in Figure 5-3.

With the first synchronization method, both oscillators work at the same frequency which is in-between the two frequencies of the oscillators working separately. This implies that their working dynamics are almost the same in both separated and synchronized cases. The auto-correlation and cross-correlation of the pressure signals from Osc.3 and Osc.4 shown in

Figure 5-4 permit to calculate the phase lag between the two pulsed jets which is $\Delta T = 0.46T$, i.e., approximately half a period.

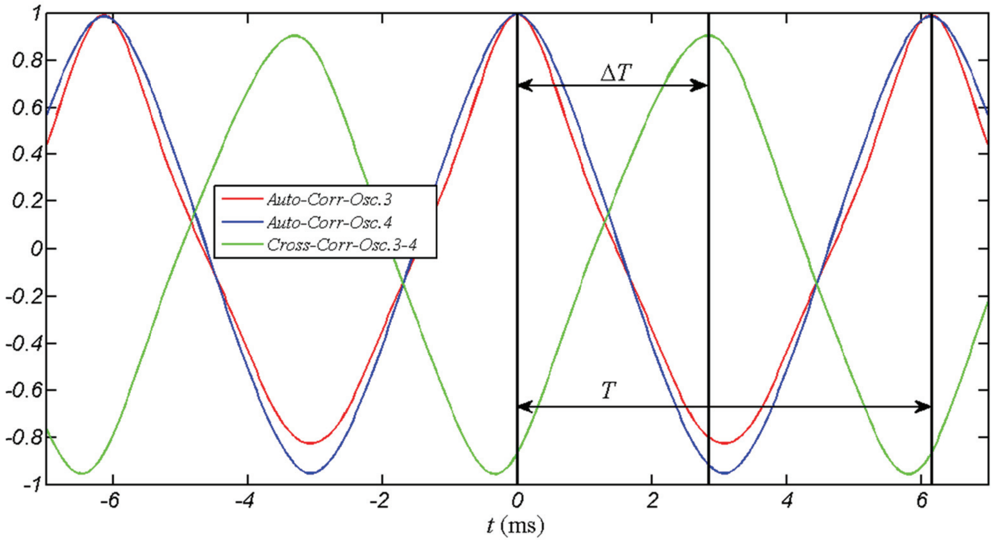

Figure 5-4. Auto-correlation and cross-correlation sequences of the pressure signals from Osc.3 and Osc.4 – 1st synchronization method

With the 4th synchronization method, the common working frequency is about 105 Hz which is much smaller than the frequencies around 150 Hz of the oscillators working separately. This large frequency change implies that the oscillators' dynamics in this synchronized case is very different from that in the separated case.

A sample of their auto-correlation and cross-correlation signal is also shown in Figure 5-5. The phase lag in this case is $\Delta T = 0.253T$, i.e., approximately a quarter period.

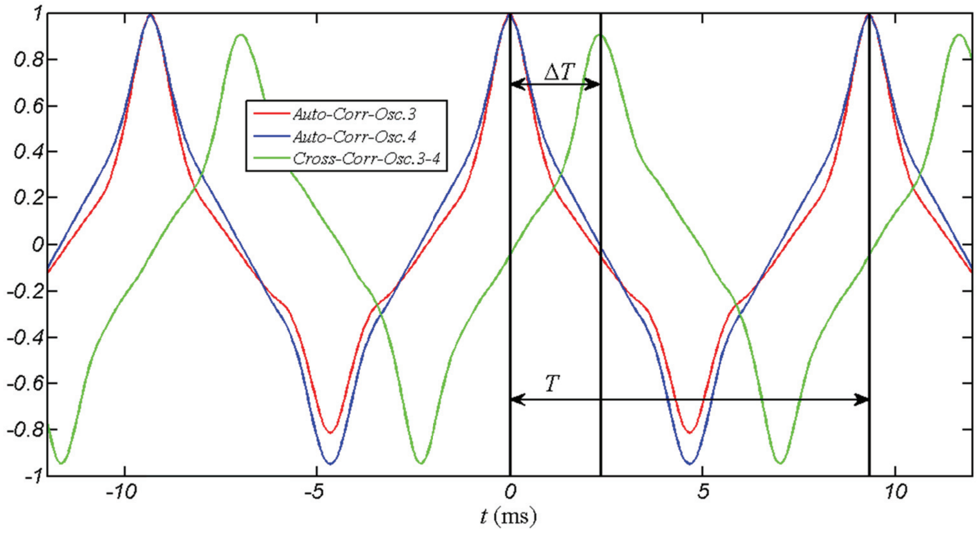

Figure 5-5. Auto-correlation and cross-correlation sequences of the pressure signals from Osc.3 and Osc.4 – 4th synchronization method

5.2 Numerical analysis of the flow dynamics in synchronized configurations

In order to better understand the oscillation dynamics when the oscillators are synchronized, the internal flow patterns have been analyzed with the help of CFD. The numerical method and settings described in chapter 3 are used. However, in order to reduce the simulation time, the FBL has been made much shorter than in the real experimental configuration. This FBL is equal to $L_f = l_{AP} = 75.62$ mm, which gives, according to Eq.(4-2), an oscillation frequency of about 1124 Hz.

These modified models of Osc.3 and Osc.4, renamed Osc.3s and Osc.4s respectively, are presented in Figure 5-6. In order to reproduce numerically, the small differences in the working frequencies observed on the prototypes, the outlets width of Osc.3s has been set to 0.375 mm while that of Osc.4s was kept to 0.5 mm as in the original design.

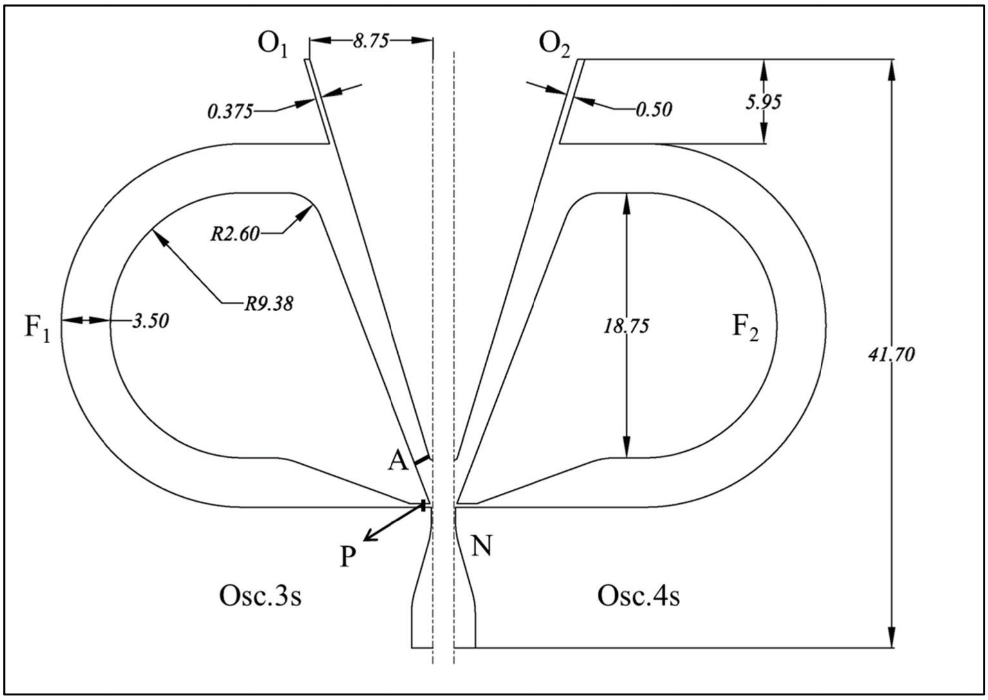

Figure 5-6. Sketch and overall dimensions of the simulated oscillators.

5.2.1 Simulation of two separated oscillators

The predicted evolution with time of the velocity U_y in the center of left outlets of both oscillators are compared in Figure 5-7, highlighting that these two oscillators have, as expected, different frequencies (1127 Hz for Osc.3s, 1104 Hz for Osc.4s) but close to the value roughly estimated by Eq.(4-2).

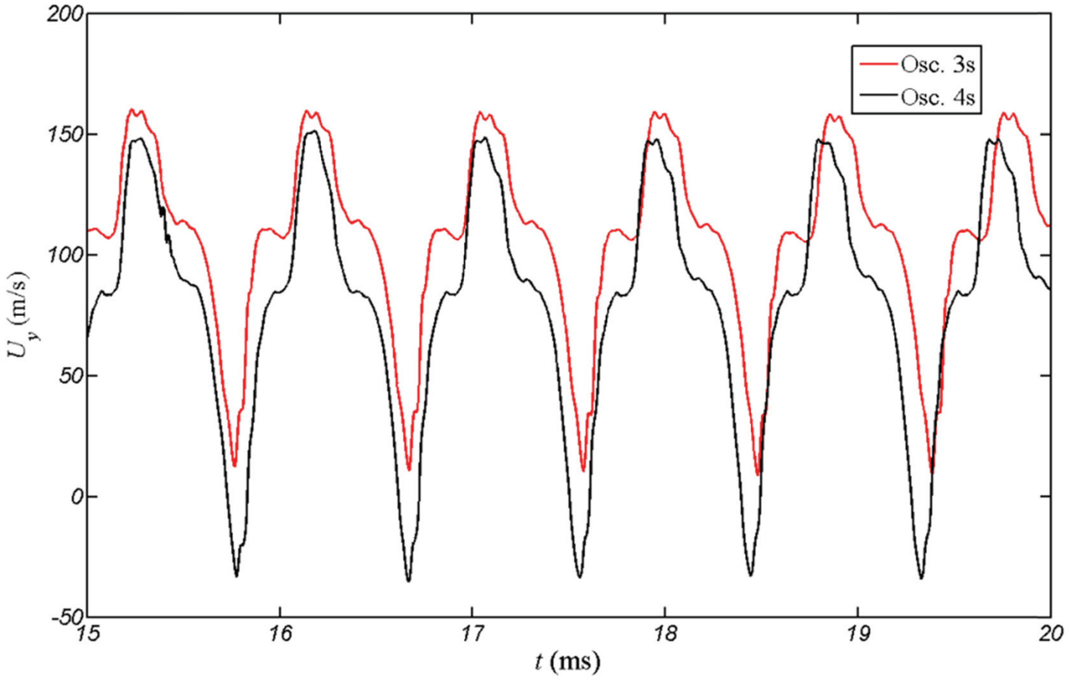

Figure 5-7. Evolution with time of the velocity U_y at the left outlets of Osc.3s and Osc.4s

5.2.2 Simulation of two oscillators synchronized with 1st inter-connection pattern

Figure 5-8 presents a sketch of the simulated configuration. In order to facilitate the analysis of the oscillator behavior, three representative sections, noted (A, D, P), have been selected: they represent the branch inlet, the loop center, and the control port, respectively. The digit 1 is relative to the sections along the tube connected to the left control port and left branch of Osc.3s; digit 2 is relative to the sections along the tube connecting the right control port of Osc.3s to the left branch of Osc.4s; digit 3 is relative to the sections along the tube connecting the left control port of Osc.4s to the right branch of Osc.3s, and digit 4 is relative to the sections along the tube connected to the right control port and right branch of Osc.4s. In this 2-D simulation, the translational periodic boundary condition is implemented to virtually connect the D2 sections and D3 sections defined on each oscillator.

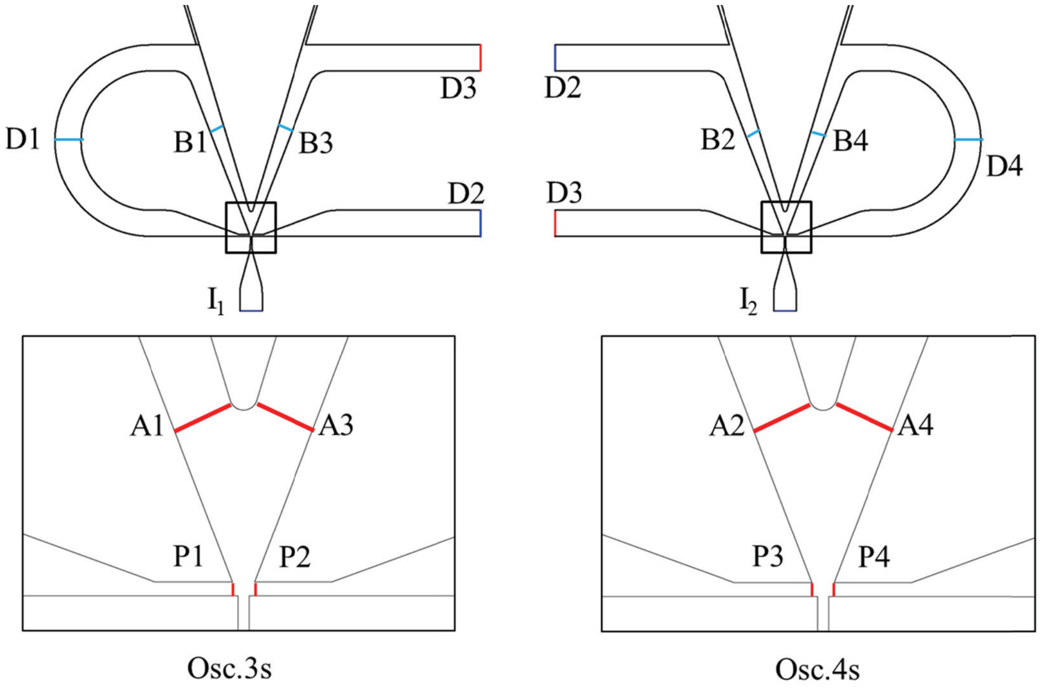

Figure 5-8. Sketch of the configuration used in the numerical simulation of the 1st synchronization method

From Figure 5-9 where the velocities U_y in the center of left outlet slots of the two oscillators are compared, it can be seen that they are successfully synchronized with an identical frequency of 1107 Hz which is also very close to the value estimated by Eq.(2-4). The phase lag is equal to

$$\Delta T = 0.3503/0.9113T = 0.384\,T \tag{5-1}$$

which is a little smaller than the phase difference of $0.46T$ found during the experiments.

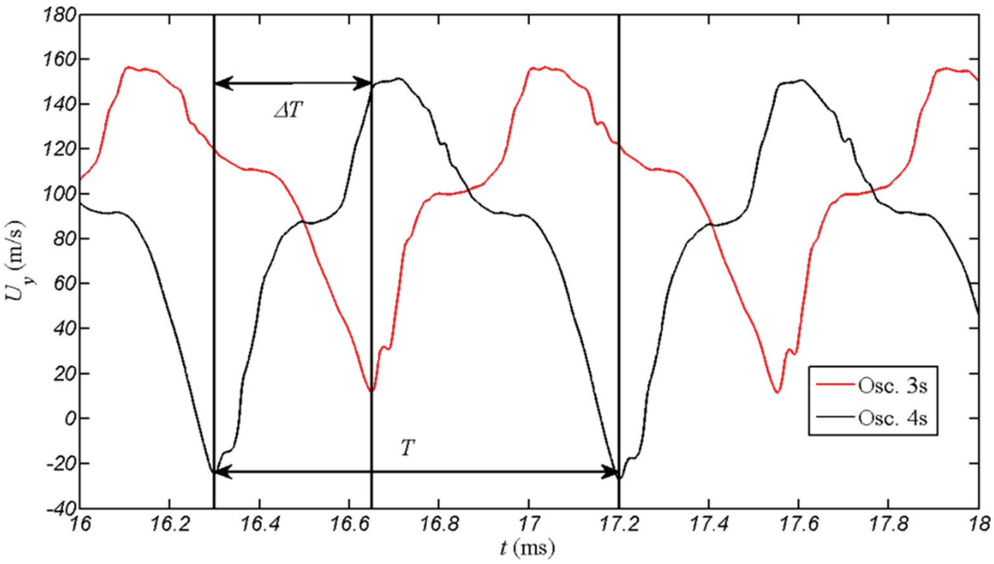

Figure 5-9. Comparison of the velocity U_y in the center of left outlets of Osc.3s and Osc.4s; 1st synchronization method

Several critical times are chosen for better analyzing the flow patterns inside the oscillators and explaining the synchronization dynamics. These times are defined according to the evolutions of velocity U_y in the branch inlet sections of each oscillator which are shown in Figure 5-10.

t_0 is defined when the main jet in Osc.3s is switching from the left branch to the right one, i.e. when the positive velocity U_y in the left branch inlet section A1 crosses the negative velocity U_y in the right branch inlet section A3. This time is assumed to be the beginning point of an oscillation period in our analysis. In the same time, the main jet in Osc.4s is attached to the right branch, which is indicated by the positive value of U_y in section A4 while U_y is negative in section A2.

t_1 is chosen when the main jet in Osc.4s is switching from the right branch to the left one. while the main jet in Osc.3s is attached to the right branch.

t_2 and t_3 are defined as one basic time unit Δt later than t_0 and t_1, respectively. In these simulations, the basic time unit, already defined in section 4.3.2 (cf. Eq.(4-3)), is $\Delta t = L_f / C_o = 0.2245$ ms.

t_4 is defined as the mid-point of a period which means $t_4 = t_0 + 0.5T \approx t_0 + 2\Delta t \approx t_1 + \Delta T$. In the second half period, it can be clearly observed that the pressure and velocity variation profiles are similar to those in the first half period, thus, detailed analysis is focused on this first half period.

Figure 5-11 presents the evolution of the pressure differences between the branch inlet sections A1 and A3, $\Delta P_{\mathrm{A1\text{-}A3}}$, and between the control port sections P1 and P2, $\Delta P_{\mathrm{P1\text{-}P2}}$, in Osc.3s together with their counterparts in Osc.4s, $\Delta P_{\mathrm{A2\text{-}A4}}$ and $\Delta P_{\mathrm{P3\text{-}P4}}$.

For each of the critical times defined above, a simplified sketch showing the main jets direction and the propagation of pressure waves along the feedback loops in each oscillator is also presented in Figure 5-12. The pressure levels in section A, D and P in each side of each oscillator are schematically represented by a level in a cylinder: an empty cylinder means that the pressure at this time has the lowest value calculated on the whole period, while a fully filled cylinder means that the pressure has reached its highest value. These pressure level representations are relative: the maximum pressure level in section A is not necessarily higher than the minimum one in section D.

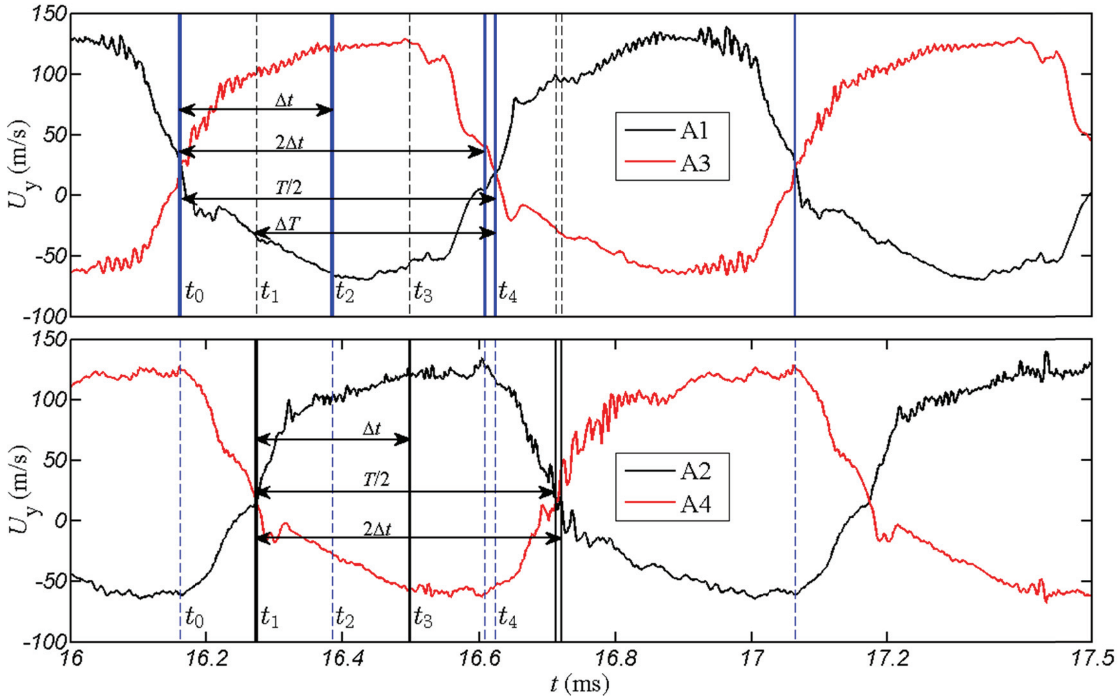

Figure 5-10. Evolution with time of the velocity U_{y} in the branch inlet sections A of Osc.3s and Osc.4s

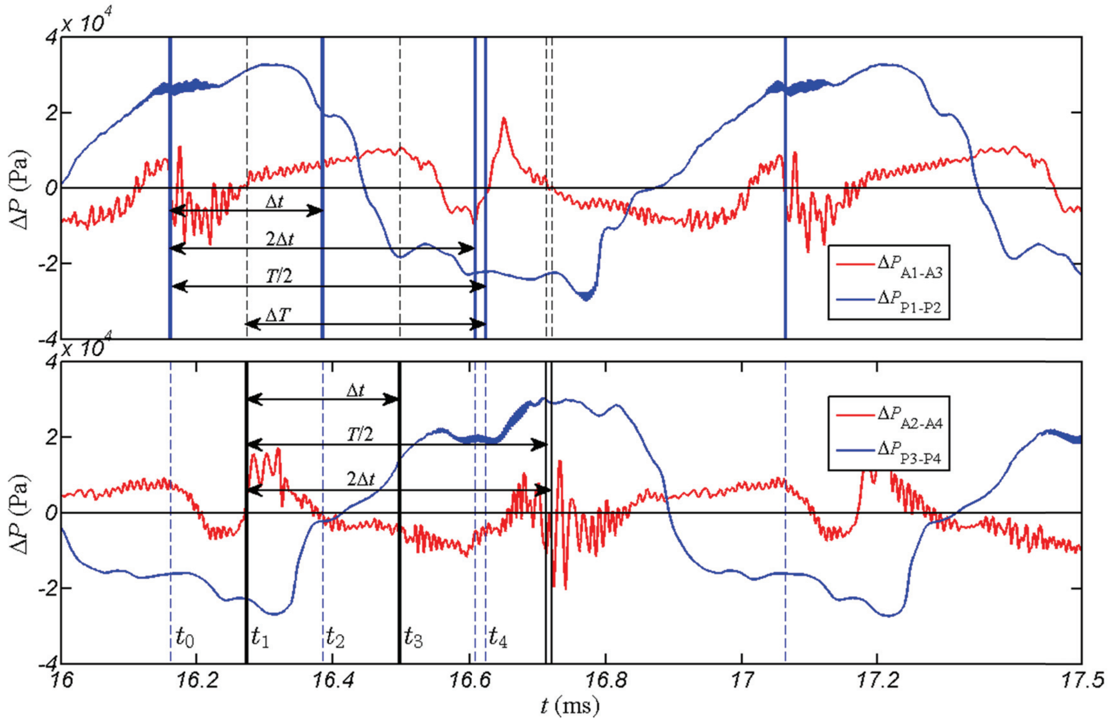

Figure 5-11. Evolution with time of the pressure differences between the control port P and branch inlet A sections of Osc.3s and Osc.4s

Time t_0: from Figure 5-11, it can be observed that at t_0, the pressure in section P1 is 27 kPa higher than that in section P2, while the pressure in section A1 is also a little higher than that in section A3. The combination of these two pressure differences provoke the switching of the main jet in Osc.3s from the left branch to the right one. Concerning the jet in Osc.4s, though the pressure in section P4 is 20 kPa higher than that in section P3, the main jet is still attached to the right branch since the pressure in section A4 is still about 6.8 kPa lower than that in section A2. This is consistent with the fact, demonstrated in section 4.4, that the jet switching mechanism in a single oscillator is provoked the combination of the pressure differences between the control ports and between the branches.

Time t_1: From t_0 to t_1, about $0.125T$ later, a high pressure compression wave (HPCW) propagates along the tube 3, from A3 to D3, and a low pressure expansion wave (LPEW) also moves from A1 to D1 due to the entrainment effect of the main jet. At the same time, in Osc.4s, a HPCW propagates from D4 to A4 and provokes the switching of the main jet from the right side to the left one.

Time t_2: After a duration of Δt from t_0, the HPCW in tube 3 arrives in section P3, which is the left control port of Osc.4s, leading to a pressure augmentation from its lower level to the higher one. Similarly, the LPEW in tube 1 arrives in section P1 leading to a pressure decrease from its higher level to the lower one. In the case of a single oscillator, the pressure in one of the control ports would decrease simultaneously when the pressure increase in the other control port, leading to the inversion of the pressure difference provoking a destabilization of the main jet. However, in this synchronized case, the pressure in P2, is maintained at its lower level since the HPCW in tube 2 needs another $0.125T$ to reach P2. Similarly, the pressure in P4, is maintained at its higher level since the LPEW in tube 4 needs another $0.125T$ to reach P4. Thus, $\Delta P_{\text{P1-P2}}$ is still positive and $\Delta P_{\text{P3-P4}}$ still negative at time t_2, although their absolute values have decreased a lot (cf. Figure 5-11). As a consequence, the main jets in both oscillators stay very stable, as it can be seen on the U_y evolution curves in Figure 5-10.

Time t_3: At $t_1 + \Delta t$, the pressure differences $\Delta P_{\text{P1-P2}}$ and $\Delta P_{\text{P3-P4}}$ are reversed since the HPCW and the LPEW arrive in sections P2 and P4, respectively. As the pressure differences in sections A have not yet reached their maximum levels, the main jets in Osc.3s and Osc.4s do not switch but become unstable. The velocities U_y in sections A3 and A2 begin to decline.

Time t_4: After almost $T/2$ or $2\Delta t$ from t_0 and $0.125T$ after t_3, the HPCW reflected from the section P3 in tube 3, reaches the section A3 and thus provoke the switching of main jet in Osc.3s from the right side to the left one. The first half period is finished.

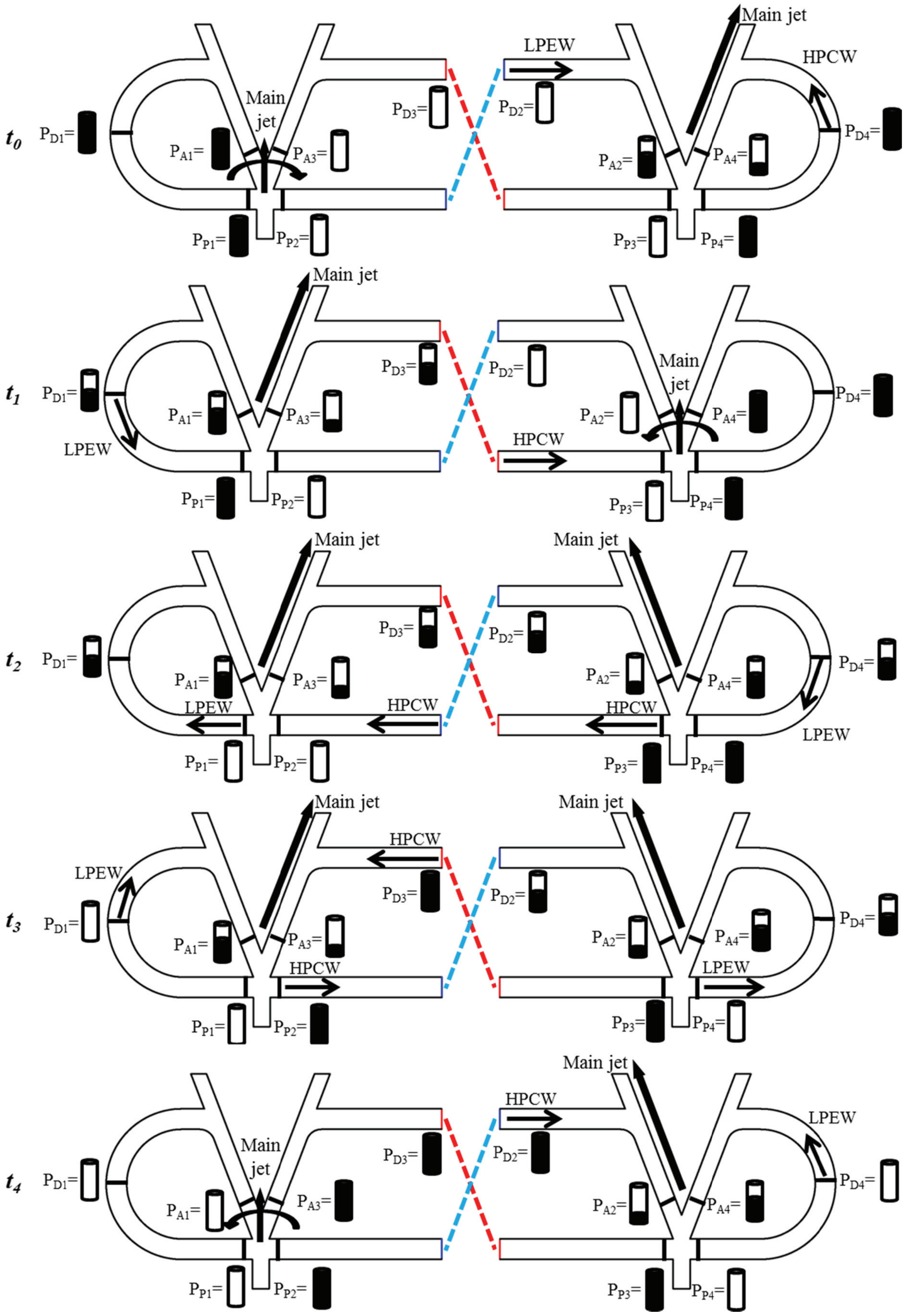

Figure 5-12. Sketch showing the main jets directions and propagation of pressure waves along the feedback loops at each defined critical time; left side Osc.3s, right side Osc.4s

5.2.3 Simulation of two synchronized oscillators with 4th inter-connection pattern

Figure 5-13 presents a sketch of the simulated configuration. Three sections, noted (A, D, P) are selected in the same way than in the previous configuration. Here, digit 1 is relative to the sections along the tube connecting the left control port of Osc.3s to the right branch of Osc.4s; digit 2 is relative to the sections along the tube connecting the right control port of Osc.3s to the left branch of Osc.4s; digit 3 is relative to the sections along the tube connecting the left control port of Osc.4s to the left branch of Osc.3s, and digit 4 is relative to the sections along the tube connecting the right control port of Osc.4s to the right branch of Osc.3s. In this 2-D simulation, translational periodic boundary conditions are implemented to virtually connect the sections D1, D2, D3 and D4 defined on each oscillator.

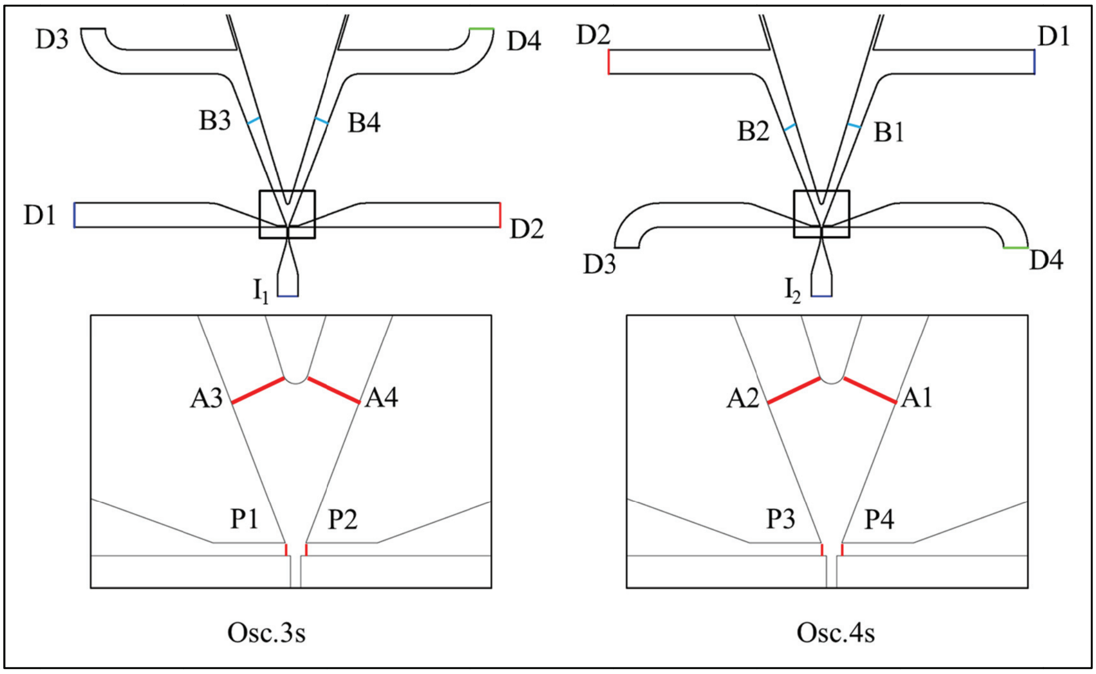

Figure 5-13. Sketch of the configuration used in the numerical simulation of the 4th synchronization method

From Figure 5-14 where the velocities U_y in the center of the left outlet slots of the two oscillators are compared, it can be seen that they are synchronized successfully with an identical frequency of 889 Hz which is much lower than the value estimated by Eq.(4-2). This frequency decrease is very similar to that observed experimentally. In addition, the phase difference is equal to

$$\Delta T = \left(\frac{\Delta T}{T}\right) T = 0.24\,T \approx \frac{1}{4} T \qquad (5\text{-}2)$$

which is almost the same as the phase difference of 0.253 T found during the experiments.

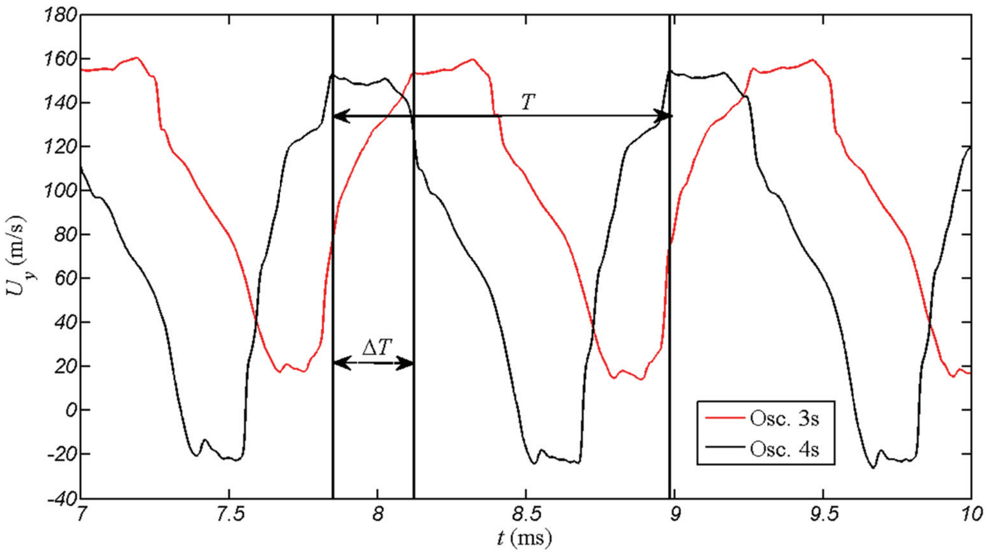

Figure 5-14. Comparison of the velocity U_y in the center of left outlets of Osc.3s and Osc.4s; 4th synchronization method

With the same analysis procedure as in the last configuration, several critical times are chosen according to the evolution of the area-averaged U_y in each A section shown in Figure 5-15. The time t_0 is chosen as the beginning point of a period when the main jet of Osc.3s is switching from the left branch to the right one, i.e. when the positive velocity U_y in the left branch inlet section A3 crosses the negative velocity U_y in the right branch inlet section A4.

t_1 is defined as one basic time unit Δt later than t_0, $t_1 = t_0 + \Delta t$.

t_2 is chosen when the main jet of Osc.4s is switching from the right branch to the left one, i.e. when the positive velocity U_y in the right branch inlet section A1 crosses the negative velocity U_y in the left branch inlet section A2. As the jet in Osc.4s switches at t_2 in the opposite direction (right to left) than the jet in Osc.3s at t_0 (left to right), thus, $t_2 = t_0 + (T/2 - \Delta T)$.

t_3 is defined as two basic time units $2\Delta t$ later than t_0, $t_3 = t_0 + 2\Delta t$.

t_4 is defined as one basic time unit Δt later than t_2, $t_4 = t_2 + \Delta t$.

t_5 is chosen when the main jet of Osc.3s is switching from the right branch to the left one, marking the end of the first half period.

Figure 5-16 presents the evolution of pressure differences between the branch inlet sections A3 and A4, $\Delta P_{\text{A3-A4}}$, and between the control port sections P1 and P2, $\Delta P_{\text{P1-P2}}$, in Osc.3s together with their counterparts in Osc.4s, $\Delta P_{\text{A2-A1}}$ and $\Delta P_{\text{P3-P4}}$. Similarly to the previous configuration analysis, for each of the critical times defined above, a simplified sketch showing the main jets direction and the propagation of pressure waves along the feedback loops in each oscillator is also presented in Figure 5-17.

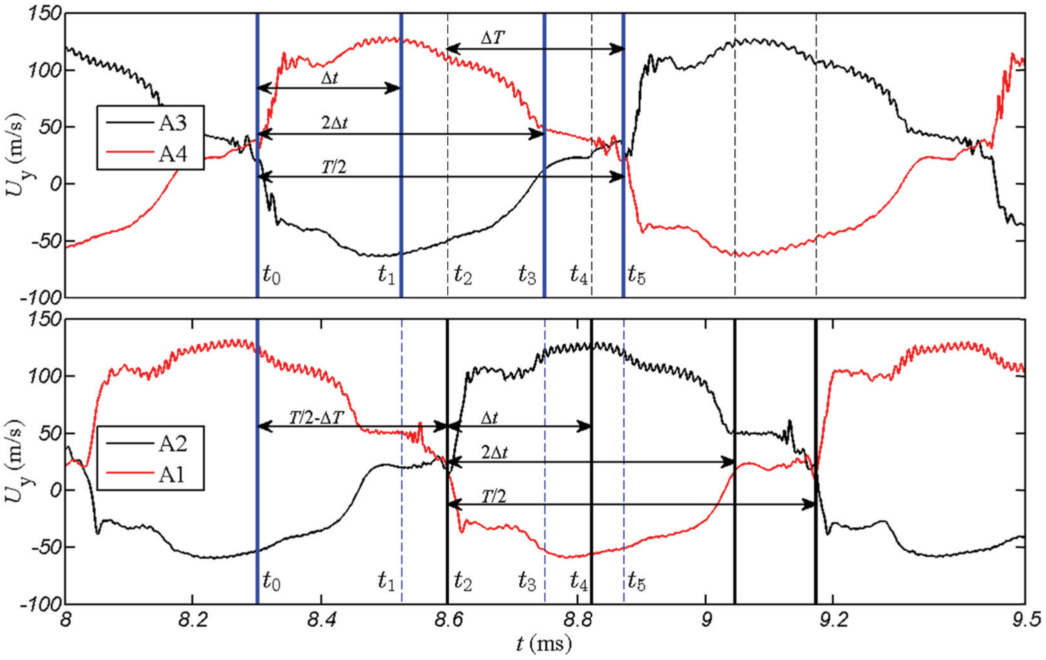

Figure 5-15. Evolution with time of the area-average velocity U_y in the branch inlet sections A of Osc.3s and Osc.4s, 4th method

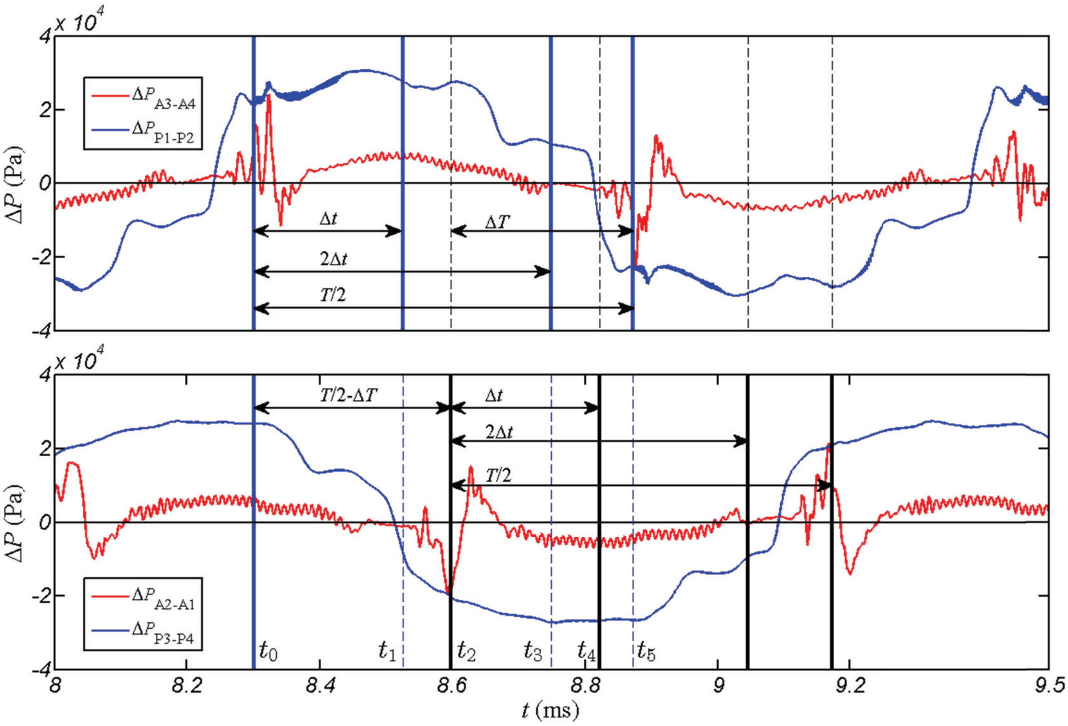

Figure 5-16. Evolution with time of the pressure differences between the control port P and branch inlet A sections of Osc.3s and Osc.4, 4th synchronization method

Time t_0: from Figure 5-16, it can be observed that at t_0, the pressure in section P1 is 21 kPa higher than that in section P2, while the pressure in section A3 is also a little higher than that in section A4. The combination of these two pressure differences provoke the switching of the main jet in Osc.3s from the left branch to the right one. In Osc.4s, at this time, the main jet has been in the right branch for almost a quarter period (cf. Figure 5-15). The pressures in both the left branch and control port of this oscillator are higher than those in its right side, resulting in a stable attachment of the main jet to the right branch.

Time t_1: One basic time unit Δt later, the HPCW coming from the section A4 along the tube 4 arrives at the control port section P4 and reflects, while the LPEW propagates from A3 to P3 and then reflects. As a consequence, the value of $\Delta P_{\mathrm{P3\text{-}P4}}$ decreases from 20 kPa to a negative value. However, the $|\Delta P_{\mathrm{A2\text{-}A1}}|$ value is still too small to provoke the jet switching, which is in accordance with what has been shown on a single oscillator in section 4.2.3.

Time t_2: The pressure difference $|\Delta P_{\mathrm{A2\text{-}A1}}|$ between the branches of Osc.4s has now reached a value large enough to provoke, in conjunction with the large value of $|\Delta P_{\mathrm{P3\text{-}P4}}|$, the switching of the jet in this oscillator. At this time, along tube 2, the HPCW starts to propagate from section A2, and along tube 1, the LPEW starts to propagate from A1. While at the same moment, the fronts of the pressure waves in tube 4 (HPCW) and tube 3 (LPEW) are already in middle of the tubes.

Time t_3: At this time, i.e. two basic time units after t_0, both the HPCW in tube 4 and the LPEW in tube 3 have reached back section A4 and section A3 respectively, which makes the pressure difference between the branches $\Delta P_{\mathrm{A3\text{-}A4}}$ changing from positive to a slightly negative value. However, the pressure difference at the control ports $\Delta P_{\mathrm{P1\text{-}P2}}$ is still largely positive, not allowing the jet switching.

Time t_4 : One basic time unit Δt later than t_2, the HPCW in tube 2 arrives in section P2 and the LPEW in tube 1 arrives in section P1, provoking the destabilization of the main jet of Osc.3s. This is particularly visible on U_{y} profiles in section A3 and A4: these 2 velocities are indeed very close and very perturbed between t_4 and t_5.

Time t_5: The conjunction of the two pressure differences $\Delta P_{\mathrm{P1\text{-}P2}}$ and $\Delta P_{\mathrm{A3\text{-}A4}}$ provokes the switching. The time difference t_5 - t_4 can be related to the deflection time.

From t_4 to t_5, under the combined effect of the two pressure differences in Osc.3s, the main jet switching is provoked in a short time from comparably stable status.

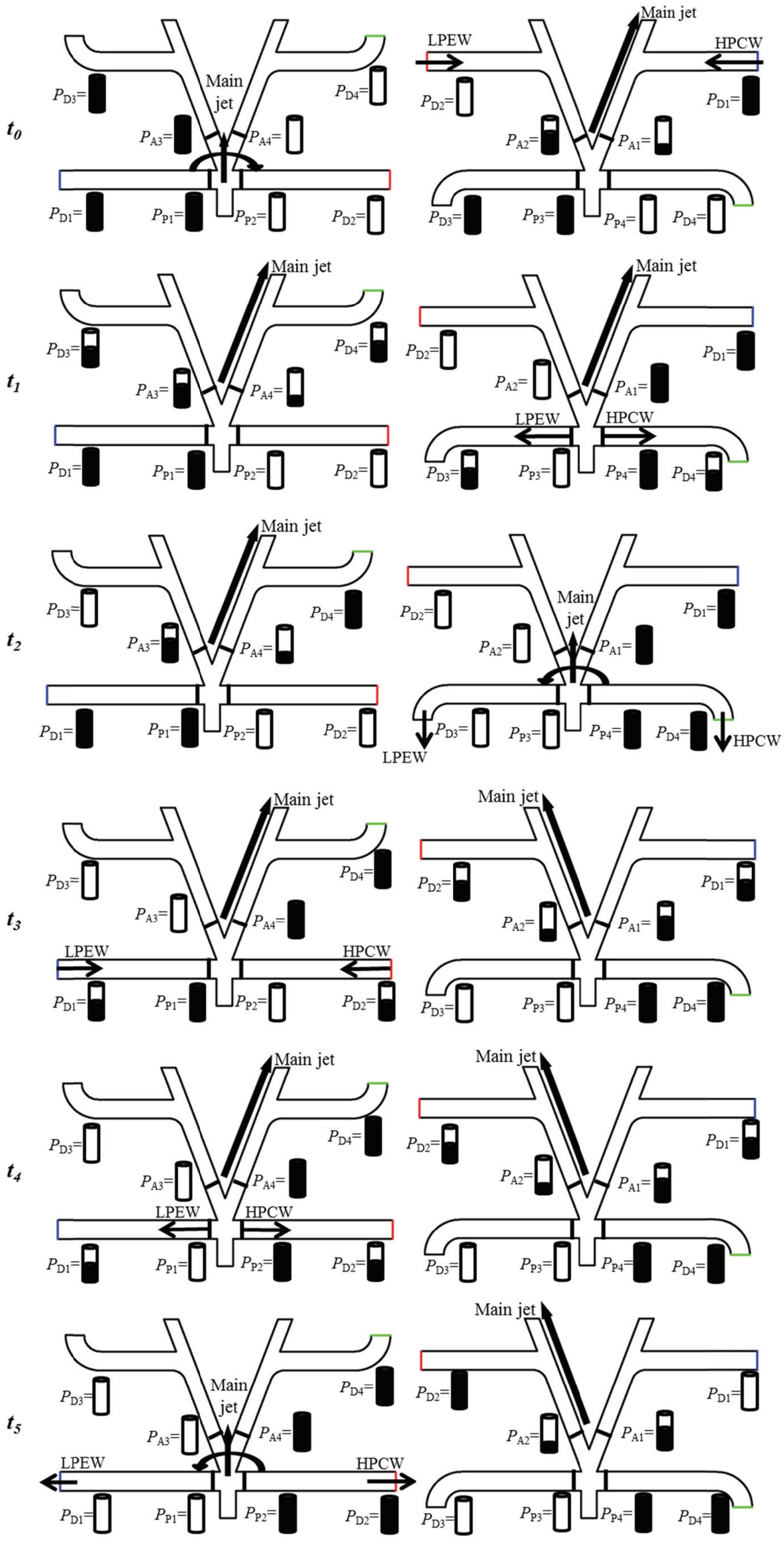

Figure 5-17. Sketch showing the main jets directions and propagation of pressure waves along the feedback loops at each defined critical time; left side Osc.3s, right side Osc.4s

5.3 Synchronization of an array of fluidic oscillators

The 1st proposed synchronization method seems to be much easier to implement for an array of fluidic oscillators than the 4th one. A numerical simulation has been conducted to verify the feasibility of this synchronization method in an array. As shown in Figure 5-18, there are four oscillators in this simulation. All of them have the same geometry except the outlet slot width as shown in Figure 5-6. Osc.3s-1 and Osc.3s-2 have an outlet width of 0.375 mm while Osc.4s-1 and Osc.4-2 have an outlet width of 0.5mm. The branches are virtually connected by translational periodic boundary conditions. The inlet pressure P_i is set to 0.25 MPa in the simulation. The outlet velocity U_y in the center of the left outlet slot of each oscillator is monitored during the simulation.

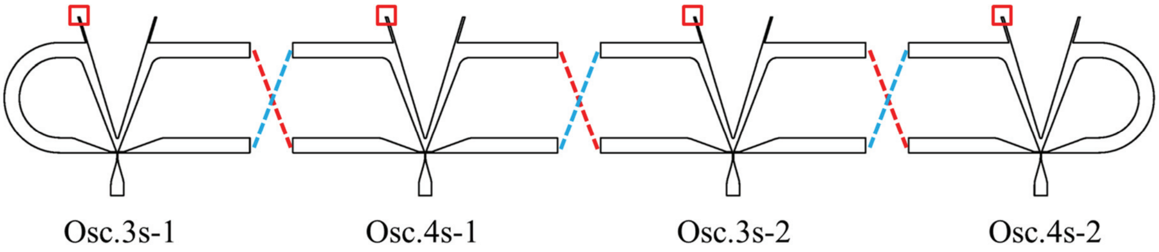

Figure 5-18. Sketch of the configuration used in the numerical simulation of the synchronization of an array of 4 oscillators using the 1st proposed inter-connection pattern

The evolution with time of monitored U_y in the center of the left outlet slot of each oscillator of the array is shown in Figure 5-19. It can be clearly observed that these oscillators are very well synchronized. Their oscillation frequency is about 1101 Hz which is close to the estimated value given by Eq.(4-2). Osc.3s-1 is almost in the same phase as Osc.3s-2 while Osc.4s-1 is nearly in phase with Osc.4s-2. The phase lag between two next oscillators is close to 0.5*T*, higher than 0.375T found numerically in the case of the synchronization of two oscillators. The outlet velocity ranges and evolution profiles with time in each oscillator are similar, despite the differences in outlet slot widths, which is also different to the case of the synchronization of two oscillators shown in Figure 5-9.

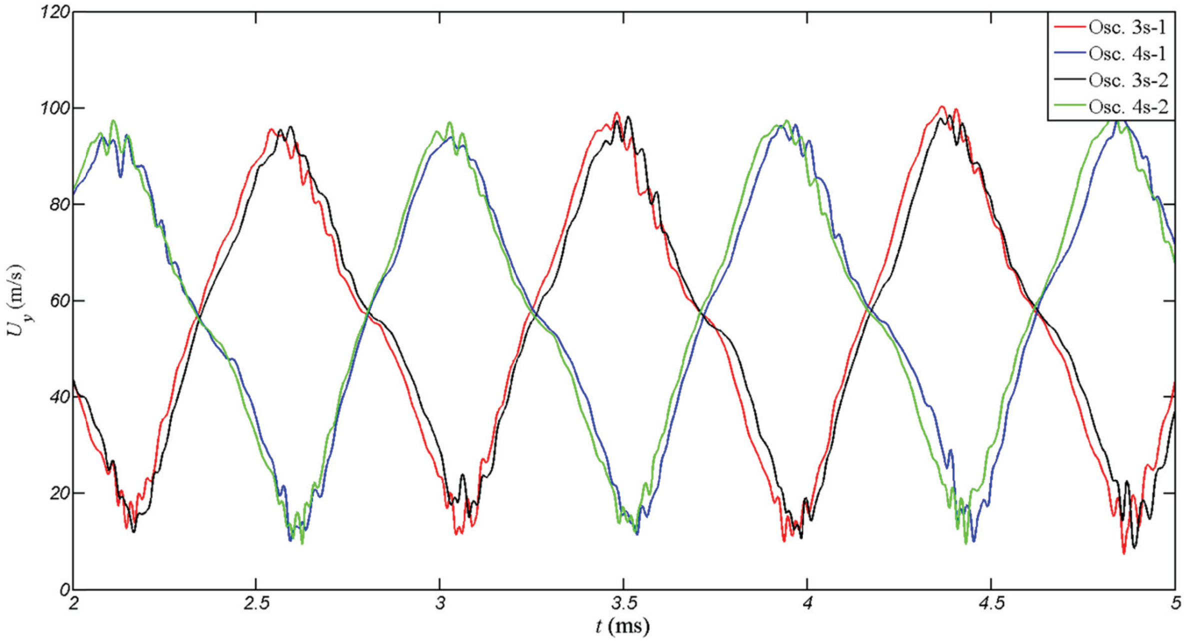

Figure 5-19. Numerical evolution with time of U_y in the center of the left outlet slot in each oscillator of the array, 4th synchronization method

5.4 Conclusions

Two synchronization methods based on inter-connections between the feedback loops of two similar oscillators have been both experimentally and numerically validated and analyzed in detail. The first method leads to a similar oscillation frequency as the one obtained when the oscillators work separately. The pulsed jets generated by the two oscillators have a phase difference close to half a period. The other method leads to a much lower frequency and the phase difference is about $0.25T$. It is found that the parameters controlling the oscillation dynamics are the same as in the case of a single oscillator, i.e. the pressure differences between the control ports and between the branch inlets of the actuators. However, as the evolution with time of these pressure differences is due to the propagation of pressure waves along the feedback loops, the differences in the inter-connection patterns thus lead to different propagation times, explaining the significant frequency difference between the two synchronization methods. The first synchronization method has also been applied to an array of 4 similar fluidic oscillators and validated through numerical simulations.

Chapter 6. Efficiency of the Oscillator Array in Controlling Separated Flow in a Ramp

An array of fluidic oscillators has been designed according to the previous studies and implemented to control a separated flow over a backward-facing ramp. The basic characteristics of this oscillator array and its efficiency in controlling the separated ramp flow are presented

6.1 Design and Characteristics of an array of fluidic oscillators

6.1.1 Design of the oscillator array

The array is made of 12 oscillators in total as shown in Figure 6-1. Rather than assembling various pieces to form the inside flow channels like the prototypes in chapter 2 (cf. Figure 2-4a), the internal flow channels in this array are milled by CNC machine in a depth of 0.37 mm which can mitigate the assembling error. The array is comprised of a base plate where the internal channels are milled and a cover plate where only the outlet slots are milled. The array's total width is 455 mm. However, it is divided into 3 pieces in the machining process as shown in Figure 6-1. The materials of both base plate and cover plate are aluminum and they are assembled together by countersunk head bolts in order to keep a smooth surface in the cover plate.

The key dimensions of each oscillator are shown in Figure 6-2a and the detailed dimensions of the switching zone are the same as in previous designs (Figure 2-2). It has a throat width of 0.2 mm, and outlet hole slot is about 0.5×1.0 mm^2 in design.

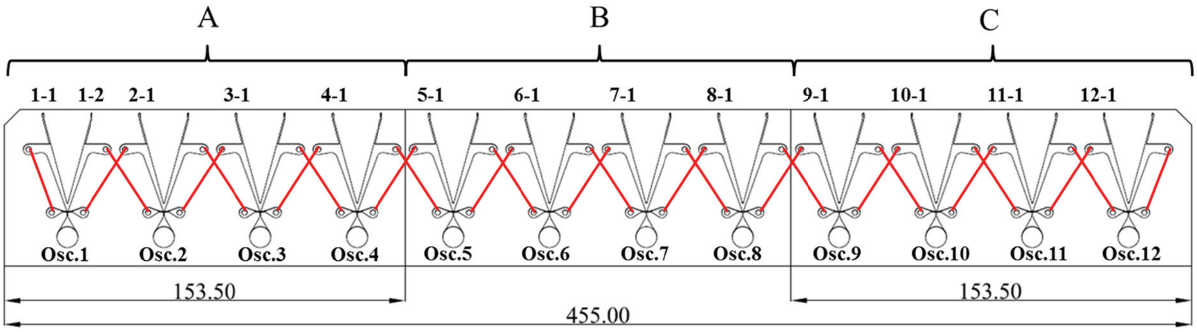

Figure 6-1. Sketch of the fluidic oscillator array

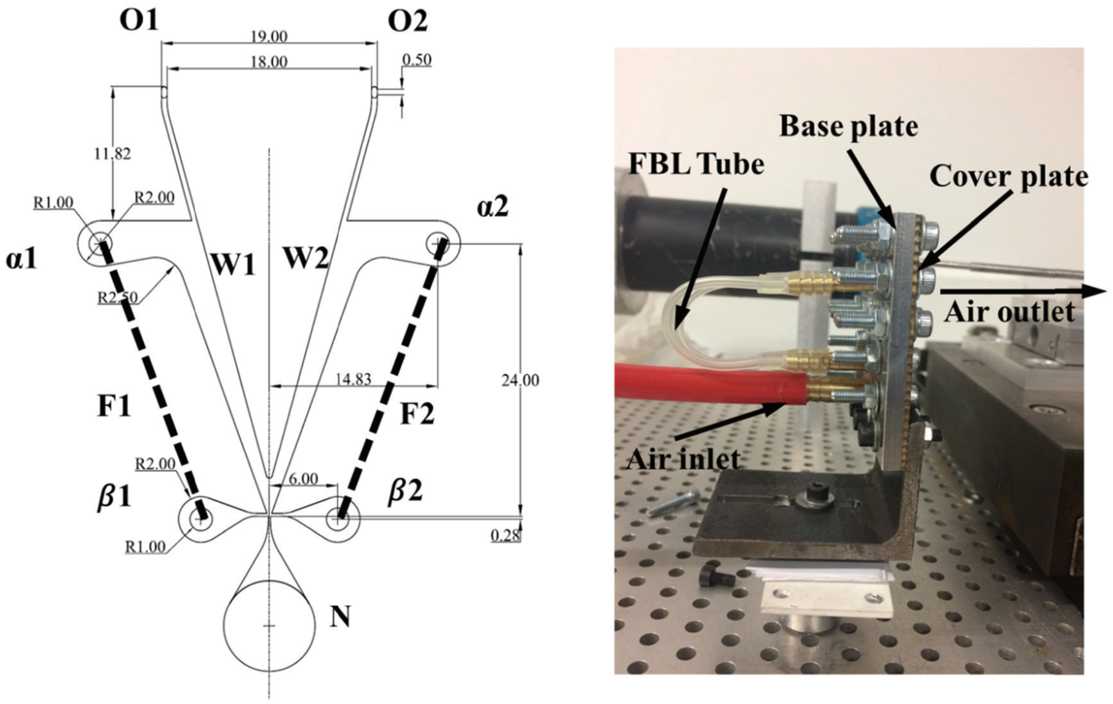

(a) (b)

Figure 6-2. a) key dimensions of the designed fluidic oscillator in the array; b) photo of a real fluidic oscillator during test

Before manufacturing the whole array, a single oscillator with the same design has been manufactured as that shown in Figure 6-2b. This oscillator has been used to check that it operates properly with much thinner channels and to provide preliminary results about its performances.

6.1.2 Preliminary tests on a single fluidic oscillator

After manufacturing this isolated oscillator, its real key dimensions are measured (3D measurement machine Alicona InfiniteFocusSL, highest resolution of 100 nm), in particular its outlet slot area and its throat section area as shown in Figure 6-3a,b,c. The outlet slot area is measured to be A_o = 0.52 mm^2, while the throat cross section area is A_t = 0.097 mm^2. Compared to the designed geometry, the deviation in the throat section area is about 20% while it is about 10% in the outlet slot area. In the other parts of the device, with larger dimensions, the deviations are much smaller and accordingly have been neglected.

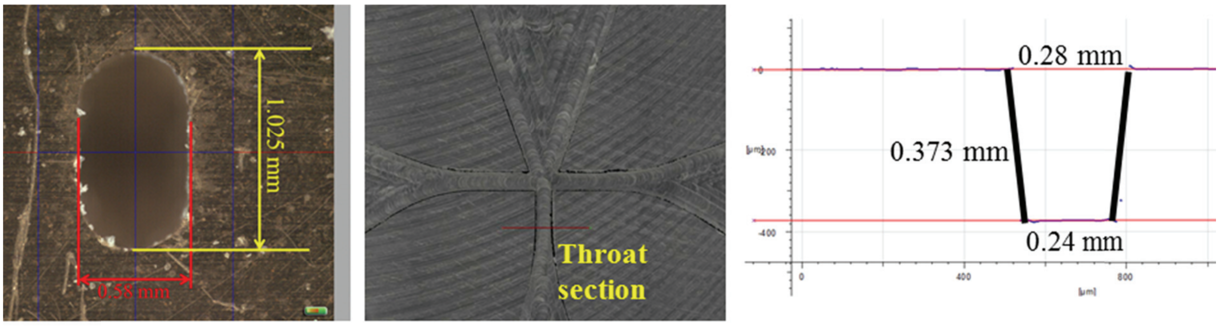

(a) (b) (c)

Figure 6-3. Verification of the oscillator's key dimensions on a 3D measurement machine Alicona InfiniteFocusSL. a) dimensions of outlet slot; b) indication of the throat section location; c) dimensions of the throat cross-section

By assuming that the flow in the throat section is sonic when P_i=0.2 MPa (as $P_i > P_{cr}$ = 0.19 MPa for a converging nozzle), the average velocity $<U>$ in the outlet slot can be calculated:

$$<U>=K\frac{P_i A_t}{2\rho_{atm} A_o \sqrt{T_i^*}}=K\frac{P_i A_t R_g \sqrt{T_{atm}}}{2P_{atm} A_o}=37\ m/s \tag{6-1}$$

where P_i is the inlet total pressure, A_t is the throat area, A_o is the outlet slot area, ρ_{atm} is the air density in atmosphere condition, T_i^* is the inlet total temperature which is treated equal to the atmosphere temperature T_{atm}, K is a constant which is 0.0404 (m s^{-1} $K^{-0.5}$) for air, R_g is the specific gas constant (287 $Jkg^{-1}K^{-1}$).

The tube used in Figure 6-2b to link the connector and form the feedback loop has a length of L_t = 80 mm and an internal diameter of 2mm. The total FBL including the connectors and the internal flow channels is L_f = 200 mm approximately. Thus, according to Eq.(4-2), the oscillator's operating frequency can be estimated to be $f = 340/(4\times L_f) = 425$ Hz.

The same hot wire anemometry system as that introduced in section 2.2 is employed to acquire both the pulsed jet frequency and the outlet velocity. However, since the outlet slot is much smaller than the utilized hot wire, the calibration process is modified in order to get a reasonable result. Rather than calibrating the hot wire on a dedicated normalized jet, it is calibrated directly in front of one of the outlet slots by the following method:

1; block the other outlet slot so that the whole inlet flow rate is ejected through this unblocked outlet slot;

2; monitor the inlet mass flow rate using a high precision flowmeter (BRONKHORST D-6210, 0-10 ln/min air flowrate range with an uncertainty lower than 3% of the measured value), thus the outlet velocity can be calculated from the inlet total flowrate.

3; monitor and save the hot wire signals;

4; increase the inlet pressure and flowrate, and then repeat step 2 and 3 until the entire velocity range is covered.

Using the calibrated function of King's law (by L.V. King[85]) between velocity in a range of 0-80 m/s and the hot wire voltage signals, after unblocking the other outlet slot, the outlet velocity and frequency response in function of inlet pressure can be measured.

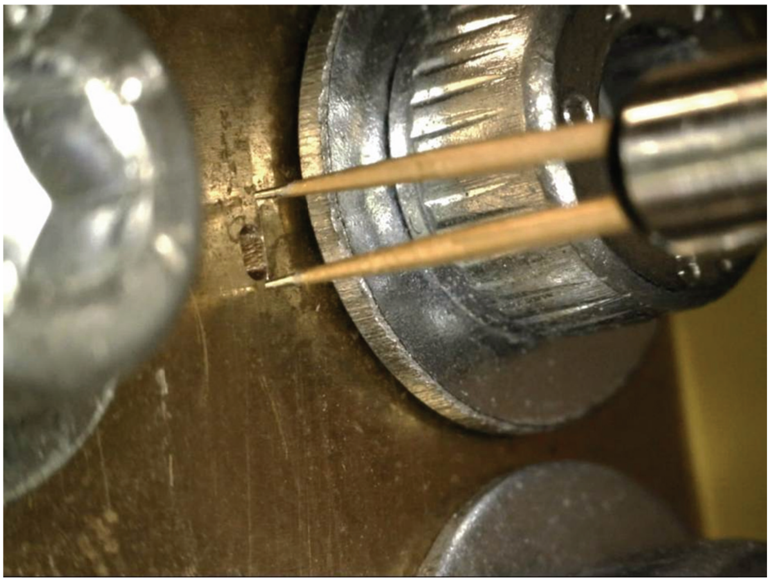

Figure 6-4. Hot wire in front of an outlet slot of the new oscillator prototype

When P_i=0.2 MPa, the measured outlet velocity sample in one outlet is shown in Figure 6-5. It can be observed that the average velocity is about 40 m/s which is very close to the calculated 37m/s, though the signals are very noisy. The amplitude is about 20m/s which is just half of the average value.

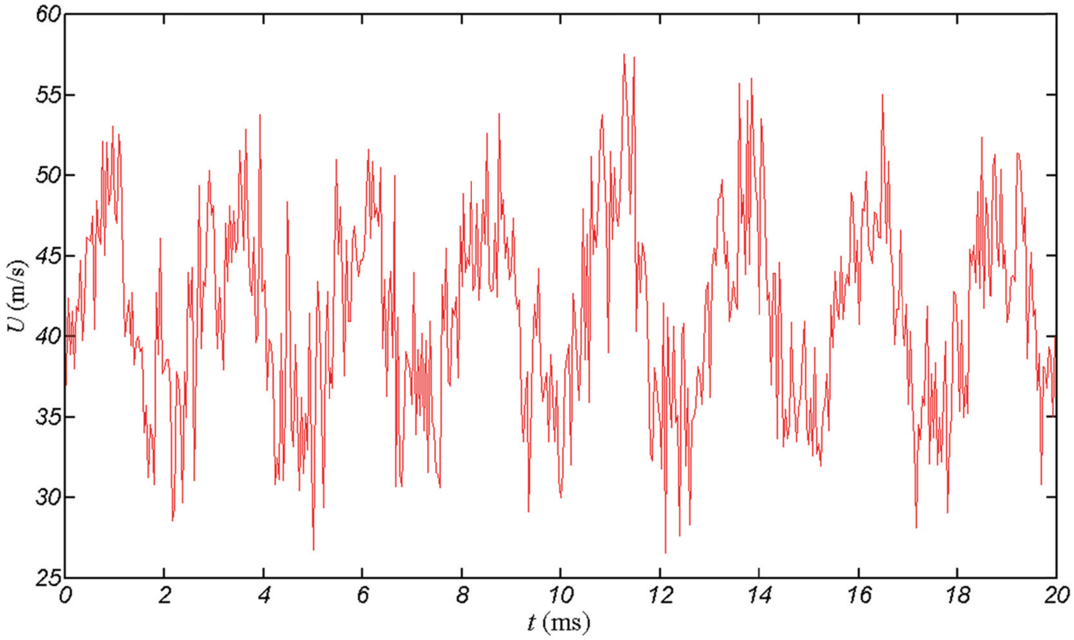

Figure 6-5. Generated jet velocity sample, P_i=0.2 MPa

The operating frequency decreases from about 410 Hz to about 390 Hz when the inlet pressure increases from 0.12MPa to 0.3MPa as shown in Figure 6-6a. This frequency is very close to the 425 Hz estimated by Eq.(4-2). In addition to the error due to the assumptions made to establish Eq.(4-2), this deviation may be explained by the more significant boundary effects of both base plate and cover plate due to the small depth of the device. It can also be observed in Figure 6-6b, that the mean outlet velocity and its root mean square increase almost linearly with the inlet pressure.

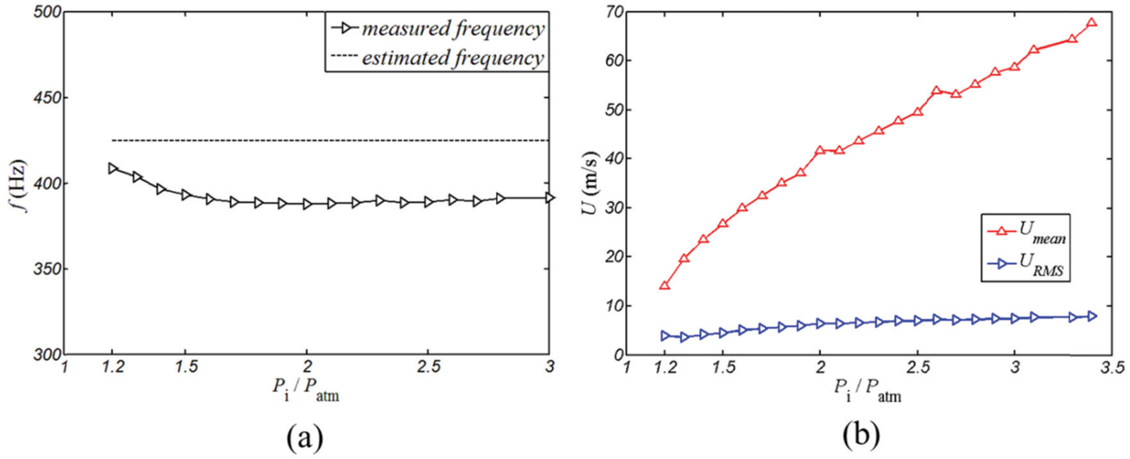

Figure 6-6. a) working frequency of the new oscillator prototype ***vs*** inlet pressure; b) mean value and RMS value of its outlet velocity ***vs*** inlet pressure

6.1.3 Synchronization test of the array

After having verified the proper operation of a single oscillator, the whole array, as shown in Figure 6-1, has been machined. The bronze connectors in the isolated oscillator (cf. Figure 6-2b) are replaced by much smaller steel ones which can much better integrate together the plastic tubes. The array is synchronized with the 1st interconnection pattern discussed in chapter 5. As indicated by the red lines in Figure 6-1, the upper connector in one oscillator is linked to the adjacent oscillator's lower connector except at the two ends of the array.

Two transient pressure sensors are used to test the synchronization of the oscillators of this array. As shown in Figure 6-7, one pressure sensor (Endevco 8510B-2, 0-2 psig pressure range and 70 kHz resonance frequency) is fixed just in front of the outlet 12-1 (cf. Figure 6-1) while the other pressure sensor (Endevco 8506-2, 2 psig pressure range and 45 kHz resonance frequency) is placed in front of the left outlet slot of each oscillator (from Osc.1 to Osc.11) sequentially. The sensor is placed just in the center of each outlet slot and is about 0.5mm from the outlet surface in order to get a better signal. The moving sensor is adjusted manually along its bracket which is parallel to the ramp surface (Figure 6-7a). The signals of these two sensors are acquired simultaneously with an acquisition frequency of 25 Hz during 10s. The inlet pressure is set to 0.2 MPa for these tests.

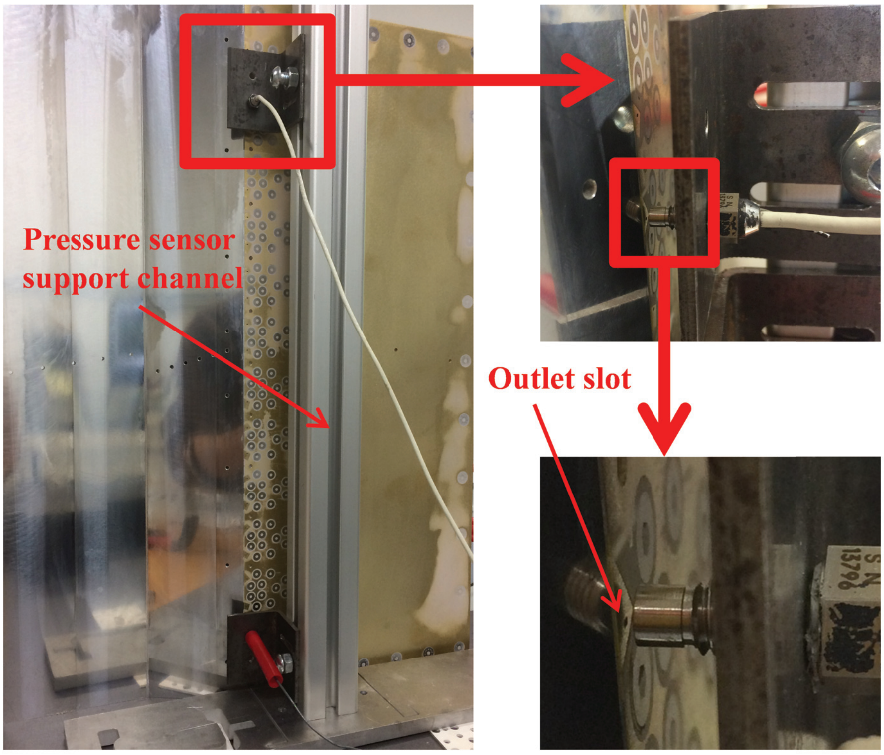

(a) (b)

Figure 6-7. test bench used for analyzing the array synchronization, a) overall view; b)zoomed views

As a result, all the oscillators have the same frequency as Osc.12 which implies that this array of oscillators is perfectly synchronized. The phase lag information is also obtained by correlation analysis of the two sensors' signals. The auto-correlation and cross-correlation signals of Osc.11 and Osc.12 are shown, for example, in Figure 6-8. These two signals have obviously an identical frequency. In addition, it can be observed that the phase difference between the two signals is $\Delta T \approx 0.4T$, where T is the oscillation period.

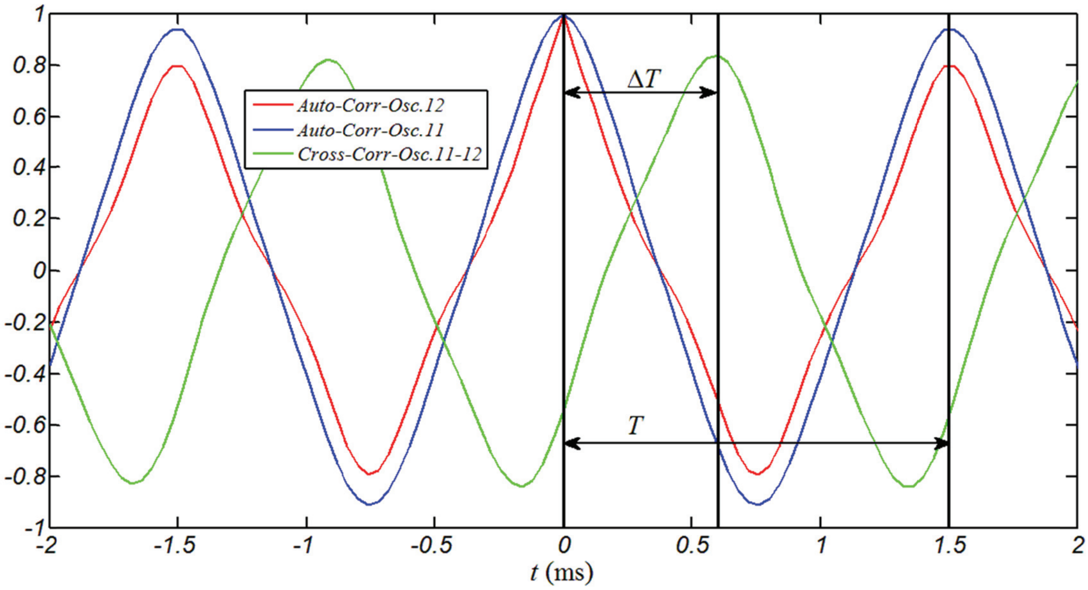

Figure 6-8. Auto-correlation and cross-correlation sequences of the pressure sensor's simultaneous signals from Osc.11 and Osc.12

The phase difference of all the oscillators of the array relative to that of Osc.12 are obtained in this way and shown in Figure 6-9. Unlike in the simulation results, done on a series of only 4 oscillators and for which the adjacent devices were in phase opposition, the phase lag between two adjacent oscillators is close to $0.5T$ but varies between $0.39T$ to $0.49T$. The origin of these irregular phase difference have not yet been completely identified but could be linked to slight differences in the supply pressure of each oscillator (generated by pressure drops in the supply circuit) and/or to small differences in the feedback tube lengths.

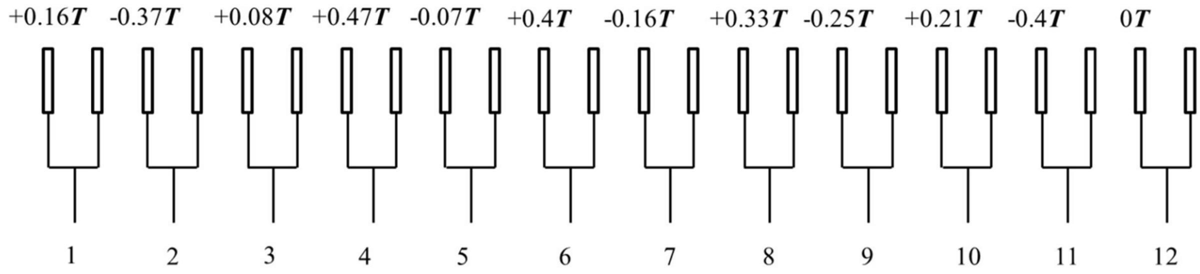

Figure 6-9. Phase lag of each oscillator relative to Osc.12

The synchronized frequency response is also measured for different supply pressures P_i as shown in Figure 6-10. The length of the tubes to synchronize the array is 100 mm with an uncertainty of 5mm. The tube's internal diameter is 1mm. With L_f =135 mm in this case, the estimated frequency is about f = 340/(4×L_f) =630 Hz which is very close to the measured one, especially when $P_i > 2.2\ P_{atm}$.

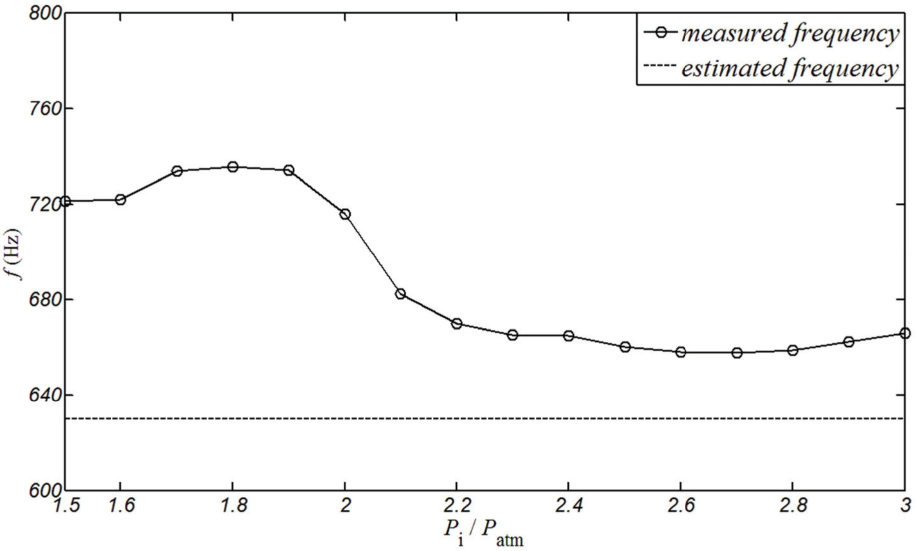

Figure 6-10. Frequency of a synchronized fluidic oscillator array as a function of the supply pressure

6.2 Description of the ramp flow test bench

The experimental assessment of the actuator efficiency was conducted in the wind tunnel S2, in PRISME laboratory, Orléans. For a preliminary test, the average velocity field of the baseline flow without control as well as the controlled flow field was measured by means of Particle Image Velocimetry (PIV). Thus, the characteristics of the wind tunnel, the ramp and the PIV system are briefly described.

6.2.1 Wind tunnel and ramp

The schematic of this wind tunnel is shown in Figure 6-11. It is an Eiffel type subsonic wind tunnel and is comprised of 4 parts. Before the air flow entering the test section part, it passes through the honeycomb and converges in a contraction ratio of 16:1. Both the honeycomb design and the contraction design can largely reduce the residual turbulence intensity and assure the homogeneity of the flow in the test section. After the test section, a diffuser is used to slow down the flow before its evacuation, which can limit the pressure fluctuations in the test section.

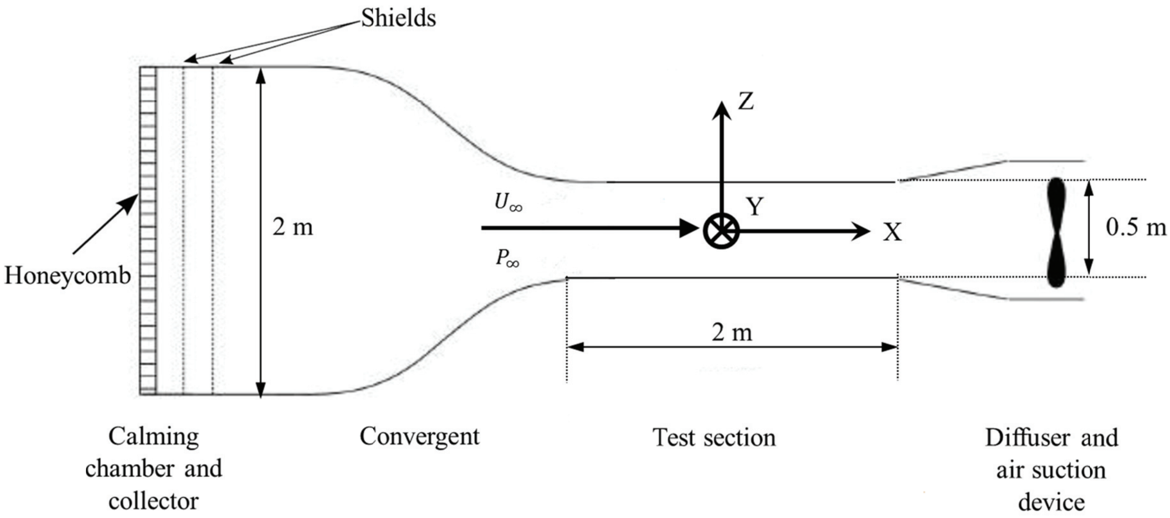

Figure 6-11. Sketch of the wind tunnel S2 in PRISME laboratory

The test section is in the center of the wind tunnel. It has a length of 2 m and a square cross-section of 0.5m×0.5m. The air flow in test section is generated by a fan which is powered by a tri-phase electrical motor in the end of the wind tunnel. The velocity entering the test section U_∞ is deducted from the pressure difference measured between the two sides of the convergent part, i.e., the largest section and the smallest section of the tunnel. The flow velocity obtained in the test section ranges between 2 ms^{-1} and 60 ms^{-1}, with a residual turbulence intensity smaller than 0.25%. More detailed information can be found in the work of Feuvrier[86].

The ramp is installed in the bottom of the test section. It is composed of four assembled parts, namely Part I, II, III and IV, as shown in Figure 6-12. The flow converges a little in Part I, then goes through Part II, and reaches the ramp in Part III, and flows out after Part IV. This design facilitates the parametric study of various ramp since Part III can be replaced easily without modifying the others parts. The ramp used in our experiments has a slant angle of 25° and a height h=30 mm.

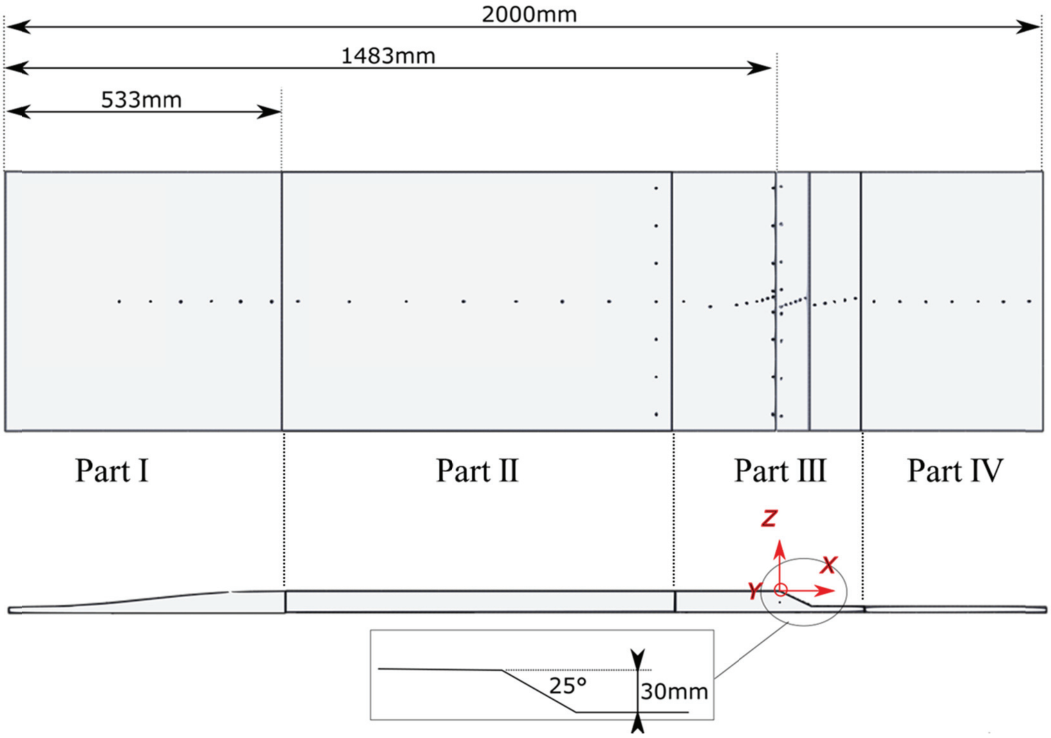

Figure 6-12. Sketch of the ramp in the test section

In this study, Part III has been fitted with the array of fluidic oscillators. As for the single fluidic oscillator shown in Figure 6-2b, the internal flow channels in the array are milled in the base plate, and the outlet slots are machined in the cover plate. Then, the cover plate, base plate and the ramp are assembled together by countersunk head screws or bolts. The center of outlet slots of the array are at a distance of 0.2mm upstream to the ramp slant edge.

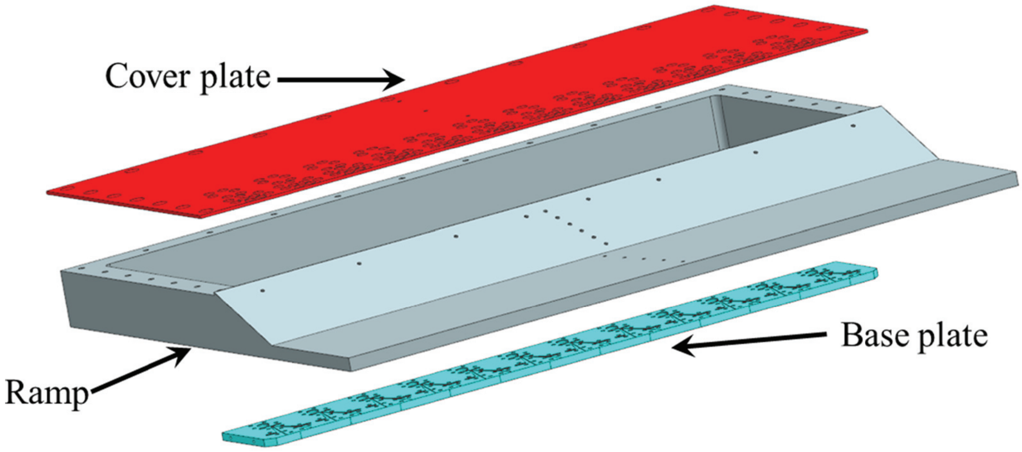

Figure 6-13. CAD model of Part III of the ramp

6.2.2 Measurement devices

The 2D mean velocity fields were captured by using a 2D-2C PIV system in the mid-span plane of the ramp, which is also the symmetry plane of the array between Osc.6 and Osc.7, as shown in Figure 6-1. The sketch of the system positions is shown in Figure 6-14. The images are recorded by a PowerView Plus® CCD camera (4MP series, 2048 × 2048 pixels^2). The camera is equipped with a Nikon® lens (Nikkor AF series, f2.8D) with a focal length of 28 mm. The camera aperture is fixed at 5.6 to limit saturation of the CCD sensor due to laser reflections on the wall. The laser beam is generated by a Quantel Twins® double-pulse Nd: Yag laser (Ultra 00 series, 2 × 200 mJ at 532 nm). A TSI brand synchronizer (series 610035) is used to synchronize the two laser pulses with the camera. The image acquisition system is managed by the Insight software (developed by TSI). This software is also used for processing images. The flow is seeded with olive oil particles (Pivtec® generator) with a diameter of about 1 µm. The time step between two images is 40 µs, and a total of 2000 images are averaged to get the mean velocity field. The image processing algorithm is a two-pass "standard" type algorithm from 64×64 px^2 to 32×32 px^2. The measured velocity fields thus consist of 127×127 vectors in an area of 337×337 mm^2. Each instantaneous velocity field is analyzed by a post-processing algorithm to eliminate the erroneous vectors. The filter used consists of defining the minimum and maximum thresholds on each of the components of the displacement.

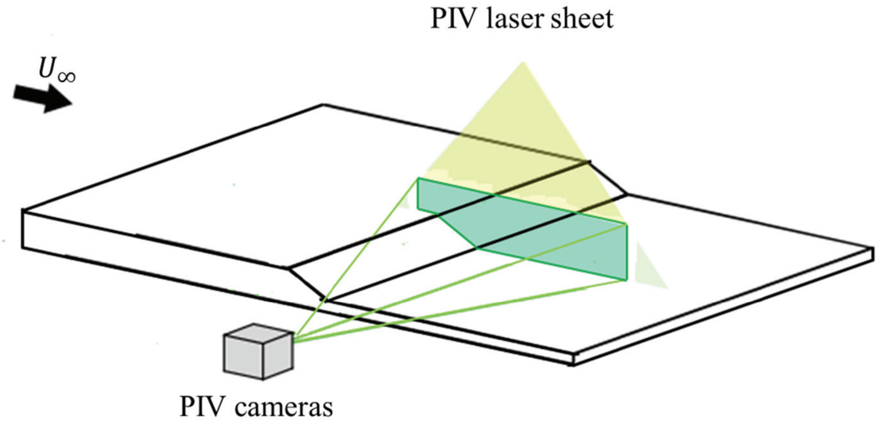

Figure 6-14. Sketch of the PIV system positions

6.3 Measured flow field

The 2D mean velocity fields are measured for 4 operating conditions which are the baseline flow without control and the controlled flows by activating the fluidic oscillator array using 3 inlet pressures. In all cases, the free stream velocity is 20 m/s, corresponding to a $Re = \rho h U_\infty/\mu = 3.8\times10^4$. In the controlled cases, inlet pressures are P_i=0.2 MPa, 0.25 MPa and 0.3 MPa respectively, and their corresponding controlling parameters are presented in Table 6-1. All the normalized parameters, F^+, V_R and C_μ are following the definitions given in section 1.5.

The characteristic length L_r is the streamwise distance between the ramp slant edge where separation occurs and the reattachment point in the baseline flow without control, which is about 145 mm as shown in Figure 6-15. f is the measured frequency of the synchronized fluidic oscillator array as shown also in Figure 6-10.

Assuming that the jet oscillates in a sinusoidal pattern, the momentum coefficient can be calculated by Eq.(1-10):

$$C_\mu = \frac{\overline{m_b U_b}}{\frac{1}{2}\rho U_\infty^2 L\omega} = \frac{N(\overline{U_b}^2 + U_b^{rms2})A}{\frac{1}{2}U_\infty^2 L_r \omega} \tag{6-2}$$

where N is the total number of outlet slots which is $N = 24$.

The mean blowing velocity $\overline{U_b}$ and the RMS value of blowing velocity U_b^{rms} are extracted from Figure 6-6b which is the velocity response to inlet pressure of the single fluidic oscillator whose internal dimensions are the same as those in the oscillator array. However, both their feedback loop tube diameter and length are different. Thus, the mean blowing velocity $\overline{U_b}$ should be the same due to the conservation of mass flow rate while there might be deviations in the value of U_b^{rms} . Nevertheless, the U_b^{rms} value is very low compared to $\overline{U_b}$ and the error due to this approximation is believed to be acceptable.

Table 6-1. Controlling parameters of three controlled flow cases

P_i /(MPa)	0.2	0.25	0.3
f /(Hz)	716	660	660
F^+	5.2	4.8	4.8
$\overline{U_b}$ / (m/s)	44	57	70
U_b^{rms} / (m/s)	6.4	7.7	9.2
V_R	2.5	3.2	4.0
C_μ	0.16%	0.27%	0.41%

6.3.1 Mean field of baseline flow

The mean flow field of the baseline flow is presented in Figure 6-15. The ramp wall is represented by the red line. The data obtained near the wall are not reliable because of the light reflection and thus are abandoned. The separation of the incoming boundary layer is induced by the sharp expansion of the test section. Downstream of the separation point, the flow is marked by a large mean recirculation region where $U_x < 0$, which extends up to the reattachment point where the separated shear layer hits the wall. The separation line is the external boundary of the recirculation region. In this study, it is defined by the isoline $U_x = 0$ on the mean streamwise velocity field, cf. the white line in Figure 6-15. The recirculation region is usually characterized by its length L_r, which corresponds to the streamwise distance between the separation point and the reattachment point. In this baseline case, $L_r / h \approx 4.8$ which is very close to that obtained in a larger scale ramp by Kourta et al[76] where $L_r / h \approx 5.0$. The topologies are comparable with different *R*e and the main difference is the location of the mean reattachment point which moves upstream for increasing *R*e[76]. L_r can also be interpreted as the streamwise scale of shear layer development.

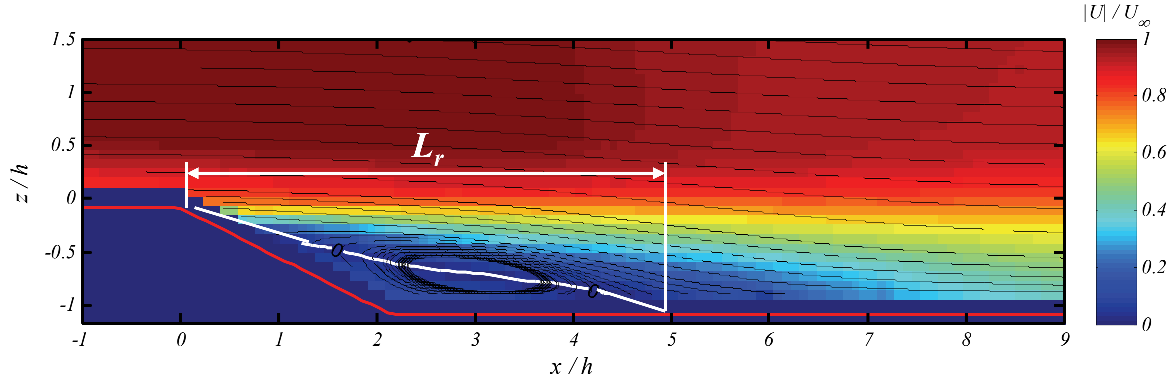

Figure 6-15. Mean flow flow field of the baseline separated flow, $Re=3.8\times10^4$

The streamwise evolution of the shear layer is often characterized by a generalized momentum thickness θ_{SL} which is defined according to Dandois et al[87] as:

$$\theta_{SL}(x) = \int_{y_{\min}}^{\infty} \frac{U_x(x,y) - U_{\min}(x)}{U_\infty(x) - U_{\min}(x)} \left(1 - \frac{U_x(x,y) - U_{\min}(x)}{U_\infty(x) - U_{\min}(x)}\right) dy \tag{6-3}$$

where $U_{\min}(x)$ is a local minimum streamwise velocity.

The expansion rate of this shear layer is defined as:

$$\chi = \frac{d\theta_{SL}(x)}{dx} \tag{6-4}$$

A constant expansion rate of θ_{SL} can be found from Figure 6-16 when $0 < x / L_r < 0.5$ which is $d\theta_{SL} / dx \approx 0.21/4.8 = 0.044$.

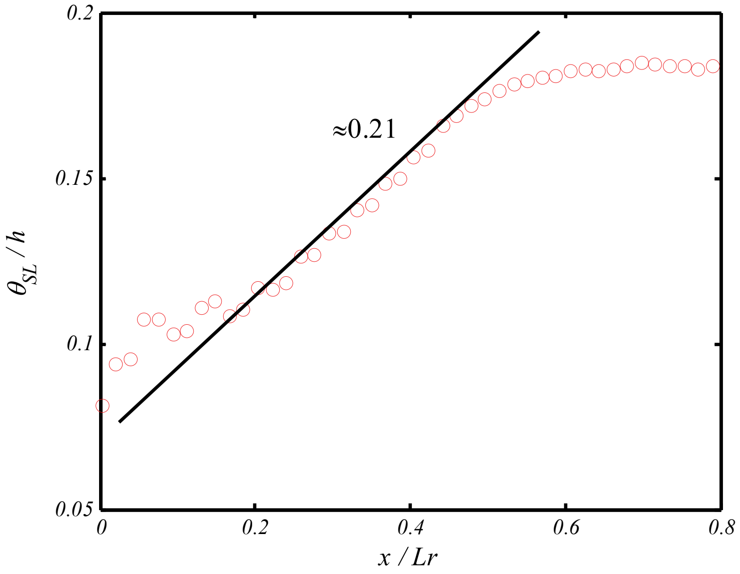

Figure 6-16. Shear layer thickness θ_{SL} evolution along streamwise direction

The spreading rates of typical free turbulent mixing layers modeled by Browand & Toutt[88] is:

$$\chi = \frac{d\theta_{SL}(x)}{dx} = 0.034\frac{U_\infty(x) - U_{\min}(x)}{U_\infty(x) + U_{\min}(x)} \tag{6-5}$$

Eq.(6-5) yield $d\theta_{SL}/dx \approx 0.045$, to be compared to the measured value of 0.044. this good agreement suggests that the separated shear layer behaves similarly to a free shear layer in a large region downstream of the upper edge of the ramp. However, the growth rate of θ_{SL}/h decreases for $x/L_r > 0.5$ and Eq.(6-5) is no longer an acceptable approximation.

6.3.2 Mean flow fields with fluidic oscillator actuation

The mean velocity fields in the streamwise direction obtained in both baseline case and controlled cases are shown together in Figure 6-17. In the first controlled case (C_μ = 0.16%), the flow separation has been totally eliminated and no reverse flow can be observed. When C_μ continues increasing to 0.27%, the situation becomes even better. In case of C_μ = 0.41%, no significant modification can be observed compared to the case C_μ = 0.27%.

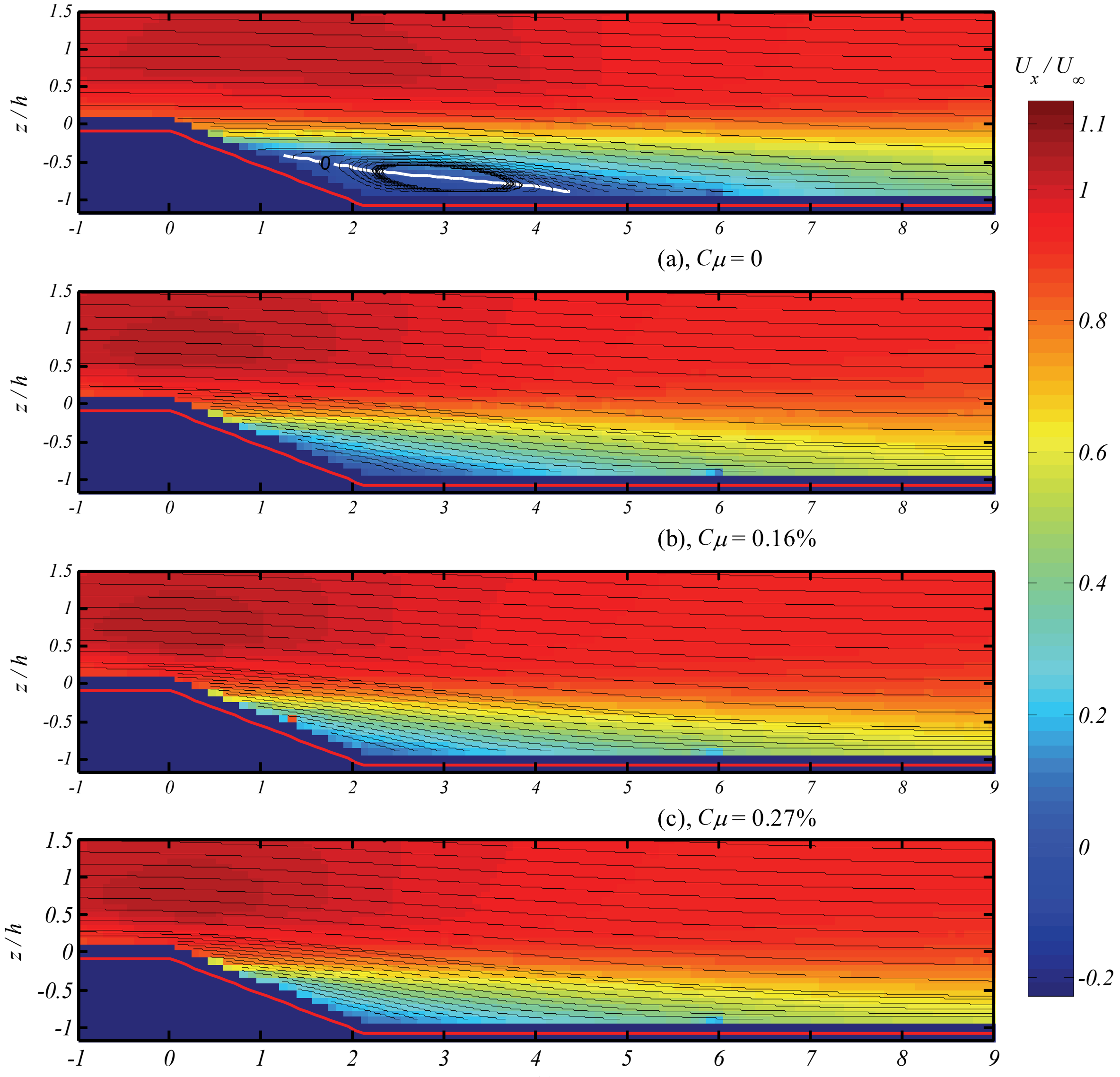

(a), $C\mu = 0$

(b), $C\mu = 0.16\%$

(c), $C\mu = 0.27\%$

(d), $C\mu = 0.41\%$

Figure 6-17. Streamlines and mean U_x field contours under various conditions

Similar observations can be obtained by plotting the profiles of the velocity differences between U_x and the free stream velocity $\Delta U = U_x - U_\infty$, as shown in Figure 6-18. In freestream (i.e. $z/h > 1$), the relative velocity is 0, thus the plot markers in each case are overlapped to the position line. While in areas where U_x is smaller than the U_∞, resulting in a negative relative velocity, (e.g. $z/h < 0.3$), the plot markers will be deviated to the left side of the position line. Blue lines are added to indicate the position where the U_x would be 0. The separation happens once the markers pass on the left of this blue line.

From the global view in Figure 6-18, the flow patterns of free-stream and separation regions in both uncontrolled and controlled cases can be clearly observed and compared. In case of baseline flow ($C_\mu = 0$), marked by the blue circles, the deviation to each vertical line is more significant compared to the controlled cases. The largest deviation appears around $x/h \approx 2.3$ where the strongest separation happens. As the flow goes further, the deviation becomes smaller and smaller, though still larger than those of controlled cases ($x/h \approx 9$). All three controlled cases (C_μ = 0.16%, 0.27%, 0.41%) show obvious improvement of the separated flow demonstrated by the sharp reduction of deviations to corresponding position lines compared to the baseline flow case. In the trailing flow, i.e. x/h >5, no obvious differences can be observed among the controlled cases. In the ramp region, a zoomed view is used to inspect the controlling effects in the three studied cases. From this zoomed view, with the help of added blue lines, it can be clearly observed that the separation is always totally eliminated, since no markers surpass the blue lines in all cases. In addition, the last two cases with higher C_μ work a little better than the case of smaller C_μ = 0.16%. However, no observable difference can be found between the case with C_μ = 0.27% and that with C_μ = 0.41%.

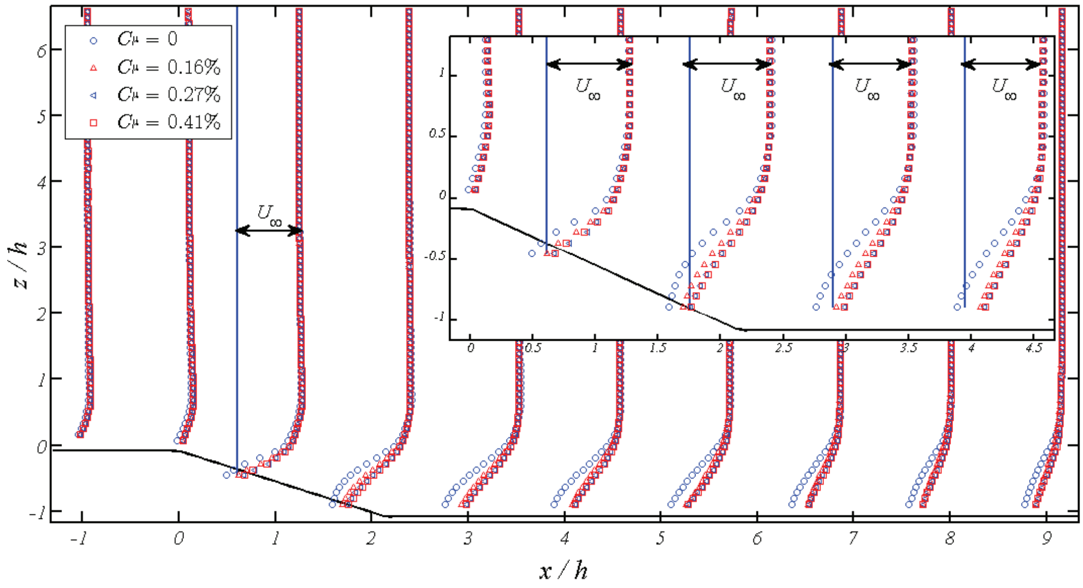

Figure 6-18. Profiles of velocity difference between U_x and U_∞ at different positions along the ramp: global view and zoomed view

Compared to the studies reviewed in Table 1-3 where the optimal C_μ equals 0.8%, the present study shows that unsteady blowing with C_μ = 0.16% is able to totally eliminate the separation in a ramp flow, utilizing a synchronized array of fluidic oscillators. Moreover, when C_μ is larger than 0.27%, no additional benefit can be obtained.

6.4 Discussion about the control mechanisms

In the following, only the baseline flow C_μ = 0 and the controlled flow with C_μ = 0.16% are analyzed and compared in order to clarify the controlling mechanisms.

6.4.1 Momentum equations governing the mean flow:

Given the Reynolds decomposition of an instantaneous velocity *U* (*x,y,z,t*):

$$U(x,y,z,t) = <U(x,y,z,t)> + u'(x,y,z,t) \tag{6-6}$$

where $<U(x,y,z,t)>$ is the ensemble-averaged or mean velocity, $u'(x,y,z,t)$ is the fluctuating velocity. Thus, for an incompressible flow, the governing Reynolds-averaged Navier–Stokes (RANS) equation in tensor form is:

$$\frac{\partial U_j}{\partial t} + U_i \frac{\partial U_j}{\partial x_i} = -\frac{1}{\rho}\frac{\partial P}{\partial x_j} + v\frac{\partial^2 U_j}{\partial x_i \partial x_i} - \frac{\partial <u_i' u_j'>}{\partial x_i} \tag{6-7}$$

where U_j are the mean velocity components, u_j' are the fluctuation velocity components, *P* is the ensemble-averaged pressure, *ρ* is the ensemble-averaged density, *v* is the kinetic viscosity, <*X*> means the ensemble-averaged value of term *X*.

In a 2-dimensional average flow and giving the emphasis to pressure gradient terms, Eq.(6-7) can be reformulated to:

$$\frac{\partial P}{\partial x} = -\rho(U_x \frac{\partial U_x}{\partial x} + U_y \frac{\partial U_x}{\partial y}) - \rho(\frac{\partial <u'u'>}{\partial x} + \frac{\partial <u'v'>}{\partial y}) + \mu(\frac{\partial^2 U_x}{\partial x^2} + \frac{\partial^2 U_x}{\partial y^2}) \tag{6-8}$$

$$\frac{\partial P}{\partial y} = -\rho(U_x \frac{\partial U_y}{\partial x} + U_y \frac{\partial U_y}{\partial y}) - \rho(\frac{\partial <u'v'>}{\partial x} + \frac{\partial <v'v'>}{\partial y}) + \mu(\frac{\partial^2 U_y}{\partial x^2} + \frac{\partial^2 U_y}{\partial y^2}) \tag{6-9}$$

From the PIV test, the variable fields of U_x, U_y, $<u'u'>$, $<v'v'>$ and $<u'v'>$ have been obtained. Thus, from, Eq.(6-8) and Eq.(6-9), the mean pressure gradient fields in both *x* direction and *y* direction can be calculated.

6.4.2 Pressure gradient field of both baseline case and controlling case

Figure 6-19 presents the pressure gradient field of the baseline flow in both y direction and x direction. The high value of $\partial P / \partial y$ in the upstream, especially above the recirculation bubble (*x/h* ≈ 3) illustrate the higher pressure which push the main stream flowing downside in the ramp, and the low value of $\partial P / \partial y$ at the end of the recirculation region and the near wall region reflects the effect of wall boundary which forces the downside flow back the main flow direction. The topology of the *x* direction pressure gradient field $\partial P / \partial x$ is much different. The flow accelerates a little just before the ramp (*x/h* < 0) because of the negative value of $\partial P / \partial x$. Then a shear layer is formed where very high values of $\partial P / \partial x$ can be found which means the flow velocity in this layer decreases quickly because of the strong entrainment effect from the main flow above the layer to the recirculation region downside the layer. In the first half part of recirculation region ($0<x/h<2.5$), the significantly negative value of $\partial P/\partial x$ shows the flow is accelerating from very low streamwise velocity. A large region of high positive value of $\partial P/\partial x$ can be found just in the end of recirculation bubble ($x/h \approx 4$). The huge pressure increase in this region plays a significant role to make the main flow separated and is a main source of flow energy loss.

In the controlled case, the pressure gradient in both directions are significantly changed as shown in Figure 6-20. Firstly, both the high positive gradient regions are moving upstream. Secondly, the highest gradient values in both direction increase a lot, e.g., the highest $\partial P/\partial y$ is increased from 750 to 1300 Pa/m. Thirdly, the highest gradient values all appear near the actuator excitation location ($x/h \approx 0$). Fourthly, the value of $\partial P/\partial x$ becomes much larger in the whole ramp region.

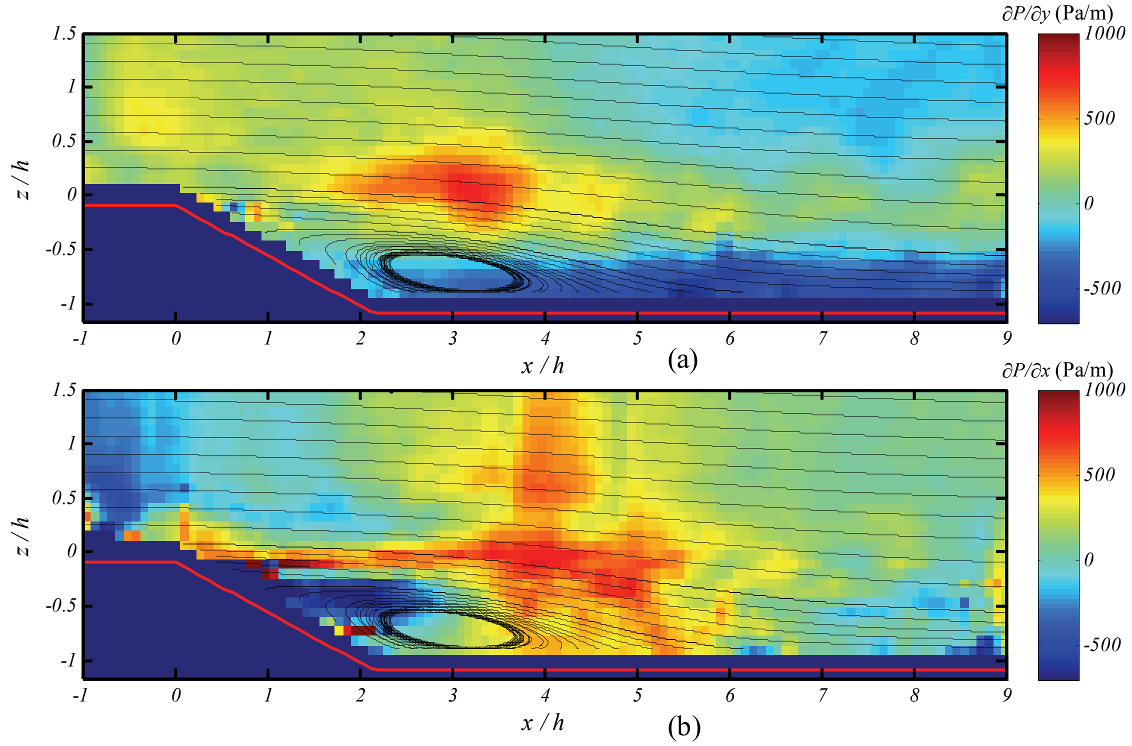

Figure 6-19. Pressure gradient field of the baseline flow. a) y direction gradient; b) x direction gradient

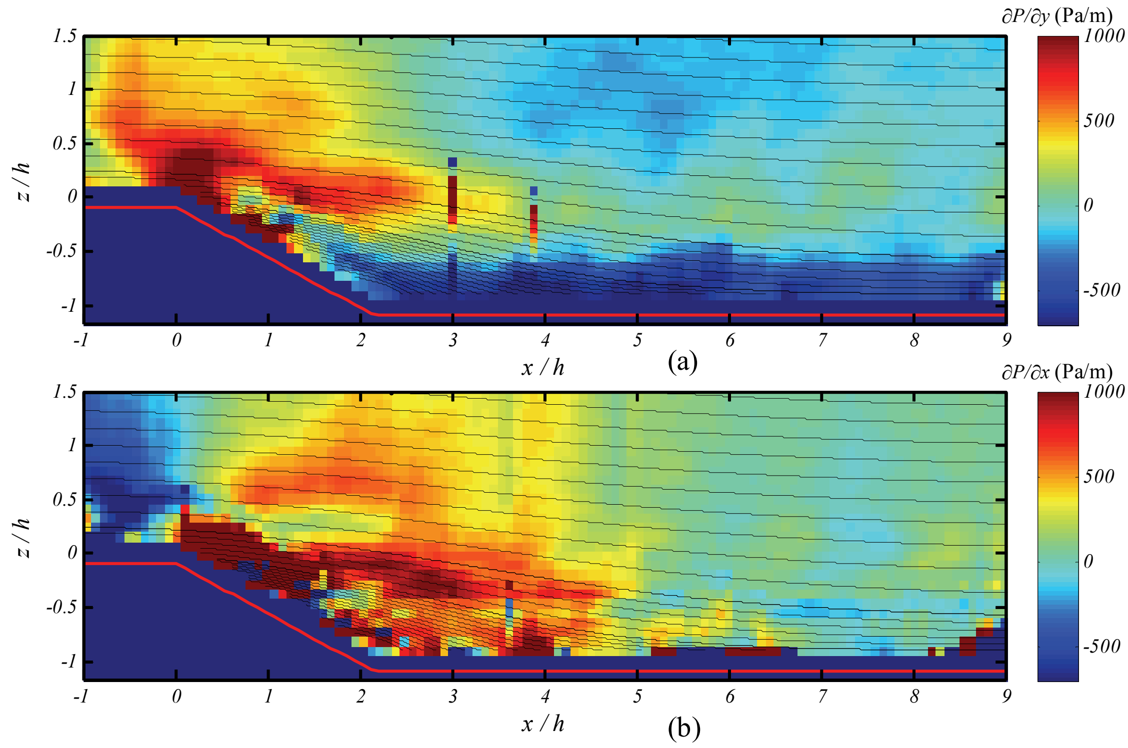

Figure 6-20. Pressure gradient field of the controlled flow, $C_\mu = 0.16\%$. a) y direction gradient; b) x direction gradient

All the above observations and comparisons demonstrate that the actuation of fluidic oscillator array largely modifies the flow field structure and the gradient field structure. For the purpose to find out the most important controlling factors, deeper analysis about each component in the governing equations should be conducted. Since the separation is mostly controlled by the x direction pressure gradient, the analysis is thus focused on Eq.(6-8).

6.4.3 Focus on analysis of pressure gradient in *x* direction:

After examining each term in Eq.(6-8) from PIV results (cf. Annex 3), it is found that some components are not significant, thus can be ignored in our analysis process. Only the important components are kept and rearranged as follows:

$$\frac{\partial P}{\partial x} + \rho U_x \frac{\partial U_x}{\partial x} = -\rho U_y \frac{\partial U_x}{\partial y} - \rho \frac{\partial < u'u' >}{\partial x} - \rho \frac{\partial < u'v' >}{\partial y} \qquad (6\text{-}10)$$

$$\frac{\partial}{\partial x}(P + \frac{1}{2}\rho U_x^{\,2}) = -\rho U_y \frac{\partial U_x}{\partial y} - \rho \frac{\partial < u'u' >}{\partial x} - \rho \frac{\partial < u'v' >}{\partial y} \qquad (6\text{-}11)$$

The static pressure plus the dynamic pressure in x direction $P + \frac{1}{2}\rho U_x^{\,2}$ is a stagnation pressure which describes the force or energy the fluid contains. Thus, the left term of Eq.(6-11) which is the gradient of this stagnation pressure can be approximately treated as the force loss or force gain denoted by Φ along the streamwise direction. Since the term related $< u'u' >$

is small (cf. Figure A3- 1), Φ is mainly controlled by the two other terms: $\psi_1 = -U_y \frac{\partial U_x}{\partial y}$ and $\psi_2 = \frac{\partial <u'v'>}{\partial y}$.

$$\Phi \sim \psi = \psi_1 - \psi_2 = -U_y \frac{\partial U_x}{\partial y} - \frac{\partial <u'v'>}{\partial y} \tag{6-12}$$

The contours of ψ_1, ψ_2, and ψ_2 in both baseline case and controlled case are presented in Figure 6-21, Figure 6-22 and Figure 6-23 respectively. Within the shear layer immediately after the separation point, both terms are positive and of the same order (cf. Figure 6-21a, and Figure 6-22a). ψ_1 represents the force gain which is related to the mean flow while ψ_2 represents the force loss along the flow which is related to the turbulence terms. In the baseline case, ψ_1 is dominant compared to ψ_2 in the shear layer(cf. Figure 6-23a), but not sufficiently to avoid the separation.

In order to overcome the separation, more forces are needed in the shear layer region. From Eq.(6-12), either increasing term ψ_1 or decreasing ψ_2 is possible to increase ψ. However, direct modification of term ψ_1 would be very costly since it is related to the main flow compared to modifying the turbulence related term ψ_2. Decreasing ψ_2 seems also difficult since the turbulence level is hard to reduce directly. However, with the actuation of fluidic oscillator array, ψ_2 can be increased easily as shown in Figure 6-22b, which means the force loss is increased because of the oscillator actuation. At the same time, as can be observed in Figure 6-21b, ψ_1 which represents the force gain is also increased. The increase in force gain from ψ_1 is however much larger than the increase in force loss from ψ_2, which is evidenced by the significant increase of ψ in the shear layer and ramp region in Figure 6-23b.

It can also observed that the topology of the ψ contours in the controlled case (cf. Figure 6-23b) is very similar to the contours of $\partial P / \partial x$ in the ramp region (cf. Figure 6-20b). In particular, the high levels of ψ in this zone explain why the flow is not separated despite the large positive values of $\partial P / \partial x$.

Thus, from the above analysis, the controlling mechanism seems to be that the actuator affect the turbulence terms, i.e. <*u'v'*>, then the turbulence terms affect the mean flow term, $-U_y \frac{\partial U_x}{\partial y}$, and this mean flow term transfers more forces from the free flow to the shear layer, which helps the flow to overcome the pressure gradient and to reattach to the wall.

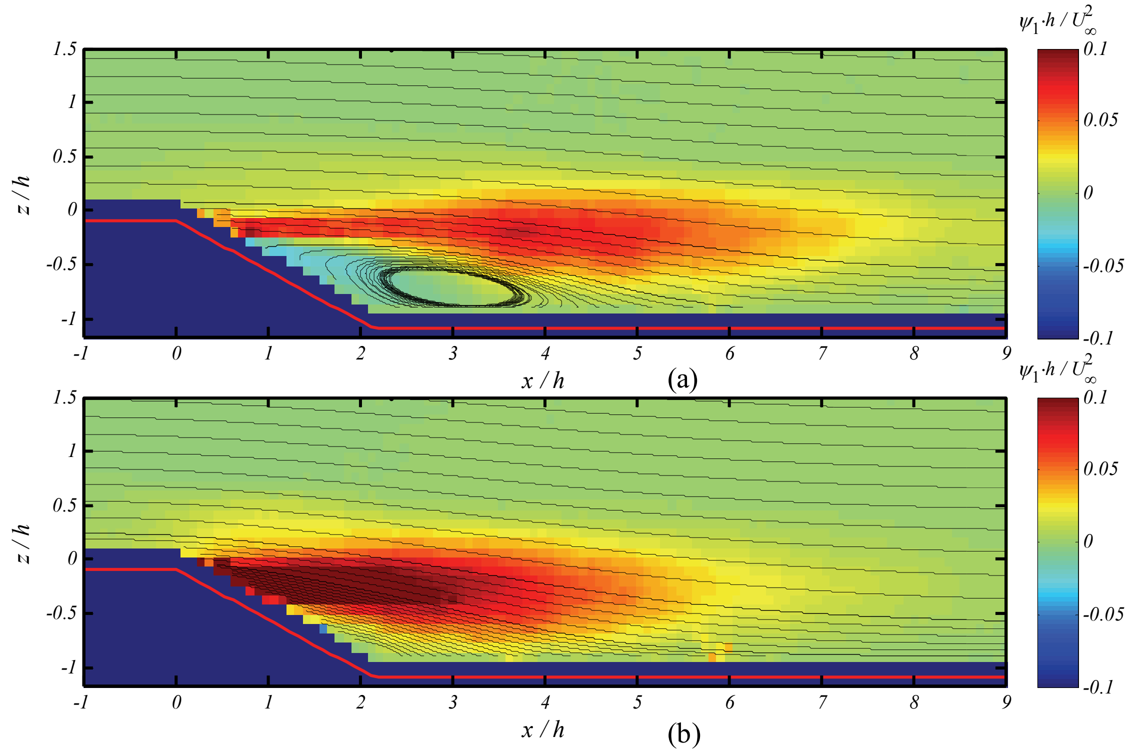

Figure 6-21. Contours of $\psi_1 = -U_y \dfrac{\partial U_x}{\partial y}$, a) baseline flow; b) controlled flow, $C_\mu = 0.16\%$

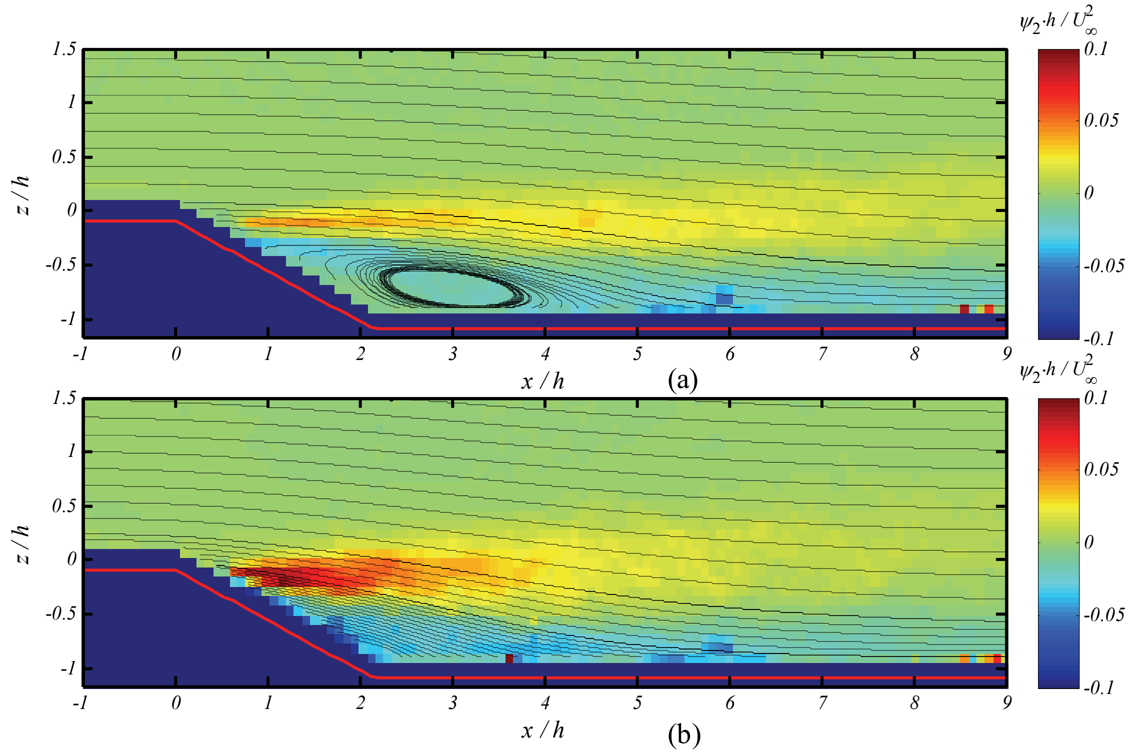

Figure 6-22. Contours of $\psi_2 = \dfrac{\partial < u'v' >}{\partial y}$, a) baseline flow; b) controlled flow, $C_\mu = 0.16\%$

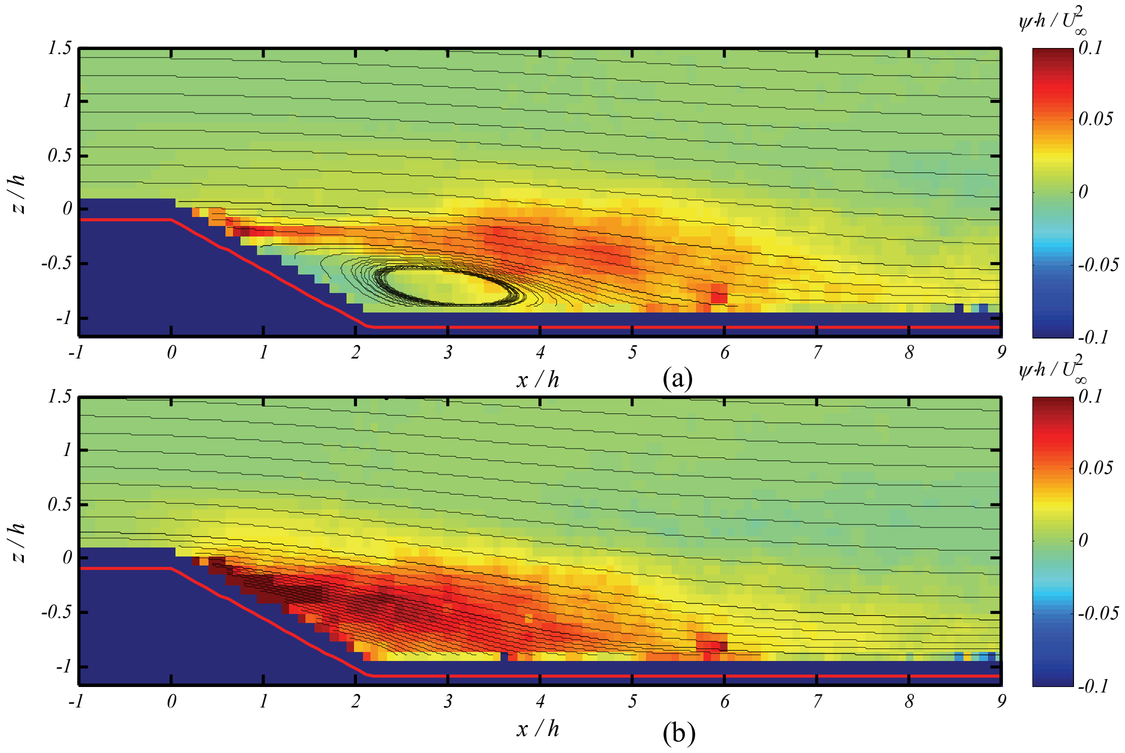

Figure 6-23. Contours of $\psi = \psi_1 - \psi_2$, a) baseline flow; b) controlled flow, $C_\mu = 0.16\%$

6.4.4 Turbulent Kinetic Energy and turbulence production analysis

The Turbulent Kinetic Energy (TKE or k) can be calculated as:

$$k = \frac{1}{2} < u_i ' u_i ' > \tag{6-13}$$

The governing equation of k is:

$$\frac{\partial k}{\partial t} + U_i \frac{\partial k}{\partial x_i} = D_{if} + \mathbf{P} - \varepsilon \tag{6-14}$$

Where

$$D_{if} = -\frac{\partial}{\partial x_i}\left(\frac{1}{2} < u_i ' u_j ' u_j ' > + \frac{1}{\rho} < u_i ' p ' > - 2\nu < u_j s_{ij} >\right) \tag{6-15}$$

$$\mathbf{P} = - < u_i ' u_j ' > \frac{\partial U_i}{\partial x_j} \tag{6-16}$$

$$\varepsilon = 2\nu < s_{ij} s_{ij} > \tag{6-17}$$

$$s_{ij} = \frac{1}{2}\left(\frac{\partial u_i '}{\partial x_j} + \frac{\partial u_j '}{\partial x_i}\right) \tag{6-18}$$

D_{if} is the diffusion term. $\mathbf{P}$ is the production of TKE, or simply the production and this term can increase the TKE of the flow. ε is the dissipation rate of TKE. From the obtained PIV results, the TKE field and production field of the mean flow can be calculated directly as:

$$k = \frac{1}{2} < u_i ' u_i ' > = \frac{1}{2} (< u' u' > + < v' v' >) \tag{6-19}$$

$$\mathbf{P} = - < u' u' > \frac{\partial U_x}{\partial x} - < v' v' > \frac{\partial U_y}{\partial y} - < u' v' > (\frac{\partial U_x}{\partial y} + \frac{\partial U_y}{\partial x}) \tag{6-20}$$

The contours of TKE and production in both baseline case and controlled case are presented in Figure 6-24 and Figure 6-25 respectively. In the baseline case, the value of TKE (cf. Figure 6-24a) progressively increases from $k/U_\infty^{\ 2} = 0.016$ at the separation point ($x/h \approx 0$) up to a maximal value $k/U_\infty^{\ 2} = 0.024$ just beyond the separation bubble in the shear layer ($x/h \approx 4$). In the controlled case however, the topology of TKE contours is totally changed (cf. Figure 6-24b): the maximal value $k/U_\infty^{\ 2} = 0.05$ is much higher and is found just downstream from the actuation location ($x/h \approx 0.5$) and the high TKE area is much larger in the ramp region. From Figure 6-25, it can be observed that the production of TKE is also largely increased immediately after the actuation location.

Thus, the fluidic oscillator array amplifies the production of turbulence evidenced both by the TKE contours and production contours, just next to the actuation location. One consequence of this is that $<u'v'>$ is increased as shown in Figure 6-26. Following the textbook of Pope[89], for a plane mixing layer which is very similar to present ramp flow, the spreading rate $d\theta_{SL}/dx$ is closely connected to the Reynolds shear stress (Eq.5-209, Eq.5-216, Eq.5-228 in Pope[89]). This means that the increase of Reynolds shear stress $<u'v'>$ would result into a faster growth of the separated shear layer. Accordingly, the recirculation length Lr decreases which is exactly what have been observed in this study.

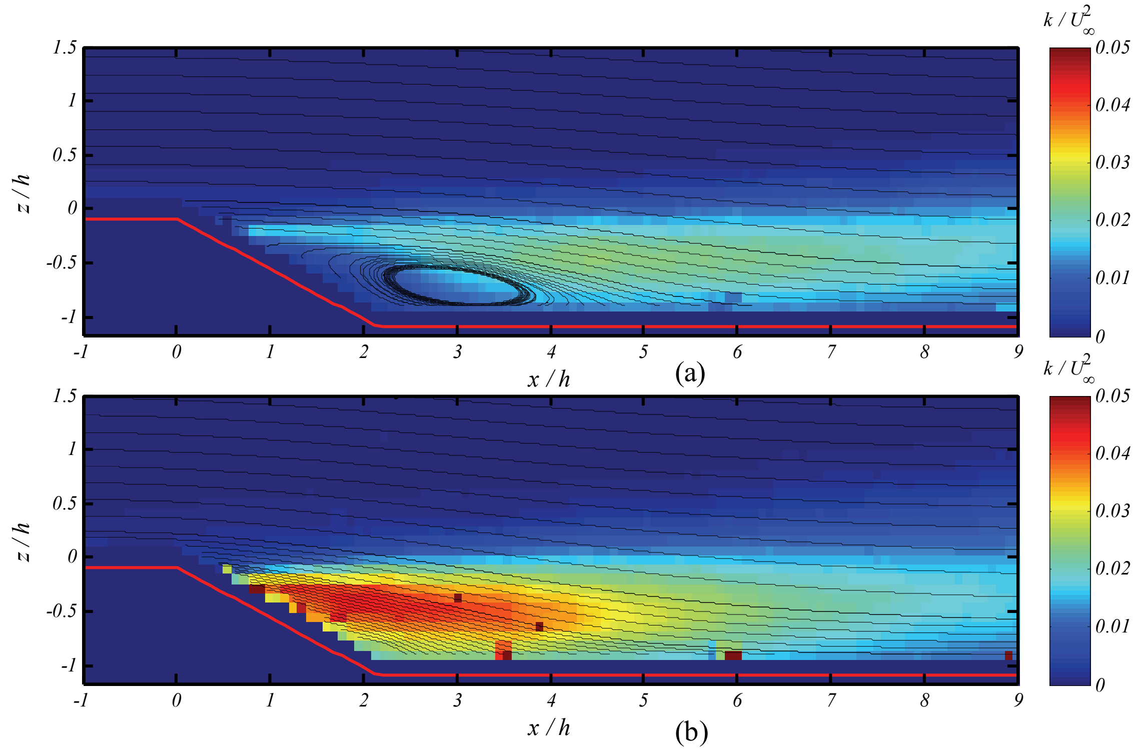

Figure 6-24. Contours of mean flow TKE, a) baseline flow; b) controlled flow, $C_\mu = 0.16\%$

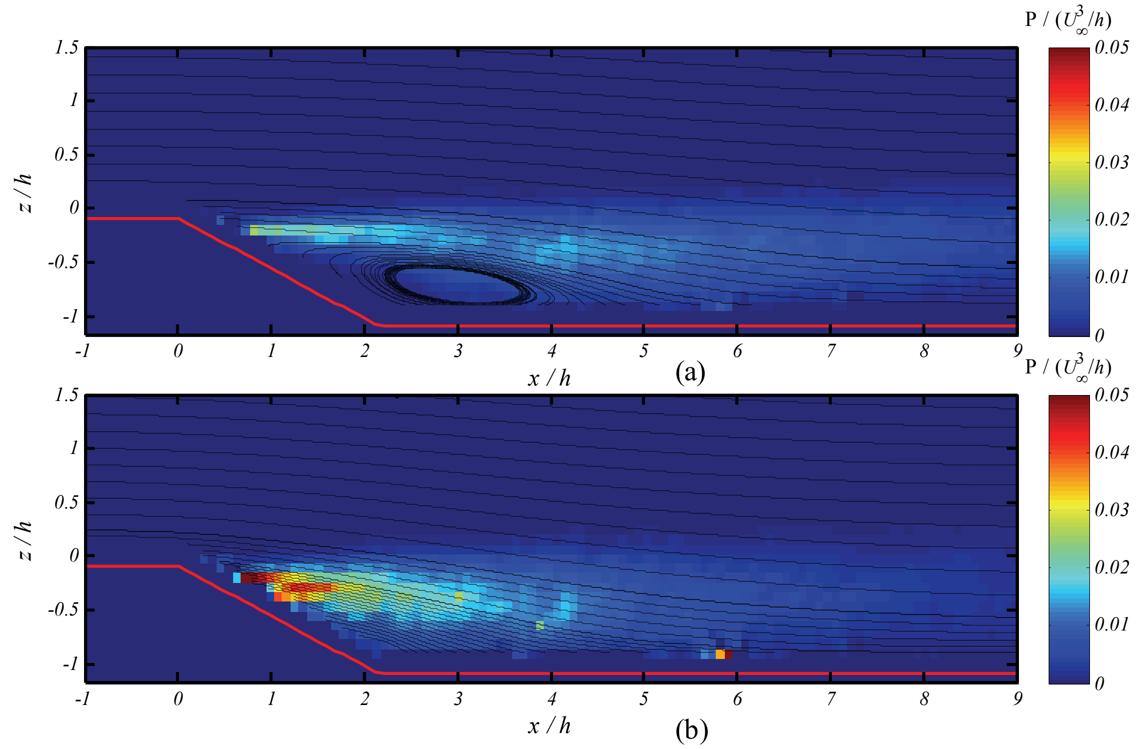

Figure 6-25. Contours of mean flow production of TKE, a) baseline flow; b) controlled flow, $C_\mu = 0.16\%$

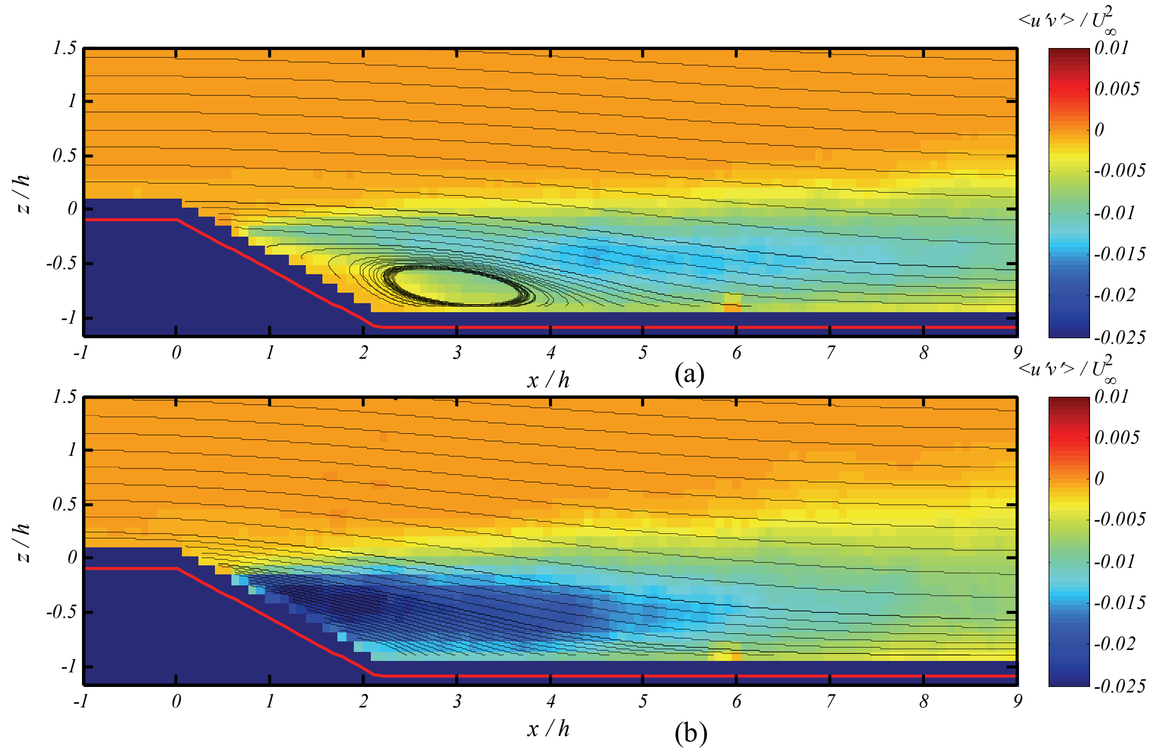

Figure 6-26. Contours of mean flow Reynolds stress component <*u'v'*>, a) baseline flow; b) controlled flow, C_μ = 0.16%

6.5 Conclusions

An array of 12 identical miniature fluidic oscillators has been designed and tested on a ramp separated flow. The chosen synchronization method of the fluidic oscillators array has been tested and proved to be successful. The efficiency of this array of fluidic oscillator to delay separation has been examined thanks to PIV measurements conducted on a ramp flow in a wind tunnel. The obtained results show that this fluidic oscillator array is very promising considering the low momentum coefficient C_μ needed to totally eliminate the separation. The detailed analysis of the underlying controlling mechanisms shows that the fluidic oscillator actuation increases the turbulence which increases the forces loss in the ramp region. However, in the same time, the modification of the turbulence terms leads to a modification of the mean flow terms due to the correlations between turbulence and mean flow. As a result, despite the increase in force loss due to the increase of turbulence terms provoked by the actuation, more force is transferred from the main flow to the shear layer. This mechanism helps the flow to overcome the pressure gradient and to reattach to the wall.

Nevertheless, despite the encouraging results which have been obtained, additional measurements and refined analysis should be performed to confirm the proposed mechanisms.

It would also be interesting to find out the most sensitive scale to the actuation and the threshold of C_μ needed to eliminate the recirculation bubble in a broad Re range.

Chapter 7. Conclusions and Perspectives

Conclusions

The main objective of the present work was to study in detail the working dynamics of a pulsing jet relaxation fluidic oscillator in order to propose guiding rules for its design and to develop an array of synchronized actuators in order to test their ability to delay the flow separation on a ramp.

After a brief introduction about various flow control strategies and typical fluidic actuators, the bibliographical study has been focused on the various kinds of fluidic oscillators, highlighting the interest to use pulsing jet relaxation fluidic oscillators for flow control applications and the lack of knowledge on the physical mechanisms governing their behavior. The core of this thesis work has then been presented in four main parts, concerning the experimental analysis of the performances of 4 oscillator prototypes, the numerical simulation of the unsteady flows in these oscillators to identify the main physical mechanisms controlling their working dynamics, the development of synchronization methods for an array of oscillators and the application of this array of fluidic actuators to the control of a ramp separated flow. The major conclusions are as follows:

- New designed prototypes have been experimentally characterized both by hot wire and transient pressure sensors. It has been confirmed that the average velocity of the generated pulsed jets is controlled by the oscillator’s throat section and the inlet pressure. However, the amplitude of the outlet velocity and its evolution with time can also be affected by the throat section and/or other internal geometrical factors such as the internal symmetry of the device. In addition, both the feedback loop length and diameter play important roles on the oscillator’s performances, in particular its frequency response. A relation, deducted from the acquired experimental data, has been proposed to estimate the oscillation frequency as a function of the feedback loops length.
- Numerical models developed in OpenFOAM have shown to offer a quite precise estimation of the operating frequency. A detailed analysis of the simulation results has shown that in a pulsing jet relaxation fluidic oscillator, the main jet deflection is provoked not only by the pressure difference between the oscillator's control ports, but also by the pressure difference between its branches. In the studied configurations, the

threshold value of the pressure difference between the control ports needed to provoke by itself the jet deflection is much higher than the pressure difference needed between the branches. However, when combining these two effects, the jet deflection becomes much easier.

- The switching mechanism has been shown to be linked to the back and forth propagation of pressure waves in the oscillator's branches and feedback loops: just after the jet switching, a High Pressure Compression Wave propagates in the branch where the jet is attached and in the corresponding feedback loop while a Low Pressure Expansion Wave propagates in the other branch and feedback loop. When these waves arrive at the control ports they reflect and the jet is destabilized by the inversion of the pressure difference at its base. The switching occurs when the pressure waves have reached back the branches provoking the inversion of the pressure difference between branches. As the pressure waves propagate roughly at the sound velocity C_o, the oscillation period T can be approximately linked to the feedback loop length L_f by the newly proposed relation $T = 4L_f / C_o$, which confirms the empirical relation deducted from the experimental results. A more precise relation has also been proposed to calculate the oscillation frequency, taking into account the flow velocity in the oscillator. These numerical simulations have also permitted to explain the non-dependence of the oscillation frequency to the supply pressure.
- Two new methods, based on interconnections between the feedback loops, have been proposed to synchronize two similar oscillators. These two methods have been validated experimentally and numerically. The first one leads to a frequency close to the one of the oscillators working separately and the pulsed jets generated by these two devices are nearly in phase opposition. The second method leads to a much lower frequency and a phase difference close to $0.25T$. The numerical simulations have also permit to explain the dynamic behavior of the synchronized oscillators and to prove the feasibility of the synchronization of an array of 4 fluidic oscillators, using the first interconnection method.
- In the last part of this work, 12 identical fluidic oscillators have been integrated in a ramp to test their efficiency to control the flow separation. The chosen method to synchronize this fluidic oscillators array has been tested experimentally and proved to be successful. The mean and fluctuating flow fields over the ramp, with and without actuation of this array of fluidic oscillators, have been acquired by PIV in a wind

tunnel. The obtained results show that this fluidic oscillator array is very promising, considering the low momentum coefficient C_μ, compared to the optimal values found in the literature, needed to totally eliminate the separation. An analysis of the turbulence flow fields has shown that the underlying controlling mechanisms were linked to an increase of the turbulence in the ramp region due to the pulsed jets generated by the oscillators, leading to a net increase, compared to the case without actuation, of the force transferred from the main flow to the shear layer.

Perspectives

Though numerous encouraging results have been obtained, some interesting points need to be further explored, to finally allow the design and development of optimized actuators which could be implemented on real systems (e.g. airfoil or car after-body):

- The validity of the simple relation proposed to estimate the oscillator's operating frequency is limited to configurations in which the feedback loops diameter/width is not too small. Additional numerical simulations would be necessary to analyze the role played by this parameter and other geometrical dimensions, such as the throat width, on the device performances.
- The amplitude and form of the pulsed jets generated by the oscillator seems to be very sensitive to its internal geometry. Numerical models should thus be improved to be able to give exploitable data on the link between the pulsed jets characteristics and the oscillator's internal geometry. Visualization of the oscillator's internal flow, e.g. by PIV or molecular tagging techniques, could also be a useful experimental tool for the validation of the numerical models.
- The synchronization methods should be further explored, in particular to find ways to control the phase lag between oscillators working in an array, as this parameter could have a strong effect on the flow control efficiency.
- Additional measurements (e.g. PIV mean and phase-averaged flow fields in various cross planes of the ramp) and refined analysis should be performed to confirm the proposed mechanisms governing the flow separation control by an array of fluidic oscillators. It would also be interesting to find out the most sensitive scale to the actuation and the threshold of $C\mu$ needed to eliminate the recirculation bubble in a broad Re range. Additional experimental analyses should also be conducted in different configurations (various $F+$, with and without synchronization, different

phase lags between actuators…), in particular to identify the role of the actuation frequency and of the synchronization on the control efficiency.

References

[1] Aubrun, S., McNally, J., Alvi, F., and Kourta, A. "Separation flow control on a generic ground vehicle using steady microjet arrays", *Experiments in Fluids* Vol. 51, No. 5, 2011, pp. 1177-1187.

[2] Melton, L., Hannon, J., Yao, C.-S., and Harris, J. "Active flow control at low Reynolds numbers on a NACA 0015 airfoil", *26th Applied Aerodynamics Conference. Number AIAA*. Vol. 6407, 2008, p. 2008.

[3] Lin, C.-Y., and Hsiao, F.-B. "Experimental Study of Flow Separation over NACA63 3 018 Wing with Synthetic Jet Control at Low Reynolds Numbers", *Journal of Mechanics* Vol. 29, No. 01, 2013, pp. 45-52.

[4] Fanping, S., Ray-Sing, L., Martin, H., and Tory, B. "Air Flow Control by Fluidic Diverter for Low NOx Jet Engine Combustion", *1st Flow Control Conference*, 2002.

[5] Guyot, D., Bobusch, B., Paschereit, C. O., and Raghu, S. "Active Combustion Control Using a Fluidic Oscillator for Asymmetric Fuel Flow Modulation", *44th AIAA/ASME/SAE/ASEE Joint Propulsion Conference & Exhibit*, 2008.

[6] Greenblatt, D., and Wygnanski, I. J. "The control of flow separation by periodic excitation", *Progress in Aerospace Sciences* Vol. 36, No. 7, 2000, pp. 487-545.

[7] Cattafesta III, L. N., and Sheplak, M. "Actuators for active flow control", *Annual Review of Fluid Mechanics* Vol. 43, 2011, pp. 247-272.

[8] Cerretelli, C., and Gharaibah, E. "An Experimental and Numerical Investigation on Fluidic Oscillators For Flow Control", *37th AIAA Fluid Dynamics Conference and Exhibit*, 2007.

[9] Gregory, J. W., Sullivan, J. P., Raman, G., and Raghu, S. "Characterization of the Microfluidic Oscillator", *AIAA Journal* Vol. 45, No. 3, 2007, pp. 568-576.

[10] Bobusch, B. C., Woszidlo, R., Bergada, J. M., Nayeri, C. N., and Paschereit, C. O. "Experimental study of the internal flow structures inside a fluidic oscillator", *Experiments in Fluids* Vol. 54, No. 6, 2013, pp. 1-12.

[11] BATIKH, A. "Contrôle de l'aérodynamique externe des véhicules aériens par des dispositifs microfluidiques: Etude de l'effet de mini et micro-jets synthétiques sur des écoulements pariétaux", Ph.D Thesis, Génie Mécanique, Université de Toulouse, 2008

[12] Ghozlani, W. "Etude expérimentale et numérique des actionneurs microfluidiques pour le contrôle actif des écoulements", Ph.D Thesis, Génie Mécanique, Université de Toulouse, 2011

[13] Comolet, R. *Mécanique des fluides expérimentale,*, 1994.

[14] Kourta, A., and Leclerc, C. "Characterization of synthetic jet actuation with application to Ahmed body wake", *Sensors and Actuators A: Physical* Vol. 192, No. 0, 2013, pp. 13-26.

[15] "Vortex Generator", http://en.wikipedia.org/wiki/Vortex_generator.

[16] Aider, J.-L., Beaudoin, J.-F., and Wesfreid, J. E. "Drag and lift reduction of a 3D bluff-body using active vortex generators", *Experiments in Fluids* Vol. 48, No. 5, 2010, pp. 771-789.

[17] Breuer, K. S. "Design, Fabrication and Performance of MEMS Actuators for Flow Control". Flow and MEMS, Von Karman Institute lecture series, 2002.

[18] Wang, L., Luo, Z., Xia, Z., Liu, B., and Deng, X. "Review of actuators for high speed active flow control", *Science China Technological Sciences* Vol. 55, No. 8, 2012, pp. 2225-2240.

[19] Morris, N. M. *An introduction to fluid logic*: McGraw-Hill, 1973.

[20] Foster, K., and Parker, G. A. *Fluidics: Components and Circuites*: John Wiley & Sons 1970.

[21] Kirshner, J. M., and Katz, S. *Design theory of fluidic components*: Academic Press, 1975.

[22] Kirshner, J. M. *Fluid amplifiers*: McGraw-Hill, 1966.

[23] Raber, R. A., and Shinn, J. N. "Fluid Amplifier State of the Art:Vol. I: Research and development, fluid amplifiers and logic". Vol. Contractor Report CR-101, NASA, 1964.

[24] Raber, R. A., and Shinn, J. N. "Fluid Amplifier State of the Art: Vol II: Bibliography". Vol. Contractor Report CR-102, NASA, 1964.

[25] Tippetts, J. R., Ng, H. K., and Royle, J. K. "A fluidic flowmeter", *Automatica* Vol. 9, No. 1, 1973, pp. 35-45.

[26] Beale, R. B., and Lawler, M. T. "Development of a wall-attachment fluidic oscillator applied to volume flow metering", *Flow: Its measurement and control in science and industry*. Vol. 1, Pittsburgh, Pa.,USA, 1974.

[27] Yang, J.-T., Chen, C.-K., Tsai, K.-J., Lin, W.-Z., and Sheen, H.-J. "A novel fluidic oscillator incorporating step-shaped attachment walls", *Sensors and Actuators A: Physical* Vol. 135, No. 2, 2007, pp. 476-483.

[28] Meng, X., Xu, C., and Yu, H. "Feedback fluidic flowmeters with curved attachment walls", *Flow Measurement and Instrumentation* Vol. 30, No. 0, 2013, pp. 154-159.

[29] Gregory, J., and Tomac, M. N. "A Review of Fluidic Oscillator Development", *43rd Fluid Dynamics Conference*, 2013.

[30] Raghu, S. "Fluidic oscillators for flow control", *Experiments in Fluids* Vol. 54, No. 2, 2013, pp. 1-11.

[31] Tesař, V., Hung, C.-H., and Zimmerman, W. B. "No-moving-part hybrid-synthetic jet actuator", *Sensors and Actuators A: Physical* Vol. 125, No. 2, 2006, pp. 159-169.

[32] Warren, R. W. "Negative feedback oscillator", United States of America Patent, US3158166, 1964.

[33] Campagnuolo, C. J., and Lee, H. C. "Review of Some Fluid Oscillators". United States Harry Diamond Laboratories, 1969.

[34] Tomac, M., N. , and Gregory, J. "Frequency Studies and Scaling Effects of Jet Interaction in a Feedback-Free Fluidic Oscillator", *50th AIAA Aerospace Sciences Meeting including the New Horizons Forum and Aerospace Exposition*, 2012.

[35] Schmidt, H. J., Woszidlo, R., Nayeri, C. N., and Paschereit, C. O. "Drag reduction on a rectangular bluff body with base flaps and fluidic oscillators", *Experiments in Fluids* Vol. 56, No. 7, 2015, pp. 1-16.

[36] Giles, B. D. "Fluidics, the Coanda Effect, and some orographic winds", *Archiv für Meteorologie, Geophysik und Bioklimatologie, Serie A* Vol. 25, No. 3, 1977, pp. 273-279.

[37] Warren, R. W. "Fluid oscillator", United States of America Patent, US3016066, 1962.

[38] Spyropoulos, C. E. "A Sonic Oscillator", *Proceedings of the Fluid Amplification Symoosium*. Vol. Vol. III, Harry Diamond Laboratories, Washington, D.C., 1964.

[39] Viets, H. "Flip-Flop Jet Nozzle", *AIAA Journal* Vol. 13, No. 10, 1975, pp. 1375-1379.

[40] HAYASHI, S., and KAMAYA, S. "A Study on Mechanism of Oscillation in Sonic Oscillators : 2nd Report, Mathematical Model of Oscillators Operated by Air", *Bulletin of JSME* Vol. 18, 1975.

[41] Raman, G., Rice, E. J., and Cornelius, D. M. "Evaluation of Flip-Flop Jet Nozzles for Use as Practical Excitation Devices", *Journal of Fluids Engineering* Vol. 116, No. 3, 1994, pp. 508-515.

[42] Arwatz, G., Fono, I., and Seifert, A. "Suction and Oscillatory Blowing Actuator Modeling and Validation", *AIAA Journal* Vol. 46, No. 5, 2008, pp. 1107-1117.

[43] Stouffer, R. D. "Oscillating spray device", US Patent, US 4151955, 1979.

[44] Raman, G., and Raghu, S. "Cavity Resonance Suppression Using Miniature Fluidic Oscillators", *AIAA Journal* Vol. 42, No. 12, 2004, pp. 2608-2612.

[45] Seele, R., Tewes, P., Woszidlo, R., McVeigh, M. A., Lucas, N. J., and Wygnanski, I. J. "Discrete Sweeping Jets as Tools for Improving the Performance of the V-22", *Journal of Aircraft* Vol. 46, No. 6, 2009, pp. 2098-2106.

[46] Woszidlo, R., Nawroth, H., Raghu, S., and Wygnanski, I. J. "Parametric Study of Sweeping Jet Actuators for Separation Control", *5th Flow Control Conference*, 2010.

[47] Phillips, E., and Wygnanski, I. "Use of Sweeping Jets During Transient Deployment of a Control Surface", *AIAA Journal* Vol. 51, No. 4, 2013, pp. 819-828.

[48] Seele, R., Graff, E., Lin, J., and Wygnanski, I. "Performance Enhancement of a Vertical Tail Model with Sweeping Jet Actuators", *51st AIAA Aerospace Sciences Meeting including the New Horizons Forum and Aerospace Exposition*, 2013.

[49] Lin, J. C., Andino, M. Y., Alexander, M. G., Whalen, E. A., Spoor, M. A., Tran, J. T., and Wygnanski, I. J. "An Overview of Active Flow Control Enhanced Vertical Tail Technology Development", *54th AIAA Aerospace Sciences Meeting*, 2016.

[50] Schmidt, H.-J., Woszidlo, R., Nayeri, C., and Paschereit, C., O. . "Experimental Investigation of the Flow Field behind a Bluff Body Equipped with Fluidic Oscillators", *53rd AIAA Aerospace Sciences Meeting*, 2015.

[51] Woszidlo, R., Stumper, T., Nayeri, C., and Paschereit, C., O. . "Experimental Study on Bluff Body Drag Reduction with Fluidic Oscillators", *52nd Aerospace Sciences Meeting*, 2014.

[52] Bobusch, B., C. , Woszidlo, R., Krüger, O., and Paschereit, C., O. . "Numerical Investigations on Geometric Parameters Affecting the Oscillation Properties of a Fluidic Oscillator", *21st AIAA Computational Fluid Dynamics Conference*, 2013.

[53] Krüger, O., Bobusch, B., C., Woszidlo, R., and Paschereit, C., O. . "Numerical Modeling and Validation of the Flow in a Fluidic Oscillator", *21st AIAA Computational Fluid Dynamics Conference*, 2013.

[54] Woszidlo, R., Ostermann, F., Nayeri, C. N., and Paschereit, C. O. "The time-resolved natural flow field of a fluidic oscillator", *Experiments in Fluids* Vol. 56, No. 6, 2015, pp. 1-12.

[55] Gartlein, S., Woszidlo, R., Ostermann, F., Nayeri, C., and Paschereit, C., O. . "The Time-Resolved Internal and External Flow Field Properties of a Fluidic Oscillator", *52nd Aerospace Sciences Meeting*, 2014.

[56] Ostermann, F., Woszidlo, R., Nayeri, C., and Paschereit, C., O. . "Experimental Comparison between the Flow Field of Two Common Fluidic Oscillator Designs", *53rd AIAA Aerospace Sciences Meeting*, 2015.

[57] Gosen, F. v., Ostermann, F., Woszidlo, R., Nayeri, C., and Paschereit, C., O. . "Experimental Investigation of Compressibility Effects in a Fluidic Oscillator", *53rd AIAA Aerospace Sciences Meeting*, 2015.

[58] Khelfaoui, R., Colin, S., Orieux, S., Caen, R., and Baldas, L. "Numerical and Experimental Analysis of Monostable Mini- and Micro-Oscillators", *Heat Transfer Engineering* Vol. 30, No. 1-2, 2009, pp. 121-129.

[59] Simões, E. W., Furlan, R., Bruzetti Leminski, R. E., Gongora-Rubio, M. R., Pereira, M. T., Morimoto, N. I., and Santiago Avilés, J. J. "Microfluidic oscillator for gas flow control and measurement", *Flow Measurement and Instrumentation* Vol. 16, No. 1, 2005, pp. 7-12.

[60] Cerretelli, C., Gharaibah, E., Toplack, G., Gupta, A., and Wuerz, W. "Unsteady Separation Control for Wind Turbine Applications at Full Scale Reynolds Number",

47th AIAA Aerospace Sciences Meeting including The New Horizons Forum and Aerospace Exposition, 2009.

[61] Luedke, J., Graziosi, P., Kirtley, K., and Cerretelli, C. "Characterization of Steady Blowing for Flow Control in a Hump Diffuser", *AIAA Journal* Vol. 43, No. 8, 2005, pp. 1644-1652.

[62] Cerretelli, C., Wuerz, W., and Gharaibah, E. "Unsteady Separation Control on Wind Turbine Blades using Fluidic Oscillators", *AIAA Journal* Vol. 48, No. 7, 2010, pp. 1302-1311.

[63] Choephel, T., Coder, J., and Maughmer, M. D. "Airfoil Boundary-Layer Flow Control Using Fluidic Oscillators", *30th AIAA Applied Aerodynamics Conference*, 2012.

[64] Tesař, V., and Peszynski, K. "Strangely behaving fluidic oscillator", *EPJ Web of Conferences,* Vol. 45, 2013.

[65] Tesař, V., Zhong, S., and Rasheed, F. "New Fluidic-Oscillator Concept for Flow-Separation Control", *AIAA Journal* Vol. 51, No. 2, 2013, pp. 397-405.

[66] Seifert, A., Bachar, T., Koss, D., Shepshelovich, M., and Wygnanski, I. "Oscillatory Blowing: A Tool to Delay Boundary-Layer Separation", *AIAA Journal* Vol. 31, No. 11, 1993, pp. 2052-2060.

[67] Nishri, B., and Wygnanski, I. "Effects of Periodic Excitation on Turbulent Flow Separation from a Flap", *AIAA Journal* Vol. 36, No. 4, 1998, pp. 547-556.

[68] Wygnanski, I., and Seifert, A. "The control of separation by periodic oscillations", *25th Plasmadynamics and Lasers Conference*, 1994.

[69] Cerretelli, C., and Kirtley, K. "Boundary Layer Separation Control With Fluidic Oscillators", *Journal of Turbomachinery* Vol. 131, No. 4, 2009, pp. 041001-041001.

[70] Seifert, A., and Pack, L. G. "Active Flow Separation Control on Wall-Mounted Hump at High Reynolds Numbers", *AIAA Journal* Vol. 40, No. 7, 2002, pp. 1363-1372.

[71] Greenblatt, D., Paschal, K. B., Yao, C. S., Harris, J., Schaeffler, N. W., and Washburn, A. E. "Experimental Investigation of Separation Control Part 1: Baseline and Steady Suction", *AIAA Journal* Vol. 44, No. 12, 2006, pp. 2820-2830.

[72] Greenblatt, D., Paschal, K. B., Chung-Sheng, Y., and Harris, J. "Experimental Investigation of Separation Control Part 2: Zero Mass-Flux Oscillatory Blowing", *AIAA Journal* Vol. 44, No. 12, 2006, pp. 2831-2845.

[73] Zhang, S., and Zhong, S. "Turbulent Flow Separation Control over a Two-Dimensional Ramp Using Synthetic Jets", *AIAA Journal* Vol. 49, No. 12, 2011, pp. 2637-2649.

[74] Joseph, P., Bortolus, D., and Grasso, F. "Flow control on a 3D backward facing ramp by pulsed jets", *Comptes Rendus Mécanique* Vol. 342, No. 6–7, 2014, pp. 376-381.

[75] Kumar, V., and Alvi, F. "Efficient Control of Separation Using Microjets", *35th AIAA Fluid Dynamics Conference and Exhibit*, 2005.

[76] Kourta, A., Thacker, A., and Joussot, R. "Analysis and characterization of ramp flow separation", *Experiments in fluids* Vol. 56, 2015, p. 104.

[77] Debien, A., Aubrun, S., Mazellier, N., and Kourta, A. "Active Separation Control Process Over A Sharp Edge Ramp ", *9th International Symposium On Turbulence and Shear Flow Phenomena (TSFP - 9),* Melbourne, Autralia, 2015.

[78] "OpenFOAM Official Site", http://www.openfoam.com/.

[79] *OpenFOAM User Guide-Version 2.3.0*, 2014.

[80] Moukalled, F., Mangani, L., and M., D. *The Finite Volume Method in Computational Fluid Dynamics-An Advanced Introduction with OpenFOAM and Matlab*: Springer International Publishing, 2015.

[81] *OpenFOAM Programmer's Guide-Version 2.3.0*, 2014.

[82] Holzinger, G. "OpenFOAM-A little User-Manual". Johannes Kepler University, Linz, Austria, 2015.

[83] Cerretelli, C., and Kirtley, K. R. "Method and system for flow control with fluidic oscillators", United States Patent, US 7128082B1, 2006.

[84] Koklu, M. "Fluidic oscillator array for synchronized oscillating jet generation", United States Patent, US9333517B2, 2016.

[85] King, L. V. "On the Convection of Heat from Small Cylinders in a Stream of Fluid: Determination of the Convection Constants of Small Platinum Wires, with Applications to Hot-Wire Anemometry", *Proceedings of the Royal Society of London. Series A* Vol. 90, No. 622, 1914, pp. 563-570.

[86] Feuvrier, A. "Controle bio-inspiré d'un sillage turbulent par stratégie passive ou auto-adaptative", PhD Thesis, Mécanique des Fluides, Université d'Orléans, 2015

[87] Dandois, J., Garnier, E., and Sagaut, P. "Numerical simulation of active separation control by a synthetic jet", *Journal of Fluid Mechanics* Vol. 574, 2007, pp. 25-58.

[88] Browand, F., and Troutt, T. "The turbulent mixing layer: geometry of large vortices", *Journal of Fluid Mechanics* Vol. 158, 1985, pp. 489-509.

[89] Pope, S. B. *Turbulent Flows*: Cambridge University Press, 2000.

[90] Moukalled, F., Mangani, L., and Darwish, M. "chapter 17, Turbulence Modeling", *The Finite Volume Method in Computational Fluid Dynamics-An Advanced Introduction with OpenFOAM and Matlab*. Springer International Publishing, 2015.

Annex 1. Preliminary Study of a First Oscillator Prototype

For flow control application, the most important parameters which characterize a fluidic oscillator are its working frequency and its outlet velocity evolution pattern as discussed in chapter 1. In order to obtain these parameters, two measurement techniques are employed: the hot wire anemometry and the transient pressure transducer. The hot wire anemometer can measure the instantaneous outlet velocity and give also access to the working frequency while the pressure transducer can only measure the oscillator’s working frequency. However, for fragility reasons, the hot wire was only employed at low inlet pressure conditions, while the pressure transducer could be used in a very large range of inlet pressure.

The first prototype tested in this section was designed during the work of W. Ghozlani [12]. After re-assembling it, its frequency response under various inlet pressures are examined both by the hot wire anemometry and pressure transducer.

A1.1 First measurements by hot wire

A1.1.1 Experimental setup

The experimental setup consists in a fluidic oscillator connected to a pressurized air tank, as shown in Figure A1-1. The pressure in the air tank can be adjusted through a valve and is monitored by a pressure sensor. The pressure in this air tank is regarded as the inlet total pressure of the oscillator. The oscillator is placed vertically and fixed by screw bolts on the platform. The flow issuing from the oscillator outlets is measured with a single component hot-wire driven by an anemometer (DISA 55M01). The hot wire probe is set on linear traverse assembly allowing for 3-D displacements, with a spatial resolution of 0.01 mm in all three directions. The hot wire is just placed parallel to the outlet slot as shown in Figure A1-1b, in the center of the right outlet and at a distance of 0.72 mm from the outlet plane. The signals of the pressure sensor in the air tank and of the hot wire are recorded by computer at a sampling frequency of 10 kHz, which is large enough to resolve the oscillation frequency. Time-series lasting 100 s are acquired in order to assure statistical convergence.

The fluidic oscillator represented in Figure A1-1 was manufactured using EDM (Electrical Discharge Machining) technique. The prototype has a width of 10 mm and the two exits and the nozzle widths are 500 μm and 200 μm, respectively. The fluidic oscillator is fixed on a flat plate.

The feedback loops are made with pneumatic tubes of 3.5 mm internal diameter. Its internal channel sketches and dimensions are shown in Figure A1-4.

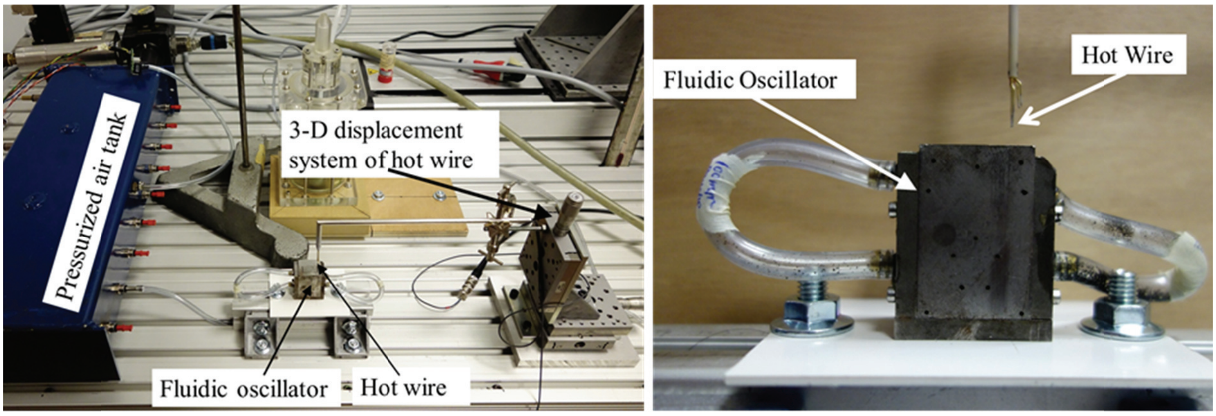

(a) (b)

Figure A1-1. a) experimental setup; b) relative positions of the fluidic oscillator and the hot wire

A1.1.2 Experimental results

Three feedback tube lengths have been tested during the experiments: 100 mm, 160 mm and 250 mm respectively. Their frequency responses are shown in Figure A1-2a. In each case, the oscillation frequency starts to increase when the inlet pressure increases, but reaches a constant and maximum value for inlet pressures higher than a critical value which is about 0.17 MPa. This variation pattern is just similar to that of a typical sonic fluidic oscillator or sweeping fluidic oscillator as demonstrated in chapter 1 (cf. Figure 1-14) that the oscillation frequency has a quasi-linear relationship with the inlet flow rate which is in line with the Mach number in the throat section. Thus, it is rational to suppose that the critical value P_{cr} leads to sonic conditions at the inlet nozzle throat section. This critical supply pressure is given by:

$$\frac{P}{P_{cr}} = \left(\frac{\gamma+1}{2}\right)^{\frac{-\gamma}{\gamma-1}} = 0.5283 \qquad \text{(A1-1)}$$

where P is the static pressure at the throat, and γ is the specific heat ratio (γ = 1.4 for air). Assuming that the atmospheric pressure just downstream the nozzle throat, this leads to a value of 1.89 bars for the critical supply pressure. In reality, due to the jet development in the oscillator branches, the static pressure just downstream from the nozzle throat is lightly lower than the atmospheric pressure which leads to a smaller value of the critical supply pressure as this can be seen on Figure A1-2a.

Moreover, this figure shows that smaller feedback loop lengths lead to larger oscillation frequency. These results are in agreement with Simoes[59], Khelfaoui[58] and Cerretelli [8], which all evidenced that the oscillation frequency has some relationship with the capacitive effect: for a given supply pressure, i.e., a given inlet mass flow rate, a longer feedback loop will need a longer time to be filled in and to reach the threshold pressure which can provoke a switching of the jet. This threshold pressure is proportional to the static pressure in the jet at the throat of the nozzle (i.e., in front of the control ports), which is itself proportional to the inlet supply pressure. This is confirmed by the proportionality between the ratio of the supply mass flow rate to the inlet supply pressure and the switching frequency clearly shown on Figure A1-2b when the sonic conditions are reached at the throat ($P_\mathrm{i} > P_{cr}$). In this case indeed, the mass flow rate is proportional to the supply pressure:

$$\dot{m} = \sqrt{\frac{\gamma}{R_g}} \left(\frac{\gamma+1}{2}\right)^{-\frac{\gamma+1}{2(\gamma-1)}} \frac{P_\mathrm{i}}{\sqrt{T_\mathrm{i}^*}} A \tag{A1-2}$$

where R_g is the gas constant ($R_g = 287\ j/K/kg$ for air).

For supply pressures lower than the critical one, the inlet mass flow rate will depend from both the supply pressure and the pressure at the throat as given by:

$$q(\lambda) = \left(\frac{\gamma+1}{2}\right)^{\frac{1}{\gamma-1}} \lambda \left(1 - \frac{\gamma-1}{\gamma+1}\lambda^2\right)^{\frac{1}{\gamma-1}} \tag{A1-3}$$

with

$$\lambda^2 = \frac{\gamma+1}{\gamma-1}\left[1 - \left(\frac{P}{P_\mathrm{i}}\right)^{\frac{\gamma-1}{\gamma}}\right] \tag{A1-4}$$

Assuming that the static pressure at the throat is the atmospheric pressure (for subsonic conditions), leads to the curve drawn on Figure A1-2b which has the same trend than the frequency curve but is not strictly proportional. However, as already mentioned, due to the development of the jet in the oscillator branches, the pressure at the throat for subsonic conditions will be slightly lower than the atmospheric pressure and cannot be calculated analytically due to the geometry complexity.

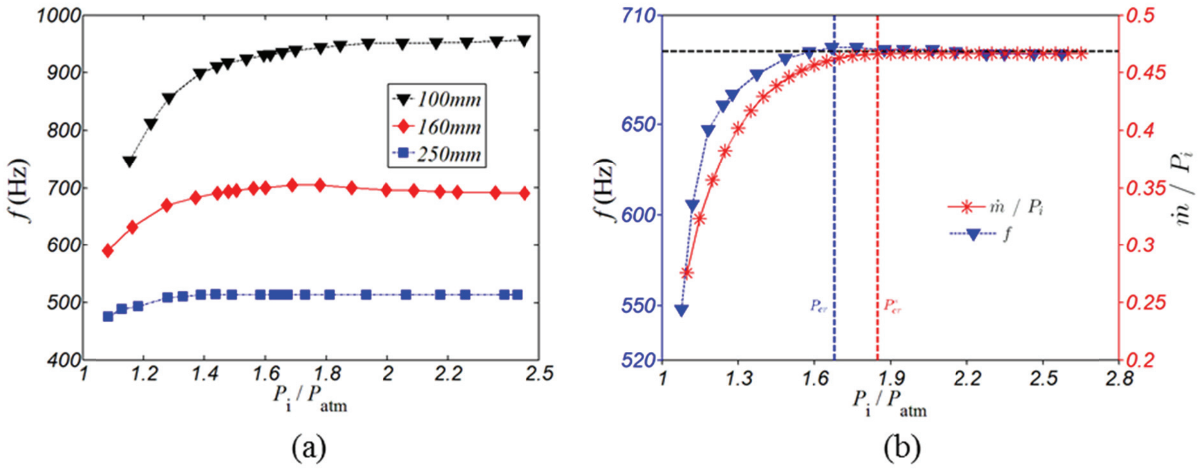

(a) (b)

Figure A1-2. a) frequency response ***vs*** inlet pressure for different feedbac tubes, L_t=100, 160, 250mm; b) variation of the oscillation frequency and the calculated value of $\dot{m} / P_i$ with inlet pressure, L_t=160 mm

During the experiments, an unexpected unstable oscillation phenomenon has been identified in case of 250 mm feedback tubes. As shown in Figure A1-3, there exists a critical inlet pressure defined as P_u. When the pressure is lower than P_u, the oscillation frequency is a unique function of the supply pressure. When the pressure is higher than P_u, however, two different oscillation frequencies may appear: the lower one (~500 Hz) which is in continuity with the frequencies related to lower supply pressures, that could be called "normal" frequency and a much higher frequency (~1500 Hz), that could be named "excited" frequency. Normally, the oscillator works in the normal mode whatever the inlet supply pressure. However, when the inlet pressure is higher than P_u, the excited mode can be activated by a perturbation on one of the outlets of the oscillator. Once activated, the oscillator will stay in the excited mode if the inlet pressure continues to increase. If the pressure is just a little bit larger than P_u, the oscillator can go back to the normal mode by introducing a perturbation at the same outlet. If the pressure is obviously larger than P_u, the oscillator is kept in its excited mode and the normal mode can only be retrieved by decreasing the supply pressure until it is lower than P_u.

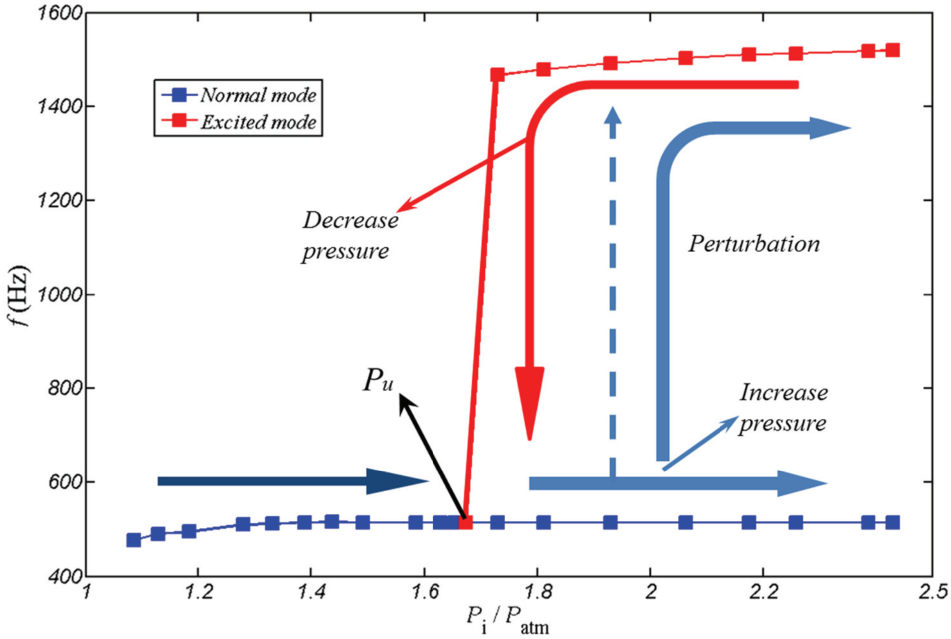

Figure A1-3. Unstable oscillation phenomenon illustration

A1.1.3 Some problems during the experiments

Assemblage:

Similar to the modified design described in chapter 2 (cf. Figure 2-4), the central part channels are formed by assembling the cover plate, air channel layer and base plate. The air channel layer is comprised of 7 pieces as shown in Figure A1-4. Each piece is located by hollow pins. The scale of the oscillator is so tiny that the assemblage quality can easily affect the internal geometry of the oscillator, especially in critical zone such as the nozzle or the splitter. From Figure A1-4 in which the various dimensions of the oscillator's central part before and after the test are shown, it is clear that almost all the dimensions have changed more or less after the assembly and disassembly: the throat width, which is the most important parameter for the oscillator's performance, is reduced by 30% (0.2 mm instead of 0.29 mm) and the width of the right outlet slot turns from 0.56 mm to 0.66 mm, i.e. 18% larger. All these unpredictable changes in the configuration bring many challenges to the analysis of the performances, in particular concerning their link with the oscillator geometrical parameters. In addition, the comparison of these experimental data with those obtained by the numerical simulations during the design process cannot lead to valuable conclusions considering these problems. As a conclusion, these assembly issues should be an important concern for the design of new prototypes.

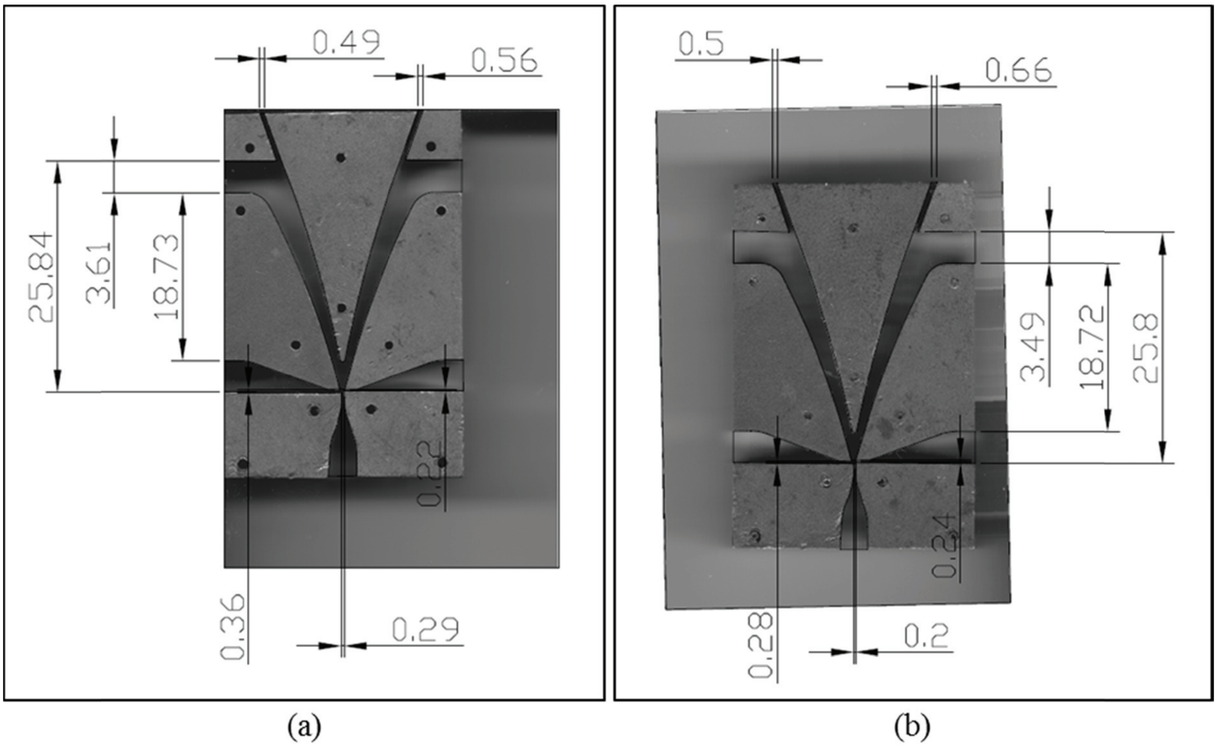

Figure A1-4. Comparison of the channel dimensions (in mm) inside the oscillator; a) before experiments, b) after experiments

Throat clogging:

The oscillator is assembled by pins and glue, however, the glue can easily partially clog the smallest internal sections.

Unfortunately, a partial clogging of the throat was discovered after the end of the experiments presented above. This partial throat blockage induces a reduction of the mass flow rate but also totally destroys the 2D flow pattern inside the oscillator, which can affect the oscillator's performance significantly and makes it difficult to compare the results with the 2D numerical simulations. In addition, it could be one of the origins of the observed unstable oscillation phenomenon.

Leakages:

Air leakages were also found during the tests, due to several problems: firstly, the different components of the oscillator are not fitted perfectly; secondly, the pins are hollow and have a C-shape rather than a round O-shape in order to get a better adaptation in assemblage process. The air can come out easily from these C-shape hollow pins.

A1.2 Measurements by pressure sensor

In order to avoid the above mentioned problems, the following solutions were tested. The liquid glue was replaced with double faced adhesive tape in order to avoid possible clogging in the channel and possible leakage of air since this adhesive tape also plays a role as a gasket. In addition, screw bolts were used to assemble the whole piece to eliminate or at least reduce air leakages.

A1.2.1 Experimental setup introduction

In this series of experiments, only the frequency response was measured using a pressure sensor (Endevco high sensitivity piezoresistive pressure transducer, model 8506-2, whose pressure range is 0-2 psi, and resonance frequency is 45 kHz).

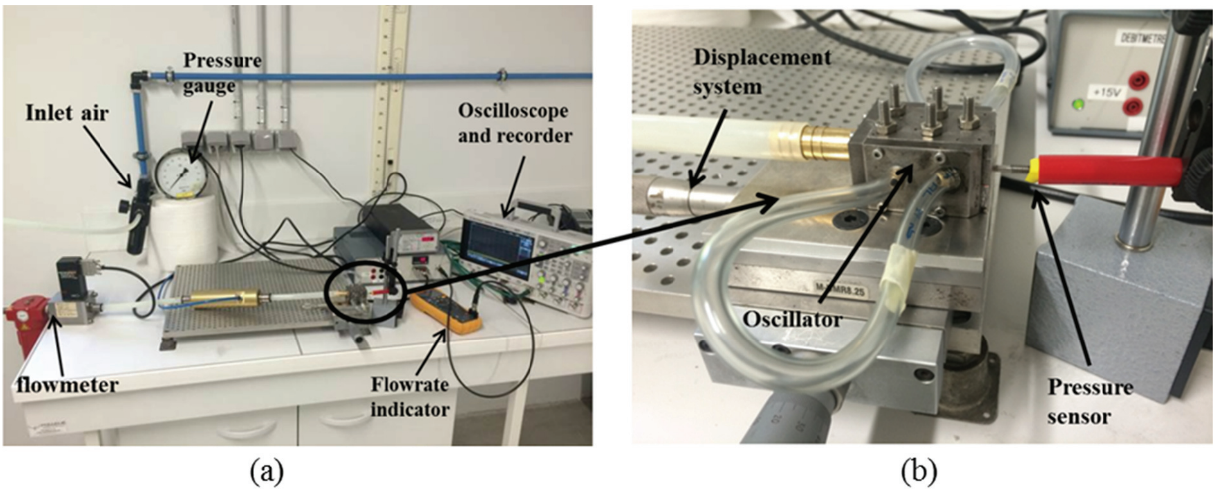

Figure A1-5. Arrangement of the experimental system; a) overall setup, b) oscillator and pressure sensor

As shown in Figure A1-5, the oscillator was installed on a two dimensional displacement system. The pressure sensor was just located in the middle of the left outlet. The distance between the sensor and outlet slot is set arbitrarily, however, it is verified that this distance has no effects on the analyzed oscillation frequency. The transient signal of pressure sensor was monitored and recorded by the oscilloscope. In each measurement, the data acquisition frequency was 25 kHz and the sample size 50,000 which was sufficient to get the main dynamic modes. A 3.5 mm internal diameter soft tube was used to realize the feedback loops. Six cases were tested with feedback tubes of L_t=140, 160, 200, 250, 350 and 500 mm.

A1.2.2 Frequency response to inlet pressure with various feedback tube lengths

The frequency response has been measured for a broad range of supply relative pressures from 0.10 MPa to 0.35 MPa. The effects of the feedback tube length are presented in Figure A1-6. The oscillation frequency starts increasing with the inlet pressure, but reaches a constant and maximum value for inlet pressures higher than the critical value, P_{cr}, which is the same pattern as described in Figure A1-2. When the inlet pressure is higher than 0.28 MPa, the frequency begins to decline slightly, which is unusual. May be it can be explained that when the main jet is too strong in too high inlet pressure conditions, it needs more time to provoke the switch.

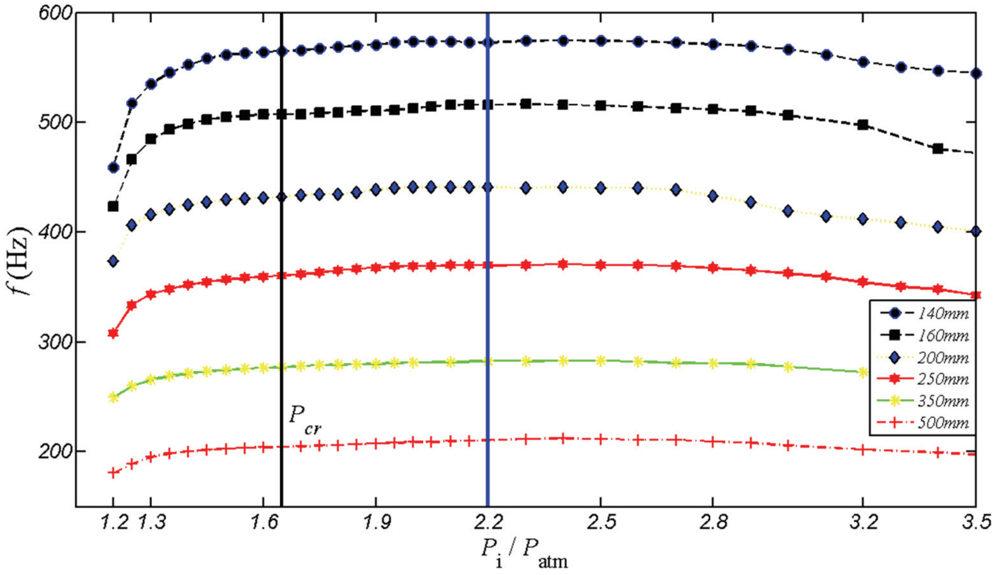

Figure A1-6. Frequency versus inlet pressure for various feedback tube lengths, D = 3.5 mm

Even if the trends are similar, the measured frequencies are much lower (more than 25 %), for the same pressure and feedback tube length, than those obtained during the first experimental campaign (cf. Figure A1-2a), for example, when L_t=160mm, P_i=0.22 MPa, the new measured frequency f = 500 Hz rather than f = 690 Hz in the previous measurement, confirming the strong influence of the leakages and assembly problems described above on the oscillator's performances.

From this series of experiments conducted for 6 different feedback tubes, it can however be shown (cf. Figure A1-7) that the maximum frequency (i.e., for a P_i of 0.22 MPa as indicated by the vertical blue line in Figure A1-6) is inversely proportional to the feedback loop length. This observation implies that it is the propagation effect rather than capability plays the key role in determining the oscillation frequency.

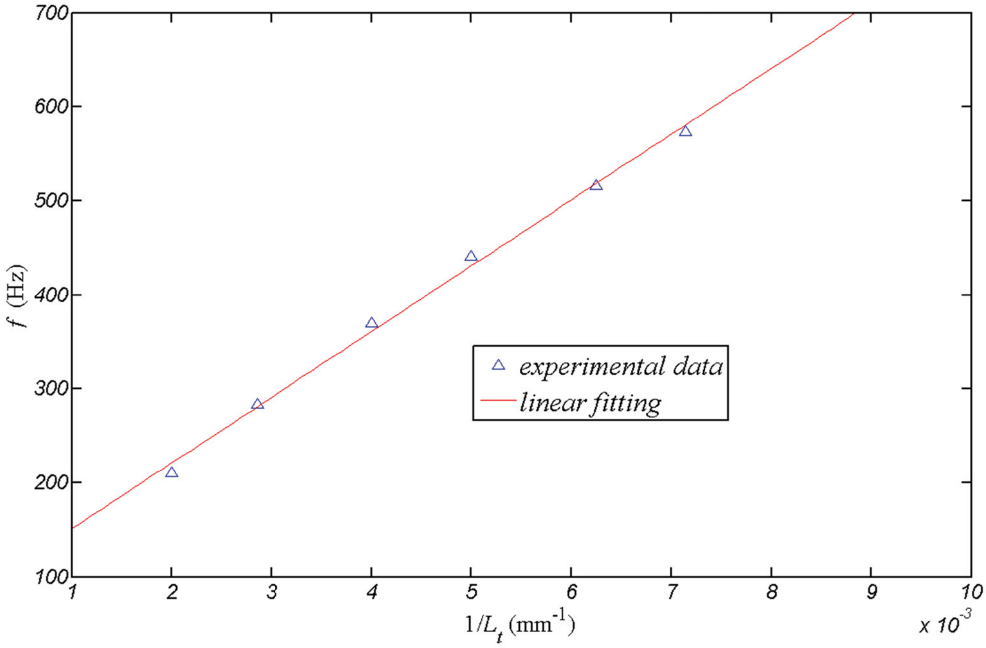

Figure A1-7. Frequency versus inverse value of connection tube length, D=3.5 mm

A1.3 Simulations by FLUENT

As described in section A1.1.3, the real internal dimensions of the oscillator have large deviations with the designed ones and are subject to modifications during the assembly process. Numerical simulations have however been performed, using the commercial CFD software ANSYS/FLUENT. The oscillator's internal geometry used in the numerical models has been obtained by scanning the disassembled prototype just after the end of the first experimental campaign (cf. Figure A1-4b).

A1.3.1 Geometry and numerical settings

The central part dimensions of the oscillator in this series of simulations are shown in Figure A1-4b. In order to limit calculation times, only 2D numerical simulations have been performed, which is reasonable considering the large ratio between the depth of the central part of the prototype (10 mm) over its sub-millimetric transversal dimensions. However, on this prototype, the two feedback loops are made with circular tubes of 3.5 mm internal diameter D. In order to conserve the same capacitive and propagative effects in the 2-D numerical simulations, the lengths of the feedback loops on the numerical models should be the same as the experimental ones but their width D' have to be adjusted to obtain the same volume for the total loop:

$$L_t \pi D^2 / 4 = L_t D' H \rightarrow D' = \pi D^2 / 4H = 0.96\,\text{mm} \qquad \text{(A1-5)}$$

The width adaption is shown in the zoom view of section I in Figure A1-8. The connection channel length is 250 mm from section I to section II.

The mesh files are generated using the software GAMBIT® and only consist of quadrangle cells in order to get high mesh quality. Zoom views of the mesh file in the width adaption part and throat part are proposed in Figure A1-8. The mesh file has a moderate density (79,600 quadrangle cells with 17 nodes in the throat section) and is adapted for the use of a wall function for the near-wall modeling. The maximum value of Y^+ is indeed around 30. The pressure based transient solver is chosen together with the SIMPLE pressure-velocity coupling algorithms. The turbulent model chosen here is the realizable k-epsilon model, associated with a standard wall function. All the spatial terms are discretized in a second order scheme.

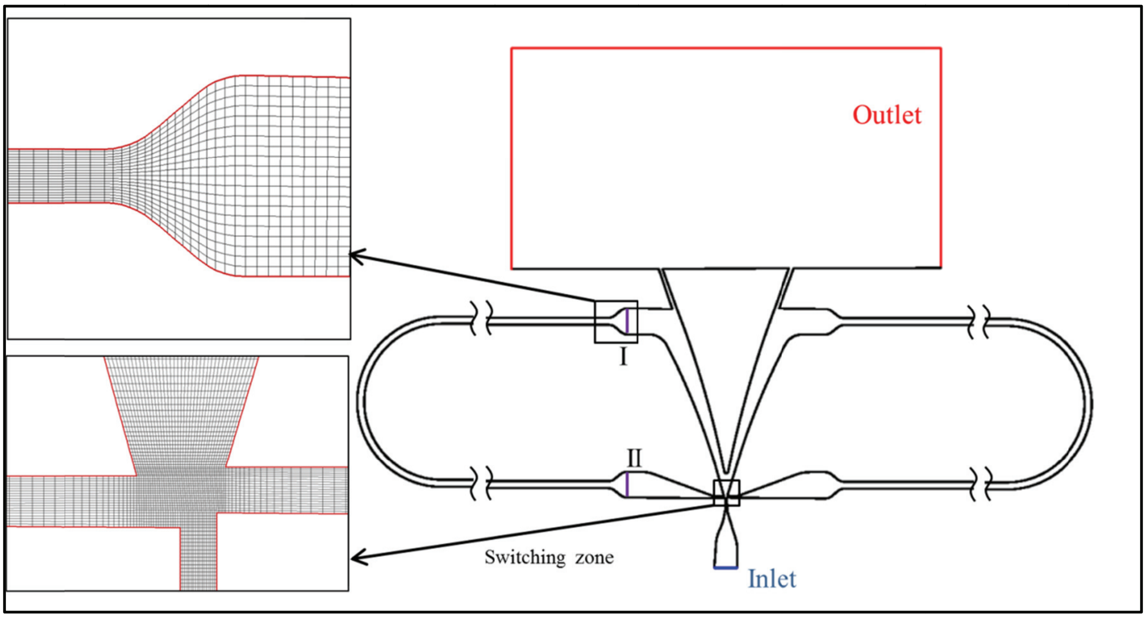

Figure A1-8. Global and zoom views of the simulated geometry

A1.3.2 Sensitivity of transient discretization formula

Different temporal discretization schemes and time steps have been compared in order to test the sensibility of the numerical models to these various settings.

Considering the choice of time step, a compromise had to be found between the 3 following classical criteria: i) At least 20 time steps per oscillation period; ii) Convergence on a time step should be reached after 5-10 iterations; iii) The cell courant number C_{CFL} should be in the range 20-40 in the most sensitive zone, where C_{CFL} is defined by:

$$C_{CFL} = U_x \frac{dt}{dx} + U_y \frac{dt}{dy} \tag{A1-6}$$

In which *dt* is the time step, *dx* is the cell dimension in *x* direction, *dy* is the cell dimension in *y* direction. After the first criterion, if the monitored frequency is 1000 Hz, the time step should smaller than 1/(1000×20)=5×10^{-5} s. For the second criterion, with the current mesh file, the time step should be smaller than 1×10^{-8} s. While after the third criterion, a time step of 5×10^{-7} s should appropriate with the current mesh file.

The predicted oscillation frequencies for different time steps and transient discretization schemes are reported in Table A1-1. The inlet pressure is 0.16 MPa for which the measured frequency was 369 Hz.

Table A1-1. Comparison of the predicted results in various settings

	Time step/(s)	Iteration number per step	Transient formula-implicit order	Simulated frequency (Hz)	Max C_{CFL}
1	5×10^{-5}	350	2nd	447	1530
2	5×10^{-6}	200	1st	380	157
3	5×10^{-6}	200	2nd	454	157
4	1×10^{-6}	40	2nd	384	35
5	5×10^{-7}	30	2nd	384	17
6	1×10^{-7}	25	2nd	457	8.5
7	5×10^{-8}	15	2nd	457	1.7

Obviously, these two settings have a strong influence on the numerical results: two frequencies were found depending on the chosen time step and transient discretization scheme, one of about 380 Hz, close to the measured frequency at 369 Hz, and a much larger one of about 450 Hz. It is however difficult to understand why a 2nd order discretization scheme and a smaller time step, which are presumed to give to more accurate results, can lead to higher discrepancies with the experimental results. In addition, due to the assembly problems described above, the close correspondence between the geometry used in the numerical models and the actual oscillator's internal geometry during the experiments was not ensured, making it very difficult to validate the numerical models in order to use them afterwards for the analysis and design of optimized oscillators.

A1.4 Conclusions

The two experimental campaigns conducted on a first oscillator prototype have evidenced important assembly difficulties leading to leakages and possible modifications of the device's internal dimensions, making it very difficult to analyze the behavior of this oscillator in relation with the geometrical and operation parameters. It has been however observed that:

- the oscillation frequency increases with the inlet pressure in a similar way than the mass flow rate until sonic conditions are reached at the throat, suggesting the existence of a capacitive effect as in the work of Khelfaoui et al. [58].
- once the flow is sonic at the throat, for a given supply pressure, the oscillator's frequency evolves linearly with the feedback tube length, showing that the propagation of pressure waves in the feedback loops could also play a role in the oscillation process.
- a so-called "unstable oscillation" phenomenon appears above a threshold inlet pressure, whose value is in relation with the feedback loops length and diameter. It has been observed that with partial blockage in the throat, it is much easier to provoke the excited mode of oscillation. However, the underlying mechanisms governing this phenomenon are still unclear up to now.

In addition, numerical models built on the CFD software ANSYS/FLUENT have shown an important sensibility to critical settings such as the transient discretization scheme and the time step, not allowing their exploitation for the design of new actuators with optimized performances.

As a consequence, new oscillator prototypes should be developed, solving the identified assembly problems, in order to get more accurate experimental data which could help in identifying and understanding the relation between the actuator's performances and the geometrical parameters and operating conditions.

In addition, more robust numerical models should be built and validated in order to facilitate the analysis of the physical mechanisms governing the internal flow oscillations and thus to draw guidelines for the design of specific actuators.

Annex 2. Sensitivity Study of the Numerical Schemes in OpenFOAM

In the framework of OpenFOAM, taking the calculation cost, accuracy and stability into consideration, the discretization schemes are chosen in a first step as shown in Table A2-1, and the boundary conditions initially utilized in each equation are listed in the following Table A2-2. During each time step, the final residual error is at least 10 orders of magnitude smaller compared to the initial residual error when solve each equation.

Table A2-1. Method and precision of the chosen discretization schemes

	Scheme name		precision
gradSchemes	Gauss linear		2nd order
LaplacianSchemes	Gauss linear corrected 0.5		Blend of 1st and 2nd order
divSchemes	div(phi,U)	Gauss limitedLinear 1	2nd order
	div(phi,e)	Gauss QUICK 2	2nd order
	div(phid,p)	Gauss limitedLinear 1	1st order
	div(phi,K)	Gauss limitedLinear 1	1st order
	div(phi,p)	Gauss limitedLinear 1	1st order
	div(phi,k)	Gauss upwind	1st order
	div(phi,epsilon)	Gauss upwind	1st order
	div((muEff*dev2(T(Grad(U)))))	Gauss linear	2nd order

Table A2-2. Boundary conditions in each equation

equation	inlet	wall	outlet
p	totalPressure	zeroGradient	totalPressure
U	pressureInletVelocity	fixedValue	zeroGradient
T	inletOutlet	zeroGradient	inletOutlet
k	turbulentIntensityKineticEnergyInlet intensity 0.05;	kqRWallFunction	inletOutlet 1
p	turbulentMixingLengthDissipationRateInlet mixingLength 0.005;	epsilonWallFunction	inletOutlet 500
omega	turbulentMixingLengthFrequencyInlet	omegaWallFunction	zeroGradient

A2.1 Geometry and mesh description

The first simulated geometry is shown in Figure A2-1. The dimensions in the central part are shown in Figure A2-1 and Figure A2-2.

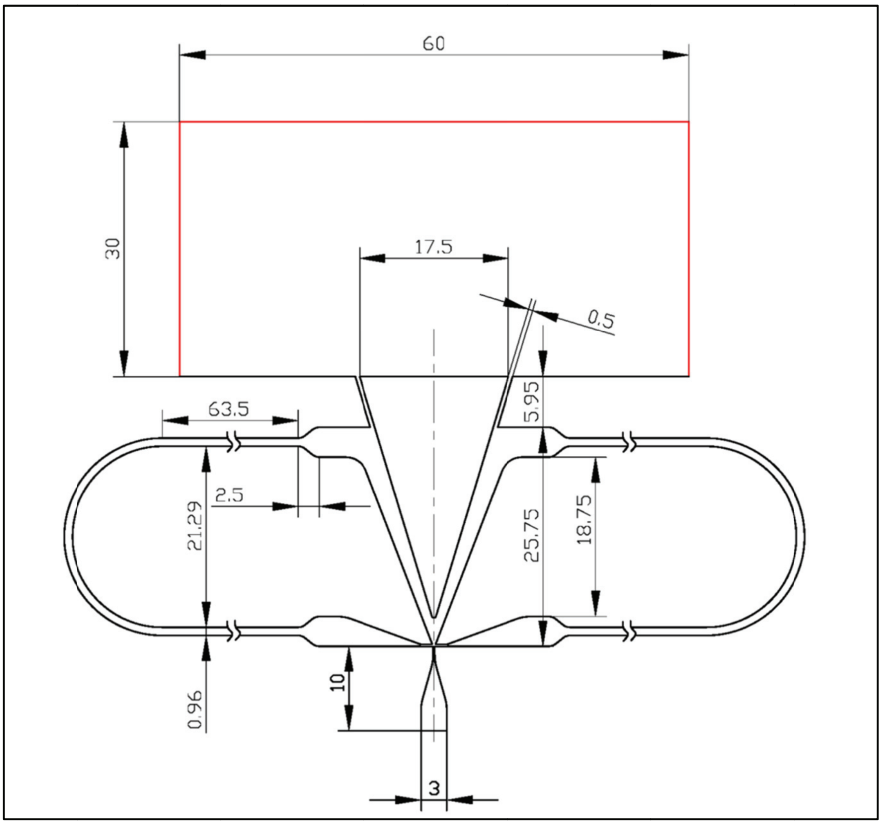

Figure A2-1. Global dimensions of the mesh geometry

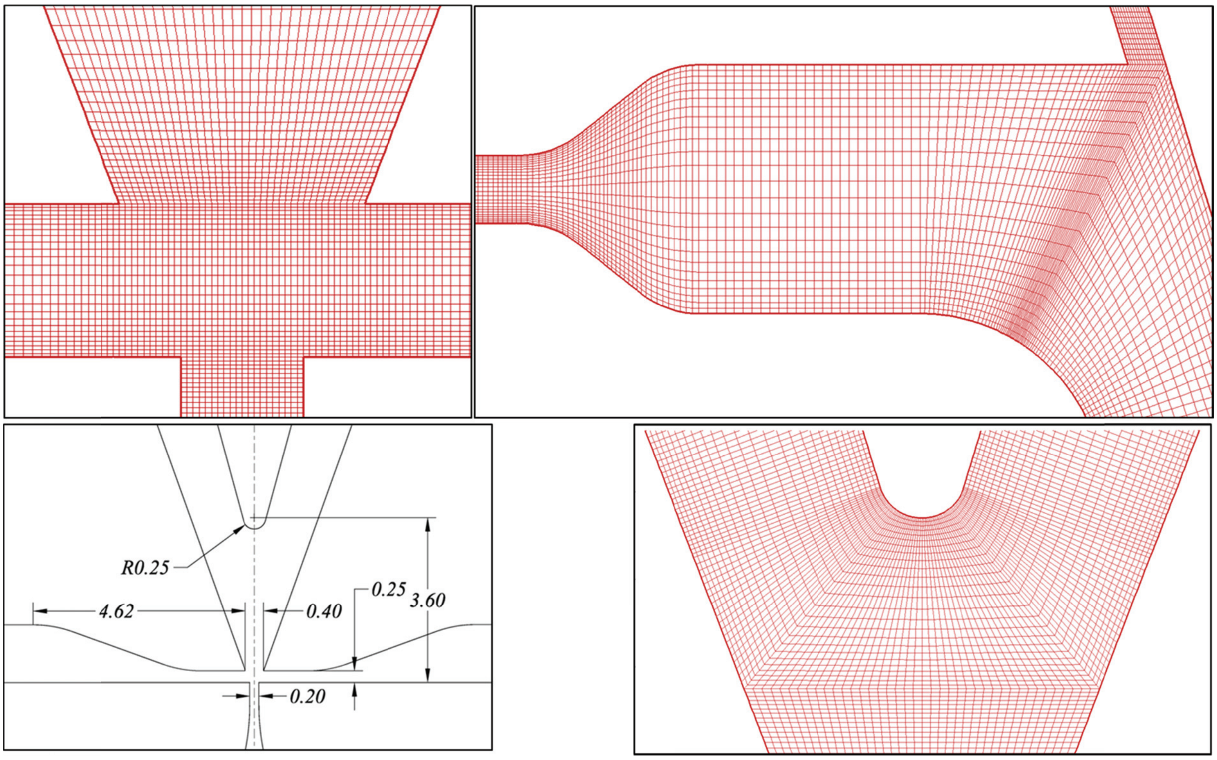

Figure A2-2. Detail of the dimensions in switching zone and cells

The mesh sample in the throat region, switching region and left outlet region are also shown in Figure A2-2. The total mesh number is 104,720, leading to a largest value of Y^+ at the wall ≈ 25 and an average Y^+ ≈ 10. The default inlet pressure $P_\mathrm{i} = 0.25$ MPa in this series of simulations and the default turbulent model is k-epsilon Realizable model.

A2.2 Effects of courant number and discretization scheme

Since in the code of OpenFOAM, the SonicFoam solver is an explicit coupled solver, the CFL rule must be followed, which means that the maximum Courant Number must be smaller than 1, though the temporal discretization scheme is implicit. The choice of time step which decides the Courant Number is critical and it is necessary to study its effects on the simulation results. For a transient case, the temporal discretization scheme may also have a large effect which is worth to be examined.

11 simulation results are shown in the following Table A2-3. In this series of simulations, the default discretization schemes and boundary conditions are as shown in Table A2-1 and Table A2-2 respectively. Two times steps were tested: 1×10^{-8} s and 5×10^{-9} s which lead to maximum courant number of 0.7 and 0.35 respectively. Four discretization schemes of the temporal term were also tested: Euler scheme which is a bounded, implicit, first order precision scheme; CrankNicolson 1.0 which is a bounded, implicit second order precision scheme;

CrankNicolson 0.5 which is the average scheme of Euler and CrankNicolson 1.0; backward is an implicit second order precision scheme. [79] Besides the default schemes of the divergence terms, the second order upwind schemes have been also applied to all the divergence terms.

Table A2-3. Various simulation setups and predicted results

Case number	Max C_{CFL}	Time Scheme	Divergence Scheme	Convergence	BCs	f / Hz	Velocity amplitude
1	0.7	CrankNicolson 0.5	default	Yes	default	640.5	(-40,185)
2	0.7	CrankNicolson 0.5	all 2nd order	No	default	--	--
3	0.7	backward	all 2nd order	No	default	--	--
4	0.35	backward	all 2nd order	No	default	--	--
5	0.35	backward	default	Yes	default	468.2	(-40,145)
6	0.7	backward	default	No	default	--	--
7	0.35	CrankNicolson 0.5	default	Yes	default	650.7	(-30,187)
8	0.7	CrankNicolson 1.0	default	No	default	--	--
9	0.35	CrankNicolson 1.0	default	Yes	default	448.7	(-56,140)
10	0.7	Euler	default	No	default	--	--
11	0.35	Euler	default	Yes	default	649.8	(-30,190)
12	0.35	backward	all 2nd order	Yes	modified	481.4	(-10,85)

As the results shown in Table A2-3, not all the simulations get the converged results: comparing the cases with the same larger Courant number (case 1, 2, 3, 6, 8 and 10), only with the case 1 conditions can we get the converged results while with the smaller Courant number (case 4,5,7,9 and 11), all the simulations get converged results except the case with the all second order divergence schemes (case 4). And this implies that the maximum Courant number has a large effect on the stability of the simulation: the smaller the maximum courant number is, the better is the calculation stability, and the more precise is the predicted results theoretically. However, the smaller courant number means a smaller time step with certain mesh file, and this leads to more calculation resource requirement. A compromise is needed in order to get an acceptable stability, precision and cost.

With the higher order temporal discretization schemes, both backward and CrankNicolson 1.0 (case 5 and 9), the predicted oscillation frequency and velocity amplitude in the center of left outlet are similar, with less than 5% difference. While compared to the results obtained by lower order schemes, the difference can be as large as 40%.

The choice of different discretization schemes of the divergence terms has big effects on the final results: with the second order upwind scheme in all divergence terms (case 2, 3 and 4), no converged results can be obtained in either condition. This means that the divergence term discretization schemes have has large effects on the simulation stability. Simulation is very sensitive to the schemes of convection terms. In theory, a higher precision scheme can lead to higher precision, and there is no reason that the second order upwind scheme in the convection terms always lead to the crash of simulation.

A second order discretization scheme is always preferred in order to get better prediction results. The reason why the calculation always crashes with second order scheme in convection terms maybe is that the boundary conditions are not conform to the physical conditions. Under this logic, in case 12, the outlet boundary conditions of both k equation and epsilon equation are modified to zeroGradient from inletOutlet; and the inlet turbulent mixingLength in epsilon equation is modified from 0.005m to 0.0005m which is more like the reality case. the predicted frequency is 481.4Hz which is similar to case 5’s 468.2Hz, while the velocity amplitude is 95 m/s which is much different to 185 m/s in case 5.

In conclusion, under the hypothesis that higher order discretization schemes and smaller time step always lead to better results, the smaller C_{CFL} value, backward temporal scheme, second order scheme in convection terms and modified boundary conditions are better choice for all the following simulations.

In the following simulations, the geometry utilized is the designed new oscillator prototype Osc.2 as shown in Figure 2-1 and Figure 2-2 and the mesh density is similar to that in Figure A2-2. At the same time of testing the effects of various numerical parameters, the predicted results can also offer some information about the performance of this new designed prototype.

A2.3 Effects of wall function

As a turbulent flow approaches a wall, its mean and fluctuating components of velocity, and consequently k, vanish creating large gradients. In addition, the very high turbulent stresses away from the wall decrease in the near wall layer to values of magnitude comparable to those of the viscous stresses. Therefore if the near wall layer is to be resolved, a substantial number of grid points will be required. [80]

Low Reynolds number turbulence models are capable of simulating the dampening effects of the wall but at the expense of using a very large number of grid points. This is the unavoidable cost that has to be paid if accurate solutions of the flow in the near wall region are required.

On the other hand, the high Reynolds number turbulence approach, exemplified by the standard k-epsilon model, avoids the need to resolve the near wall layer through the use of wall functions. In this method, theoretical profiles between the boundary surface and the first near-wall code are assumed and superimposed. Compared to the previous approach, wall functions reduce significantly the computational cost. The main disadvantage of this methodology however, is related to the validity of these profiles, which are only known and justified in near-equilibrium boundary layers. [80]

OpenFOAM offers both high Reynolds number turbulence models like the k-epsilon model family and low Reynolds number turbulence model like the k-omega SST model, and different wall functions for both the normal condition and the low Reynolds number condition.

The flow inside the oscillator has a very complex flow pattern: the jet is oscillating between the two branches and feedback loops which leads to the velocity difference between the two sides of the oscillator. Take the mesh file in Figure A2-2 for example, when the main jet is attached to left branch, the Y^+ value is in an order of 30 in the beginning of attachment and decreases to less than 5 in the left feedback loop; while in the right side branch, the Y^+ value is always less than 1 in the right feedback loop. This complexity leads to the difficulty of choosing the appropriate turbulent model and wall function. In the switching zone in which the flow is in the highest velocity and complexity, the Y^+ value varies the most (from 5 to 30). And in this condition, it is not sure that if the application of low Reynolds number turbulence model or high Reynolds number turbulence model is appropriate. If the largest Y^+ value inside the entire oscillator is smaller than 1, the application of kOmegaSST and the low Reynolds number wall functions would be the most precise choice. However, this needs much denser mesh file, speciously near the wall, and much smaller time step in order to keep the same maximum courant number. In order to avoid the high calculation cost, the tests of different wall function and turbulence model were carried out firstly.

Two simulations were carried out in the same new designed geometry Osc.2 and the same mesh file with moderate density which is similar to that described in Figure A2-1. The numerical schemes and boundary conditions are the same as the modified ones described above in the first simulation. While in the other simulation, the boundary conditions of wall in both k and epsilon equations are modified to the low Reynolds number wall functions.

Table A2-4. simulation results with different wall function

	p	U	f (Hz)	U_y range (m/s)
Simu 1	kqRWallFunction	epsilonWallFunction	506	(-10,170)
Simu 2	kLowReWallFunction	epsilonLowReWallFunction	545	(60,150)

As can be seen in Table A2-4, compared to the predicted frequency with normal wall function 506 Hz, the predicted frequency with low Reynolds number wall function is 545 Hz, about 9% larger. And in the same time, the amplitude of the U_y is much smaller in the latter case. All these differences indicate that the choice of wall function is critical to the precision of simulation results.

A2.4 Effects of outlet boundary condition in p equation

With the modification of outlet boundary condition of p equation from totalPressure to fixedValue, both the predicted frequency and the amplitude of outlet velocity have little change which can be observed in Figure A2-3.

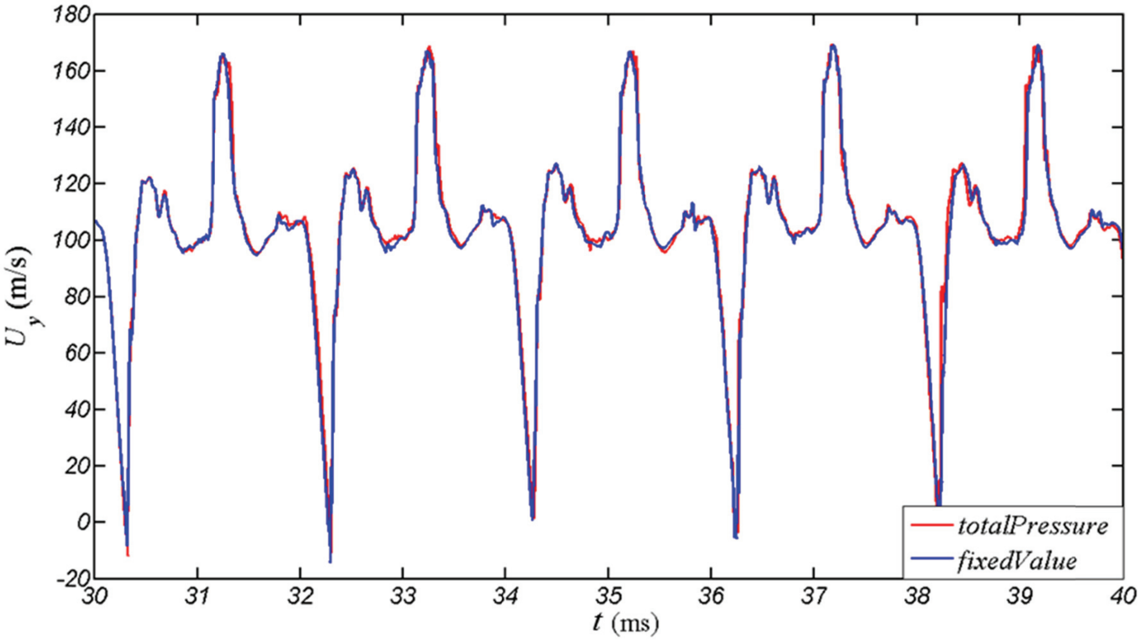

Figure A2-3. Predicted velocity in left outlet center with different outlet boundary condition of p equation

Thus, discretization methods and boundary conditions shown in Table A2-5 and Table A2-6 is preferred in the following simulations.

Table A2-5. modified discretization method of all terms

	Scheme name	precision
ddt	backward	2nd order
gradSchemes	Gauss linear	2nd order
LaplacianSchemes	Gauss linear corrected 0.5	Blend of 1st and 2nd order
divSchemes	Gauss linearUpwind grad( )	2nd order

Table A2-6. Modified boundary condition in all equations

equation	inlet	wall	outlet
p	totalPressure	zeroGradient	fixedValue
U	pressureInletVelocity	fixedValue	zeroGradient
T	inletOutlet	zeroGradient	inletOutlet
k	turbulentIntensity-KineticEnergyInlet intensity 0.05;	kqRWallFunction	zeroGradient
epsilon	turbulentMixingLength-DissipationRateInlet mixingLength 0.0005;	epsilonWallFunction	zeroGradient
omega	turbulentMixingLength-FrequencyInlet mixingLength 0.0005;	omegaWallFunction	zeroGradient

A2.5 Effects of turbulence model choice

In base of the previous works, various turbulence models were also tested. With the same discretization methods in Table A2-5 and boundary conditions in Table A2-6, not all the simulations can get the converged results. In order to get the converged results, some discretization method should be modified in some terms. As shown in Table A2-7, with the current mesh and numerical settings, only the k-e realizable turbulence model can get a converged results, while for the standard k-epsilon model and RNG k-e model, the convection terms or divergence terms should be discretized in a default method as shown in Table A2-1. And in the case of k-omega-SST turbulence model, besides the default schemes in convection terms, the transient term scheme should also be modified to a Euler scheme which is a 1st order precision scheme.

Table A2-7. Simulation results with various turbulence models

	Transient term	Convection term	f (Hz)	U_y range (ms^{-1})
k-epsilon	backward	default	542.6	(70, 125)
RNG k-e	backward	default	452.8	(-31, 130)
k-e Realizable	backward	2nd order Upwind	506.4	(-10, 170)
k-Omega-SST	Euler	default	488.9	(-10, 180)

As can be clearly observed in the above table, the difference between the predicted results using different turbulence models is huge. Compared to the results by k-e Realizable model, the predicted frequency by k-epsilon model is 7% higher and the U_y range is 70% smaller; while with the RNG k-e model, the frequency is 10% lower and the U_y range is 11% smaller. For the case of k-Omega-SST model, the frequency is only 3.4% lower and the U_y range is very similar (5% larger). With the preference of higher order schemes and the higher calculation stability, with the current mesh, the k-e realizable turbulence model is preferred.

A2.6 Effects of mesh density choice

The effect of the mesh density has been also verified with the kOmegaSST turbulence model. The mesh density next to the boundary has been increased a lot which can be observed in Figure A2-4. With this mesh file, the maximum Y^+ throughout the domain is about 1 in order to apply the low Reynolds number wall function in k and Omega equations. In this case, there are 406000 quad cells in total which is about 4 times of the normal mesh, and the corresponding time step is 1×10^{-9}s, which is only one fifth of the previous one in order to insure the same maximum courant number. Under these conditions, just getting the same simulated period, at least 20 times of the calculation resources are needed which is unacceptable in general.

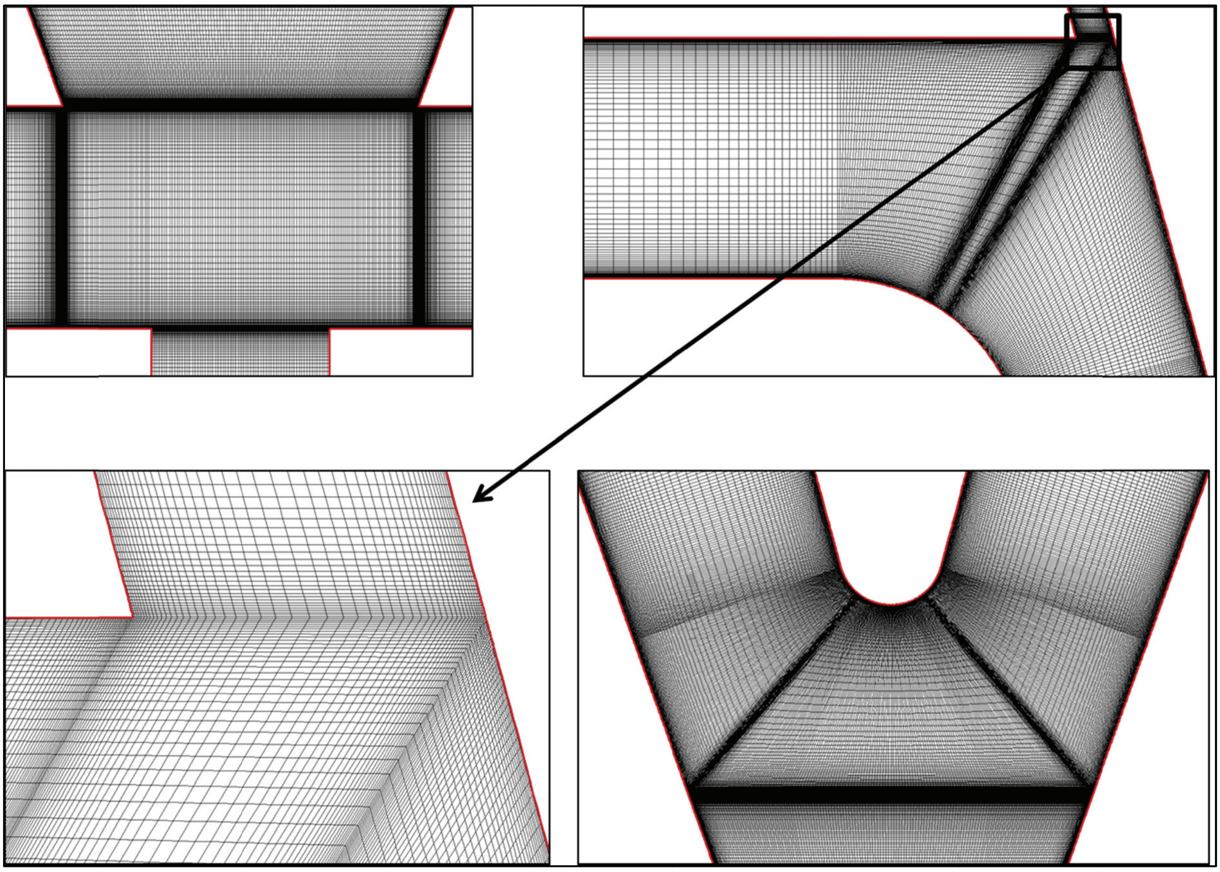

Figure A2-4. Glimpses of the dense mesh

However, with this mesh file, together with the k-Omega-SST model and low Reynolds Numebr wall function, their simulated results are the most reliable compared to other choices, considering their treatment of both viscous sub-layer and the damping effect of turbulence near the wall [90]. Thus, the predicted results can be one of the choices to validate the other numerical settings.

The predicted frequency and U_y range with both 1st order and 2nd order temporary discretization schemes are compared in Figure A2-5. With this dense mesh file, under the 2nd order upwind discretization scheme of convection terms, both Euler and backward temporary schemes lead to similar frequency (~510 Hz) and U_y range (25~170 m/s). Compared to the results with also the kOmegaSST model, but in normal mesh shown in Table A2-8, the predictions have 4% deviation in frequency, and 15% deviation in U_y range. However, the k-e Realizable model gives predictions of 0.9% deviation in frequency. Thus, the k-e Realizable model along with the normal mesh and relevant settings would be the best alternative choice of the k-Omega-SST model with dense mesh, especially considering the frequency prediction capability.

Table A2-8. Comparison of predicted results with kOmegaSST turbulence model

	Mesh density	Temporal scheme	*f* (Hz)	U_y range (ms^{-1})
k-Omega-SST	Normal	Euler	488.9	(-10, 180)
k-Omega-SST	Dense	Euler	513	(25, 170)
k-Omega-SST	Dense	backward	511	(25, 170)

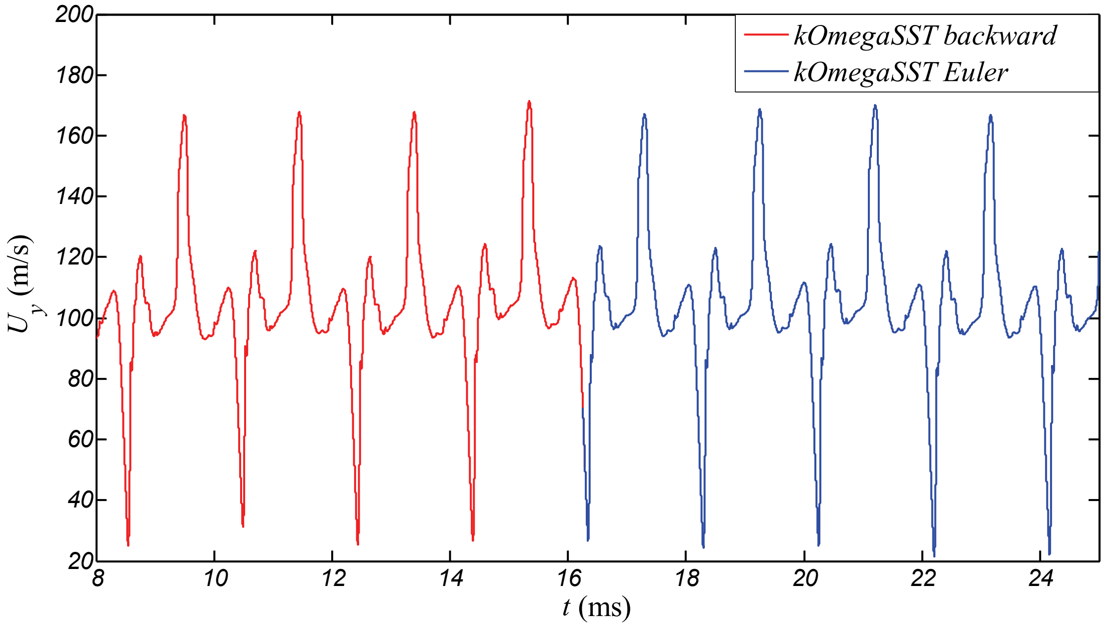

Figure A2-5. Comparison of predicted results with different temporal schemes, k-Omega-SST turbulence model

A2.7 Remarks and comments

Considering the calculation precision and efficiency, the realizable k-epsilon turbulent model, with moderate mesh density and normal wall function would be the best choice for the following work. The chosen discretization schemes and boundary conditions for each equation are the same as that in Table A2-5 and Table A2-6 respectively.

Annex 3. Components of turbulent flow measured by PIV

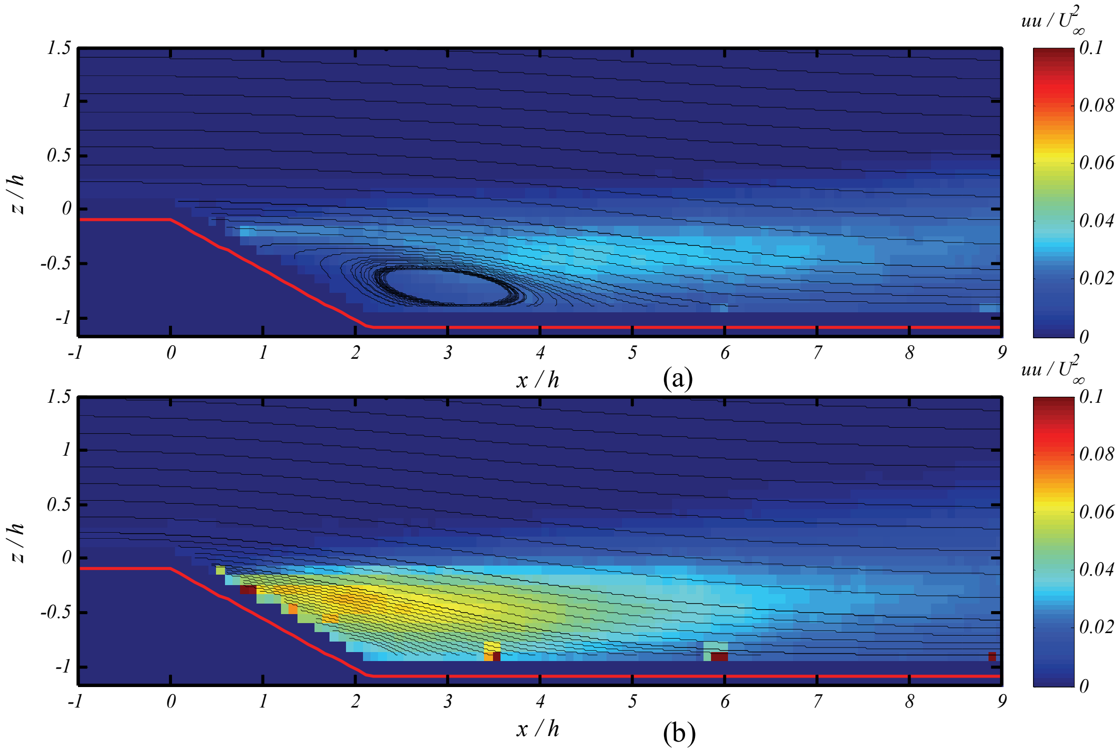

Figure A3- 1. Reynold stress component $<u'u'>$ contours, a) baseline flow; b) controlled flow, $C_\mu = 0.16\%$

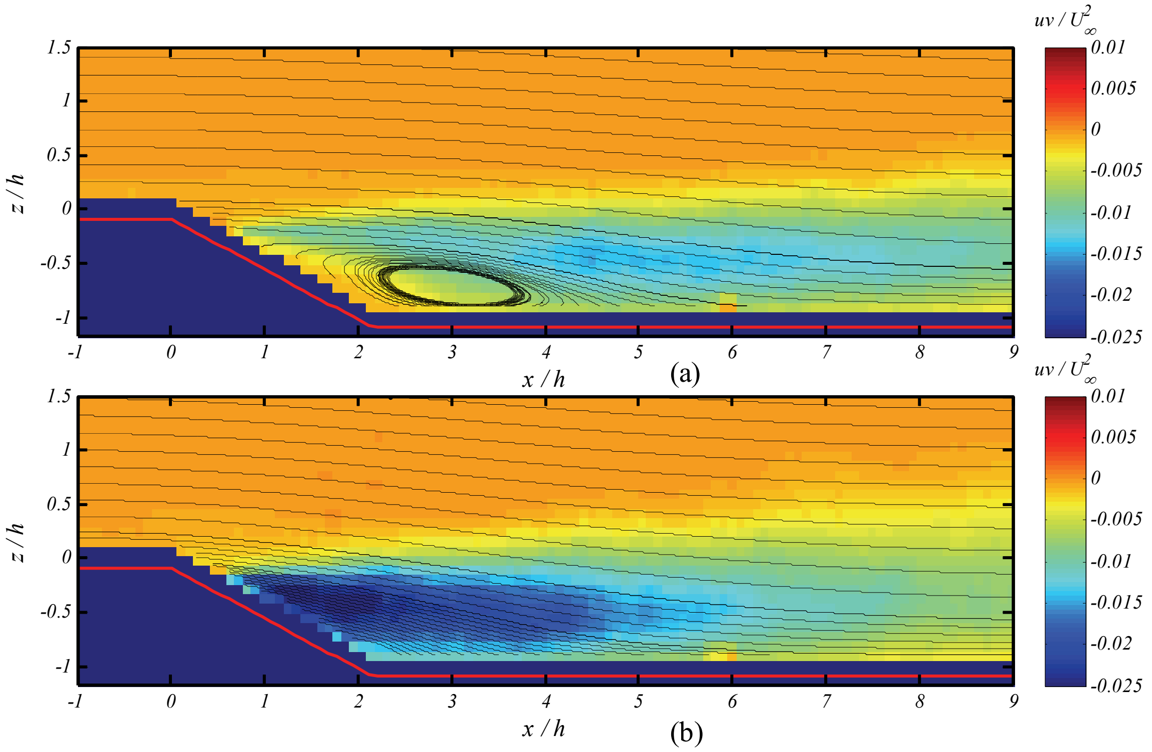

Figure A3- 2. Reynold stress component <*u'v'*> contours, a) baseline flow; b) controlled flow, $C_\mu = 0.16\%$

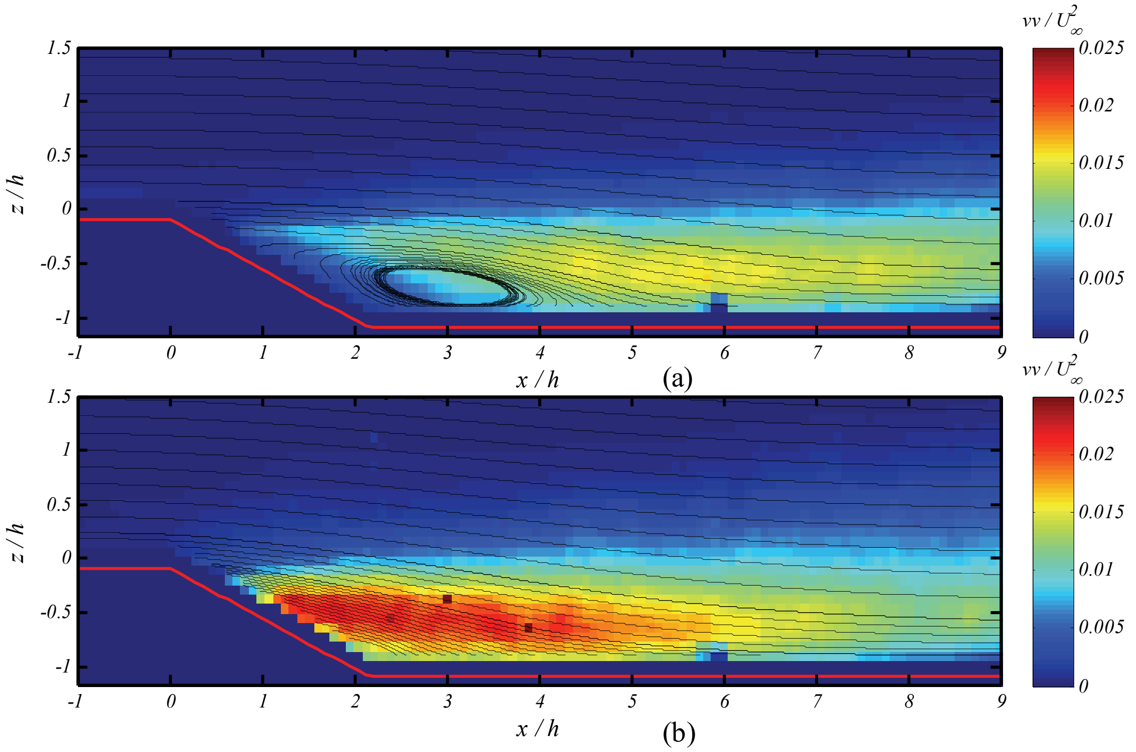

Figure A3- 3. Reynold stress component <*v'v'*> contours, a) baseline flow; b) controlled flow, $C_\mu = 0.16\%$

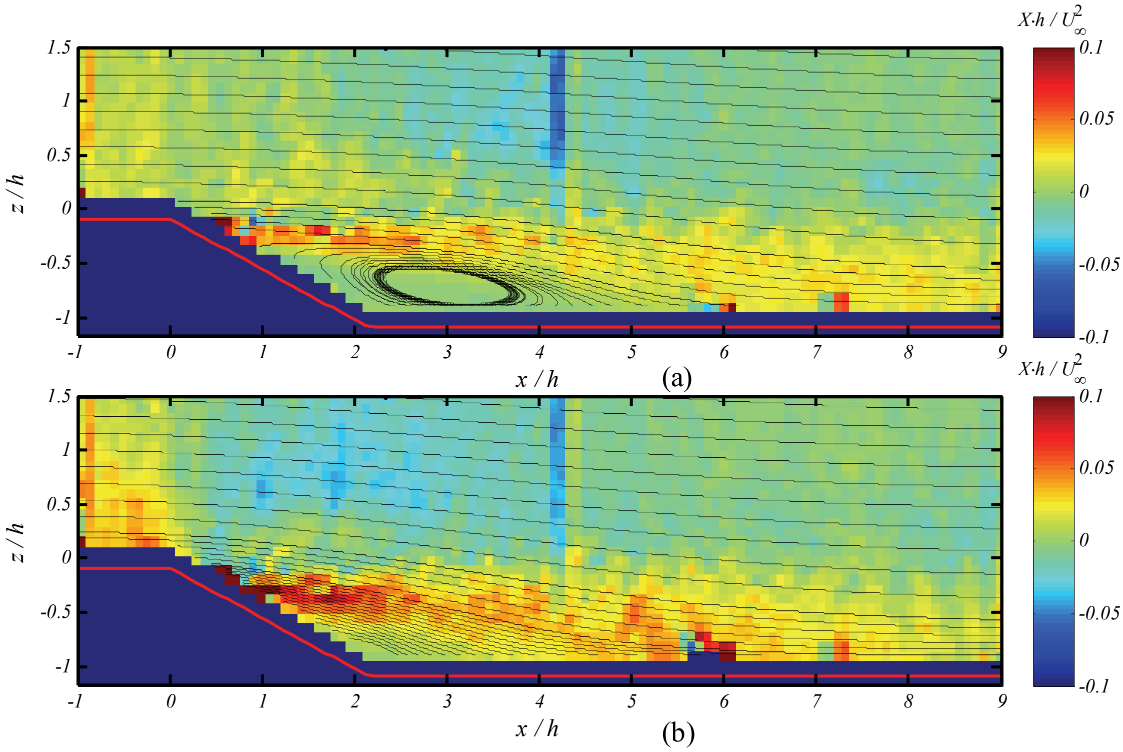

Figure A3- 4. Contours of $X = U_x \frac{\partial U_x}{\partial x}$ scaled by $\frac{U_\infty^2}{h}$, a) baseline flow; b) controlled flow, C_μ = 0.16%

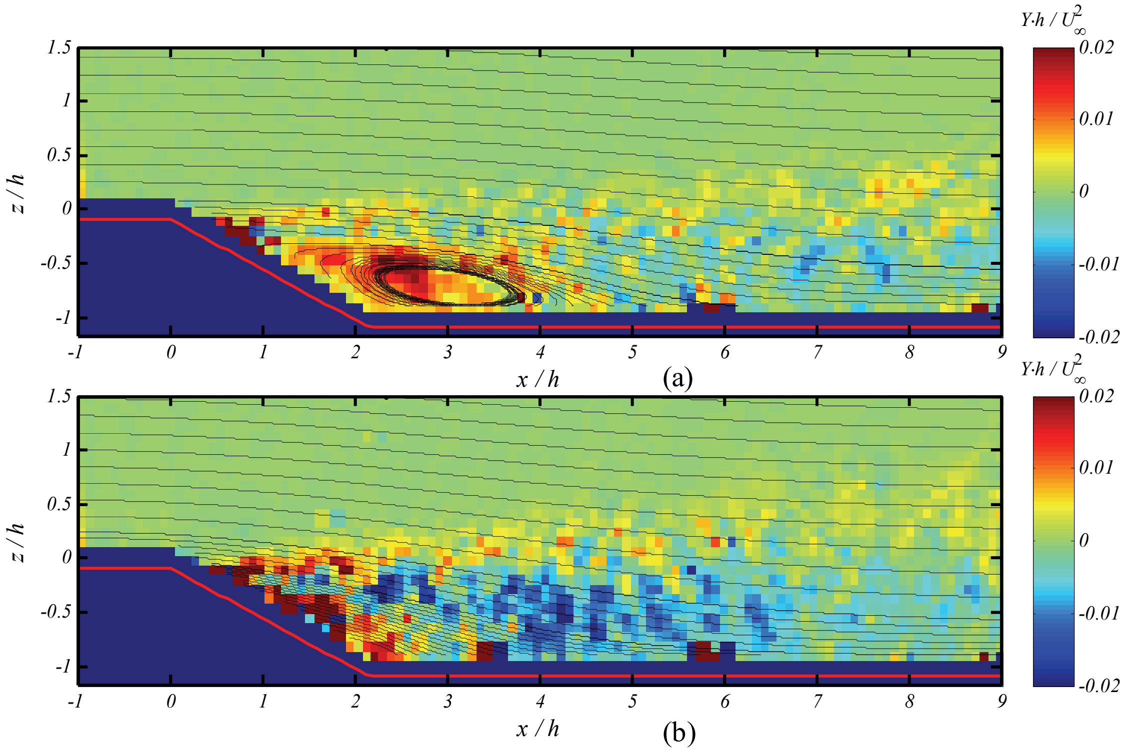

(a)

(b)

Figure A3- 5. Contours of *x* direction gradient of Reynold stress component <*u'u'*>, $Y = \frac{\partial < u'u' >}{\partial x}$ scaled by $\frac{U_\infty^2}{h}$, a) baseline flow; b) controlled flow, $C_\mu = 0.16\%$